Scientific Visualization of Stress Tensor Information with Applications to Stress Determination by X-ray and Neutron Diffraction

Mecit Yaman

A dissertation submitted to the Department of Physics of the University of Cape Town in partial fulfilment of the requirements for the degree of Doctor of Philosophy

University of Cape Town
June, 2007

This thesis is approved by

_____

_____

_____

"States of stress may be illustrated in various ways by means of diagrams, but complete diagrammatic representations cannot easily be found." A.E.H. Love, 1892

"Truth is not found by addition and multiplication only." Max Müller, 1882

Abstract

Applied and/or residual mechanical stresses are important factors concerning the endurance and deformation of solid materials. Consequently, non-destructive stress determination in polycrystalline solids, with x-ray, neutron and synchrotron diffraction, has been extensively used to characterize stresses, in a wide range of applications in materials science and engineering. However, most stress determination measurements, still, do not take into account the tensor characteristics of mechanical stress, and confine the analysis to less complicated vector and, more often, scalar methods. In most cases, the unavailability of a user friendly conceptual tool for the exploration, analysis and presentation of tensorial stresses hinders complete analysis.

The visual analysis of mechanical stress facilitates physical understanding of the tensor quantity which is concealed in scalar and vector methods. In this study, the principles and techniques of scientific visualization are used to develop a visual analysis of mechanical stresses. Scientific visualization is not only applied to the final tensorial quantity obtained from the diffraction measurements, but the visual methods are developed from, and integrated into current residual stress analysis practices by relating the newly developed visual techniques to the conventional techniques, highlighting its advantages.

This study consists of the mathematical analysis of the tensor character of mechanical stresses, discussion of the principles and techniques of scientific visualization (visual data analysis) in physical research, and tensor determination, visual analysis and presentation of residual stresses obtained from diffraction measurements. This thesis concludes with three case studies from materials research and engineering that demonstrate the use of the visual tools developed.

Acknowledgements

I am grateful to Professor M. Harting for the suggestion of the topic as well as providing guidance, supervision, counselling, and financial assistance– the STRESS research group has been a challenging as well as enjoyable work environment throughout the course of this work. I also thank the fellow members of the STRESS group for valuable discussions and support, and the staff of the Department of Physics of the University of Cape Town for constant assistance. I would like to thank Professor R.D. Kriz for making it possible to use the facilities at the visualization laboratory at the Virginia Tech, and for insightful discussions. I would like to thank Professor A.D. Krawitz for the provision of one of the first tensor datasets obtained from a neutron diffraction measurement. Finally, it is a great pleasure to acknowledge that, in all that I have ever achieved, no one has more claim than my parents.

Symbol	Definition	Components
x_i, x_i'	Cartesian coordinate systems	x_1, x_2, x_3 and x_1', x_2', x_3'
(β_{ij})	direction cosine matrix	β_{ij}
Φ	scalar function	
$\mathbf{R}$	vector function	R_i
$\mathbf{T}, (T_{ij})$	second order tensor	T_{ij}
$\mathbf{S}$	symmetric tensor	$S_{ij} = S_{ji}$
$\mathbf{A}$	anti-symmetric tensor	$A_{ij} = -A_{ji}$
$\boldsymbol{\upsilon}$	eigenvector	υ_i
λ_i	eigenvalues	
δ_{ij}	Kronecker delta function	
ε_{ijk}	Permutation function	
$\mathbf{a} \cdot \mathbf{b}$	inner product of vectors **a**, **b**	
ΔM	mass	
B	material continuum	
S	surface	
$\hat{\mathbf{n}}$	unit normal vector	n_1, n_2, n_3
$\overset{n}{\mathbf{T}}$,	stress traction vector	$\overset{n}{T}_i$
$\boldsymbol{\sigma}_i$	stress vector	
$\boldsymbol{\sigma}, (\sigma_{ij})$	stress tensor	σ_{ij}
$\sigma_1, \sigma_2, \sigma_3$	principal stresses	
ξ_1, ξ_2, ξ_3	principal axes	
σ_n	normal stress component	
τ	shear stress component	
$\mathbf{u}$	displacement vector	u, v, w
$\mathbf{e}, (e_{ij})$	strain tensor for finite deformations	e_{ij}
(ε_{ij})	infinitesimal strain tensor	ε_{ij}
$\varepsilon_1, \varepsilon_2, \varepsilon_3$	principal strains	
C_{ijkl}	elasticity constants	
S_{klmn}	elastic compliances	
υ	Poisson ration	
E	Youngs modulus	
χ	Stress function	

Table of Contents

1 Introduction

The functionality of all natural or man-made materials ultimately depends on their structural form. One of the main factors concerning the stability and deformation of these structures is the applied or residual mechanical stress [1]. In general, mechanical stress is a complex physical quantity involving interacting forces and surfaces which cannot be mathematically described as a scalar or a vector. For a mathematical analysis of physical entities such as stress and strain, the full tensor description must be used. In fact, the original concept of tensors was the product of the effort to understand and control the fracture of solids [2].

Despite the fact that the theoretical framework for the description of mechanical stress (and strain) had been finalized in the early nineteenth century, until recently experimental methods in stress determination and analysis have been limited to scalar descriptions of the tensor stress components [1, 3]. This restriction was, of course, partly due to the limitations of equipment and experimental techniques, but also the unavailability of conceptual tools to explore, analyze and represent tensor information hindered the complete analysis. For example, until recently stress determination by means of x-ray or neutron diffraction, which are principle stress determination techniques in materials science and engineering, were limited to either scalar $\sin^2\psi$ analysis or the measurement of three orthogonal stress vectors [1, 3]. Although, when applied correctly, these partial approaches provide reliable criteria for engineering decision making, they fall short in revealing the tensor stress state. Today, advancements in diffraction technology and the availability of high energy beamlines, such as synchrotrons and neutron diffraction facilities, enable researchers to determine full stress tensor profiles by collecting gigantic amounts of diffraction data in relatively short times [4]. The challenging issue in the analysis of such large diffraction datasets is not just the sheer amount of the numerical data to be processed, but a complete analysis requires the development and application of suitable and easy-to-use conceptual tools. This thesis is concerned with the development of conceptual visual tools for the complete (tensor) analysis of stress information obtained from diffraction measurements.

One such visual method to help explore the diagonalized stress tensor is the Mohr circle [5] which was developed prior to the introduction of digital computers. With the advent of digital computers and the introduction of scientific visualization – the formal discipline concerning the graphic representation of complex or very large scientific data – in the 1990's, tensor visualization became a major field of research [6, 7]. The goal of tensor visualization is to develop conceptual methods for the exploration and interpretation of tensor data. Besides mechanics of materials, tensor visualization has diverse application in areas such as flow visualization in aerodynamics, diffusion tensor visualizations in medicine, stress visualization in geomechanics, *etc*. The common expected benefit of tensor visualization in all these fields is to obtain new information regarding the nature of the physical process which otherwise remain hidden. However, general methodologies for visualizing tensor data must be tailored to more specific problems [8]. In this thesis, the application of scientific visualization in the context of scientific research, and particularly in stress determination, is presented in detail to introduce and highlight the benefits of using scientific visualization in basic physics research.

In order to evaluate the promises of scientific visualization in the field of stress analysis, firstly, scientific visualization is placed in context within the broader scientific enquiry. Scientific visualization is presented as an integral part of the scientific approach which includes the setting of a scientific hypothesis, the collection of numerical data and building of the physical and mathematical models. Secondly, the visual exploration of the scientific data is achieved through a visualization mapping process, in which a visual object is used to represent the quantitative data. This visualization process, or pipeline, is discussed with emphasis on visualization goals, data structures, visualization mapping (the design of a visual icon) and visual extensions (the visual attributes of the icon). The rendering, perception and cognition of the visual icon are essential elements of scientific visualization, and therefore discussed in detail. In addition, Brodlie's taxonomy for scientific data [9] is used for the classification of the data. This approach results in the introduction of the concept of *data isomorphism* into scientific visualization. The idea of data isomorphism is used to differentiate between, for example, multiple scalar fields and tensor fields. This concept is later used to justify the use of specific visualization idioms for tensors in distinction to scalars and vectors.

Following the discussion of the principles of scientific visualization, a structured review of scalar and vector visualization techniques is given with examples. Afterwards, the tensor visualization techniques are described with emphasis on the stress tensor. This section includes a review of Mohr circles. Point tensor icons are then classified, according to the mapping processes as eigenicons, traction based icons, and the stress quadric surface. A new hybrid stress icon is introduced, the PNS icon, that maps principal, normal and shear stress information simultaneously, and is therefore more effective for the representation of the complete stress information.

The application of scientific visualization for the analysis of stress tensor information of residual stress data obtained by diffraction methods is scarce. To our knowledge only one publication addresses this problem, leading to preliminary results as discussed in section 4.3.7.2. In this work the main emphasis is on the visualization of different levels of tensor information contained in the diffraction datasets depending on the experimental approach. Therefore, the point icons are used in conjunction with the results of the conventional $\sin^2\psi$ method, to illustrate the use of icons in the context of a diffraction experiment. The ambiguity of $\sin^2\psi$ plots, for the cases of flat, linear and non-linear or sloping $\sin^2\psi$ plots, regarding the underlying tensor stresses is clearly illustrated. Five different point icons are individually discussed, and the advantages and disadvantages of each one are discussed in detail, according to the principles of scientific visualization.

Furthermore, in three different case studies, scientific visualization techniques are used to explore stress profiles obtained by x-ray and neutron diffraction. Case study 1 involves the application of visualization to explore the stress depth profile in a titanium specimen, before and after different doses of krypton implantation [10]. The resulting stress states are visualized for unimplanted, low dose implanted and high dose implanted specimens. The use of visual icons for the representation of stress tensors, simplifies and makes it easier to conceptualize the effect of implantation on the stress state. In case study 2, the scientific visualization of the tri-axial tensor stress profile of a shot-peened titanium alloy (Ti-6Al-4V) component is discussed [11]. Hidden features of the stress state, such as the principal stress directions and shear stresses are revealed using the visual icons. In case study 3, the effects of welding and

heat treatment on the stress profile of a hardened HP-9Ni-4Co-0.3C steel component are studied. The tensor stress profiles were determined using neutron diffraction by Winholtz and Krawitz [12]. The visualizations reveal significant information regarding the directionality of the principal stresses and the shear character of the stress tensors.

2 Tensor Description of Stress and Strain

The mathematical theory of the deformations of solids was developed mainly by the French mathematicians C. Navier, A. Cauchy and S. D. Poisson in the first half of the nineteenth century [13]. This mathematical formulation is based on the continuum assumption and comprises geometric analysis of deformation, or strain, and the mathematical analysis of stress in solids. The concepts of stress and strain are subsequently integrated by the experimental Hooke's law which was discovered by the English scientist R. Hooke two centuries prior to the development of the mathematical theory. The theory of elasticity makes use of the concept of tensors, which is a natural extension of the concept of scalars and vectors, to quantify the geometric deformations of surfaces and volumes as well as the forces acting on them. The tensor concepts introduced in this chapter have a two fold importance. Firstly, the tensor concepts for stress and strain are the backbone of the techniques used for the determination of tensor stress by diffraction methods. Secondly, the design of visualization idioms for second order tensors is based on the mathematical properties of tensors.

In this chapter formal mathematical definitions of scalars as zeroth order tensors, vectors as first order tensors, and second order tensors are given. Important properties of second order tensors relevant to visualization are described by drawing parallels with scalars and vectors. This is followed by the tensor definition of stress and strain separately in continuum mechanics. Properties of the three dimensional tensor stress and derived quantities are emphasized, *e.g.* the traction or stress vector, coordinate transformations of stress tensors and principal stresses are described, all of which are later used in developing the visualization schemes. The review of the stress tensor is followed by the definition of the strain tensor, with discussions of diagonal and off-diagonal elements of the strain tensor, and the geometric meaning of the linear strain tensor elements. In the final section stress and strain tensors are related by the fourth rank elasticity tensor and common engineering and scientific representations of the elasticity tensor are given.

2.1 Analytical Definition of Scalars, Vectors and Tensors

Two fixed sets of rectangular Cartesian coordinates (RCC), (x_1, x_2, x_3) and (x_1', x_2', x_3') are related by the transformational law

$$x_i' = \beta_{ij} x_j \ , \tag{2.1}$$

where β_{ij} is the direction cosine (see Figure 2-1) between the unit vectors along the coordinate axes x_i' and x_j, *i.e.*

$$\beta_{ij} = \cos(x_i', x_j) \, . \tag{2.2}$$

The inverse transformation is given by

$$x_j = \beta_{ij} x_i' \ . \tag{2.3}$$

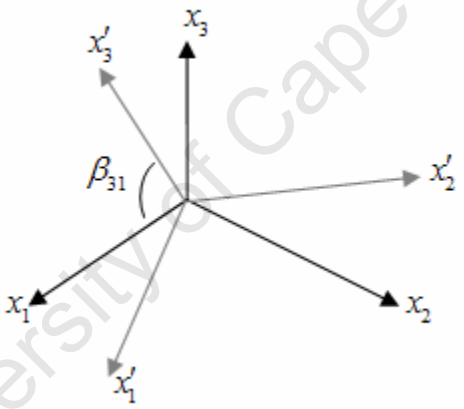

Figure 2-1 Cartesian coordinate axes x_i' and x_j showing the direction cosine β_{31} of the angle between x_1 and x_3'.

A system of variables is termed scalar, vector or tensor depending on how it is transformed from one coordinate system (x_1, x_2, x_3) to another (x_1', x_2', x_3') [14]. Accordingly, a mathematical quantity is called a scalar or tensor of rank zero, if it has only a single component Φ in the variables x_i and a single component Φ' in the variables x_i', and if Φ and Φ' are numerically equal at the corresponding points

$$\Phi'(x_1', x_2', x_3') = \Phi(x_1, x_2, x_3) \, . \tag{2.4}$$

A system of variables is called a vector or a tensor of rank one, if it has three components R_i in the variables x_i and three components R_i' in the variables x_i', and if the components are related by the transformation law

$$R_i'(x_1', x_2', x_3') = \beta_{ij} R_j(x_1, x_2, x_3), \tag{2.5}$$

where β_{ij} are the direction cosines of Equation (2.2). The inverse transformation is

$$R_i(x_1, x_2, x_3) = \beta_{ji} R_j'(x_1', x_2', x_3'). \tag{2.6}$$

Generalizing these definitions, a tensor of rank two is defined as a system which has nine components T_{ij} in the variables (x_1, x_2, x_3) and nine components T_{ij}' in the variables (x_1', x_2', x_3'), and if the components are related by the characteristic tensor transformation law

$$T_{ij}'(x_1', x_2', x_3') = \beta_{ik}\beta_{jl} T_{kl}(x_1, x_2, x_3), \tag{2.7}$$

and the inverse transformation

$$T_{ij}(x_1, x_2, x_3) = \beta_{ki}\beta_{lj} T_{kl}'(x_1', x_2', x_3'). \tag{2.8}$$

Subscripts (i, j, k, l) range from 1 to *n*, where $n = 3$ in this case, is the dimensionality of the reference coordinate system. Further generalization to higher rank tensors is immediate. Thus an *n*-dimensional tensor of rank *m* has n^m components. Second rank Cartesian tensors in three dimensional space have nine independent components. Since the definitions are based on transformations from one rectangular Cartesian coordinate system to another, these tensors are known as Cartesian tensors.

2.1.1 Symmetric tensor decomposition and diagonalization

Any second order tensor **T** can be decomposed into symmetric (**S**) and antisymmetric (**A**) parts [15]. From the general second order tensor **T**

$$\mathbf{T} = \left(T_{ij}\right) = \begin{pmatrix} T_{11} & T_{12} & T_{13} \\ T_{21} & T_{22} & T_{23} \\ T_{31} & T_{32} & T_{33} \end{pmatrix}, \tag{2.9}$$

the symmetric part is obtained by

$$\mathbf{S} = \frac{\mathbf{T} + \mathbf{T}^T}{2}, \tag{2.10}$$

where $\mathbf{T}^T$ is the transpose of **T**. The antisymmetric part of **T** is

$$\mathbf{A} = \frac{\mathbf{T} - \mathbf{T}^T}{2} \ . \tag{2.11}$$

Thus,

$$\mathbf{T} = \mathbf{S} + \mathbf{A} \ . \tag{2.12}$$

For the symmetric tensor **S**, off diagonal elements are equal, $S_{ij} = S_{ji}$, leaving six independent components,

$$\mathbf{S} = \left(S_{ij} \right) = \begin{pmatrix} S_{11} & S_{12} & S_{13} \\ & S_{22} & S_{23} \\ & & S_{33} \end{pmatrix} . \tag{2.13}$$

For the antisymmetric tensor **A**, the diagonal elements are null, $A_{ii} = 0$. The remaining elements are antisymmetric about the diagonal, $A_{ij} = -A_{ji}$. Thus there are three independent components, corresponding to a pseudo-vector called the axial vector [16].

$$\mathbf{A} = \left(A_{ij} \right) = \begin{pmatrix} \cdot & A_{12} & A_{13} \\ -A_{12} & \cdot & A_{23} \\ -A_{13} & -A_{23} & \cdot \end{pmatrix} . \tag{2.14}$$

The second order tensor **T** can be taken as the transformation matrix of a solid body, where the antisymmetric part **A** corresponds to the rigid body rotation by an axial vector, and the symmetric part **S** corresponds to the deformation of the solid body [17]. The diagonal elements of the symmetric tensor **S** correspond to linear elongations or dilatations and off-diagonal elements correspond to shear deformations.

An important property of an *n*-dimensional symmetric tensor **T** is that there always exist *n* eigenvalues λ_i and *n* mutually perpendicular eigenvectors $\boldsymbol{\upsilon}_i$ such that

$$\mathbf{T} \cdot \boldsymbol{\upsilon} = \lambda_i \boldsymbol{\upsilon}_i \qquad\qquad i = 1, ..., n \ . \tag{2.15}$$

The above equation can be written as

$$(\mathbf{T} - \lambda_i \mathbf{I}) v_i = 0 \qquad\qquad i = 1, ..., n \ , \tag{2.16}$$

where **I** is the unit matrix. The resulting linear system of equations has non-trivial solutions if and only if the determinant $\left| \mathbf{T} - \lambda_i \mathbf{I} \right| = 0$. For a three dimensional symmetric tensor $\left(T_{ij} \right)$ the determinant can be written as

$$\begin{vmatrix} T_{11}-\lambda & T_{12} & T_{13} \\ & T_{22}-\lambda & T_{23} \\ & & T_{33}-\lambda \end{vmatrix} = 0, \tag{2.17}$$

or

$$-\lambda^3 + I_1\lambda^2 - I_2\lambda + I_3 = 0, \tag{2.18}$$

where

$$I_1 = T_{11} + T_{22} + T_{33}, \tag{2.19}$$

$$I_2 = \begin{vmatrix} T_{22} & T_{23} \\ T_{32} & T_{33} \end{vmatrix} + \begin{vmatrix} T_{33} & T_{31} \\ T_{13} & T_{11} \end{vmatrix} + \begin{vmatrix} T_{11} & T_{12} \\ T_{21} & T_{22} \end{vmatrix} \tag{2.20}$$

and,

$$I_3 = \begin{vmatrix} T_{11} & T_{12} & T_{13} \\ T_{21} & T_{22} & T_{23} \\ T_{13} & T_{23} & T_{33} \end{vmatrix}. \tag{2.21}$$

I_1, I_2, and I_3 are independent of the coordinate transformations and therefore remain unchanged after the tensor transformation, (Equation (2.7)). Equation (2.18) can be written using its roots $\lambda_1, \lambda_2, \lambda_3$ as

$$(\lambda - \lambda_1)(\lambda - \lambda_2)(\lambda - \lambda_3) = 0. \tag{2.22}$$

Equations (2.19), (2.20), and (2.21) in terms of these three eigenvalues are:

$$I_1 = Trace(\mathbf{T}) = T_{ii} = \lambda_1 + \lambda_2 + \lambda_3; \tag{2.23}$$

$$I_2 = \frac{1}{2}(T_{ii}T_{jj} - T_{ij}T_{ij}) = \lambda_1\lambda_2 + \lambda_2\lambda_3 + \lambda_1\lambda_3; \tag{2.24}$$

$$I_3 = \frac{1}{6}(T_{ii}T_{jj}T_{kk} - 3T_{ii}T_{jk}T_{jk} + 2T_{ij}T_{jk}T_{ki}) = \lambda_1\lambda_2\lambda_3. \tag{2.25}$$

I_1, I_2, I_3 are called the tensor invariants [14], and are independent of the components of the tensor **T** in different coordinate systems.

The roots of the determinant of the symmetric tensor **T**, λ_1, λ_2, and λ_3 completely represent the tensor **T** in a special reference coordinate system known as the eigensystem of the tensor. The eigensystem of a tensor can be obtained by means of diagonalization, which is equivalent to the eigenvalue decomposition. Using the symmetric second rank tensor **T,** with components T_{ij} defined in the x_i coordinate system, and $\lambda_i, \mathbf{v}_i$ as the eigenvalues and corresponding eigenvectors, if the axes of a

primed coordinate system x_i' are chosen to coincide with the orthogonal eigenvectors $\mathbf{\upsilon}_i$, then the tensor components can be written in the x_i' coordinate system as

$$\left(T_{ij}'\right)=\begin{pmatrix}\lambda_1 & 0 & 0\\ 0 & \lambda_2 & 0\\ 0 & 0 & \lambda_3\end{pmatrix}. \tag{2.26}$$

If the three eigenvalues are non-degenerate, $\lambda_1 \neq \lambda_2 \neq \lambda_3$, there exist three unique orthogonal eigenvectors along the principal directions

$$\mathbf{\upsilon}_i \cdot \mathbf{\upsilon}_j = \lambda_i \lambda_j \delta_{ij}, \tag{2.27}$$

where δ_{ij} is the Kronecker delta function. If $\lambda_1 = \lambda_2 \neq \lambda_3$, then $\mathbf{\upsilon}_3$ is fixed, but an infinite number of pairs of vectors $\mathbf{\upsilon}_1$ and $\mathbf{\upsilon}_2$ can be determined orthogonal to $\mathbf{\upsilon}_3$. If $\lambda_1 = \lambda_2 = \lambda_3$ then any set of orthogonal axes may be used as the eigenvectors.

2.2 Continuum approach

A material continuum is a mathematical abstraction for which the densities of mass, momentum, and energy are continuous functions of space in the mathematical sense [18]. The idealized concept of a material continuum can be used with materials where the fine structure of the matter can be ignored. Assume ΔM to be the mass of a portion of a continuum occupying a volume ΔV containing the point *P*. The average density of this portion of the continuum is defined as the ratio of ΔM to the volume ΔV. In a continuum it is assumed that the limit of the average density exists as the volume ΔV shrinks through a sequence of smaller volumes $\Delta V_1, \Delta V_2, \Delta V_3, \ldots$ converging on *P* (see Figure 2-2), such that

$$\Delta V_n \subset \Delta V_{n-1} \qquad P \in \Delta V_n. \tag{2.28}$$

If the limit of $\Delta M_n / \Delta V_n$ exists as $n \to \infty$ and $\Delta V_n \to 0$, the limiting value is defined as the density of the mass distribution at point *P* and denoted by $\rho(P)$

$$\rho(P) = \lim_{\substack{n\to\infty \\ \Delta V_n \to 0}} \frac{\Delta M_n}{\Delta V_n}. \tag{2.29}$$

If the density is well defined everywhere in ΔV_0, the continuous mass distribution forms a continuum. The following definitions of stress and strain tensors are based on the continuum model.

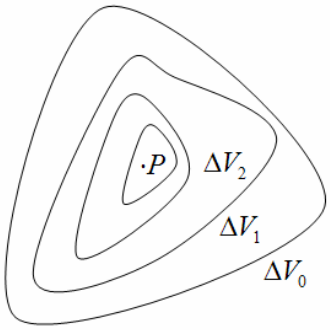

Figure 2-2 The idea of continuum: infinitesimal spatial domain ΔV_n contains ΔM_n amount of matter as the volume converges on P, so that the density is well defined everywhere in the spatial region.

2.3 Definition and Properties of the Stress Tensor

Stress is a second rank tensor quantity defined in continuum mechanics to specify the interaction between adjacent parts of a material body with each other [19]. The tensor formulation of stress based on the continuum approach was first given by Cauchy in 1822 [20]. In a material continuum B occupying a spatial region V, and enclosed by surface S, the interaction between the material outside S and that inside can be divided into two kinds of interaction: (i) body forces due to action-at-a-distance type of forces, *e.g.* gravitational or electromagnetic forces, that can be expressed as force per unit volume and (ii) surface forces due to the action across a boundary surface S. In Figure 2-3, to express the surface forces a small surface element of area ΔS is considered on the imaginary surface S with a unit normal vector $\hat{\mathbf{n}}$ with its direction outward from the interior of S. The material on either side of ΔS exerts a force $\Delta \mathbf{F}$ on the surface element ΔS. The force $\Delta \mathbf{F}$ depends on the location, size of the surface area and the orientation of the normal $\hat{\mathbf{n}}$. As ΔS tends to zero, the ratio $\Delta \mathbf{F} / \Delta S$ tends to a definite

limit $d\mathbf{F}/dS$, and the moment of the force acting on the surface ΔS about any point within the area vanishes in the limit [14]. The limiting vector can be written as

$$\overset{n}{\mathbf{T}} = \frac{d\mathbf{F}}{dS}, \tag{2.30}$$

where the superscript n denotes the direction of the normal $\hat{\mathbf{n}}$ of the surface dS. $\overset{n}{\mathbf{T}}$ is called the traction or the stress vector and represents the force per unit area acting on the surface. The description of interaction between the inside and outside of an imaginary closed surface in a material using the stress vector is called the stress principle of Euler and Cauchy [14].

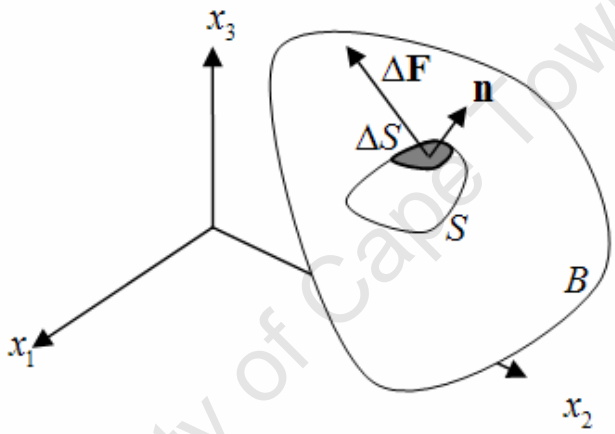

Figure 2-3 Stress principle of Cauchy and Euler: the interaction between adjacent points in a continuum is described by the surface force $\Delta\mathbf{F}$ acting on an imaginary surface ΔS with a unit normal $\hat{\mathbf{n}}$. The limiting vector $\Delta\mathbf{F}/\Delta S$ as $\Delta S \to 0$ is called the traction or the stress vector.

If surfaces ΔS_n, $n = 1,2,3$ can be taken parallel to one of the coordinate planes, then the normal of ΔS_n is in the positive direction of the x_n-axis. The traction acting on ΔS_n has three components $\overset{n}{T}_1, \overset{n}{T}_2$, and $\overset{n}{T}_3$, along the direction of the coordinate axes x_1, x_2, x_3 respectively, where the index i of $\overset{n}{T}_i$ denotes the components of the force, and the symbol n indicates x_n-axis normal to the surface on which the force acts. Introducing a new notation, the components of the stress tensor are obtained

$$\overset{n}{T}_1 = \sigma_{n1}, \qquad \overset{n}{T}_2 = \sigma_{n2}, \qquad \overset{n}{T}_3 = \sigma_{n3}.$$

These components of tractions acting on the surface, ΔS_n, $n = 1,2,3$ can be arranged in a square matrix as in Table 2-1.

	Components of stresses		
	x_1	x_2	x_3
Surface normal to x_1	σ_{11}	σ_{12}	σ_{13}
Surface normal to x_2	σ_{21}	σ_{22}	σ_{23}
Surface normal to x_3	σ_{31}	σ_{32}	σ_{33}

Table 2-1 Components of the tensor (σ_{ij}) matrix.

In the matrix notation the stress tensor is

$$\boldsymbol{\sigma} = (\sigma_{ij}) = \begin{pmatrix} \sigma_{11} & \sigma_{12} & \sigma_{13} \\ \sigma_{21} & \sigma_{22} & \sigma_{23} \\ \sigma_{31} & \sigma_{32} & \sigma_{33} \end{pmatrix}. \tag{2.31}$$

The components σ_{11}, σ_{22}, and σ_{33} are known as the normal stresses, and the remaining components are called the shear components. Stress components are taken positive if the stress vector $\Delta\mathbf{F}$ is parallel to the unit vector $\hat{\mathbf{n}}$, and negative if antiparallel. Normal stress can either be tension, $\Delta\mathbf{F}$ and $\hat{\mathbf{n}}$ pointing in the same direction or compression, $\Delta\mathbf{F}$ and $\hat{\mathbf{n}}$ pointing in opposite directions. If the traction is perpendicular to the surface normal then the resulting stress is pure shear. In the most general case, the traction can be decomposed into a normal and a shear component as shown in Figure 2-4.

The traction or the stress vector in a given direction $\hat{\mathbf{n}}$ can be obtained using Cauchy's formula

$$\overset{\mathbf{n}}{\mathbf{T}} = \boldsymbol{\sigma} \cdot \mathbf{n}, \tag{2.32}$$

or in the index notation

$$T_i = \sigma_i = \sigma_{ji} n_j. \tag{2.33}$$

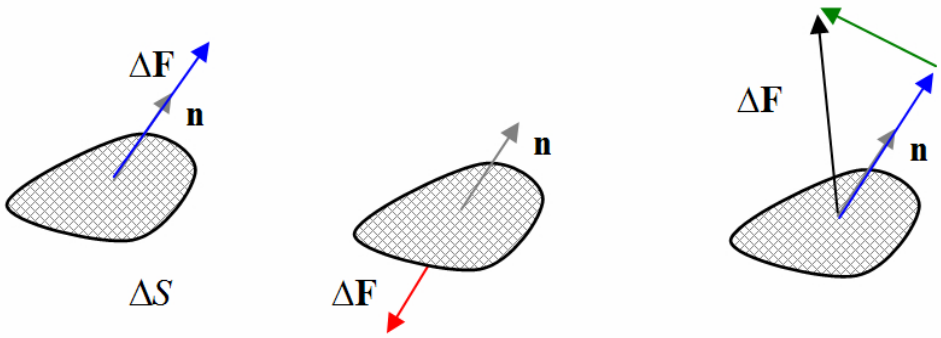

Figure 2-4 Alignment of the traction with respect to the surface normal: (a) tensile; (b) compressive; and (c) normal and shear stresses.

2.3.1 Equations of Equilibrium

In equilibrium, the total force and total moment acting on the body is zero. The equilibrium conditions can be written by selecting an arbitrary closed surface S enclosing a volume V, in a body in equilibrium, as shown in Figure 2-5. The equilibrium of forces is

$$\iint_S \sigma \cdot dS + \iiint_V F_i dV = 0, \tag{2.34}$$

or

$$\iint_S \sigma_{ji} n_j dS + \iiint_V F_i dV = 0, \tag{2.35}$$

where n_j is the unit normal vector of the differential surface element dS. Using Gauss' theorem to convert the surface integral to a volume integral, equilibrium of forces is obtained as

$$\frac{\partial \sigma_{ji}}{\partial x_j} + \mathbf{F}_i = 0, \tag{2.36}$$

where $\mathbf{F}_i$ is the total body force per unit volume. The equilibrium of the total moment of the body forces and surface forces with respect to the origin is

$$\iint_S \varepsilon_{ijk} y_j \sigma_{nk} dS + \iiint_V \varepsilon_{ijk} x_j F_k dV = 0, \tag{2.37}$$

where x_j, y_j are the coordinates of the differential surface element and volume element respectively (see Figure 2-5). ε_{ijk} is the permutation symbol which is defined as:

$\varepsilon_{ijk} = 0$ if the values of i, j, k do not form a permutation of $1, 2, 3$,

$\varepsilon_{ijk} = +1$ if the values of i, j, k form an even permutation of $1, 2, 3$,

$\varepsilon_{ijk} = -1$ if the values of i, j, k form an odd permutation of $1, 2, 3$.

Using Gauss' theorem to rewrite the surface integral and equation (2.36) to eliminate the body forces it can be shown that [18]

$$\varepsilon_{ijk}\sigma_{jk} = 0, \tag{2.38}$$

or

$$\sigma_{ij} = \sigma_{ji}. \tag{2.39}$$

Thus the condition of static equilibrium enforces the stress tensor to be symmetric and the gradients (2.36) to be zero if body forces are not present. However these conditions are not sufficient to uniquely determine the full stress state in a material. Other relations must be used to completely determine the state of stress in a body [19].

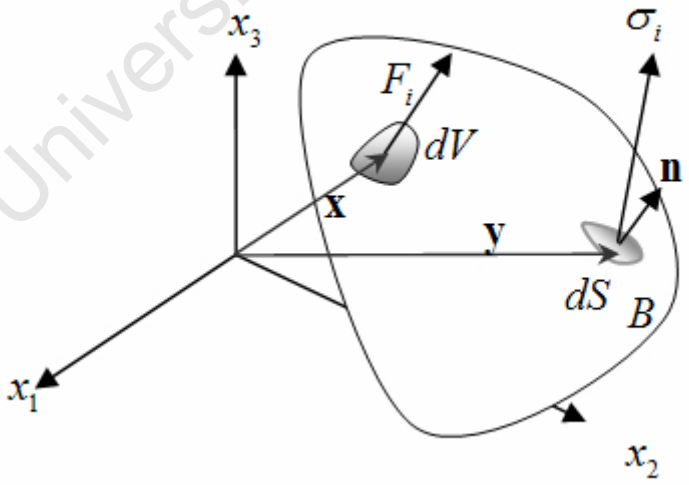

Figure 2-5 Equilibrium condition of body forces and stress vectors.

2.3.2 Coordinate transformations and principal stresses

The original coordinate system x_i in which the stress tensor $\boldsymbol{\sigma}$ is defined is chosen arbitrarily. It is possible to describe the same stress state using another coordinate system x_i' by the new tensor $\boldsymbol{\sigma}'$. If two coordinate systems are related by the coordinate transformation function of equation (2.1), $\boldsymbol{\sigma}'$ and $\boldsymbol{\sigma}$ are related by the tensor transformation function

$$\sigma'_{kl} = \beta_{ki}\beta_{lj}\sigma_{ij} . \tag{2.40}$$

It was shown in Section 2.1.1 that second rank symmetric tensors can be diagonalized by means of a coordinate transformation. Similarly, since the stress tensor is symmetric it can be transformed into a new coordinate system where the new tensor components are

$$\sigma'_{ij} = \begin{pmatrix} \sigma_1 & 0 & 0 \\ 0 & \sigma_2 & 0 \\ 0 & 0 & \sigma_3 \end{pmatrix} . \tag{2.41}$$

These particular coordinate axes, where the stress matrix has zero off-diagonal elements, are called the principal axes, and the corresponding stress components are called the principal stresses. The coordinate planes defined by the principal axes are called the principal planes. The diagonalization of the stress tensor and the transformation of components is illustrated in Figure 2-6.

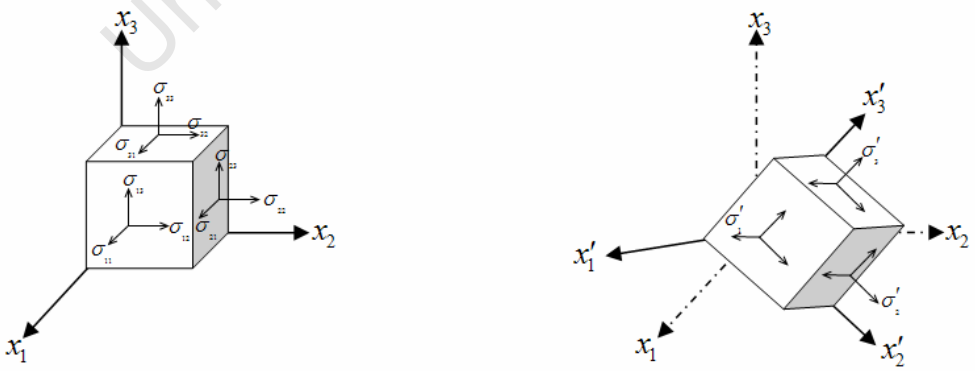

(a) (b)

Figure 2-6 Transformation of stress tensor components under rotation of coordinate axes from x_i to x_i'.

By the same reasoning of Section 2.1.1, the stress tensor invariants are defined as

$$I_1 = \sigma_1 + \sigma_2 + \sigma_3,$$
$$I_2 = \sigma_1\sigma_2 + \sigma_2\sigma_3 + \sigma_3\sigma_1, \text{ and} \tag{2.42}$$
$$I_3 = \sigma_1\sigma_2\sigma_3,$$

where $\sigma_1, \sigma_2,$ and σ_3 are the principal stresses.

2.3.3 Normal and shear stresses

The traction $\overset{n}{\mathbf{T}}$ acting on a point in the direction of $\hat{\mathbf{n}}$ can be obtained using Cauchy's formula, $T_i = \sigma_{ji} n_j$. $\overset{n}{\mathbf{T}}$ can be decomposed into two components, a component parallel to the surface normal, and another component on the surface as shown in Figure **2-7**. The normal component of $\overset{n}{\mathbf{T}}$ along $\hat{\mathbf{n}}$ is the normal stress acting on the surface element, and in tensor notation is given by

$$\sigma_n = T_i n_i = \sigma_{ij} n_i n_j. \tag{2.43}$$

The magnitude of the shear component of $\overset{n}{\mathbf{T}}$ tangent to the surface is given by

$$|\boldsymbol{\tau}|^2 = T^2 - \sigma_n^2. \tag{2.44}$$

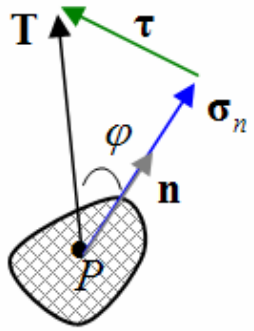

Figure 2-7 Normal σ_n and shear τ components of the stress traction $\overset{n}{\mathbf{T}}$.

Shear stresses are zero along the principal directions (equation (2.44)). In the reference frame of the principal axes, local maximum shear stress directions and magnitudes are given in Table 2-2 (see also Figure 2-8). They act on planes containing one of the principal axis and aligned at 45° to the other two.

Direction vectors			Maximum shear stress
$n_1 = \pm\frac{1}{\sqrt{2}}$	$n_2 = \pm\frac{1}{\sqrt{2}}$	$n_3 = 0$	$\lvert\boldsymbol{\tau}_{12}\rvert = \frac{1}{2}\lvert\sigma_1 - \sigma_2\rvert$
$n_1 = \pm\frac{1}{\sqrt{2}}$	$n_2 = 0$	$n_3 = \pm\frac{1}{\sqrt{2}}$	$\lvert\boldsymbol{\tau}_{13}\rvert = \frac{1}{2}\lvert\sigma_3 - \sigma_1\rvert$
$n_1 = 0$	$n_2 = \pm\frac{1}{\sqrt{2}}$	$n_3 = \pm\frac{1}{\sqrt{2}}$	$\lvert\boldsymbol{\tau}_{23}\rvert = \frac{1}{2}\lvert\sigma_2 - \sigma_3\rvert$

Table 2-2 Maximum shear stress directions and magnitudes in the reference frame of the three principal stresses.

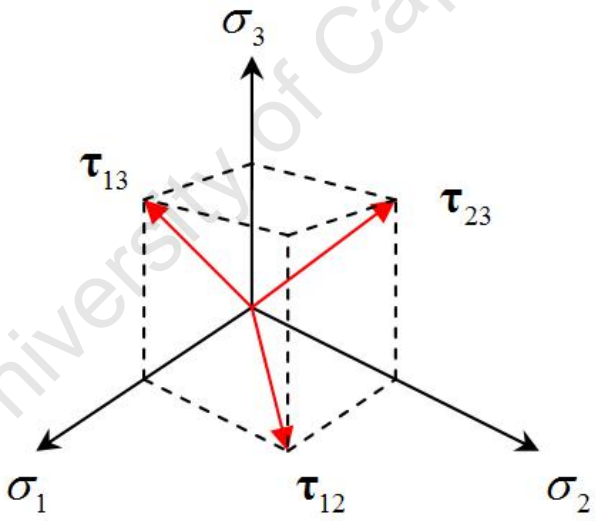

Figure 2-8 Local maximum shear stress directions lay on the principal stress planes and make an angle of 45° with the other two principal stresses. The absolute maximum shear stress acts on a plane which makes an angle of 45° with the largest and the smallest principal axes. Its magnitude is $\tau = \frac{1}{2}\lvert\sigma_{\max} - \sigma_{\min}\rvert$.

If the sum of diagonal elements of the stress tensor is zero, then the stress state is termed *pure shear* [14]. Therefore $Trace(\sigma_{ij})$, the first stress invariant, is zero in the pure shear stress state. This can be written as

$$\delta_{ij}\sigma_{ij} = 0. \tag{2.45}$$

Any stress tensor can be decomposed into a pure shear term, known as the stress deviator, and a uniform normal stress term

$$\sigma_{ij} = \hat{\sigma}_{ij} + \frac{1}{3}\delta_{ij}\sigma_{kk}. \tag{2.46}$$

The first term, $\hat{\sigma}_{ij}$ is the stress deviator, and $\frac{1}{3}\delta_{ij}\sigma_{ij}$ is characterized by a single scalar known as the pure hydrostatic stress [14].

Another scalar quantity of engineering interest is the von Mises stress. The von Mises stress characterises the onset and amount of plastic deformation under triaxial loading. It is most applicable to ductile materials [21]. For a general stress tensor, the von Mises stress is given as

$$\sigma_v = \sqrt{\frac{\left(\sigma_{xx}-\sigma_{yy}\right)^2 + \left(\sigma_{yy}-\sigma_{zz}\right)^2 + \left(\sigma_{xx}-\sigma_{zz}\right)^2 + 6\sigma_{xy}^2 + 6\sigma_{xz}^2 + 6\sigma_{yz}^2}{6}}, \tag{2.47}$$

or from the principal stresses as

$$v = \sqrt{\frac{(\sigma_1-\sigma_2)^2 + (\sigma_1-\sigma_3)^2 + (\sigma_2-\sigma_3)^2}{6}}. \tag{2.48}$$

2.4 Definitions and properties of the strain tensor

In this section the strain tensor is defined geometrically, and its properties relevant to visualization are discussed. Forces applied to solids cause deformation and, when a medium deforms elastically, small volumetric elements change position, orientation and/or deform. As the continuum moves from one configuration to another, the matter in the neighbourhood of each point is translated and rotated as a rigid body, and deformed. Second order tensors can be used to represent the state of strain in a continuum. When a solid body undergoes deformation, every particle that constitutes the body take up a new position, which can be described by a new set of coordinates. The strain tensor describes the relative displacement of points in a continuum. The strain tensor can either be defined in the *Lagrangian space*, where the reference frame

is attached to the particles, and therefore absolute displacement of the particles can be traced in terms of their initial positions, or alternatively, the strain tensor can be defined in the *Eulerian space*, where the reference frame is fixed in space and therefore only the instantenous position of particles is known [18]. In the first part of this section the Lagrangian definition of strain is described. Afterwards the consequence of the case of infinitesmal strain in the Eulerian and Lagrangian formalism will be highlighted.

Assume that P and Q are two neighbouring points in a body before deformation. The position vectors to these points are a_i and $a_i + da_i$, respectively (Figure 2-9). After deformation these points move to new positions P' and Q' with new coordinates x_i and $x_i + dx_i$. Therefore, the relative displacement vector between P and Q after a given deformation is the difference of the displacement vectors $u_i(Q)$ and $u_i(P)$ of the two points, and can be written as

$$du_i = u_i(Q) - u_i(P) = u_i(a + da) - u_i(a), \tag{2.49}$$

or in the differential form as

$$du_i = \left(\frac{\partial u_i}{\partial u_j} \right)_P da_j, \tag{2.50}$$

where the partial derivatives are evaluated at point P.

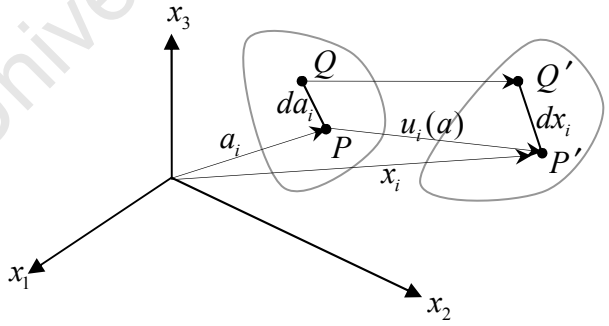

Figure 2-9 Deformation of a body and the relative displacement of two adjacent points. Transformation of each point is defined by the vector $u_i = x_i - a_i$.

To differentiate between the rigid body motion and straining the difference between the square of the differential lengths between P', Q' and P, Q can be used. The square of the lengths are

$$\begin{aligned} |PQ|^2 &= (da)^2 = da_i da_i \\ |P'Q'|^2 &= (dx)^2 = dx_i dx_i \end{aligned} . \tag{2.51}$$

Therefore,

$$(dx)^2 - (da)^2 = dx_i dx_i - da_i da_i \tag{2.52}$$

Using the equation (see Figure 2-9)

$$x_i = a_i + u_i(a) . \tag{2.53}$$

the difference of the position vectors can be expressed in the differential form as

$$dx_i = \left(\frac{\partial x_i}{\partial a_j} \right)_P da_j . \tag{2.54}$$

Rewriting (2.52) using (2.54) we obtain

$$(dx)^2 - (da)^2 = \left[\frac{\partial x_r}{\partial a_i} \frac{\partial x_r}{\partial a_j} - \delta_{ij} \right] da_i da_i \tag{2.55}$$

where r is a dummy index. Replacing x_r in terms of the displacements

$$\begin{aligned} (dx)^2 - (da)^2 &= \left[\frac{\partial}{\partial a_i}(a_r + u_r) \frac{\partial}{\partial a_j}(a_r + u_r) - \delta_{ij} \right] da_i da_i \\ &= \left[\left(\delta_{ij} + \frac{\partial u_r}{\partial a_i} \right) \left(\delta_{ij} + \frac{\partial u_r}{\partial a_j} \right) - \delta_{ij} \right] da_i da_i \\ &= \left[\frac{\partial u_i}{\partial a_j} + \frac{\partial u_j}{\partial a_i} + \frac{\partial u_r}{\partial a_i} \frac{\partial u_r}{\partial a_j} \right] da_i da_i \end{aligned} . \tag{2.56}$$

The Lagrangian nonlinear strain tensor is defined as

$$L_{ij} = \frac{1}{2} \left[\frac{\partial u_i}{\partial a_j} + \frac{\partial u_j}{\partial a_i} + \frac{\partial u_r}{\partial a_i} \frac{\partial u_r}{\partial a_j} \right], \tag{2.57}$$

and the differential deformation can be calculated from the Lagrangian strain as

$$ds_0^2 - ds^2 = 2L_{ij} da_i da_j . \tag{2.58}$$

The definition of strain in the a_i coordinate system is called the Lagrangian form [18]. Similarly the strain can be obtained using x_i as the independent coordinates instead of a_i. In this case the Eulerian nonlinear strain tensor is obtained as

$$E_{ij} = \frac{1}{2}\left[\frac{\partial u_i}{\partial a_j} + \frac{\partial u_j}{\partial a_i} - \frac{\partial u_r}{\partial a_i}\frac{\partial u_r}{\partial a_j}\right]. \tag{2.59}$$

It can be seen that the Lagrangian and Eulerian nonlinear strain tensors are symmetrical:

$$\begin{aligned} L_{ij} &= L_{ji}, \\ E_{ij} &= E_{ji}. \end{aligned} \tag{2.60}$$

Assuming the derivatives of the displacements to be small, the term involving the derivatives in (2.57) and (2.59) can be neglected in comparison with the other two terms, so that both the Lagrangian and the Eulerian nonlinear strain tensors reduce to

$$\varepsilon_{ij} = \frac{1}{2}\left(\frac{\partial u_j}{\partial x_i} + \frac{\partial u_i}{\partial x_j}\right), \tag{2.61}$$

known as the Cauchy's infinitesimal strain tensor.

2.4.1 Geometric meaning of the strain tensor

The diagonal elements ε_{ii} of the strain tensor represent the dilatation/contraction; *i.e.* change of length per unit length of a vector parallel to the coordinate-axes as shown in Figure 2-10. Cross terms, or the off-diagonal elements, are related to the shear strains. Shear strains represent the change of angle between the perpendicular directions. For example, in Figure 2-10 (c-e) ε_{ij} is equal to the change in angle ϕ between the corresponding axes

$$\varepsilon_{ij} = \frac{1}{2}\left(\frac{\partial u_i}{\partial x_j} + \frac{\partial u_j}{\partial x_i}\right) = \frac{1}{2}\phi\,. \tag{2.62}$$

In engineering usage, off-diagonal strain components are doubled, and are known as the engineering shearing strains or detrusions [14]. The geometric meanings of typical strain tensors are illustrated in Figure 2-10. From the figure the deformations corresponding to the each term of the strain tensor can be seen.

(a)

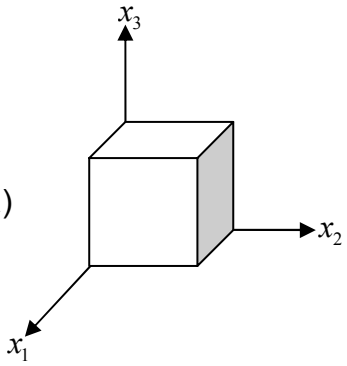

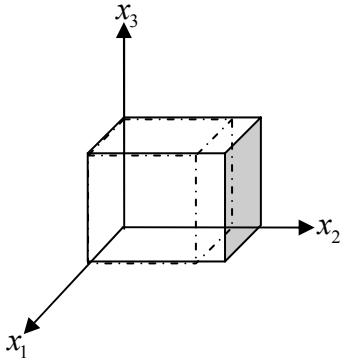

$$\varepsilon_{ij} = \begin{pmatrix} 0 & 0 & 0 \\ & \frac{\partial u_2}{\partial x_2} & 0 \\ & & 0 \end{pmatrix}$$

(b)

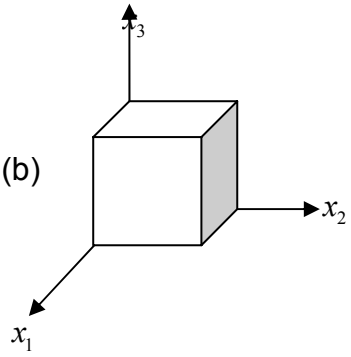

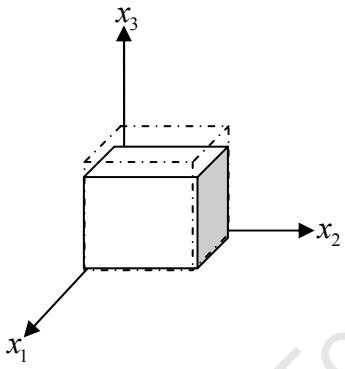

$$\varepsilon_{ij} = \begin{pmatrix} 0 & 0 & 0 \\ & 0 & 0 \\ & & \frac{\partial u_3}{\partial x_3} \end{pmatrix}$$

(c)

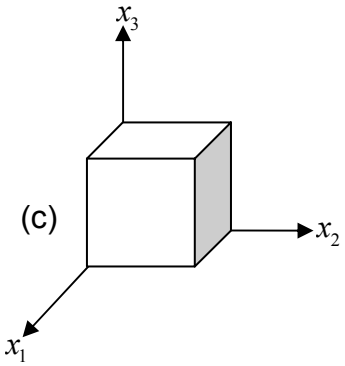

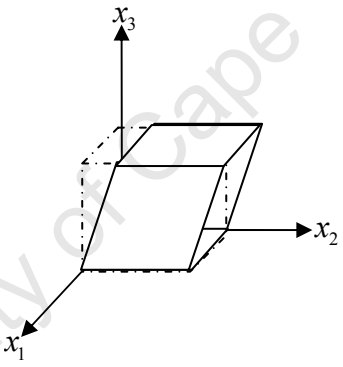

$$\varepsilon_{ij} = \begin{pmatrix} 0 & 0 & 0 \\ & 0 & \frac{1}{2}(\frac{\partial u_2}{\partial x_3} + 0) \\ & & 0 \end{pmatrix}$$

(d)

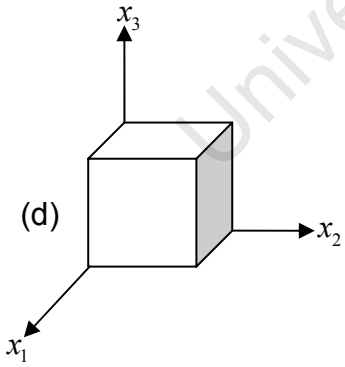

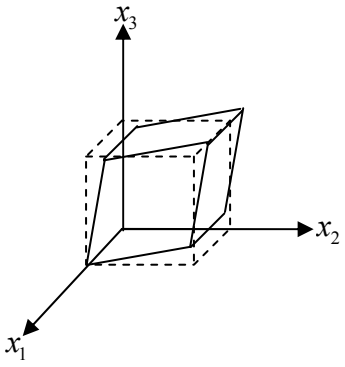

$$\varepsilon_{ij} = \begin{pmatrix} 0 & 0 & 0 \\ & 0 & \frac{1}{2}(\frac{\partial u_2}{\partial x_3} + \frac{\partial u_3}{\partial x_2}) \\ & & 0 \end{pmatrix}$$

(e)

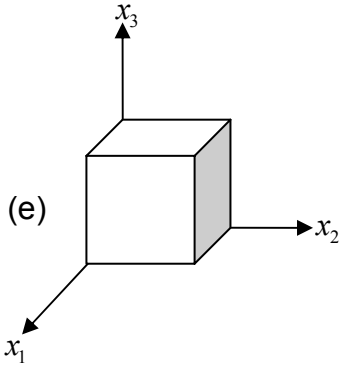

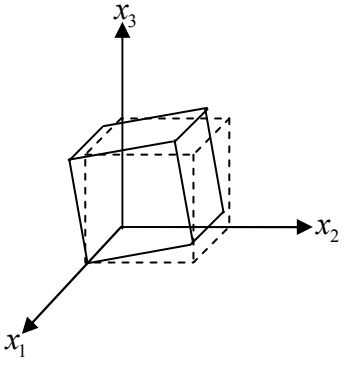

$$\varepsilon_{ij} = \begin{pmatrix} 0 & 0 & 0 \\ & 0 & \frac{1}{2}(\frac{\partial u_2}{\partial x_3} - \left|\frac{\partial u_3}{\partial x_2}\right|) \\ & & 0 \end{pmatrix}$$

Figure 2-10 The geometric meaning of the strain tensor:

(a) dilatation along x_2

(b) contraction along x_3

(c) shear strain $\varepsilon_{23} = \frac{1}{2}(\frac{\partial u_2}{\partial x_3} + \frac{\partial u_3}{\partial x_2})$ where $\frac{\partial u_2}{\partial x_3} > 0, \frac{\partial u_3}{\partial x_2} = 0$

(d) shear strain $\varepsilon_{23} = \frac{1}{2}(\frac{\partial u_2}{\partial x_3} + \frac{\partial u_3}{\partial x_2})$ where $\frac{\partial u_2}{\partial x_3} > 0, \frac{\partial u_3}{\partial x_2} > 0$

(e) shear strain $\varepsilon_{23} = \frac{1}{2}(\frac{\partial u_2}{\partial x_3} + \frac{\partial u_3}{\partial x_2})$ where $\frac{\partial u_2}{\partial x_3} < 0, \frac{\partial u_3}{\partial x_2} > 0$

All the mathematical features of the stress tensor can be applied to the strain tensor, since both quantities are symmetric second rank tensors. By analogy with properties of the stress tensor the following can be defined:

(a) three principal strains $\varepsilon_1, \varepsilon_2, \varepsilon_3$ and corresponding principal strain directions $\mathbf{\upsilon}_1, \mathbf{\upsilon}_2, \mathbf{\upsilon}_3$;

(b) principal strain planes perpendicular to a principal strain directions;

(c) the diagonal form of the strain tensor $\begin{pmatrix} \varepsilon_1 & & \\ & \varepsilon_2 & \\ & & \varepsilon_3 \end{pmatrix}$;

(d) three strain tensor invariants in tensor notation

$$\begin{aligned} I_1 &= \varepsilon_{il}\delta_{ij}, \\ I_2 &= \frac{1}{2}\varepsilon_{ik}\varepsilon_{ik}, \\ I_3 &= \frac{1}{3}\varepsilon_{ik}\varepsilon_{km}\varepsilon_{mi}. \end{aligned} \tag{2.63}$$

2.5 Elastic strain-stress relations

The strain tensor and the stress tensor are related using the constitutive relations, which are experimental constants depending on the mechanical properties of the individual material. For a large number of hard solids the measured strain is

proportional to the applied load and, in the elastic regions disappears upon unloading. This behaviour is known as Hooke's law and, in terms of stress and strain tensors is

$$\sigma_{ij} = C_{ijkl}\varepsilon_{mn}, \tag{2.64}$$

where C_{ijkl} are the elasticity constants. Equation (2.64) can also be written as

$$\varepsilon_{kl} = S_{klmn}\sigma_{mn}, \tag{2.65}$$

where S_{klmn} are called the elastic compliances. Both C_{ijkl} and S_{klmn} are fourth rank tensors with 81 constants, corresponding to the indices k,l,m,n taking values 1, 2, and 3. Symmetries in the elasticity tensor reduce both tensors, in the most general anisotropic case, to 21 independent elements. For an isotropic material, Equation (2.64) can be written as [22]

$$\sigma_{ij} = 2\mu\varepsilon_{ij} + \lambda\delta_{ij}\varepsilon_{kk}, \tag{2.66}$$

where λ and μ are Lamé's constants. μ is referred to as the shear modulus. In terms of the strains, equation (2.66) is

$$\varepsilon_{ij} = \frac{1}{2\mu}\sigma_{ij} + \frac{-\lambda}{2\mu(3\lambda+2\mu)}\delta_{ij}\sigma_{nn}, \tag{2.67}$$

where $\mu \neq 0$ and $3\lambda + 2\mu \neq 0$. In terms of Poisson ratio υ and Youngs modulus *E,* equation (2.67) is given by

$$e_{ij} = \frac{1}{E}\left((1+\upsilon)\sigma_{ij} - \upsilon\delta_{ij}\sigma_{kk}\right). \tag{2.68}$$

The conversion factors for the elastic constants are given in Table 2-3.

Constants	λ,μ	E,υ
λ	λ	$\frac{\upsilon E}{(1+\upsilon)(1-2\upsilon)}$
μ	μ	$\frac{E}{2(1+\upsilon)}$
E	$\frac{\mu(3\lambda+2\mu)}{\lambda+\mu}$	E
υ	$\frac{\lambda}{2(\lambda+\mu)}$	υ

Table 2-3 Conversion factors of elastic constants [19].

3 Scientific Visualization Overview

In the Oxford English Dictionary visualization is defined as 'the power or process of forming a mental picture or vision of something not actually present to the sight; a picture thus formed.' In scientific visualization, both the subject matter to be visualized and the processes and techniques employed for visualization are elements of the scientific domain. Thus, as much as the goal of general visualization is to bring forth a vision before the eye that was previously concealed, the object of scientific visualization is to enable insight into quantitative scientific data [23]. Although many concepts of scientific visualization have been used, more or less intuitively, by great scientists such as Descartes, Faraday and da Vinci, as an independent field it is very much an emerging discipline. There is therefore no generally accepted theoretical framework, classification or even terminology. Because the applications and influences of scientific visualization are based in different natural and social science disciplines, there have been various partial classification schemes [24-26], which are based on either the visualization process or the type of data under consideration. It is therefore necessary for the purpose of this work to define a clear framework which is based on the concept of a visualization pipeline [7] and the underlying geometry in the mapping [27] of data sets, as well as the classification of the data structures [28].

Visualization, the use of imagery to express an idea, is a powerful tool in literature, art and politics. However this non-scientific visualization has no definitive rules, and no unambiguous interpretation, and therefore is not objective. In contrast scientific visualization has definite rules, clear goals, and is not subjective to personal interpretation. However this is not to say that the results of a particular scientific visualization task will be interpreted in the same way by different people with diverse backgrounds. Although much work has been done, it is not so clear how to objectively evaluate the effectiveness of a visualization [29]. Scientific visualization can be classified into two major subsets, namely information visualization, and data visualization as shown in Figure 3-1.

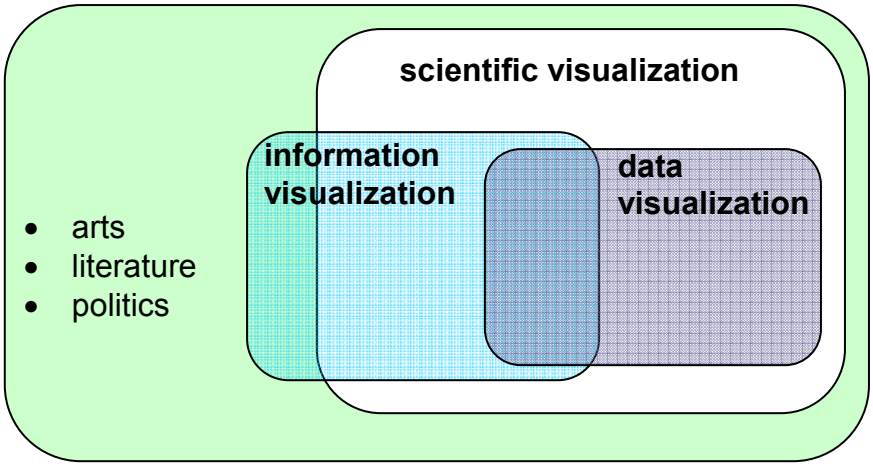

Figure 3-1 The classification of visualization using a Venn diagram.

In data visualization, entities are represented visually using specific algorithms to make certain hidden features of the data visible, or to reveal possible correlations between different segments of the dataset. For example, the visualization of the ozone concentration in the atmosphere reveals an 'ozone hole' above Antarctica (Figure 3-10, page 52.) The main difference between information visualization and data visualization is that the goal of information visualization is to find an appropriate representation of abstract or complex datasets. Information visualization datasets are usually multidimensional and multivariate, and the domain of the entity is given as a higher dimensional or abstract space, where data is not physically connected with three space dimensions and one time dimension, *i.e.* spatial-temporal data [13, 30]. Accordingly, a visualization task to show the demographics of the countries in Africa falls under information visualization. Information visualization is, however, very broad and it is sometimes difficult to distinguish it from data visualization or non-scientific visualization. For example, what kind of visualization is a Venn diagram, and where does the Venn diagram of Figure 3-1 fit into itself?

Scientific visualization is not presentation graphics. In presentation graphics, the information to be communicated is readily available, and a graphic description is used for the efficient presentation of this information, while in scientific visualization often a number of preparatory steps are required, *e.g.* formatting, transformations or filtering of raw data, and conceptualization of the underlying physical processes prior

to actual rendering. In this aspect scientific visualization is also different from imaging techniques such as computed tomography (CT) or magnetic resonance imaging (MRI) where representations are directly obtained from the datasets.

Scientific visualization can be defined as an inter-disciplinary enterprise to develop and execute conceptual models for the visual exploration of scientific data. The primary task of scientific visualization is to develop a well-defined visualization system, known as a **visualization idiom** consisting of data pre-processing operations, visualization mappings and rendering algorithms [7], which is described in detail in Section 3.1. Prior to the availability of digital computers a number of scientific visualization techniques were developed. For example, the representation of scalars with height maps, vector quantities as directed arrows, and the representation of electromagnetic field lines are common ways of visualization. An ingenious visual model is the Feynman diagram, used to describe the interactions between elementary particles in the form of vertices and lines denoting particles and processes in space-time [31]. Another example, precluding the availability of digital computers, is the use of Mohr circles [5] to study normal and shear components of two and three dimensional stresses. In recent times, driven by increasing computational power, a wide range of research has benefited from scientific visualization. Examples are common weather maps in meteorology, molecular modelling of drugs in pharmaceutical research, brain diffusion tensor visualizations in medicine, oil exploration research in geomechanics, flow visualization in aeronautics, and mechanical strength visualizations in welds and other engineering components [32, 33].

The application of scientific visualization is inevitably application specific, and the interpretation of visualization requires background knowledge arising from the particular research area. Nevertheless, there are common elements in all visualization tasks. These common elements can be listed as: (1) building insight into the dataset using the particular physical background knowledge; (2) understanding of visual cues (icons and their visual attributes); and (3) familiarity with the appropriate computational and graphical tools, and designing visual icons according to human perception and human-computer interaction principles [28]. Based on these basic features, in this chapter, an overview of scientific visualization is presented.

3.1 Visualization in the context of the scientific enquiry

Scientific visualization is part of a larger process of scientific enquiry, a cyclic model of which is given schematically in Figure 3-2 [28]. According to this model, scientific investigation starts with scientists proposing a hypothesis or a foundation for their enquiry in the form of a mathematical or a computational model. The base model is then tested against the data, collected by means of observation, or by laboratory experiments, or by computational models from simulations. Processing of raw data to obtain information enables the investigator to come to provisional results. The process starts once again, however with more insight, to refine or re-formulate the hypothesis. Each turn of the cycle produces more insight and better understanding of the phenomenon under study. The integration of scientific visualization in the scientific method facilitates all creative processes involved, as outlined for each stage below.

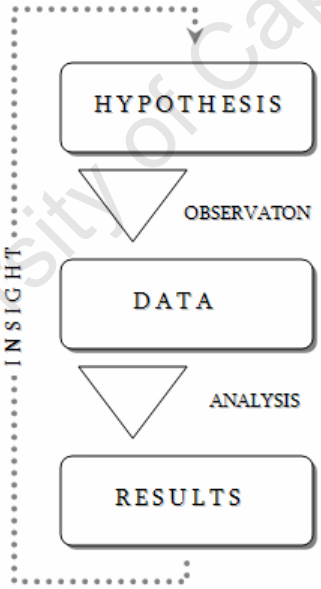

Figure 3-2 A particular cyclic model of scientific enquiry which includes activities where scientific visualization may be applied [28].

Hypothesis: There is an inextricable connection between visual modelling of data sets and the scientific hypothesis. The success of a visualization idiom is a good indication of the strength of the underlying hypothesis. As an example, consider the

development of astronomy. The position of six planets, sun, moon and bright stars were collected by Ptolemy in the second century CE. The geocentric model of the heavens was used to analyze Ptolemy's data for centuries. The astrolabe, a visual aid in the form of an analogue computer, as shown in Figure 3-3a, was used to calculate the position of stars as precisely as possible [34, 35]. Compared to the modern heliocentric view, the geocentric model was extremely complicated and entailed many assumptions, but was still ineffective to explain the peculiar movement of certain planets at different times in their orbit. Only when the heliocentric view was finally advanced in sixteenth century by Nicholas Copernicus [36], were empirical models and corresponding visualization idioms greatly simplified. In Figure 3-3, a complex astrolabe of the Middle Ages is shown next to a renaissance visualization of the simple circular orbits advanced by the heliocentric hypothesis.

(a) (b)

Figure 3-3 (a) The astrolabe, an analogue computer designed according to the geocentric model of the heavens used to visualize the trajectories of the sun, moon and the stars on the night sky (b) Engraving of the heliocentric solar system from Copernicus's notes in *De Revolutionibus orbium coelestium libri* (after [36, 37]).

Observation & Data Collection: Scientific visualization is now widely used in the design and control of experiments and instant analysis of the results obtained. This enables efficient use of resources and time. Examples of first visual approaches to experimental setup and data collection include software such as LabVIEW [38, 39] and TESTPOINT [40]. The use of such software in experimentation is not confined to automation, but virtual instrumentation integrates the experimental design, and observation stages, with the data analysis and evaluation processes. In large scale research facilities, the use of scientific visualization based on real time visual indicators is expected to steer experiments, known as "computational steering" [41], or model simulations for more efficient data collection [4].

Computation & Data Analysis: The primary role of scientific visualization is to provide insight into large and/or complex intractable datasets. This is achieved by means of a visual idiom that transforms the data into a visual geometric object, or pattern, by use of algorithms, or special shape metrics that define the object or pattern geometry. Specific examples of these are the tensor icons discussed in this work, and field lines or contour lines, respectively. These will be discussed in more detail in section 3.4.

Results & Insight: Visual representations that highlight critical features, with information rich and intuitive graphics, facilitate coming to accurate results and conclusions quickly and decisively. For example, Feynman diagrams can be used to show all the processes occurring during particle interactions in quantum electrodynamics [31]. This graphical method, of representing the interaction of elementary particles, was introduced as an aid for the subsequent calculation of the processes that occur between elementary particles and photons, in the course of the development of quantum electrodynamics (see Figure 3-4). Feynman diagrams, like Venn diagrams visualize results and insight, and can be classified as information visualization in the broader scientific visualization scheme of Figure 3-1.

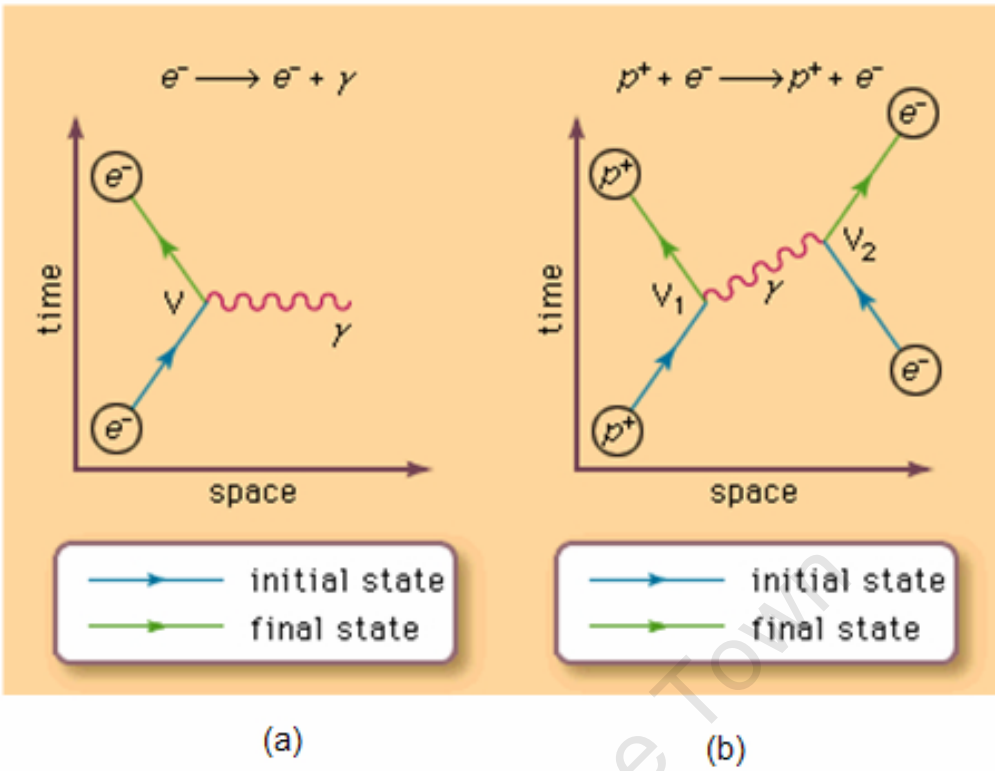

Figure 3-4 Feynman diagrams: (a) a basic vertex (V) showing the emission of a photon (γ) by an electron (e^-); and (b) a more complex interaction between a proton and an electron with two vertices, V_1 for emission, and V_2 for absorption of a photon. The calculation of a particular process in quantum electrodynamics must include terms equivalent to all lines (particles) and vertices (interactions) [42].

3.2 Elements of visualization models

After emphasizing scientific visualization in context with traditional scientific research, we look closely to the step-by-step process of scientific visualization. Any visualization model can be expressed as such a visualization pipeline [43] consisting of different elements, shown in Figure 3-5. This expands on traditional visualization models which until recently only included three steps:

1. Construction of an empirical model from data;
2. Selection of geometric models and shape metrics to depict the data; and
3. Rendering of images in various media.

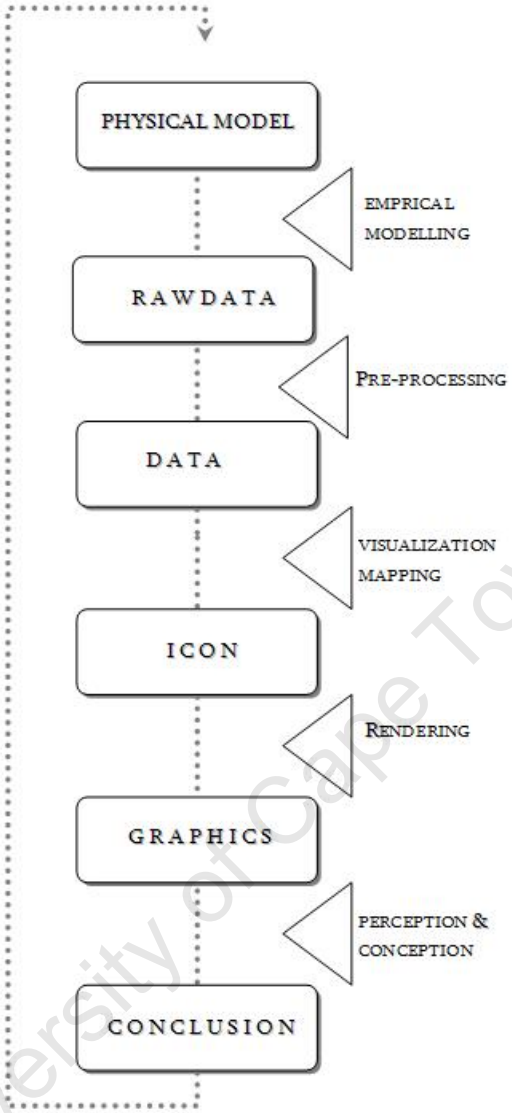

Figure 3-5 Scientific visualization pipeline.

However, since 'a graphic is never an end in itself; it is a moment in the process of decision making' [44], human perception and cognition of visual images is also included in the visualization pipeline [45].

3.2.1 Data types

Irrespective of the source of scientific data, be it obtained from computer simulations, practical experiments or natural observations, the qualitative nature of the collected data depends on the both hypothesis, or physical model, and the empirical modelling processes. As pointed out in section 3.1 above, there is a connection between visualization and the underlying scientific model. Subsequent visualization mapping processes are also determined by the quantitative properties of the dataset, *i.e.* scalar, vector, tensor quantities and the spatial resolution of the dataset (discrete/ continuous, sparse/dense). Scientific visualization should therefore be introduced early into the research to ensure that the data obtained is appropriate for the entire visualization pipeline.

The first steps in the visualization pipeline (Figure 3-5) to examine the physical model, are the preparation of a suitable dataset through collection, and pre-processing of the raw data. Pre-processing of the raw data is a mathematical process of data preparation for the subsequent processes that includes: data enrichment or enhancement procedures, such as sampling, re-sampling, regularization, interpolation, extrapolation, normalization, curve fitting, filtering and smoothing; and subset creation procedures such as segmentation, and feature detection [46].

Following the classification given in reference [28] the data set available for visualization can be grouped according to the type and dimension of the data, as well as according to the domain in which the data is defined. The domain is a mathematical space, which in general is not position space but the space spanned by the numbers of independent variables: $x_1, x_2, ...x_n$, where n is the dimension of the domain. The quantity to be visualized can be described by a function of the coordinate or position in the domain: $F(x_1, x_2, ...x_n)$. This function can be one the following types:

- scalar function: $F(x_1, x_2, ...x_n) = f_1$;
- vector function: $F(x_1, x_2, ...x_n) = (f_1, f_2 ... f_k)$, where the dimension k is not necessarily the same as n, the dimension of the domain;
- second rank tensor function: $F(x_1, x_2, ...x_n) = (f_{ij})$ where $i, j = 1,..k$.;

- higher rank (m) tensor function: $F(x_1, x_2, ...x_n) = (f_{ij..m})$ where $i, j, ..m = 1, ..k$.

A useful notation [47] to classify the entity, in terms of its type and dimension of the domain, is to use the letter E for entity, or any other meaningful symbol, with a subscript for the dimension of the domain and a superscript P, S, V or T to indicate point, scalar, vector and tensor data respectively. In this sense, a point entity is a binary function –either a data point is present or not present– so for example, if data points are simply scattered in an n-dimensional space, the point entity E_n^P is used. A scalar entity S in n-dimensional space is identified as E_n^S . The dimension of a vector or tensor entity is further denoted with subscripts to the letters V and T. For example, temperature on a metal plate can be written as the scalar entity T_2^S , the three-dimensional electric field vector can be denoted with $E_3^{V_3}$, and the tri-axial stress tensor in three dimensions as $\sigma_3^{T_{33}}$.

If the entity E is not defined continuously over the domain, but defined discretely over finite but continuous regions, the domain dimension is written in square brackets, *e.g.* census data taken over a fixed period every five years can be denoted by $E_{[1]}^S$. If the entity is not defined over a domain but is a list for a number of cases (as in the case of the result of a repeated observation), it is called an enumerated type, and the dimension of the domain is shown in braces $\{n\}$, *e.g.* the annual oil production of the OPEC countries is $E_{\{1\}}^S$. To indicate multivariate functions of the same type, the total number of functions is indicated on the superscript. For example, temperature and pressure in the volume of a gas can be denoted by $(T, P)_3^{2S}$. Time is often an additional dimension and is treated differently. It can be denoted separately in the domain subscript. For example the time dependence of electric and magnetic fields can be denoted as $(E, B)_{3+1}^{2V_3}$.

In cases where the function cannot be represented in its original form, reduction of data complexity (data type or dimensionality) is required; *e.g.* by scalar extractions from vectors or second order tensors, or 2–D projections of 3–D functions. Data reduction results in information loss. However this might be necessary in cases where

the data density is too high, either for the human brain to grasp the underlying information, or because the visualization idiom is not capable of mapping the high information density. In such cases a balance between complete visualization and perceptibly effective visualization must be found.

The representation of three multivariate scalar functions is not the same as the representation of a vector field: the first one is denoted with E_3^{3S}, and the latter as $E_3^{V_3}$. However, this classification of the data types, according to the spatial domain and function type, enables the discussion of isomorphism of data types. In mathematics, isomorphism is defined as a one to one function of an algebraic structure onto another that preserves all algebraic relations [48]. For example, consider the following three data types defined in three dimensional space:

- nine scalar fields E_3^{9S};
- three vector fields $E_3^{3V_3}$;
- a general second rank tensor $E_3^{T_{33}}$.

The number of independent variables (domain dimension) is 3, and the total number of dependent variables is equal to 9, for each of these entities (Figure 3-6). Thus in total all the entities have (3+9) variables. In principle, a potential visualization algorithm, that can be used to represent 12 different variables can be used for all entities. Because such isomorphic visualizations do not differentiate between the data types such as scalars, vectors and tensors, to capture the inherent structure of the data types, specific mapping processes are designed for different types as discussed in the next section.

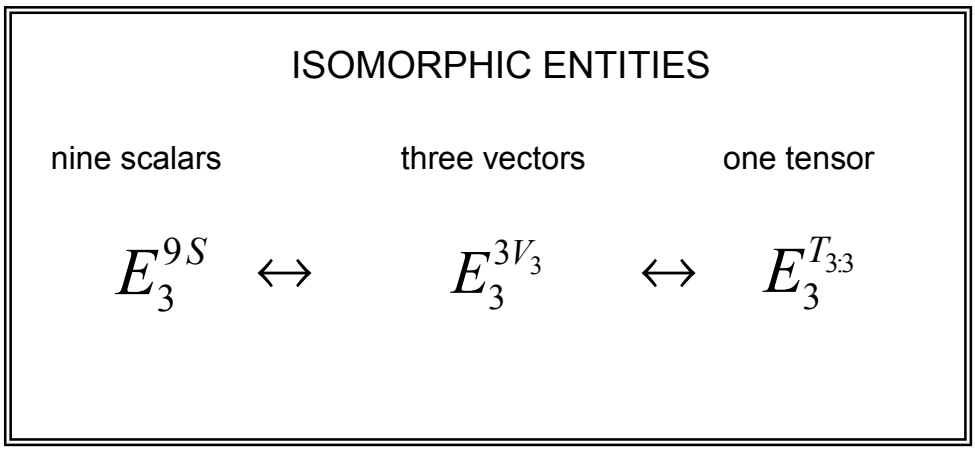

Figure 3-6 Defined in a three dimensional domain, nine scalars, three vectors, and a second rank tensor are isomorphic, *i.e.* they all have 3+9 variables to be visualized.

3.2.2 Mapping

The following step in the visualization pipeline is the creative step of visualization mapping. This process shares the same goal with art, to communicate visually and symbolically, but in precise and objective ways. These goals are achieved by mapping the dataset onto the properties or characteristics of an image or visual object. Unlike mathematical mapping, however, the design of the visual object, and its attributes, is an integral part of the visualization process. This essential step is explained by means of an example. Consider the vector $\vec{A}$, given by three coordinates (r,θ,ϕ) in the spherical coordinate system. The properties of the vector $\vec{A}$, of interest to visualization, might be listed as its components, magnitude, and orientation which corresponds to the (θ,ϕ) angles. Upon the recollection of an arrow, it can be seen that the arrow, as a visual object, has similar characteristics. The characteristics of the arrow that can be used in visualization are not only length and orientation, but also thickness, size of the arrow head, colour, transparency, line style (full, dotted or dashed), texture (if the arrow body has a cylindrical surface), *etc*. The visualization mapping, from the vector $\vec{A}$ to the visual arrow, can be achieved by scaling the arrow length to the magnitude of vector $\vec{A}$, *i.e.* length ~ $\left|\vec{A}\right|$, which possibly includes a

change of units, and the direction of vector $\vec{A}$ to the direction of the visual arrow, using the spherical coordinates (θ, ϕ), as shown in Figure 3-7. The selection of a set of compatible characteristics between the dataset and the visual object is the essential step of visualization mapping. Such a visual object is generally referred to as a visualization icon and the properties of visual icons are discussed in section 3.3. The mapping of the dataset onto a specific icon is generally achieved using a lookup table, which parametrically defines icon's attributes using dataset values, known as the shape metric [49]. The main challenge in visualization is to find appropriate icons, or to develop new ones, for a particular visualization task, and to combine the icons such that the information is enhanced and not obstructed [50].

The visualization mapping step might be as easy as assigning a colour map to a scalar quantity, or it can be as complex as creating global streamlines based on the topology of a vector field. This stage is application dependent, and techniques used must be considered in a particular context. The information to be conveyed is user-specific, and usually the interpretation of the resulting visualization requires expert knowledge.

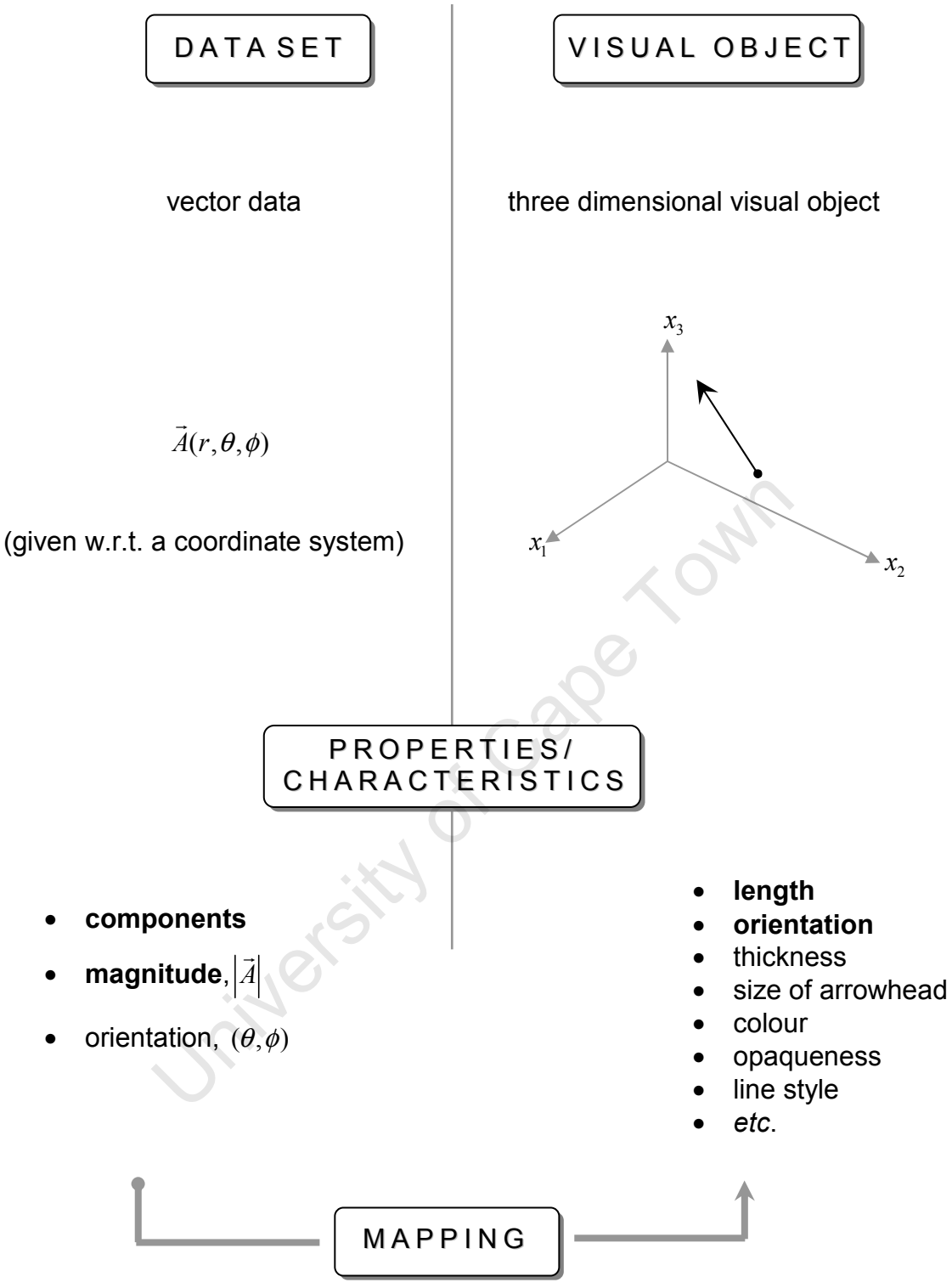

Figure 3-7 The illustration of the visualization mapping process for vector data to an arrow object.

3.2.3 Rendering

The third stage of scientific visualization is to realize or render geometric objects, designed by the visualization mapping process, on the computer screen or another medium, such as a sheet of paper. Rendering involves combinations of a wide range of techniques to produce a graphic representation, or a picture of, the chosen icon and its attributes. These include the appropriate use of palette (colour, greyscale, black and white), line style, perspective and shading, typography, as well as background and contrast setting, final image resolution, image area selection, lighting, and interactive techniques. This step in the visualization pipeline is intimately connected with the choice of medium, the attributes of the icon, and the mapping of the data on the icon. Therefore rendering cannot be discussed in general terms, but is application dependent and will be discussed in the examples in chapter 4, Visualization Techniques, on a case by case basis.

3.2.4 Perception

The final step in the visualization pipeline is the psychological step of visual perception, which is the interpretation of the visual stimuli by the brain, determined by the physiology and psychology of the human visual system. The perception and interpretation of scientific visualization depends on the context, attention focus, expectations, prior knowledge, past experiences and subjective biases [46, 51]. Successful visualization applications balance the two processes of data encoding, performed in the mapping procedure, and information decoding in the human visual system. In the decoding process, even the perception of an object in a picture is in general a complex task, starting with recognition of an object by its shape, orientation, and location in the picture. Furthermore perception of depth of a three dimensional object in a two dimensional representation is given by perspective drawing and shading. For scientific visualization the icon and its visual extensions, have to be chosen so that they can be easily perceived and the information carried can be unambiguously interpreted. Visual icons and the perception of their attributes is discussed in the next section. For a more complete discussion of the human visual system in the context of scientific visualization see for example [50, 52].

The perception of visualizations might be further hindered by visual cluttering or occlusion in the rendered image. Visual clutter is the result of using too many geometric shapes, so that eye or brain cannot distinguish or interpret the information contained. Occlusion is a special case of visual cluttering, in which visibility is reduced by icons overlapping or masking other icons. If the use of a large number of individual icons causes visual clutter or occlusion, the visualization domain can be reduced to subsets and visualized separately. If the full structure picture is required, local/global representations can be used. As discussed in the next section, local representations are achieved with glyphs or point icons which are effective for emphasizing features at particular points in the domain. Global representations, on the other hand, are used to display the overall structure of the system. A combination of both may be necessary to convey the required information without causing information overload. In general, information overload should be avoided as much as possible to improve interpretation, since this is the ultimate goal of scientific visualization.

3.3 Visualization icons and their attributes

The quintessence of the visualization pipeline is the encoding of data onto a visual representation and the decoding, or interpretation, of the information by the same or another person [50]. The essential core of the encoding stage is the visualization mapping of the structure of the data onto the attributes of the representation. The enforcement of regularity principles between the data and perceptual elements enhances gestalt perception, the perception of the whole being more than the sum of its parts [53].

In scientific visualization the visual representation is usually referred to as an icon. Visualization icons are classified according to their data sources as point icons, local icons or global icons. Point icons, also referred to as glyphs, are defined at a point in the domain and derive their attributes from the local value of a quantity at that point. Local icons are defined in a region of interest, or at the vicinity of a point, and defined by the properties of the local region. Global icons represent the overall structure or the

topology of the system [54]. In Figure 3-8, the same vector field is shown using point icons, local icons and global icons. The choice of a scientific visualization icon depends on both its available attributes, often referred to as visual extensions, and the goals of the visualization process, which depend on the data attributes. Icons and symbols are the subject of semiotics, developed as a science by C.S. Pierce and Ferdinand de Saussure, whose theories are based on the fundamental distinction between the signifier (signifiant) and the signified (signifié) [55].

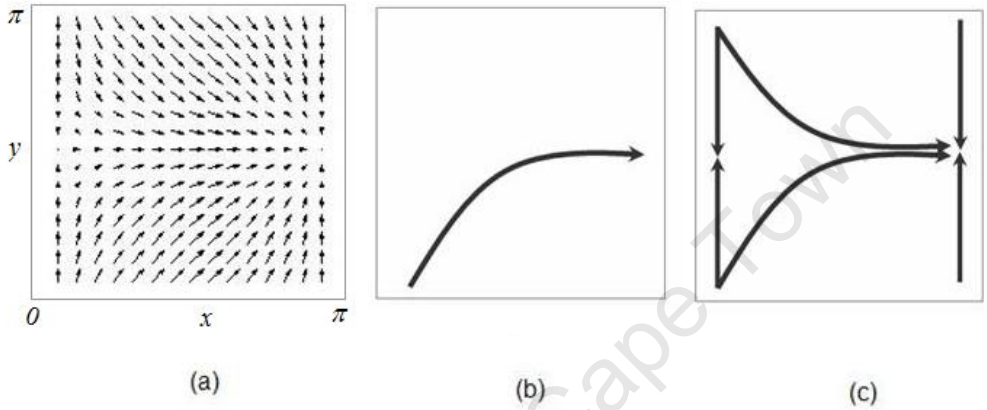

Figure 3-8 The vector field, $\sin(x)\hat{\mathbf{i}} + \cos(y)\hat{\mathbf{j}}$, is represented by: (a) point icons; (b) streamline, a local icon; (c) vector topology is depicted from the critical points by streamlines, a global icon.

For effective representation of data with visual elements, a structural correspondence between the signifiant (visual elements) and signifié (data) is necessary. This correspondence should be defined between the structure of data and the perceptual structure of the icons. In Figure 3-9, this is illustrated for relational data structures and perceptual elements. The close similarity between the classification of perceptual structures and the classification of relational data structures enables the use of structurally related visual attributes for the depiction of corresponding data attributes [56]. This correspondence is especially important for mapping the corresponding tensor information on the relavent visual attributes, *e.g.*colour and size versus stress type and magnitude.

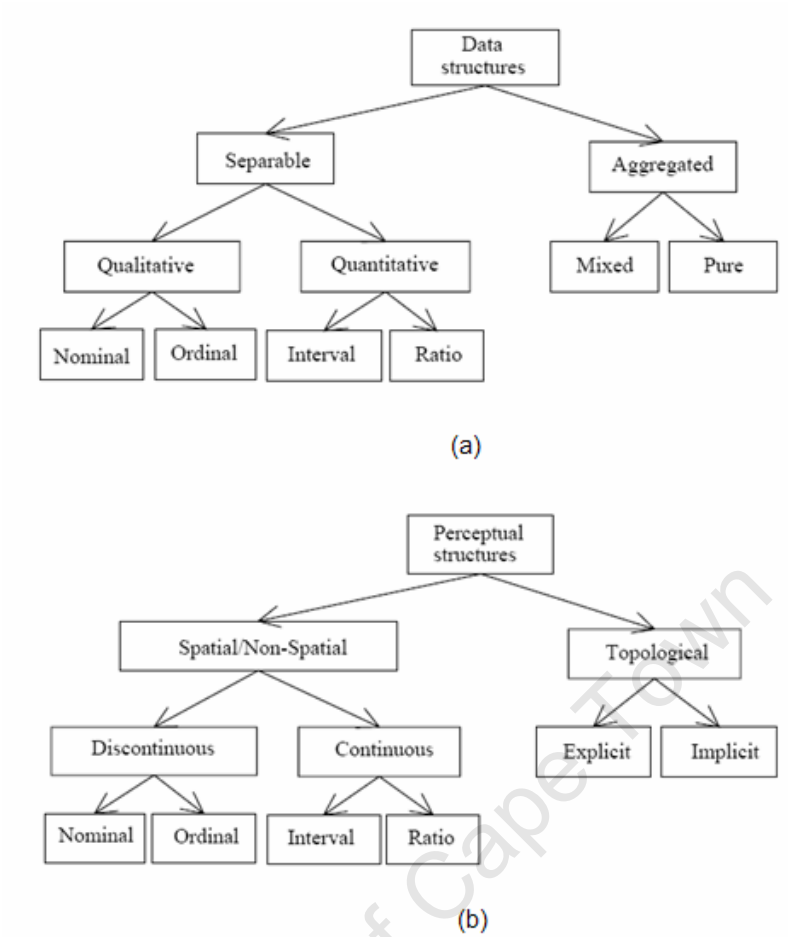

Figure 3-9 The structural correspondence of (a) relational data structures and (b) perceptual structures [56].

Goals in scientific visualization can be very diverse. For example in Figure 3-10, the goal of the visualization is to compare images, positions and data sets to reveal overall change in the global ozone concentrations between October 1979 and October 1989 [57]. In another example in Figure 3-11 the goal is to correlate three variables of a simulated ionized stellar plasma (density, temperature and energy) over time. The visualization enables the study of the evolution of the three variables simultaneously to reveal process dynamics [58]. Visualization can also be used to search for extreme values in datasets, such as the major shocks and expansions in the flow around a complex aerodynamic body, as shown in the examples of the space shuttle in Figure 3-12 [59].

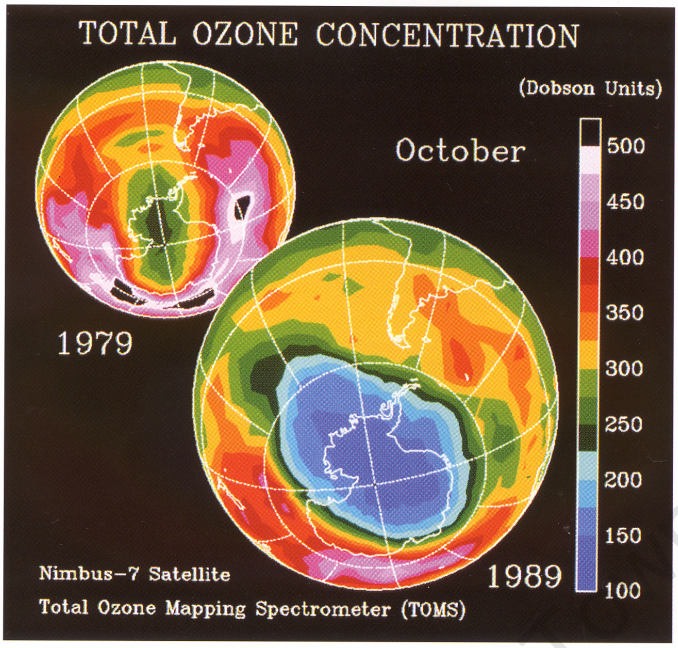

Figure 3-10 Comparing images reveals the decrease of global ozone concentrations above Antarctica between 1979 and 1989 [57].

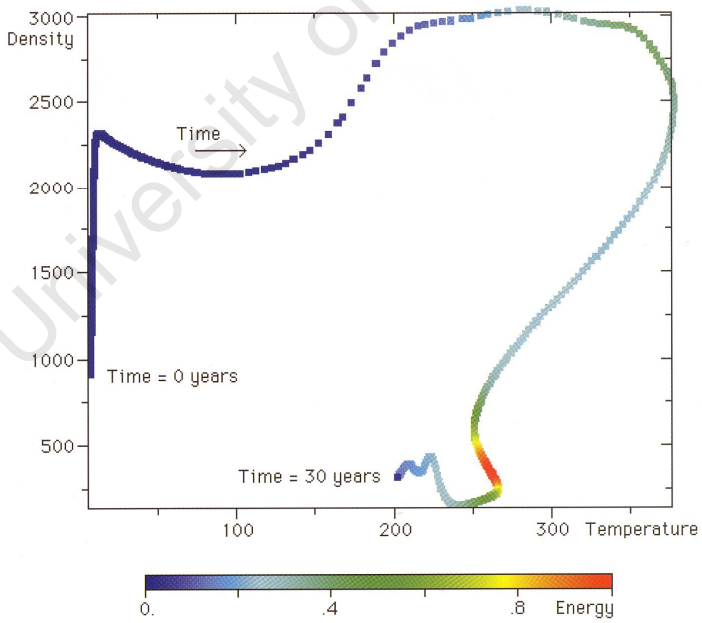

Figure 3-11 Time ordered coloured squares show the relationship between density, temperature and energy over time in an ionized stellar plasma simulation [58].

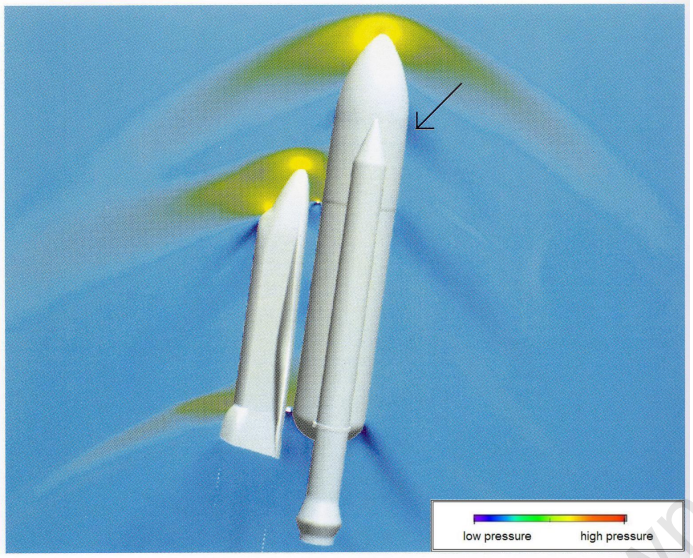

Figure 3-12 Colour mapping identifies extreme pressure values by superimposing a model of the space shuttle model on a slice of a 3–D pressure visualization. The arrow indicates a dark blue region, corresponding to a low pressure expansion region, which is possibly caused by the nose of the outer solid rocket booster [59].

A useful method of identifying visualization goals is to build a taxonomy of data types and actions, or analyses, to be performed on the datasets. The visualization goal is then determined uniquely by combining elements symbolically from both classification lists. Table 3-1 shows an example classification [46] which identifies nine actions and seven types of data, so for example a typical visualization goal of 'comparing scalar values' would be shown by 7A. According to this scheme these actions are:

- *Identify*, meaning to establish the collective characteristics by which an object is distinctly recognizable, *e.g.* identifying temperature values with iso-lines;
- *Locate*, meaning to determine the absolute, or relative, position and extent of an object, *e.g.* locating a city on a country map;
- *Distinguis*h, meaning to recognize an object as different or distinct, where no identification is required, *e.g.* distinguishing tumour growth in healthy tissue;
- *Categorize*, meaning to place multiple objects in specifically defined divisions, *e.g.* grouping organ systems in an organism;

- *Cluster*, meaning to join similar or related data that need to be either conceptually or physically grouped. Clustering is distinct to categorizing, in the fact that clustering creates groups, whereas categorizing identifies the existing groups;
- *Rank*, meaning to give an order or position with respect to similar objects in a data type;
- *Compare*, meaning to examine so as to notice similarities and differences;
- *Associate*, meaning to link, or join, in a relationship two or more objects;
- *Correlate*, meaning to establish a direct connection, which is important and possibly hidden. The connection may be causal, complementary, parallel or reciprocal.

The data types of this taxonomy are:

- *Scalar* describes a quantity specified by a single number on an appropriate scale, such as temperature, pressure or density;
- *Nominal* describes an entity which can be in a group of other entities, such as a specific automobile manufacturer amongst other manufacturing companies;
- *Direction* describes the orientation relative to a reference position or axis, of another position or motion, *e.g.* compass needle direction or the hands of a clock;
- *Shape* describes a real or abstract object distinguished by its outline or surface;
- *Position* describes the absolute (with respect to reference frame) or relative (with respect to another object) location of an object;
- *Spatially Extended Region or Object* (*SERO*) are entities that extend between points, forming areas in 2–D and volumes in 3–D space. A 3–D representation of the human brain is a spatially extended object;
- *Structure* describes a combination of other data types that can be considered as a single object, such as the water molecule which is a specific combination of hydrogen and oxygen atoms.

Actions	Data types
1 Identify	A Scalar
2 Locate	B Nominal
3 Distinguish	C Direction
4 Categorize	D Shape
5 Cluster	E Position
6 Rank	F SERO
7 Compare	G Structure
8 Associate	
9 Correlate	

Table 3-1 Taxonomic determination of visualization goals formed by combining an action and a data type from each list [46].

After the identification of visualization goals, a single icon, or a combination of visualization icons can be used to achieve these goals. This requires the consideration of the attributes in terms of their perceptual structure. Although visual extensions can be classified according to the geometric structure, which maps on to the data structure, as described above, they are more usually classified according to their perceptual complexity. Perception of length, width, colour, line orientation, line intersections, shape curvature, and contrast are basic, or pre-attentive extensions. Complex visual attributes include shape, depth, texture and gestalt perception. Two other quantities which describe the perceptual complexity are the representational accuracy and the perceptual dimension. Representational accuracy is the measure of how accurately the human visual system can identify a quantitative variable using a particular visual attribute. Perceptual dimension is the number of dimensions that can be perceptually differentiated. The smallest unit of display space necessary to represent the visual attribute is called its spatial requirement. Following from these definitions, information content and information density can be defined as [50]

$$Information\ Content = Representational\ \ Accuracy \times Perceptual\ Dimension\ , \qquad (3.1)$$

$$Information\ Density = \frac{Information\ Content}{Spatial\ Requirement} \quad . \tag{3.2}$$

Below is a brief description of the important visualization extensions. It is important to note that these descriptions now refer to the attribute of the visual representation in display space, and not to the structure of the data which is mapped onto it. Similarities between the two may be misleading.

Position: position is the specific location of an object in the display space. This implies a reference scale and may be defined either relatively or absolutely with respect to a frame of reference. Position has the highest representational accuracy of all visual attributes [50]. However, its use is usually reserved for the representation of the independent spatial/ temporal coordinates of a system, *i.e.* the position of a point icon generally identifies the position at which the scientific data is visualized. For example in Figure 3-13, the positions of the three capital cities of South Africa are shown by the positions of the encircled stars on the map.

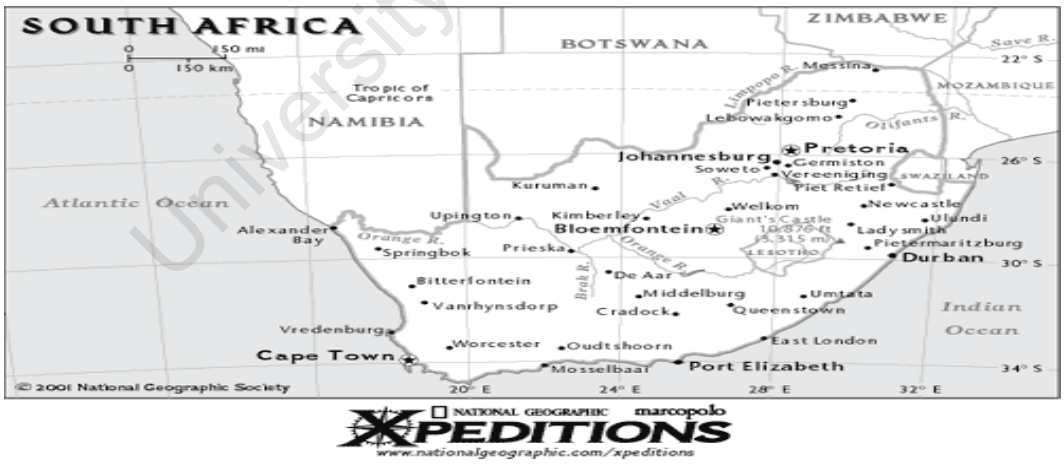

Figure 3-13 The position of the three capital cities of South Africa are indicated with encircled stars, Cape Town, Pretoria and Bloemfontein.

Direction: directional information is required for the representation of scalar gradients, vectors, flow fields and second order tensors. Arrows, cones, pyramids, cylinders are icons with direction extensions (see Figure 3-14).

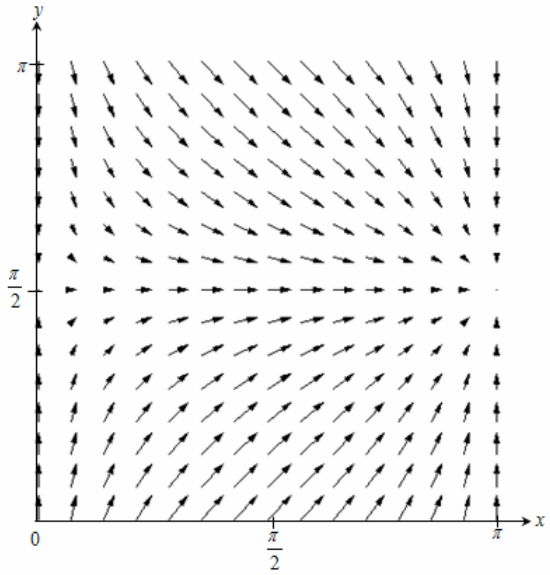

Figure 3-14 The vector field plot of the function $\mathbf{F}(x, y) = \sin(x)\mathbf{i} + \cos(y)\mathbf{j}$, using directed arrows, reveals field direction.

Length, area, volume: length, area and volume are the basic geometric primitives for visualization icons. The perceptual dimension is one in the case of length. However the use of lines to convey directional information is usually not effective due to the ambiguity of directional information on a directed line segment in a 3–D volume. On the other hand, surface icons can show directions by their surface normal and by the magnitude of their surface area. The use of volume as a visual extension or as an attribute of an icon should not be confused with the technique referred to as "volume visualization", which refers to the mapping of the data structure onto the attributes of a volume elements in a 3–D domain. In the latter case, however, particularly if colour, transparency, or texture are used as the visual extension, volume visualization allows the recognition of regions within the global map which have the attributes of volume and position. Figure 3-15, shows the Open Inventor based graphical user interface with data obtained from an online visualization of the data of a molecular dynamics simulation (shearing of a block) with about one million of atoms. The kinetic energy distribution is color coded displaying interfering shock waves (green) and emitter of the shock waves (red).

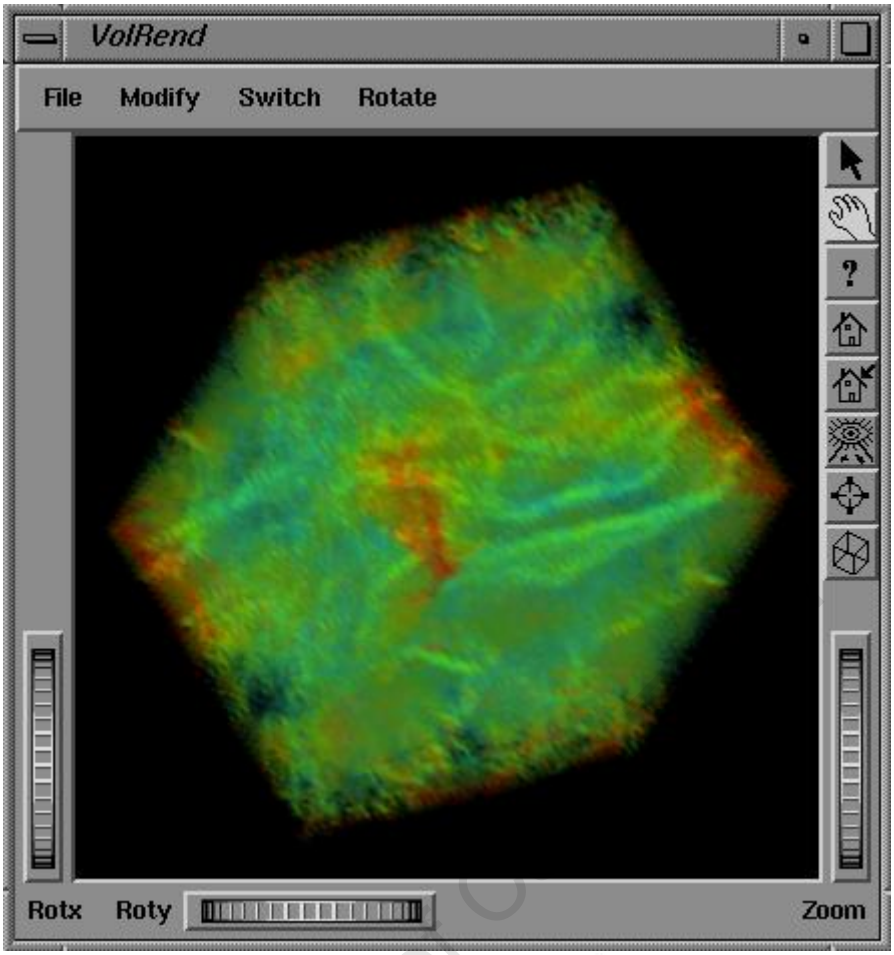

Figure 3-15 The volume representation of a molecular dynamics simulation involving the shearing of a block. The kinetic energy distribution is mapped on the voxels [60].

shape: the shape of an icon can be used to encode information in multiple dimensions. Three dimensional objects can be used to simultaneously display three scalars by scaling width, breadth and height of the object. For example, a cylinder with a disc around, as shown in Figure 3-16, can be used, not only to represent three scalar quantities simultaneously, but the alignment of the cylinder can also represent direction. This point icon is actually known as the Haber glyph [43] and will be discussed fully in section 4. However, shape recognition is highly orientation dependent and rotated objects might be perceived as different shapes. Thus care must be applied in the selection of the representation of three dimensional shapes on the two dimensional screen or paper. 3–D surface shading and lighting can change perception and must be taken into account in the interpretation of colour in illuminated scenes. Diffuse light usually gives better results [53].

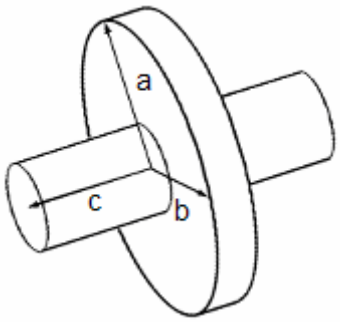

Figure 3-16 A cylinder and an elliptical disc around it can represent three scalar quantities, *a*, *b* and *c* using the radius of the disc and the half-height of the cylinder. The orientation of the shape can also be used to represent an orthogonal coordinate system using the three axes, **a**, **b** and **c**, in which the eigenvectors of a second rank tensor can be visualized [43].

Familiar shapes can be used to improve recognition, *e.g.* traffic signs utilize this ability of the brain. More complex but familiar shapes, for example the cartoon human face shape known as the Chernoff icon [61], can be used to harness this ability to recognise patterns in multidimensional data. Figure 3-17 shows a set of typical cartoon faces whose features, such as the overall shape and curvature of mouth, correspond to the six characteristic variables of a fossil animal in a multivariate observation. This representation makes it easy for the human mind to grasp many of the essential regularities and irregularities present in the data required for actions such as categorise, compare and distinguish in Table 3-1 above.

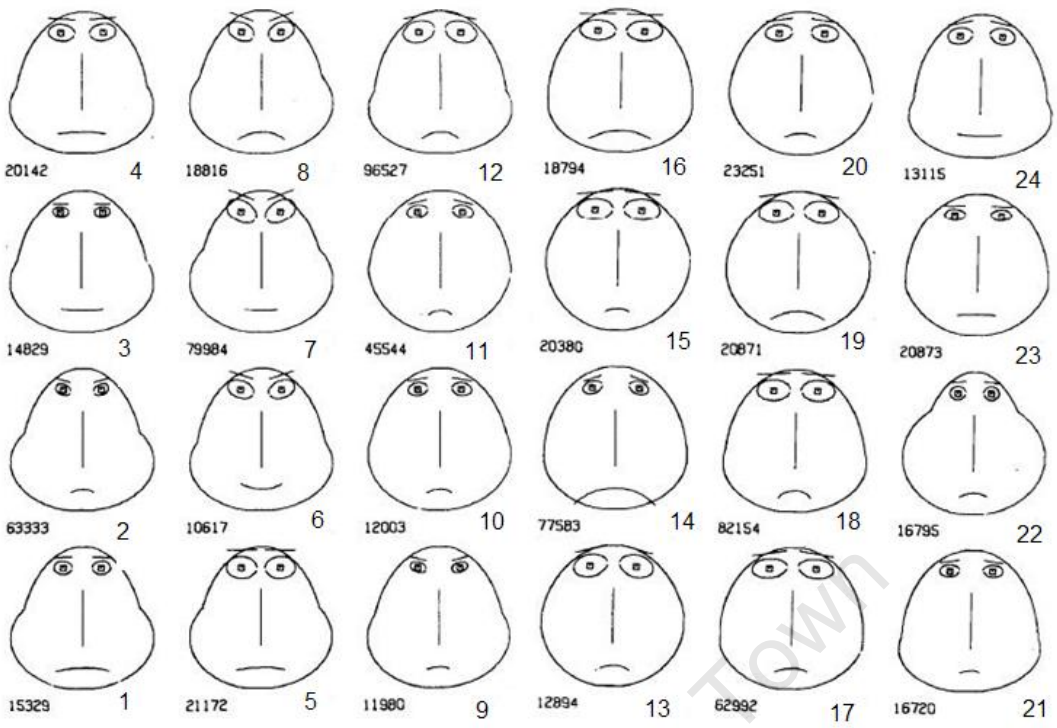

Figure 3-17 Chernoff faces are used to cluster multivariate qualitative data of six variables, from fossil data. For example faces no. 1, 2, 3, 9, and 22, and faces 4, 5, 12 and 24 can be placed in two separate groups. The major advantage to be derived from using the faces is heightened qualitative awareness [61].

Colour: colour is sensed by the three types of light sensor in the human eye, that respond to red, green and blue wavelength bands. The RGB (red-green-blue) colour scheme is designed to match the visual physiology of human eye, in which all colours are produced by relative constitutions of red, green, and blue (see Figure 3-18a). Another colour scheme, called the HSV colour scheme, is designed according to human perception [46]. The HSV colour system can be represented by an inverse cone that describes hue, saturation, and value parameters, as shown in Figure 3-18b. Hue can be thought of as the dominant colour, value is the physical intensity or brightness of the light, and saturation is the relative amount of the hue. Although both descriptions include three independent dimensions, it is not easy, and even colour experts find it difficult, to separate the components of a particular colour [62]. Colour and illumination of the surroundings affect colour perception, and colour is a complex

component to manage in scientific visualization. Often in practice, therefore, hue values are used to create mathematical (scalar) colour look-up tables, which are used with colour legends. The use of realistic, logical or intuitive colour scales increases understanding. For example a blue or violet colour can be associated with ‘cold’, and red and yellow with ‘hot’, or high saturations with ‘high density’, and light colours with lower values, or even red to indicate critical and dangerous practices, compared to green with safe practices [52]. Colour extension are used in Figure 3-10, 3-11 and 3-12 (pages 52–52) to denote scalars; ozone concentration in the atmosphere, energy of a stellar gas, and high-low pressure regions around a space shuttle, respectively.

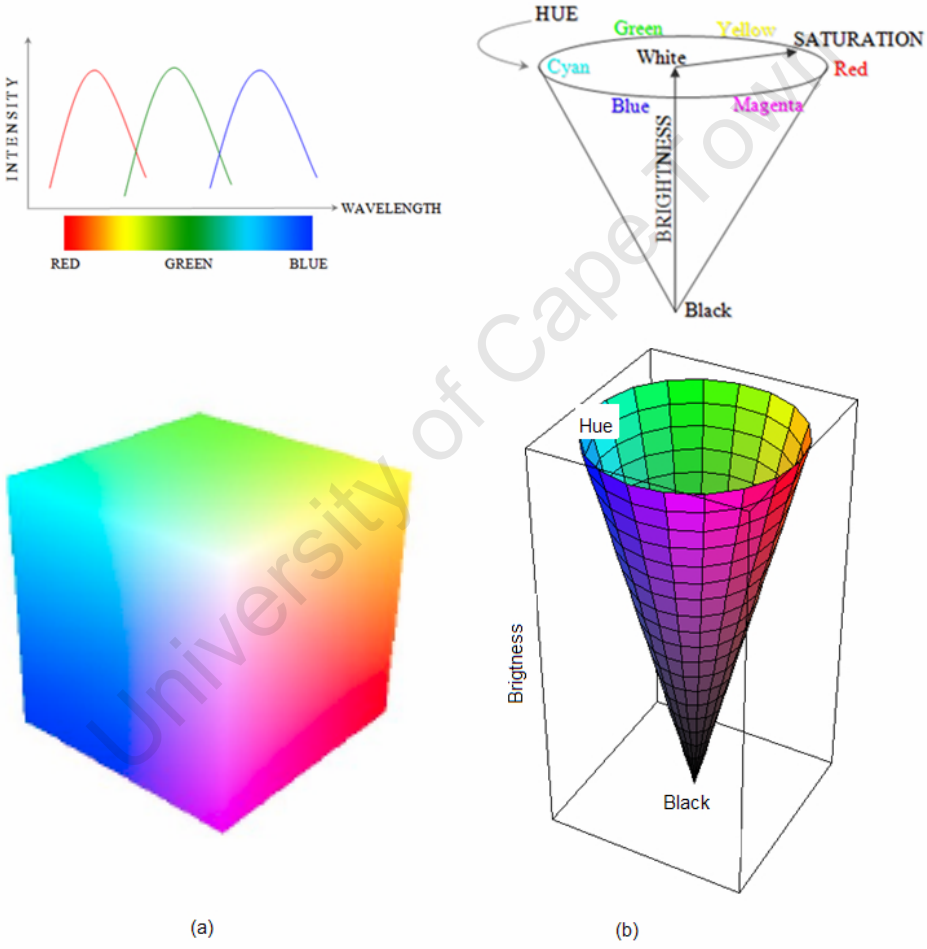

Figure 3-18 (a) Relative absorbance of light by the three types of receptors in human retina, and the RGB colour space based on this scheme. (b) Definition of HSV colour scheme and the corresponding HSV colour space.

Texture: texture, like colour, can be applied to surfaces to add an additional information dimension. Directional or structural information can be depicted with textures, *e.g.* to represent flow on a surface. Texture information can be characterised by spatial frequency, contrast and orientation [63, 64]. A simple application of texture, where elevation or depth of a landscape is depicted with bumps proportional to the actual height is shown in Figure 4-3 on page 63. Figure 3-19 [64] shows the magnetic field generated by two dipoles, using a more complicated texturing mapping. The field orientation is mapped to the texture orientation, and the field strength is mapped to the texture contrast, and also inversely to texture size.

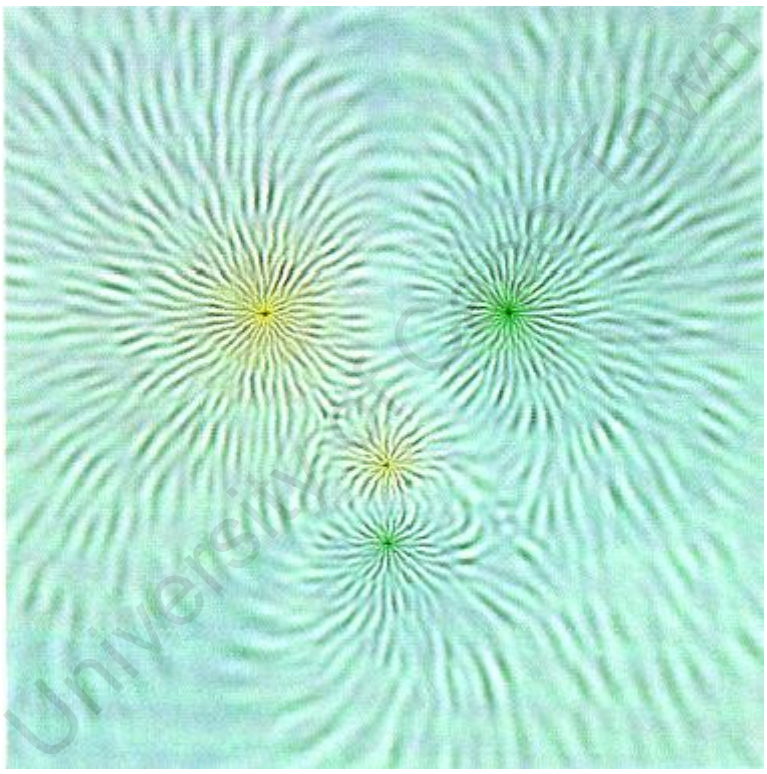

Figure 3-19 Visualization of the magnetic field lines of two dipoles using the texture extension. Texture orientation, texture contrast, and texture size characteristics are used. Hue and value parameters of the HSV colour scheme are used for the rendering [64].

The quantitative measures of the different visual extensions, as discussed above, are shown in Table 3-2. Texture and shape have the largest perceptual dimensions, and therefore a number of different variables and features can be represented with these extensions. For example, textures and common shapes are used in maps to

differentiate between a number of different geographic, or demographic, segments and local features. As described above the theoretical dimension of colour space is three, but the perceptual dimension is usually lower than this. The perceptual dimension of 3–D direction is only two, due to the use of perspective in rendering a 2–D, image but can be increased to three by animation techniques. The perceptual dimension of length, area and volume are all restricted to one, *i.e.* the relative size. Finally it should be noted that, the extensions with the highest information content are position, shape and texture, and the lowest information density is carried by area and volume extensions.

	Perceptual dimension	Representational accuracy	Spatial requirement	Information content	Information/ Density
Position on scale	1-3	High	Low (≥0)	High	High
Length	1	High	Medium (1)	Medium	Medium
Area	1	Medium	Medium (2)	Low-Medium	Low
Volume	1	Medium	High (3)	Low-Medium	Very low
3–D direction	2	Medium	Medium (1)	Medium	Medium
Shape	≥3	Low-Medium	High (3)	Medium-High	Medium-High
Texture	≥3	Low-Medium	Medium (1-3)	Medium-High	Medium-High
Colour	2	Low	Low (≥0)	Medium	High

Table 3-2 Classification of visual attributes according to perceptual dimension, representational accuracy, spatial requirement, information content, and information density [50].

4 Visualization Techniques

This chapter describes the methods, or the algorithms, that transform quantitative scientific data to visual representations, or visual models, so that these visual models can be, later, realized on the computer screen or any other media. This process is known as the visualization mapping process in the scientific visualization pipeline (see Figure 3-5, page 41). The essence of visualization mapping is to design visual icons that map quantitative data to the visual attributes of the icon. Visualization algorithms are classified here as either scalar, vector or tensor algorithms. A wide range of visualization mapping techniques are discussed for scalars and vectors before discussing the visualization of tensors in detail.

4.1 Techniques for scalar visualization

4.1.1 One dimensional domains

The most common form of scalar visualization in a one dimensional domain is simple graphing. For example line graphs, that connect a given set of points in the $x-y$ Cartesian coordinate system represent single or multiple scalar data, E_1^S and E_1^{mS}, by the ordinate and the domain by the x–coordinate, respectively. The plotted graph enables the user to visualize the general behaviour of the underlying function $y = f(x)$. For discrete datasets, $E_{\{1\}}^S$, bar charts are often used. Histograms are statistical bar charts used to display the frequency distribution of statistical data of type $E_{[1]}^S$.

4.1.2 Two dimensional domains

Contouring and color mapping are the best known examples to visualize scalar data on a two dimensional domain, or a surface. Perhaps the best known examples using

these techniques are the physical geography maps in an atlas. A third well known example is the use of perspective drawing to produce a pseudo-3D image.

Colour mapping identifies scalar quantities with colours through a look-up table. A look-up table is an array of colour elements $colour(i)$ with n elements. A minimum $s_{\min}$ to a maximum $s_{\max}$ scalar range is associated with the look-up table. Scalar values outside this range can be fixed to the maximum and minimum colour value, or to any other predetermined colour. Each scalar value s is linked to a $colour(i)$ by taking the next higher integer solution to the equation [30]

$$i = n\left(\frac{s - s_{\min}}{s_{\max} - s_{\min}}\right). \tag{4.1}$$

The colour look-up table must be designed to emphasize the inherent information in the dataset, which usually requires an iterative trial-and-error process. If the dataset is not linear, a logarithmic or exponential transfer function can be used to map scalar values to colours. It must be kept in mind that lookup tables can exaggerate unimportant details, or create artefacts, because of unexpected interactions between data, colour and human perception [46].

In traditional map making, colour maps are used to indicate elevation of landscape of the earth surface as shown in Figure 4-1 [65]. In this case the icon is the whole map of the two dimensional domain with a single visual extension or attribute of colour, and the data type is E_2^S. Besides labelling of towns and other features, additional graphic design techniques, such as shading, are used to give an indication of 3–D structures.

If a restricted set of colours is used, with a good contrast between neighbouring values, the boundary value corresponding to a specific height is visible on the map. A contour line has been automatically generated. However colour extension has low representational accuracy as listed in Table 3-2, for a better quantitative description of the scalar field, additional contour lines can be used. Contour lines, or iso-lines, are lines that trace the equal scalar values in a scalar field. Contour lines are shown for a flat map in Figure 4-2a and for the three dimensional impression of the same landscape in Figure 4-2b [66].

Figure 4-1 Colour mapping used in traditional map making to indicate landscape elevation and sea level depth. In this map, the combination of relief colouring and hill-shading gives a pseudo-3D portrayal of the landforms [65].

Scalar functions in two dimensional domains can be shown using an offset surface using the free third dimensional in a perspective image, see Figure 4-2b. This representation has great advantages if interactive computer graphics are used allowing, for example to pan, tilt and zoom, or walk through features. The main advantage of such height maps is the accurate display of quantitative information, (position and shape has high representational accuracy, Table 3-2) [9]. Wire-frame, solid colour or shaded surface representations can also be used to represent the surfaces in height maps.

Another attribute, which was used qualitatively by traditional map makers as in Figure 4-1, is the texture which is the "feel and appearance" of a surface. The physiology of the eye is more responsive to the changes in texture than to changes in colour, making the topological shape stand out. More complex texture mapping can be applied by changing height, density, regularity, luminance and orientation of the pixel elements [67, 52], see Figure 3-17 (page 58). By using look-up tables for these

visual attributes, multiple scalar information can be mapped on surfaces. Texture, like colour, when used on surfaces, reveals global structures without visual clutter.

Colour and textures can be applied to planar or curved surfaces by adding graphic detail. They can therefore be used on height maps to denote another independent scalar field in the same domain, as if draped over the surface, thus enabling double scalar field data, E_2^{2S}, representation. In Figure 4-3, a hemisphere of the earth is mapped redundantly with both colour and texture. Height and depth measurements at a location texture the map by creating bumps proportional to height at the location of each height measurement; colour redundantly encodes height (blue, low; red, high). Thus, in a similar manner contour lines emerging out of a colour map, a height map is created by the applied bump texture.

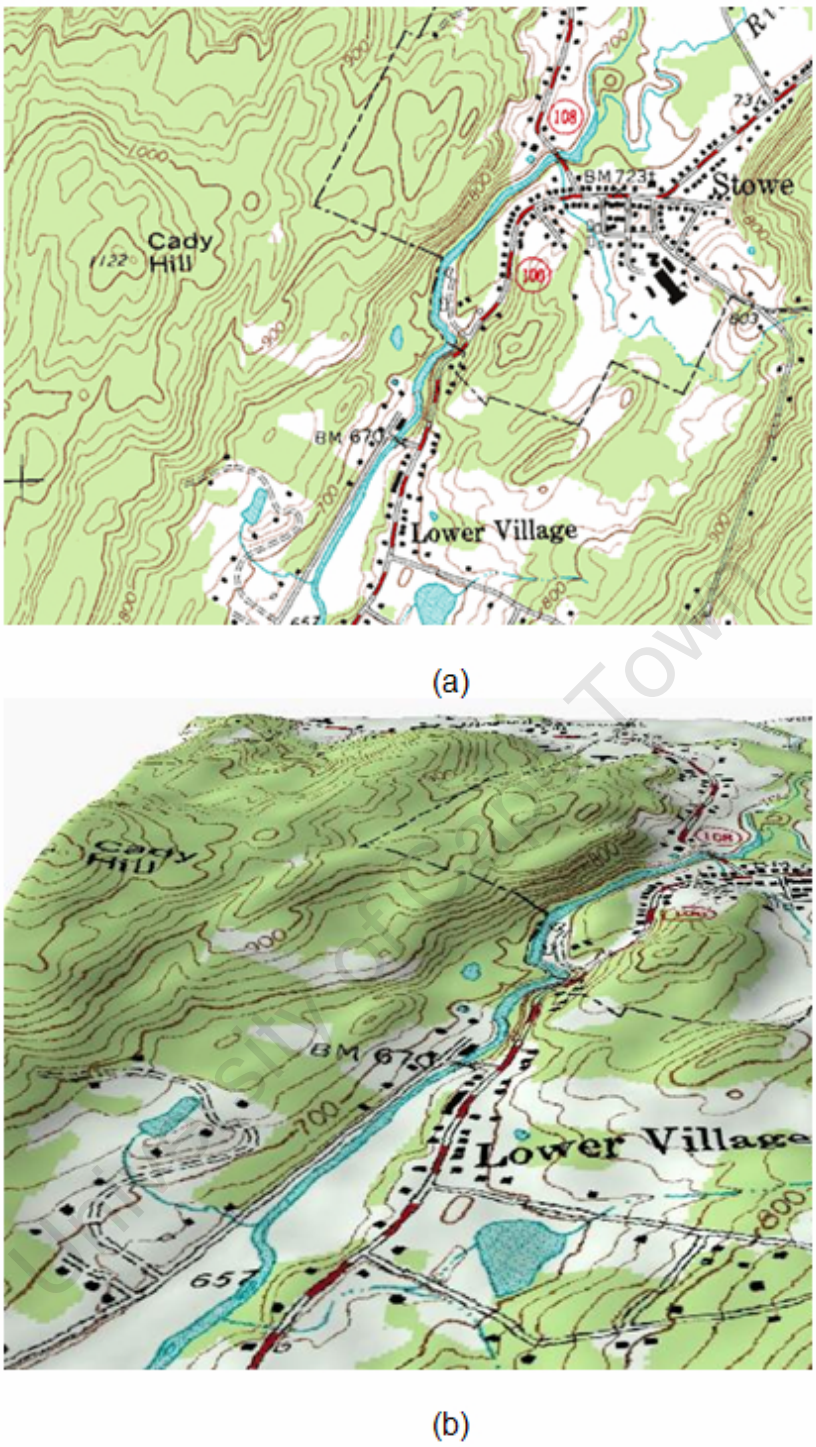

Figure 4-2 (a) Contour lines show a region's topographic relief. Each line represents the intersection between the land and particular elevation above sea level. (b) The same region is shown with height maps to indicate how contour lines follow the terrain. Note that the height map representation is a three dimensional representation of the elevation field. Perspective and shading are used to give the three dimensional impression [66].

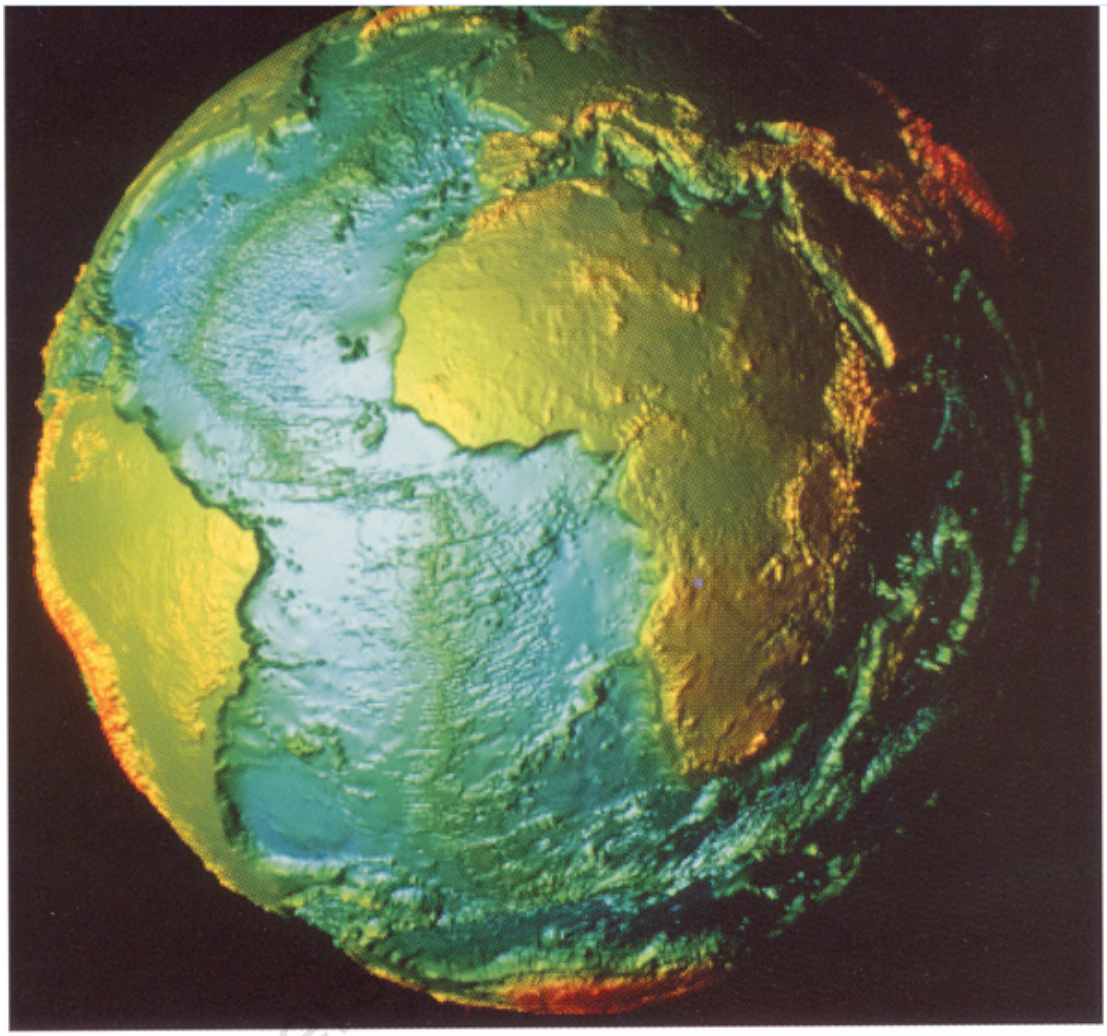

Figure 4-3 Topography and bathymetry (the topology of the ocean floor) elevation data from -9877 m to 7220 m is shown using a bump map, a simple texture where the height measurement at a location is represented by a bump proportional to the height at that location. Redundant colour mapping improves the shape recognition. [68]

4.1.3 Three dimensional domains

Iso-surfaces, also called 3–D contours, lie in a volume so that all the values on the isosurface are equal to some constant value. Although they are a natural generalization of iso-lines, the necessary surface detection algorithms are complex, and fitting of triangles, or higher polygons, is required to define the surface in three

dimensions [30]. Development of special rendering algorithms for isosurface construction has received much attention, and recent algorithms are fast enough to be used interactively, see for example the "visible woman" in Figure 4-4 [69, 70].

Figure 4-4 Isosurface extraction of the skeleton of the Visible Woman dataset, composed of 1714 slices of 512×512 images at 16 bit (910 MB in total), rendered using a novel ray tracing technique enabling up to 8 frames per second on a four processor system [69].

Another technique for volumetric data visualization is to use particle systems. By randomly placing small particle-like objects in a scalar field, the structure of the scalar field can be explored, *e.g.* by assigning colour of the particle to the value of the field. This enables exploration of complex fields without visual clutter, provided the density

of the particles is not too high. Particle algorithms can be used to display iso-lines and iso-surfaces, thus decreasing the computational load of iso-line, and isosurface extraction. Spray rendering techniques use 'smart particles' with initial attributes such as colour, trajectory, and lifespan [71-73]. These particles are sprayed into a scalar field and allowed to interact with the local field according to their attributes to produce various effects. This is analogous to physically using iron filings to map a 2–D magnetic field. To improve limited 3–D perception of small particles, finite size objects like spheres and cones are suggested [74].

Scalar field topology and features of the scalar fields can be extracted to display the global structure instead of local features. The topology is defined by connecting critical points, *e.g.* local maxima and minima, and saddle points, by integral curves tangent to the gradient of the scalar field, as in Figure 4-5. Iso-contours are also used to support topological structure [75].

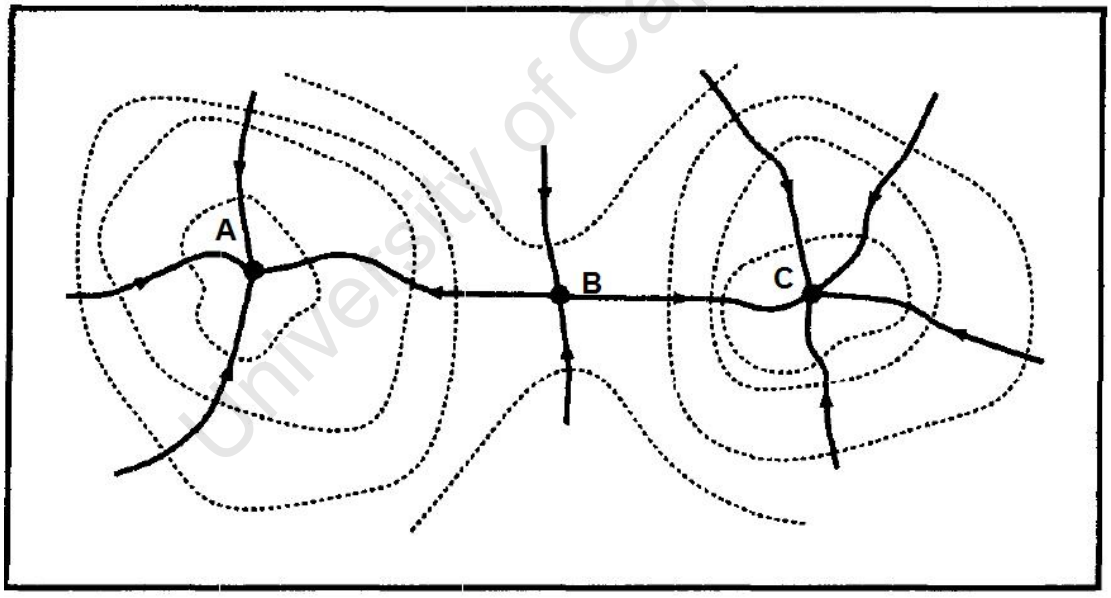

Figure 4-5 Isocontours (dotted lines) of part of a scalar field along with critical points, A and C (local maxima) and B (saddle point). Integral curves along the gradients intersect at the critical points, after [75].

All the previous scalar visualization techniques use scalar data to construct well defined geometric primitives, in the form of triangles and polygonal meshes that construct the graphic object. However, if the required visualization is volumetric, *i.e.*

it is not appropriate to model the data using geometric primitives such as points, lines or polygonal surfaces, the whole volume is visualized directly by assigning colour and partial opacity to each voxel (volume element) via three dimensional transfer functions. Such techniques are generally referred to as volume visualization. In a similar manner to colour lookup tables, transfer functions assign rendering parameters such as transparency and colour to differentiate sections in the dataset. Although several techniques are available to create transfer functions for general volumes [76-78], hand tuning and trial–and–error estimation give the best results. In the case of complex volumetric datasets, where transfer functions result in noisy scenes, a 2–D projection of volumetric data, termed a maximum intensity projection (MIP) can be used [79]. Efficiency and compactness are important factors in volume visualization to reduce computation and memory usage. When used interactively, volume visualization can increase perception dramatically.

4.1.4 Higher dimensional domains

Kriz suggests the use of an interactive method [80] to investigate the functional dependence of *k* scalar quantities, *i.e.* a dataset of the type E_P^{kS}, by considering them as points in a parametric space, *i.e.* a dataset of the type E_k^P. Because the visualization of both data types are isomorphic with each other and with a general set of *m* scalar quantities in an *n* dimensional domain, E_n^{mS}, for $k = m + n$, a visualization technique suitable for one of the data types can also be used for the visualization of the other two. The goal of this visualization is to study data in the E_n^{mS} form and look for possible relationships between the m scalar parameters. Note that the domain dimensions and the entity parameters are interchangeable, *i.e.* the visualization technique is isomorphic with changes to the domain and parameter entities. To demonstrate how this technique uncovers interesting relationships in a spatial-temporal domain, an example is given next. In Figure 4-6, the total number of scalar entities $k = 7$, of which any three (P5-P7) are represented in a four dimensional domain spanned by the other four parameters. The domain is rendered using 3 space-like dimensions (P1-P3) and one time like dimension (P4) which can be interactively stepped backwards and forwards using a dial, as shown in Figure 4-6a. To study the

relationship between the parameters, iso-surfaces in the 3–D domain are used. The possible intersection of any two iso-surfaces indicates a relationship between the two parameters. For example in Figure 4-6 b and c, the intersection between the two isosurfaces of P5 and P6 indicates a relationship between the parameters. If the intersection remains unchanged while stepping through the time-like parameter, then the correlation exists independent of the 4–D domain, *e.g.* pressure and temperature at position and time. Thus isosurfaces are drawn not in 3–D domain but in the 4–D domain. If a triple intersection is found between the isosurfaces of three parameters, as shown in Figure 4-6c, then there is a triple correlation between the variables. To find a triple correlation more easily, any two isosurfaces are colour coded with the value of the third parameter, to see if a constant colour is observed at the intersection. The same relation can be confirmed by including an isosurface of the colour coded parameter, if the intersection coincides with the intersection of two other isosurfaces.

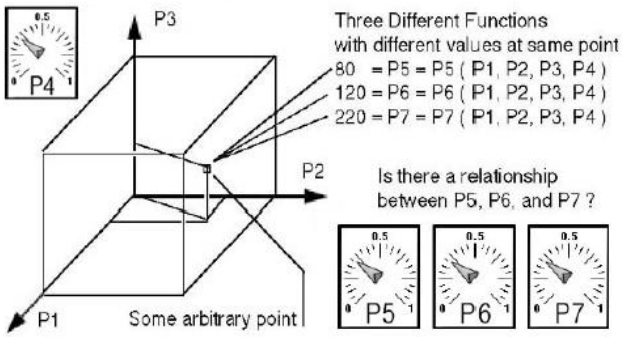

(a)

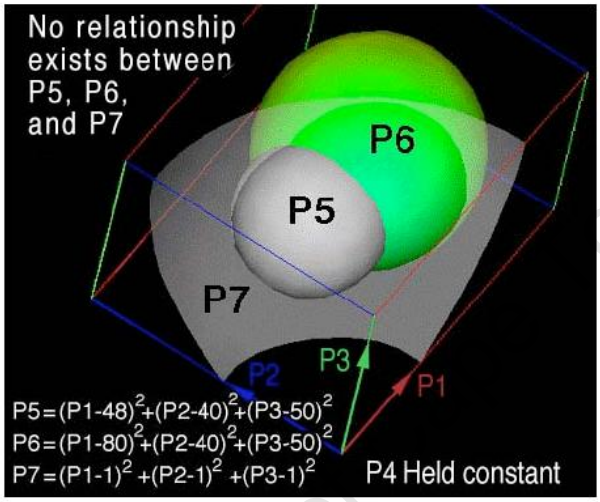

(b)

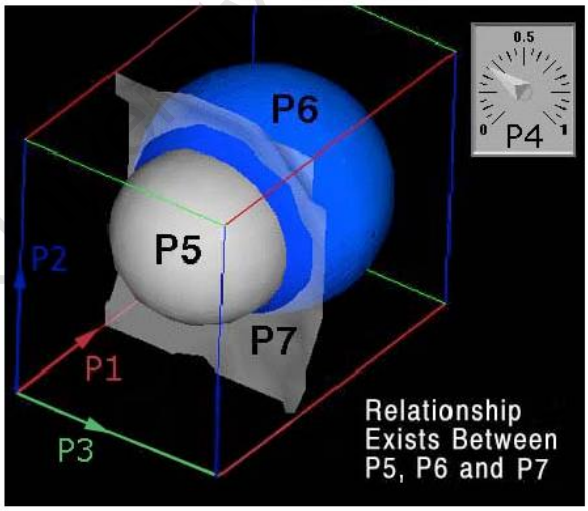

(c)

Figure 4-6 (a) General parametric space (P1, P2, P3, P4) with three arbitrary dependent parameter (P5, P6, P7) (b) no relationship exists between P5, P6 and P7 (c) the intersection of P5, P6 and P7 indicates a relationship [80].

4.2 Techniques for vector visualization

The visualization of vector data is complex compared to the visualization of scalar data. Vectors are first rank tensors and therefore have a number of components, which is equal to their dimension. A vector has at least two components, $\vec{A} = (A_1, A_2)$, or more usually three components $\vec{A} = (A_1, A_2, A_3)$, in the physical sciences. Even for the simplest case, the representation of a two dimensional vector in a one dimensional domain $E_1^{V_2}$, the total number of domain and entity dimensions is three, which necessitates either 3–D computer graphics or the construction of a model object by a sculptor. In this context, it should again be emphasized that the dimension of the dataset to be visualized has not necessarily be the same or limited with the dimensionalty of the domain, e.g. in the example of a 3D electric field vectors on a Gaussian surface (dataset dimensionality 3, domain dimensionality 2) as discussed in Section 3.2.1.

Scalar visualization techniques can be used for vectors, to visualize derived scalars such as magnitude, or the individual components of the vector. One such method, that uses scalar visualization techniques for the representation of vectors, is bivariate colour mapping using the HSV colour model, where hue represents the vector direction and saturation and intensity represent the vector magnitude [81, 82]. However, this entails information loss because a three dimensional vector field $E_3^{V_3}$ is essentially different from three disparate scalar fields E_3^{3S}. Therefore its representation should be distinguished from that of three scalar fields.

The elementary approach to the visualization of a three dimensional vector quantity at a point $E_P^{V_3}$, is to use an arrow. The mapping of a vector quantity on the attributes of an arrow icon was discussed before (section 3.2.2, page 45). In this case, the mapping process is intuitive where the 3–D direction of the vector is mapped on to the direction of the arrow, and the length of the arrow is scaled by the magnitude of the vector. Higher dimensional vectors need extra visual attributes to be represented using the arrow icon, such as colour, texture, *etc*. In this section, however, the discussion of visualization techniques is limited to three dimensional vectors defined in two and

three dimensional domains, $E_2^{V_3}$ and $E_3^{V_3}$ respectively, which are the most common vector entity types encountered in physical sciences.

4.2.1 The hedgehog method

The elementary visual representation of a vector is to map the vector dimensions onto the domain using an arrow, or other directed icons, at different positions of the domain. If the visualization domain is two-dimensional the resulting arrow plots are sometimes called hedgehogs due to the spiky result [83], as shown in Figure 4-7. In this representation the oriented icon is based at the point in which the vector is associated, and is oriented along the vector direction.

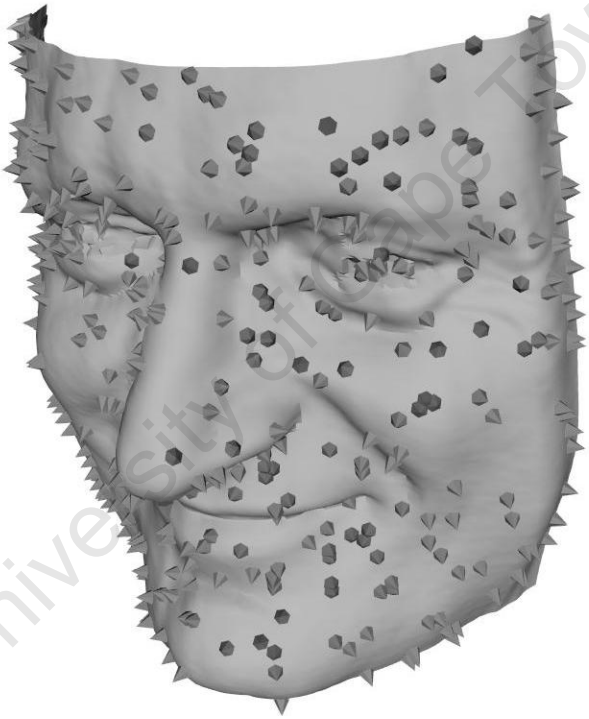

Figure 4-7 The normals of a three dimensional face shape are represented using directed cones in the hedgehog method [30].

There are many variations of this technique that use different oriented point icons, or glyphs, such as cones, cylinders, pyramids, *etc*. The use of different icons enables the use of colour on the icon surface to indicate a different, or extracted, scalar quantity.

4.2.2 Vector field lines

If a large number of point icons are used in the hedgehog method, they may easily cause clutter on the visualization window and obscure the visualization. For example, the electric field of three point charges, visualized using the hedgehog method (Figure 4-8a), is cluttered due to the high number of vector icons used. A local representation of the underlying electric field with the well known electric field lines can be used overcome clutter (Figure 4-8b). In the next section, the field line representation of an electric field, which follows the sampling of arrow icons to represent the electric field vector at discrete points is described in detail.

A practical way to draw the electric field vectors and the electric field lines is to use the electric potential

$$\phi=\sum_{i=1}^{n}\frac{Q_i}{\sqrt{(x-x_i)^2+(y-y_i)^2+(z-z_i)^2}}, \tag{4.2}$$

where (x_i, y_i, z_i) are the coordinates of the charge Q_i and (x, y, z) are the coordinates of the position of the charge Q_i where the electric field potential is calculated with respect to some reference coordinate system. From the potential, the electric field vector at any point $P(x, y, z)$ can be obtained using the gradient operator,

$$\vec{E}=-\nabla\phi=\frac{-\partial\phi}{\partial x}\mathbf{i}+\frac{-\partial\phi}{\partial y}\mathbf{j}+\frac{-\partial\phi}{\partial z}\mathbf{z}\,. \tag{4.3}$$

The parametric description of streamlines originating from the seed point (x_0, y_0, z_0) can be calculated by solving the differential equations

$$x(t)=\frac{dE_x}{dt}, y(t)=\frac{dE_y}{dt}, z(t)=\frac{dE_z}{dt} \tag{4.4}$$

using the seed points as boundary conditions

$$x(0)=x_0, y(0)=y_0, z(0)=z_0\,. \tag{4.5}$$

In Figure 4-8b, the same electric field is visualized using the electric field lines. A total of 64 random seed points are selected in the 3–D bounding box, and integrated in both directions, until the field line converges on one of the charges. A random colouring scheme on the electric field lines improves perception.

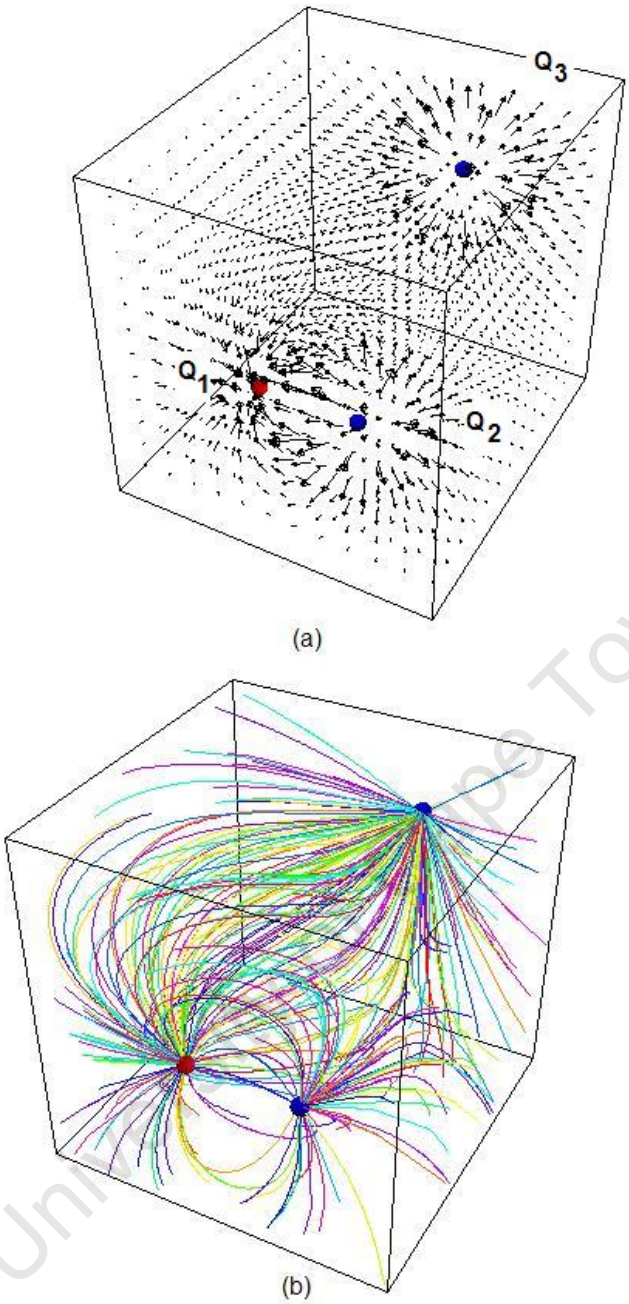

Figure 4-8 The electric field visualization due to three point charges, $-Q_1 = Q_2 = Q_3 = +1$. Positive charges are blue and the negative charge is shown in red. (a) Using the hedgehog method, *i.e.* the electric field vector is drawn at regular intervals in the 3–D volume of the charges; (b) Electric field lines (streamlines) originate and terminate at the point charges. The attraction between opposite charges and repulsion between similar charges can be seen clearly.

4.2.3 Streamlines and streaklines

In this section the idea of electric field lines is generalized to visualize time dependent and time independent vector fields. A well known technique for the visualization of the vector field $\vec{A}(x,y,z,t)$ is to insert a test particle or particles in the vector field at specific points and allowing them to interact with the vector field. This technique is used, for example, with smoke particles in wind tunnels for aerodynamics tests, to observe the behaviour of the flow field around automobiles (Figure 4-9).

Figure 4-9 Wind tunnel testing of the aerodynamics of a commercial automobile. Smoke particles introduced near the wind source reveals how air moves around the automobile. The study identifies high pressure regions, where the streamlines are more dense, as well as possible turbulence patterns [84].

In the case of time invariant a vector field $\vec{A}(x,y,z)$, the trace of a test particle can be followed by placing it at a specific position known as the seed point, $\vec{x}_0$, and allowing it to move along the local vector field direction to a nearby point $\vec{x}_1$

$$\vec{x}_1 = \vec{x}_0 + \vec{A}(x_0, y_0, z_0)\Delta t\,, \tag{4.6}$$

where the step size Δt is small enough that gradient of the vector field is not too large between points $\vec{x}_0$ and $\vec{x}_1$. The trace of the test particle is obtained by iterating the integration step for a definite number of steps as

$$\vec{x}_{n+1} = \vec{x}_n + \vec{A}(x_n, y_n, z_n)\Delta t\,, \tag{4.7}$$

or until the test particle leaves the defined volume, as seen in Figure 4-10a. This form of integration is known as Euler's method. However, Equation (4.7) is rarely used in Scientific Visualization practices but shown here to emphasize the concept. Steady integration methods such as the second and higher order Runge-Kutta method [85] are usually preferred. Integration with the first order Runge-Kutta method which uses the average of the vector field at successive positions is

$$\vec{x}_{n+1} = \vec{x}_n + \left(\frac{\vec{A}(x_n, y_n, z_n) + \vec{A}(x_{n+1}, y_{n+1}, z_{n+1})}{2} \right) \Delta t \,. \tag{4.8}$$

The locus of all such displacement vectors $\vec{x}_n$ is known as a streamline. For time-dependent vector fields, $\vec{A}(x, y, z, t)$, different streamlines can be obtained depending on the time of integration as shown in Figure 4-10b. The time dependent streamlines, known as streaklines, are the set of particle traces at a particular time t_i that have previously passed a specified point $\vec{x}_i$. Streaklines are used to explore the time dependence of a vector field, such as the development of a non-steady flow field.

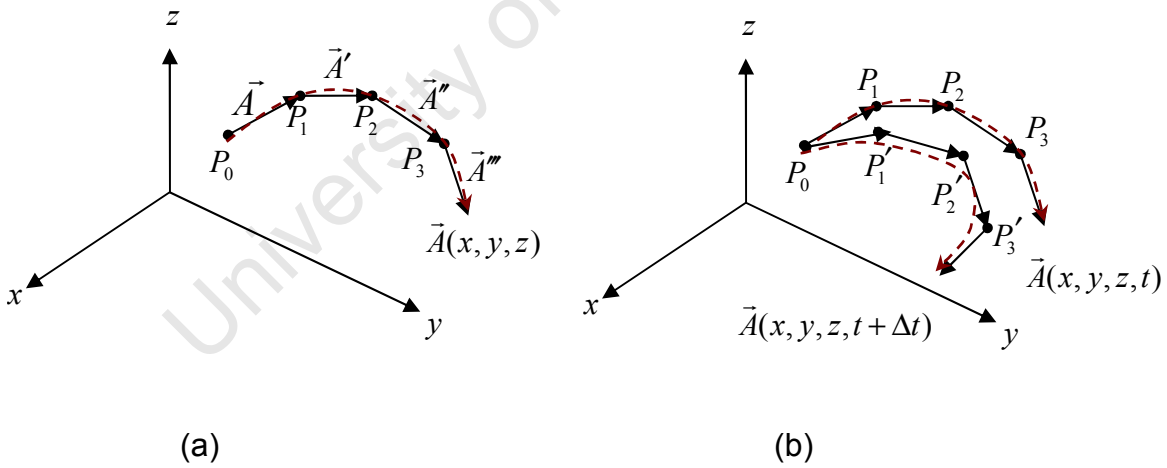

Figure 4-10 (a) One streamline of a time independent vector field $\vec{A}(x, y, z)$. Integration starts at seed point P_0 and terminates after a sufficient number of iterations. (b) Two streamlines starting from the same seed position P_0 of a time dependent vector field $\vec{A}(x, y, z, t)$. The change of trajectory of the streamlines indicate the unsteady behavior of the vector field. Time dependent streamlines are also called streaklines.

The streamlines of a three dimensional flow velocity field in a kitchen is shown in Figure 4-11. Scalar colouring indicates flow velocity: red, high; blue low. The seed points are selected to be near the kitchen stove. Two sets of different streamlines are observed: one group reduces speed as they travel upwards and leave the kitchen from the upper air passage hole; another travels faster and lower towards the door.

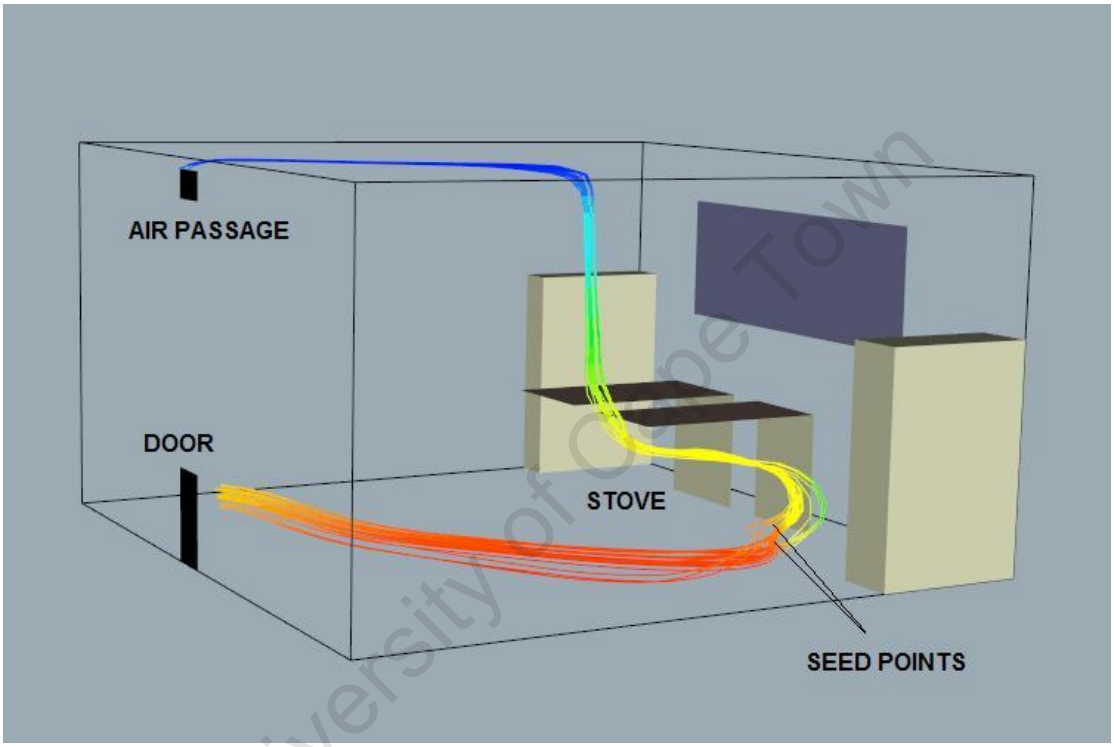

Figure 4-11 The air flow field in a kitchen is visualized by streamlines, with colour coding indicating flow speed along the streamline directions. Seed points are selected next to the kitchen stove. Two sets of streamlines are observed. One set of streamlines ascends and travels towards the air passage with low speed, and the other stream moves fast on the kitchen floor towards the door [30].

Multiple streamlines can be combined to give visually better pictures. In other cases, cylindrical tubes are used, to aid perception and add an extra spatial dimension for visualization mapping. The success of streamline integration visualizations depends on the selection of suitable seed points, step size and the integration algorithm [86-88]. Usually a multiple set of seed points are used to reveal the global behaviour

of the vector field. Despite the fact that a definitive error analysis is still required, the vector integration techniques are qualitatively very beneficial [30].

4.2.4 Warping

The representation of vectors in three dimensional domains, $E_3^{V_3}$ is complex, and visualization techniques usually map partial features of the vector field. For example the warping technique, based on distortions of a regular shape or object, or the probe volume, according to the local vector field aims to represent the overall behaviour of the vector field by the distorted object geometry. Lines, surfaces or 3–D volumes are used to visualize the vector field as probe volumes. For example, in Figure 4-12a, the displacement vectors of a vibrating beam are visualized using a rectangular volume, and Figure 4-12b shows the visualization of a flow field by means of warping three probe planes in a vector field.

Similarly, vector displacements of a surface of an object can be visualized with displacement plots. A scalar displacement field along the surface normal, of an object is calculated using the scalar product of the vector field and the surface normal over the whole surface of the 3–D object. In this way, the object surface is expanded or contracted along local surface normals revealing regions of positive, negative and zero displacements. This technique can be used, for example, to reveal the vibration modes of 3–D bodies. The first torsional mode of a vibrating beam is shown in Figure 4-13 using displacement plots. Displacements are also mapped to colour redundantly to enhance perception. The colour look-up table is set so that the nodal lines are represented by black.

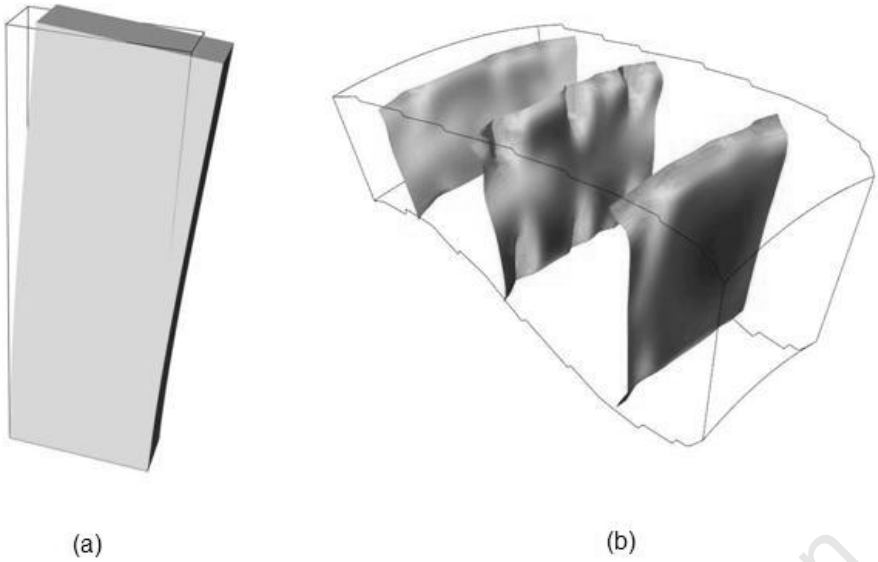

Figure 4-12 (a) The displacement vectors of a vibrating beam is visualized using a rectangular volume. (b) Flow field is visualized by deforming an inserted plane according to the local flow field [30].

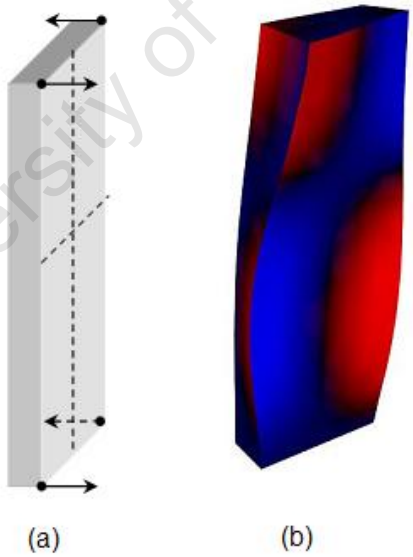

Figure 4-13 (a) The first torsional vibrational mode of a beam is visualized using the displacement plots (dashed lines indicate nodal points). Blue and red colours indicate maximum displacement and black indicates zero displacement corresponding to the nodal points. After [30].

4.2.5 Volumetric techniques

In cases where the hedgehog method is not effective, due to field complexity or visual cluttering, texture attributes can be used to visualize the general behaviour of a vector field on a two dimensional domain. In texture based visualizations, randomly placed spots, called spot noise, are used to synthesize textures over planar or curved surfaces. This is achieved by bending a spot noise along a local stream surface [89, 90]. Another texture based method is based on the simulation of the brush strokes of an oil painting artist to create texture, as shown in Figure 4-14. In this way velocity, vorticity, divergence, strain rate and shear information can be represented [91]. Another alternative algorithm to create textures is the line integral convolution (LIC) which uses curvilinear filters to locally blur an input noise along a vector field giving better visuals at the cost of computational load due to the integration [92]. Also, recent improved LIC algorithms, *e.g.* [93], are more than a magnitude faster than the originally proposed method.

Figure 4-14 Texture is used to show the main flow in a backward facing step, high speed flow together with recirculation behind the step can be seen [91].

For the visualization of 3–D vector data volumetric methods can be used by directly by assigning colour and opacity values, based on the direction and magnitude of the vector respectively, at each point in the 3–D domain [94, 95]. Flow fields can also be visualized by volume rendering of the behaviour of clouds and smoke similar to particle visualization similar to texture methods as shown in Figure 4-15 [96].

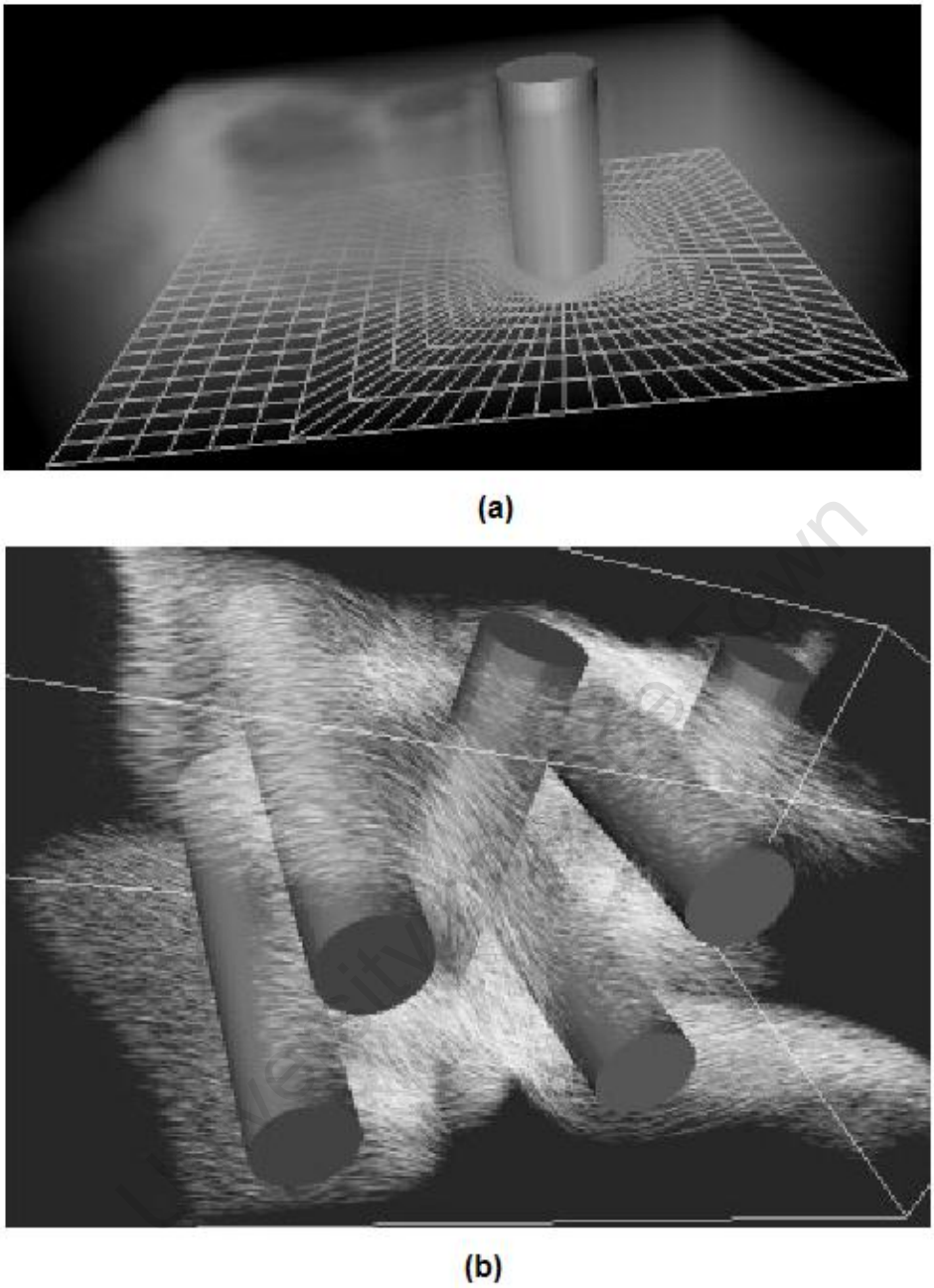

Figure 4-15 (a) Volume rendering of air flow around a cylindrical column. (b) Texture rendering of a flow through a complex volume [96].

4.2.6 Vector field topology

It was mentioned earlier that the effectiveness of the streamline integration depends on the selection of the appropriate seed points and the integration algorithms. If the

choice of a set of seed points is not intuitive, unlike the case of electric field lines, the overall global structure of the vector field must be taken into account for a definitive description of the vector field. One approach for the construction of the topology of the vector field is to find the critical points in the vector field. The critical points are those at which the magnitude of the vector field vanishes. Furthermore the critical points are classified using the Jacobian matrix of the vector field at the critical point. For a two dimensional vector field $\vec{A}(x, y)$ the Jacobian matrix at the critical point $P(x_0, y_0)$ is given by

$$J_{ij}(x_0, y_0) = \begin{pmatrix} \frac{\partial A_x}{\partial x} & \frac{\partial A_x}{\partial y} \\ \frac{\partial A_y}{\partial x} & \frac{\partial A_y}{\partial y} \end{pmatrix}_{(x_0, y_0)} . \tag{4.9}$$

The types of the critical point are determined from the eigenvalues of $J_{ij}(x_0, y_0)$. The eigenvalues may be real or imaginary, if the Jacobian is not a symmetric tensor. Two complex eigenvalues can be taken as $R_1 + iI_1$ and $R_2 + iI_2$ with R_1 and R_2 the real, and I_1 and I_2 the imaginary parts. In general the imaginary part of the eigenvalue is represents the rotation in the field and the real part represents the attracting or repelling nodes. In Figure 4-16 the classification of the critical points according to the complex eigenvalues is shown. The vector field topology of two dimensional fields can be obtained by combining these critical points.

In three dimensions the Jacobian has always at least one real value, with two coplanar complex eigenvalues. The real value indicates an attracting or repelling flow towards the planar fields described in the two dimensional case (Figure 4-16). The topology of the three dimensional field is then drawn by connecting the critical points with streamsurfaces [97]. However, for the three dimensional case, the critical points are not the only flow features, and are not sufficient enough for the definitive description of a complex vector field [52].

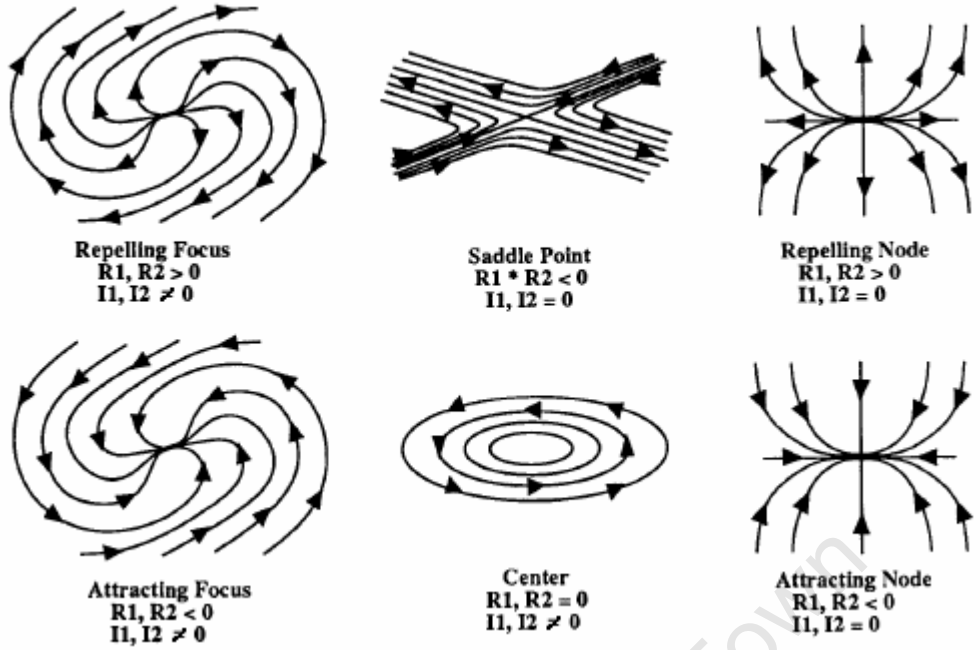

Figure 4-16 Classification of the critical points of a two dimensional vector field [52].

4.2.7 Visualization of the Jacobian of a vector field

As it was shown previously, the Jacobian matrix is an important feature describing the behaviour of vector fields. To visualize the Jacobian matrix, or the Jacobian tensor, of a vector field, a local icon can be used to map field properties in the vicinity of a point [83]. Although this icon is designed for vector field visualization, the physical quantity it maps is the local velocity gradient tensor, or the Jacobian of the velocity field. The components of the Jacobian are the spatial derivatives of the velocity vector given as the tensor $J_{ij} = \frac{\partial v_i}{\partial x_j}$. This tensor is decomposed into normal and shear components along the flow direction (vector direction). The Jacobian matrix icon is shown in Figure 4-17. The length of the arrow is scaled by the vector magnitude, curvature of the arrow shows local streamline curvature, and stripes of the cylindrical shaft show the rotation of the flow field. A half ellipsoid at the bottom of the shaft encodes the acceleration of the velocity vector. Convergence and divergence are described by bending the circular membrane orthogonal to the flow field. Shear is encoded by the angle of a ring shaped surface with respect to a reference frame.

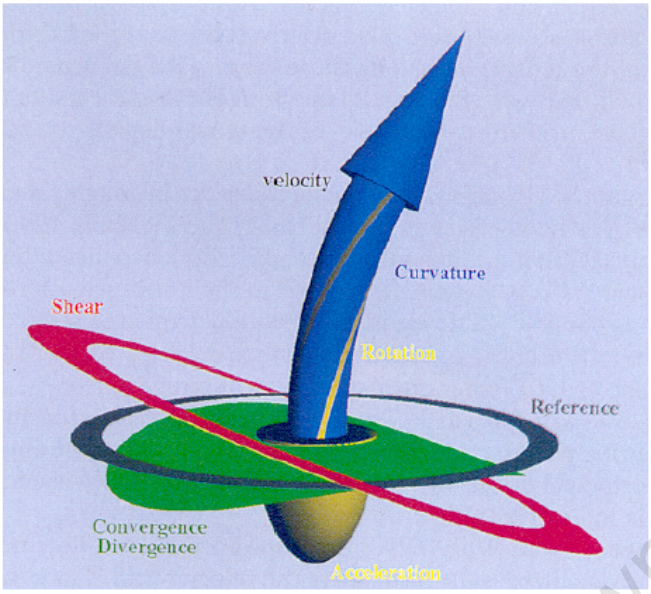

Figure 4-17 The Jacobian of a vector field is visualized using an icon that represents the local field behavior of a flow field [83].

4.3 Techniques for tensor visualization

The graphical representation of second or higher order tensor quantities is remarkably complex in comparison to that of scalars and vectors, which are zeroth and first rank tensors respectively. This complexity is partly due to the high number of components of the tensor quantity. The total number of components of a tensor is n^m, where n is the dimensionality of the tensor and m is the rank of the tensor. Accordingly, n-dimensional second rank tensors have in total n^2 components. It was mentioned in Section 4.2 that for a 3–D vector in a 3–D domain, the total number of variables to be visualized would be 3+3. The overwhelming complexity of the visualization task can be seen by considering the total number of variables for the three dimensional tensor case.

Using the formalism of chapter 3, example tensor data can be represented by $E_3^{T_{33}}$, where the superscript $T_{3:3}$ denotes that the entity E is a second rank tensor, whose components are the elements of a 3×3 matrix; and the subscript 3 shows that the entity is defined in a 3–D domain. Therefore, the number of variables for the entity $E_3^{T_{33}}$ is

(3 + 9). The complexity of the visualization task is not only due to mapping the 12 variables onto a visual icon. For the tensor entity new visualization techniques are required, in which the tensor structure of the entity is emphasised in distinction to multivariate scalar visualization. Due to isomorphism, multivariate, multidimensional visualization techniques may, in principle, be used for tensor visualization, *i.e.* one can use scalar visualization techniques to visualize each component of the tensor quantity independently and concurrently. Similarly the rows or the columns of the tensor matrix can be visualized individually using any of the vector visualization techniques. However such visualizations suffer from two main shortcomings. Firstly the large number of total variables presents an obvious perceptual block for the cognition of the information. Secondly, and more importantly, these alternative representations of the isomorphic entities cannot be considered tensor visualization, since the entity being visualized is a multiple scalar or vector field. A graphical representation should be classified distinctively as tensor visualization when the visualized entity is $E_n^{T_{nn}}$, and not $E_n^{n^2 S}$ or $E_n^{nV_n}$.

Specific visualization efforts in tensor visualization have been mainly concentrated on the second rank symmetric tensors due to the abundance of such quantities in physical sciences, such as the stress and strain tensor in mechanics [43, 80] and geomechanics [98], brain diffusion tensor in biomedicine [52], momentum flux density in fluid mechanics [54] *etc*. In this section, visualization techniques for second rank symmetric tensors are presented using the stress tensor, which is frequently encountered in continuum mechanics and mechanical engineering, wherever possible. In line with scalar and vector visualization, the tensor visualization icons are grouped according to their spatial extents, as point icons and global icons. Furthermore, both types of tensor icon can be grouped according to the visualization mapping process. For tensor visualization the two main mapping processes are *diagonalization* and *traction-based* mapping. Besides these two mapping approaches, the Cauchy stress quadric is used for the visualization of the stress tensor. This icon is a tensor isosurface that is obtained by neither diagonalization nor using the traction vector.

Based on the insight from the above, a novel icon called the PNS (principle/normal/shear) icon is developed. This new icon has features derived from all of the traditional icons. Using the PNS icon, principle stresses and the normal and shear character of the stress can be depicted. In this way, the PNS icon is more effective in presenting the full tensor information for second rank symmetric tensors.

4.3.1 Diagonalization: Visualization of principal stresses

As described in section 2.3.2, a symmetric second rank tensor can be diagonalized to reduce the rank of the tensor, and the reduced form can be visualized. Any stress tensor can be represented by its 3 principal stress components and their orientation in 'stress space'. This is equivalent to the combination of three orthogonal eigenvectors and their orientation with respect to a reference coordinate. Because eigenvalue/eigenvector decomposition is the skeleton of all such icons, they are termed *eigenicons*. The principal axis transformation aligns the coordinate system with the principal directions of the tensor to obtain the three orthogonal vectors as shown in Figure 2-6 (page 24). In this way, the rank 2 tensor is reduced to a rank 1 tensor. However, to be complete, it is necessary to show the orientation information as well. Thus, the representation of the tensor must show both the internal structure and the orientation of the tensor in a vector space which has the units of the tensor components, and directions of the coordinate axes which have physical meaning. In practice this means that the coordinate axes in this space should be parallel or should have a fixed orientation to the corresponding axes in the domain.

4.3.2 Mohr circles: Visualization of normal and shear stresses

Along the principal stresses directions, shear stresses are null. In general, shear stresses may exist along other directions, depending on the couplings of principal stresses. For example, where all principle stresses are equal, no shear stress exists, whereas if one or more principal stresses are different from the others, then there is a distribution of shear stresses in 3–D space. This complex presence of shear stresses is conventionally investigated using a basic graphic representation known as the Mohr

circle [5, 14], which can be classified as a scientific visualization which has been recently used in a computer based visualization system to visualize shear behaviour in geology [99]. The Mohr circle is essential in understanding the traction vector, normal and shear stress distribution of the stress traction vector. In this sense, the Mohr circle is an elementary visualization concept which facilitates the conception of the more sophisticated 3–D icons.

In their most basic form, Mohr circles are used for the visualization of bi-axial stress states. The visualizations always depict the stress tensor in the principle stress coordinate system, and therefore they can only be used after diagonalization. The normal and shear components of the principal stresses, in any given plane, are depicted with the Mohr circles, which is equivalent to representing the traction vectors, with normal and shear components, in all possible directions in a plane. In Figure 4-18a, bi-axial principal stresses σ_1 and σ_2 in the $x-y$ plane are shown. Normal and shear components of the principal stresses acting on a hypothetical plane that makes an angle ϕ with σ_1 are given by [14]

$$\sigma_n = \frac{\sigma_1+\sigma_2}{2} + \frac{\sigma_1-\sigma_2}{2}\sin 2\phi, \tag{4.10}$$

$$\tau = \frac{\sigma_1-\sigma_2}{2}\cos 2\phi, \tag{4.11}$$

where $\sigma_1 \geq \sigma_2$. The locus of σ_n and τ in equations (4.10) and (4.11) defines the Mohr circle with its centre at $\left(\frac{\sigma_1+\sigma_2}{2}, 0\right)$, and radius $r = \frac{\sigma_1-\sigma_2}{2}$ (Figure 4-18b.) The normal stress component on a plane, making an angle of ϕ with σ_1 (Figure 4-18a), is equal to the abscissa of point R (Figure 4-18b), and the shear component is equal to the ordinate of the point *R*. Tension is taken as positive and compression as negative. In (Figure 4-18c), another Mohr circle is shown for a compression-tension stress couple. Points B and B' show maximum shearing stresses at $\phi = 45^\circ$. Points A and A' represent pure shear stresses where normal stresses are zero. Note that for the two dimensional isotropic stress state, $\sigma_1 = \sigma_2$, the Mohr circle would shrink to a single point, indicating the absolute absence of shear stresses.

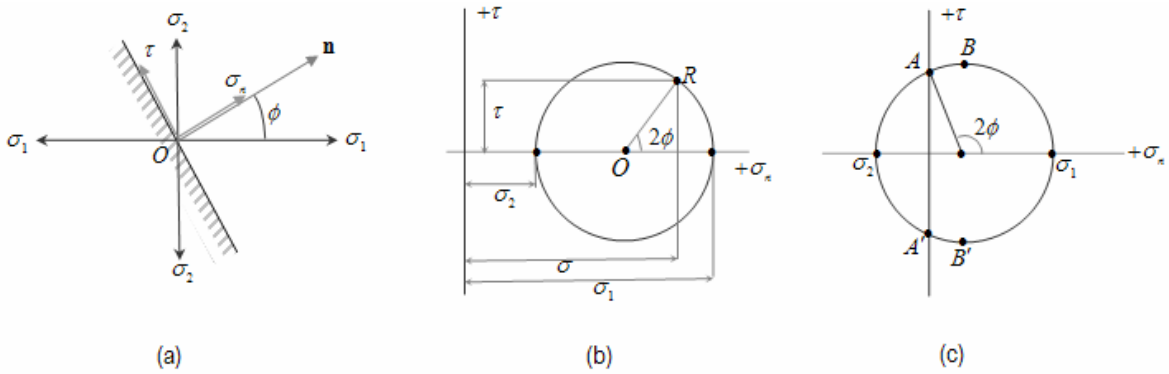

Figure 4-18 (a) Components of the bi-axial principal stresses on a plane making angle of ϕ. (b) Mohr circle representation stress components σ_1, σ_2. (c) Mohr circle for a tension-compression stress couple, $\sigma_1 > 0 > \sigma_2$.

Similarly, a tri-axial stress tensor can be visualized using three Mohr circles drawn for each pair of the principal stresses, as shown for the tri-axial stress state $\sigma_1 < 0 < \sigma_2 < \sigma_3$ in Figure 4-19. Each point in the shaded area corresponds to a traction vector with normal and shear components given by the abscissa and ordinate of the point. For a detailed analysis of tri-axial case see for example [14].

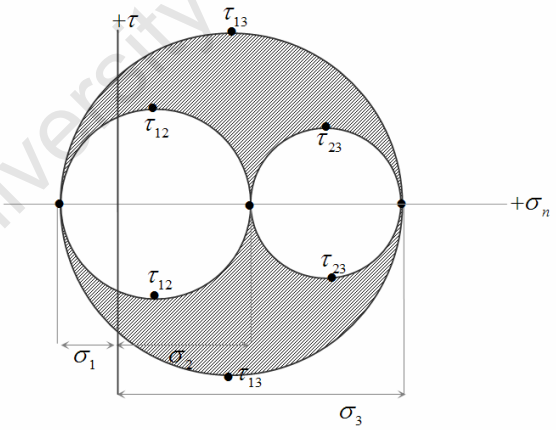

Figure 4-19 Mohr circles the for tri-axial stress state, $\sigma_1 < 0 < \sigma_2 < \sigma_3$. Local maximum shearing stresses $\tau_{12}, \tau_{13}, \tau_{23}$ are indicated.

It is interesting to note the reduction of the geometrical complexity of the shaded area for a cylindrically symmetric case, $\sigma_1 = \sigma_2 < \sigma_3$, where all possible traction vectors

are denoted by the area between two cocentric circles. For the isotropic stress state, $\sigma_1 = \sigma_2 = \sigma_3$, the shaded area vanishes altogether.

From the Mohr circle representation it can be concluded that the complexity of a stress state depends on the position of the principal stresses on the abscissa of the Mohr circle plane. These complexities of stress states are investigated using 3–D icons with references to the Mohr circle in the next sections.

4.3.3 Point eigenicons

The visualization of the symmetric tensor in the principle stresses coordinate system can be achieved simply by drawing the three eigenvectors of the tensor. This can be done using the elementary vector icons or using any other three dimensional object with length, width and height dimensions, such as jacks, ellipsoids, cylinders, disks, *etc.*, as shown in Figure 4-20. The two step mapping process for eigenicons is: (1) the alignment of the axes of the 3–D object with the principal stress directions; and (2) scaling of the dimensions with the corresponding principal stress magnitudes.

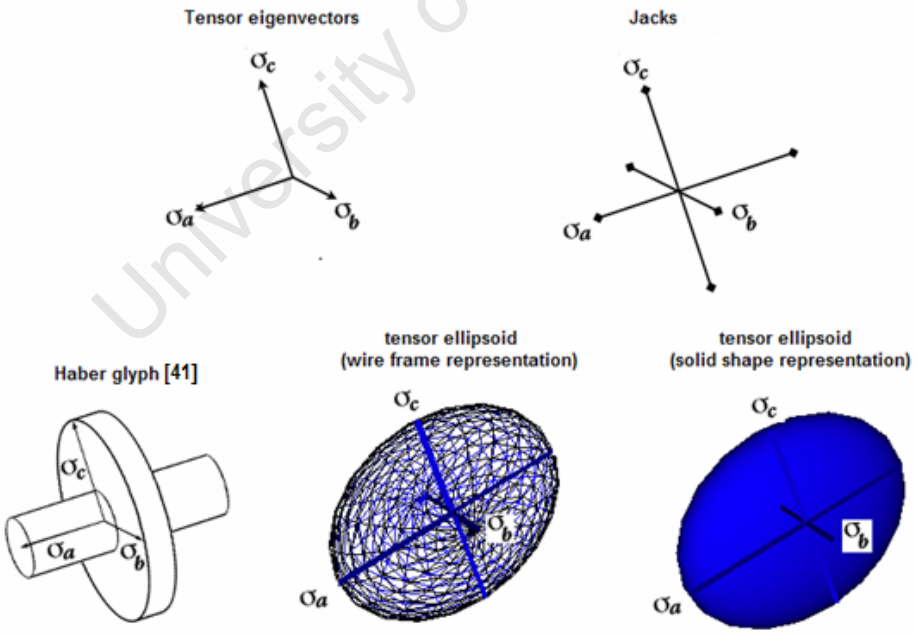

Figure 4-20 Eigenicons.

Tensor ellipsoids, which are frequently used in scientific visualization, are ellipsoidal surfaces with semi-axes scaled with tensor eigenvalues and aligned with the tensor

eigenvectors. The enclosing of an ellipsoidal surface around the three arrows not only improves visual perception but also provides an extra visualization extension, the surface area of the ellipsoid. On the ellipsoidal surface, any derived scalar quantity of the tensor such as, one of the tensor components, eigenvalues (see for example [110]), or trace, can be colour mapped. Therefore using colour mapping on the poles of the ellipsoidal shapes, positive and negative principal stresses can be differentiated and hence compressive and tensile stresses can be distinguished (see Figure 4-21). Of course, this is not a problem if all the eigenvalues are always positive, such as for diffusion tensors.

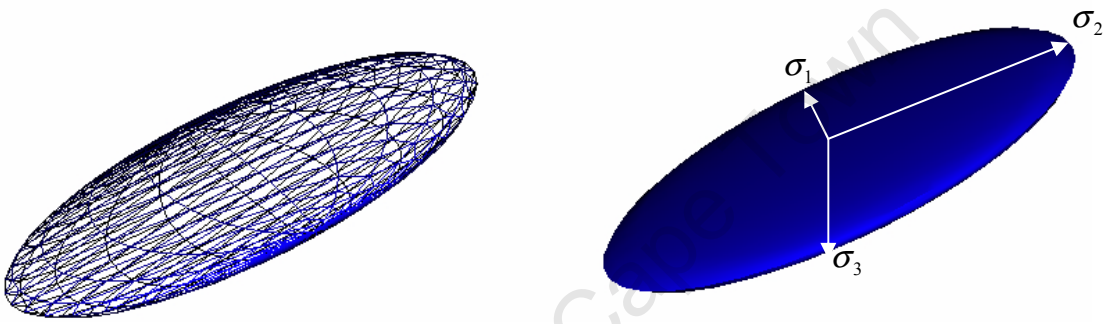

Figure 4-21 Wire-frame and surface representation of a tensor ellipsoid. The eigenvalues of the tensor are $[\sigma_1 = 8, \sigma_2 = 15, \sigma_3 = -10]$. The ellipsoidal representation does not differentiate between positive and negative principle stresses.

Another drawback is the visual ambiguity of the perception of the ellipsoid axes. Westin et al. use a disk and a rod to differentiate between different eigenvalues to address the inherent perceptual ambiguity in ellipsoids (Figure 4-22a) [100]. The use of too many ellipsoids in a small volume might cause visual clutter or occlusion when nearby icons overlap or screen one another. To address this problem, see-through ellipsoids with bands along the equators can be used [101], as shown in Figure 4-22b and c.

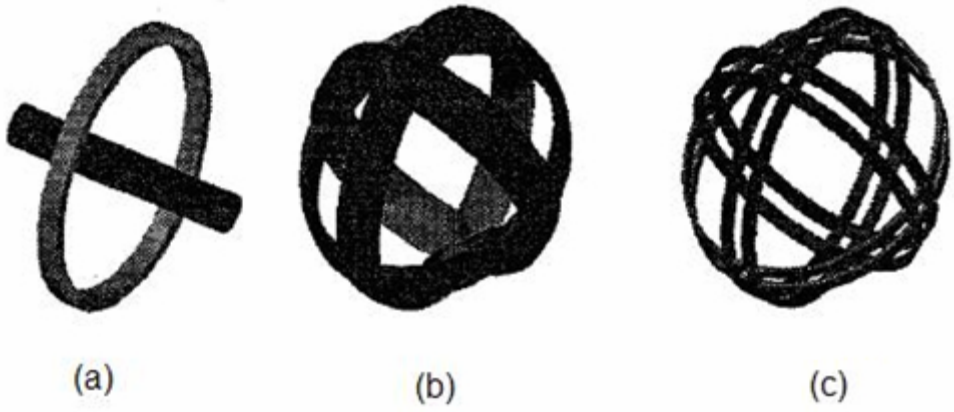

Figure 4-22 See-through eigenicons [101].

Another eigenicon is the Haber glyph [43], which is a cylindrical rod with an elliptical disc around it, as shown in Figure 4-20. The cylindrical rod is directed along, and scaled with, the major eigenvector to represent the principal direction of the tensor. The other two eigenvectors are the semi major and semi minor axes of the disc. Colour is used on the Haber glyph to differentiate between compression and tension, *e.g.* between a negative and positive eigenvalue. Colour is applied to the shaft and disk surface to indicate the magnitudes of the principal stresses; blue for tension, red for compression and green for shear. Haber glyphs are effective in presenting a pronounced eigenvector (principal stress). In Figure 4-23, the stress tensors in a brittle material, due to crack propagation are visualized using Haber glyphs. In this visualization, additionally, colour and a height map are used simultaneously to represent two derived scalar quantities obtained from the stress tensor: the strain energy density and kinetic energy, respectively. The characteristic stress of the elastic wave pattern emitted at the growing crack is revealed by the shape, orientation and colour of the Haber glyphs.

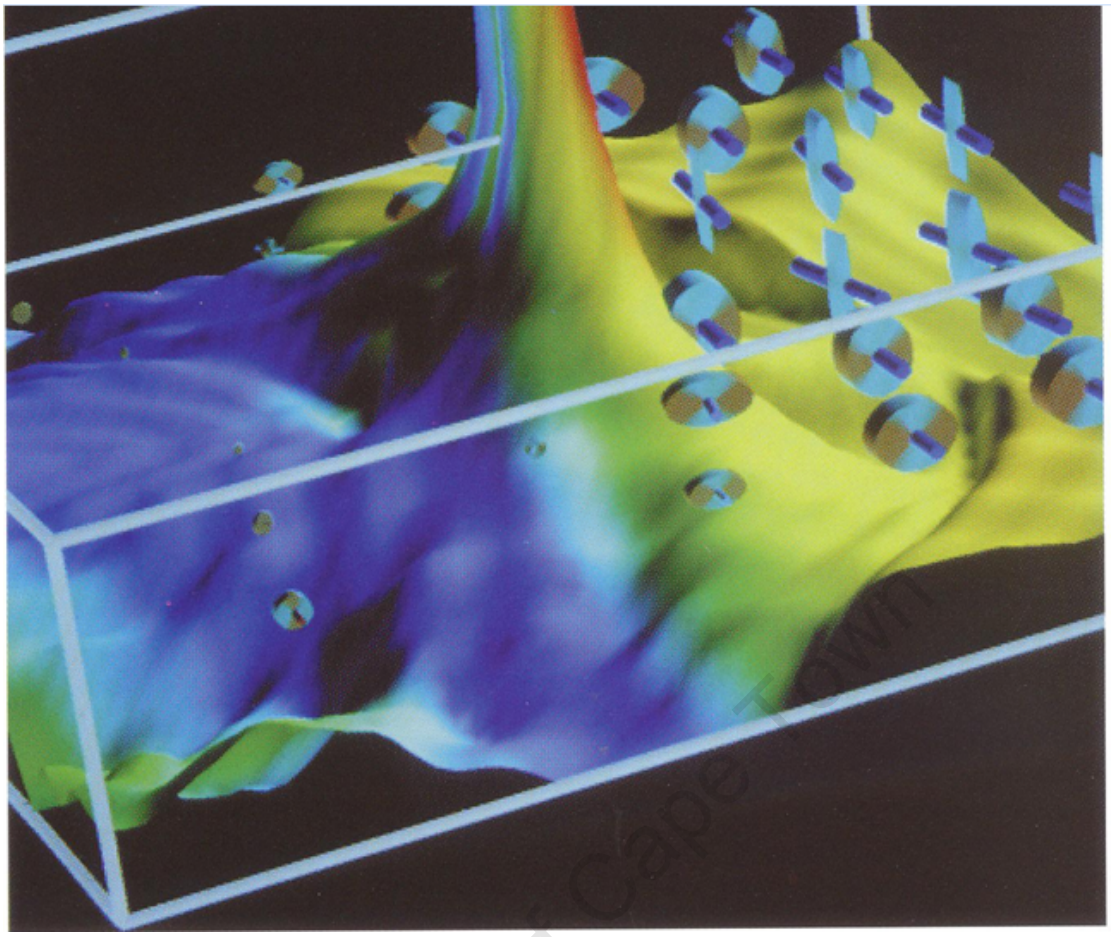

Figure 4-23 Haber glyphs are used to visualize the stress tensors around a crack tip in a brittle material [43].

Superquadric icons are designed to improve the perception of the eigenicon surfaces [102]. A superquadric icon surface is parametrically defined in the spherical coordinate system (r,θ,ϕ) using the shape metrics (α,β) by the equations

$$\begin{aligned} x &= \cos_s^{\alpha}\theta\cos_s^{\beta}\phi \\ y &= \sin_s^{\alpha}\theta\cos_s^{\beta}\phi \\ z &= \sin_s^{\beta}\phi \end{aligned}, \qquad (4.12)$$

where the three dimensional spherical domain is described by the $-\pi \le \theta \le \pi$ and $-\frac{\pi}{2} \le \phi \le \frac{\pi}{2}$ rotations. In Figure 4-24 the hydrostatic stress tensor, $\sigma = \begin{pmatrix} 1 & & \\ & 1 & \\ & & 1 \end{pmatrix}$ is visualized using different (α,β) values. An intuitive choice of the shape metrics improves visualization. For example: for the representation of the nearly isotropic tensor $\sigma_1 \approx \sigma_2 \approx \sigma_3$, the $(\alpha,\beta)=(1,1)$ shape metric can be selected; for a cylindrical

symmetry, $\sigma_1 > \sigma_2 \approx \sigma_3$, the shape metric $(\alpha, \beta) = (1, 0)$ can be used; and for a highly directional tensor $\sigma_1 >> \sigma_2 \approx \sigma_3$, the shape metric $(\alpha, \beta) = (1, 2)$ can highlight the pronounced principal stress direction.

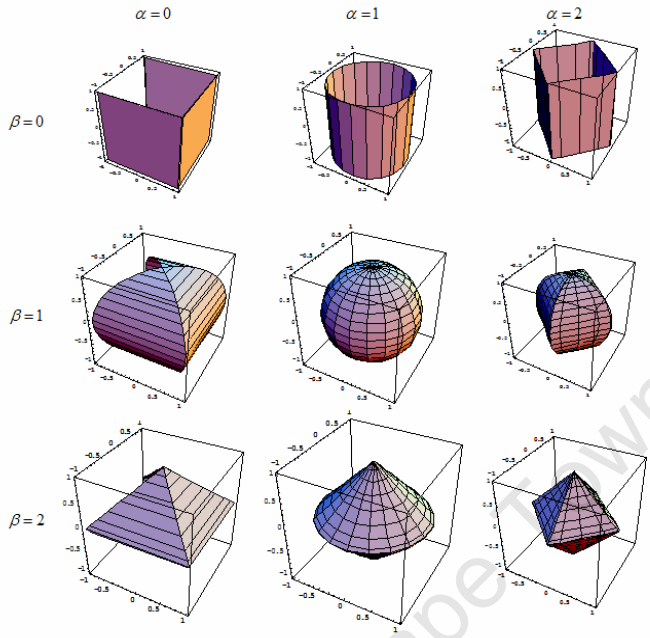

Figure 4-24 Superquadric icons.

In Figure 4-25, a two dimensional portion of a brain diffusion tensor visualization is shown using superquadrics. Laidlaw suggests
normalization of the eigenvalues if the goal of the visualization task is to emphasize the directionality of the tensors [103]. If the sizes of the eigenicons in a visualization vary considerably, an appropriate scale can be found, which balances the size of the largest icon and the smallest one, so that the largest one does not occlude small ones, and that the small ones are visible.

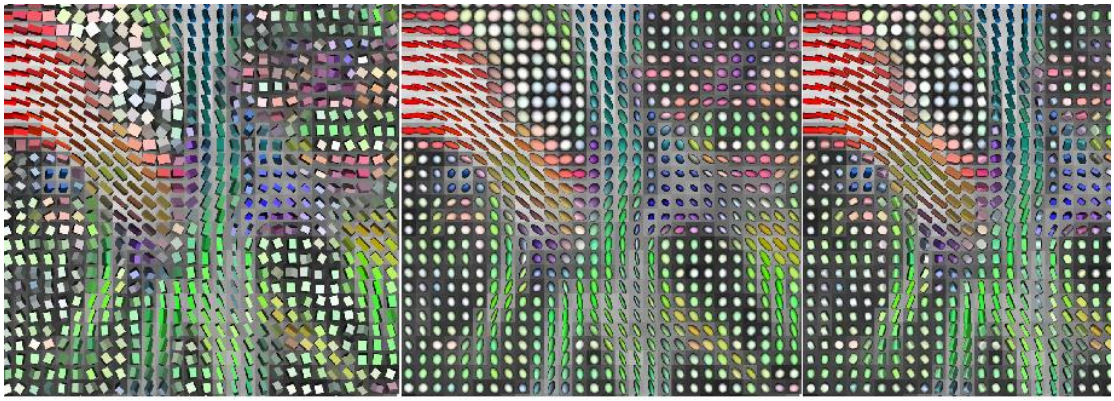

Figure 4-25 A two dimensional portion of a brain diffusion tensor visualization using superquadrics with three different shape metrics (a) $(\alpha,\beta)=(0,0)$ (b) $(\alpha,\beta)=(1,1)$ (c) $(\alpha,\beta)=(1,0)$. The tensors are normalized to emphasize directional information [104].

4.3.4 Traction based point icons

4.3.4.1 Lamé stress ellipsoid

The stress tensor is the compact form of expressing all possible stress vectors (tractions) at a point. Infinitely many stress vectors can be drawn at a point P corresponding to different planes passing through it. Two of these possible tractions are shown in Figure 4-26. The components of a stress vector σ_i acting on a surface with normal components n_j is given by

$$\sigma_i = \sigma_{ji} n_j \,. \tag{4.13}$$

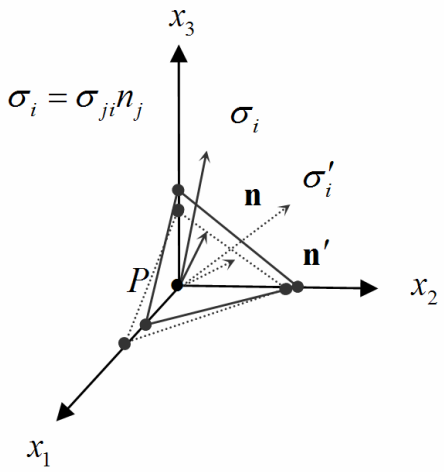

Figure 4-26 Stress vectors at a point along the unit normal vectors.

The locus of the tips of all stress vector at point *P* traverses an ellipsoidal surface known as the Lamé stress ellipsoid. Thus, drawing the Lamé stress ellipsoid is equivalent to drawing all possible stress vectors at a point *P*.

This description of the Lamé ellipsoid is mathematically equivalent to the eigenicon ellipsoid description of the stress ellipsoid, *i.e.* the Lamé stress ellipsoid can be constructed by either using diagonalization or the stress vector. This can be seen from the fact that the stress vectors along the principal directions of a tensor are equal to principal stresses. Since the same vectors are used as semi-axes for the eigenicons, both representations are equivalent.

Using the principal stresses $\sigma_{11} = \sigma_1$, $\sigma_{22} = \sigma_2$ and $\sigma_{33} = \sigma_3$ the traction along any unit vector $\mathbf{n}$ is given by

$$\overset{n}{T}_i = \sigma_{ji} n_j , \tag{4.14}$$

or

$$\begin{aligned} \overset{n}{T}_1 &= \sigma_1 n_1 , \\ \overset{n}{T}_2 &= \sigma_2 n_2 , \\ \overset{n}{T}_3 &= \sigma_3 n_3 . \end{aligned} \tag{4.15}$$

Since $\hat{\mathbf{n}}$ is a unit vector we have

$$n_1^2 + n_2^2 + n_3^2 = 1 . \tag{4.16}$$

Substituting (4.15) in (4.16)

$$\frac{\left(\overset{n}{T}_1\right)^2}{(\sigma_1)^2} + \frac{\left(\overset{n}{T}_2\right)^2}{(\sigma_2)^2} + \frac{\left(\overset{n}{T}_3\right)^2}{(\sigma_3)^2} = 1 , \tag{4.17}$$

the equation for the ellipsoidal surface is obtained in the reference system of the principal stress directions $\overset{n}{T}_1, \overset{n}{T}_2$, and $\overset{n}{T}_3$. The construction of the Lamé ellipsoid is illustrated in Figure 4-27 .

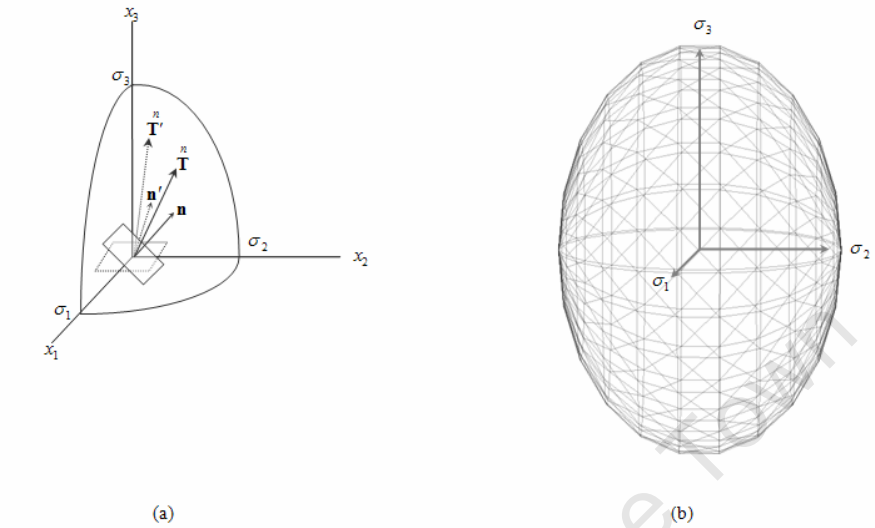

Figure 4-27 (a) A portion of ellipsoidal surface as the locus of traction vectors at a point. (b) Complete Lamé stress ellipsoid shown using wireframes.

Note that it is not necessary to diagonalize the stress tensor prior to the stress vector extraction. The Lamé ellipsoid can be drawn using tensor components defined in any coordinate system, since the stress vectors of a specific stress tensor remain unchanged under coordinate transformations. The ellipsoidal representation does not depend on the reference coordinate system since it is an invariant of the stress tensor. The total length of the semi-axes corresponds to the first stress invariant I_1, the surface area of the ellipsoid corresponds to the second invariant I_2, and the volume of the ellipsoid corresponds to third invariant I_3.

Lamé stress ellipsoids can be used effectively for the depiction of various stress types. For the cylindrically symmetric stress state where two principal stresses are equal, the Lamé ellipsoid is a surface of revolution, and any two axes can be taken as the principal stresses. If all three principal stresses are equal in magnitude, *i.e.* the stress state is isotropic, the ellipsoidal surface is a sphere and any three mutually orthogonal directions can be taken as the principal stresses. If one of the principal stresses is close

to zero the ellipsoid becomes an oblate shape. If one principal stress is very large compared to the other two stresses, the Lamé ellipsoid becomes a needle like prolate shape along the larger principal stress. The Lamé stress ellipsoid representation for typical stress tensors is illustrated in Figure 4-28.

In Figure 4-28, the first three tensor matrices (A,B and C) are uniaxial stresses along the *x*-, *y*- and *z*-axes, respectively. The next three tensor matrices (D, E and F) are bi-axial stresses in the *x*-*y*, *x*-*z* and *y*-*z* planes respectively. In the second column, the first matrix (G) corresponds to hydrostatic tension, and is represented by a sphere due to isotropy. The following two representations (H and I) are representations of two different stress tensors. (H) is a tri-axial stress tensor with all tensile stress components, where the principal stress along *y*- direction is twice as large as the principal stresses along *x*- and *z*- directions. However, the tensor shown as (I) has mixed stresses both compressive and tensile. As discussed above, although (H) and (I) are distinct stress states, the ellipsoid representation does not differentiate between the two. The principal stresses of the pure shear stress state (J) are equivalent to the principal stresses of the tensor shown in (K). Note that the trace of (J) and (K) are both zero. Therefore, upon diagonalization (J) becomes (K), which can be seen from both icons.

It is important to note that the full tensor matrix can be obtained from the oriented Lamé ellipsoid by means of a reverse coordinate transformation. Notwithstanding this fact, the ellipsoidal representation of stress tensor is not complete due to two shortcomings. The first is that the Lamé ellipsoid does not indicate the sign of the traction vectors. Therefore compressive, tensile or shear stresses cannot be differentiated. Secondly, shear stresses are zero in the reference frame of the principal axes, and are not shown *explicitly* by the visual attributes of the Lamé ellipsoid. The relative orientation of the Lamé stress ellipsoid with respect to the reference coordinate system is one indication of the presence of shear stresses. Simultaneous presence of tensile and compressive stresses in the tensor is another indication of shear stresses. Since the maximum shear stress is always along the bisectors of principal stress directions, it can be observed directly from Figure 4-28. However pure shear stress, if present, cannot be differentiated directly from Figure 4-28, compare (H) with (I), (J) and (K).

	σ	Lamé Stress Ellipsoid		σ	Lamé Stress Ellipsoid
A	$\begin{pmatrix} 1 & 0 & 0 \\ & 0 & 0 \\ & & 0 \end{pmatrix}$	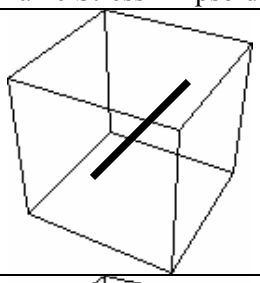	**G**	$\begin{pmatrix} 1 & 0 & 0 \\ & 1 & 0 \\ & & 1 \end{pmatrix}$	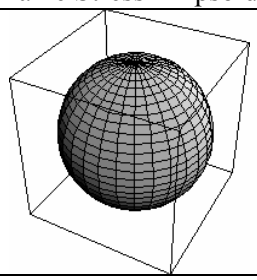
B	$\begin{pmatrix} 0 & 0 & 0 \\ & 1 & 0 \\ & & 0 \end{pmatrix}$	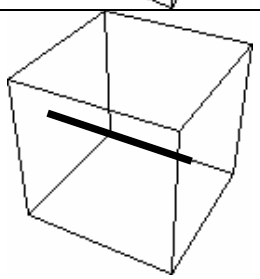	**H**	$\begin{pmatrix} 1 & 0 & 0 \\ & 2 & 0 \\ & & 1 \end{pmatrix}$	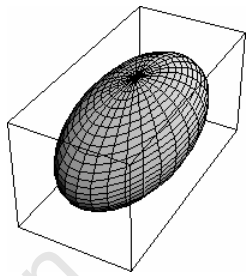
C	$\begin{pmatrix} 0 & 0 & 0 \\ & 0 & 0 \\ & & 1 \end{pmatrix}$	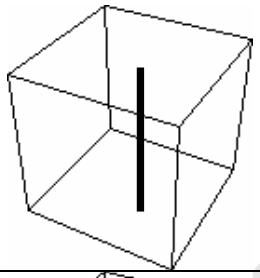	**I**	$\begin{pmatrix} 1 & 0 & 0 \\ & -2 & 0 \\ & & 1 \end{pmatrix}$	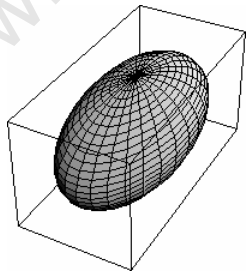
D	$\begin{pmatrix} 1 & 0 & 0 \\ & 1 & 0 \\ & & 0 \end{pmatrix}$	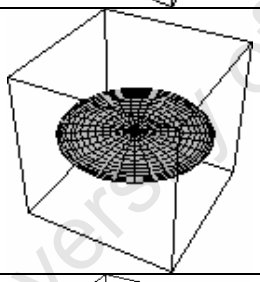	**J**	$\begin{pmatrix} 0 & 1 & 1 \\ & 0 & 1 \\ & & 0 \end{pmatrix}$	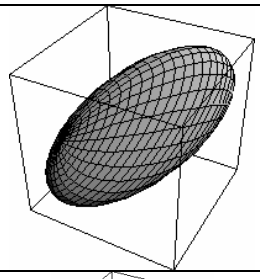
E	$\begin{pmatrix} 1 & 0 & 0 \\ & 0 & 0 \\ & & 1 \end{pmatrix}$	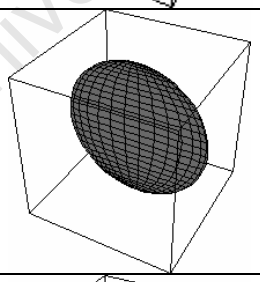	**K**	$\begin{pmatrix} -1 & 0 & 0 \\ & -1 & 0 \\ & & 2 \end{pmatrix}$	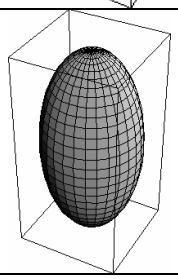
F	$\begin{pmatrix} 0 & 0 & 0 \\ & 1 & 0 \\ & & 1 \end{pmatrix}$	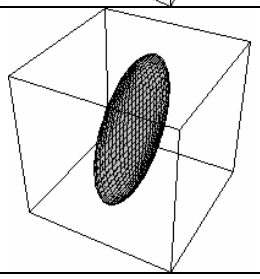			

Figure 4-28 Lamé stress ellipsoids for example stress tensors.

4.3.4.2 Reynolds and HWY icons

The Reynolds and HWY icons are also traction-based icons, which are specially designed to visualize only the normal and shear stresses respectively. The Reynolds icon was originally developed for the visualization of fluid turbulence [105, 106]. It is a mathematical surface such that the radius vector from the centre of the icon to any point on the surface is proportional to the magnitude of the normal component of the traction in that direction, $r \propto \sigma_n$. The HWY icon, defined similarly for the shear stress, is a mathematical surface such that the radius vector from the centre of the icon to any point on the surface is proportional to the magnitude of the shear component of the traction, $r \propto \tau$ [107, 108].

The magnitude of the radius vector for these icons is determined by decomposing the stress vector into a normal component

$$\sigma_n = \sigma_{ij} n_i n_j , \tag{4.18}$$

and a shear stress component

$$\tau = \sqrt{\sigma_i \sigma_i - \sigma_N{}^2} . \tag{4.19}$$

Reynolds and HWY icons for various stress tensors are shown in Figure 4-29 and Figure 4-30 respectively. The 3–D distribution and anisotropy of the normal components of the stress tensor is seen from the Reynolds icon. For the uniaxial stress tensors (A, B, and C) peanut shaped Reynolds icons show directional stresses, *i.e.* high anisotropy. As the principle stresses become equal in magnitude, the shape of the icon becomes toroid-like for the bi-axial case in (D, E and F) and finally spherical for the tri-axial isotropic stress state (G). Reynolds icon representations of (H) and (I) are not equivalent, as they were for the Lamé stress ellipsoid. The icon for the (H) tensor matrix can be obtained by elongating the isotropic sphere of (G) along the larger *y*-principal stress. However icon (I) cannot be obtained similarly. There is a fundamental difference between (H) and (I): the presence of pure shear stresses in the case of (I). Pure shear stress directions are those in which normal stresses vanish, giving rise to the gorge along pure shear directions. The same behaviour is seen from the matrices (J) and (K) in which the presence of pure shear stresses results in a similar shape: a toroidal shape along the same-sign principal stresses and a peanut

shape along the different-sign stress component. Since (K) represents the diagonalized components of (J), the shape of the icons are similar, only oriented differently in space. From these representations of the Reynolds icon, the normal stress distribution of any hypothetical tensor matrix, once it is diagonalized, can easily be produced mentally. It should be noted that, although only the normal component of the stress tensor is extracted with the Reynolds icon, the resulting icons give an indication of the presence of shear stresses as well.

On the other hand, the HWY glyph which maps the shear stresses has the same shape for all the tensor matrices, except for the isotropic stress tensor where it vanishes altogether due to the absence of any shear stresses. These can be understood by referring to the Mohr circles. Mohr circles also reduce to a point for the isotropic stress tensor. For any other stress tensor, after diagonalization, the shear stresses are found at the maximum and minimum values of the ordinate of the Mohr circle, corresponding to 45° degrees with respect to the principal stresses, as shown in Section 4.3.2 (page 90). Therefore the maximum shear directions are fixed at 45° degrees, also fixing the icon shape. Note that pure shear directions are not fixed and depend on the magnitudes of the principal directions. However there are no visual cues for the pure shear stresses in the HWY glyph.

In Figure 4-30, for the uniaxial stress tensors (A, B and C) maximum shear directions are observed on a cone at 45° to the uniaxial principal stress which is predicted. However the same shape is also encountered for the bi-axial stresses: the HWY icons are same for the following pairs: (A,F), (B,E) and (C,D). Along the principal stress directions, the HWY icon surface always vanishes since there is no shear stress along these directions, irrespective of the magnitude of the principal stresses. The shape of the HWY glyphs therefore does not change because: (1) maximum shear stresses are along cones aligned at 45° to the principal stresses; and (2) along the principal stress directions shear stresses are always null. The HWY icon does not display *pure* shear directions. Compare (I) where there is pure shear stress due to compression and tension, and (H) where there is no *pure* shear stress. Finally for the un-diagonalized stress tensor (J), the HWY icon simply aligns itself along the principal stress directions (K).

	σ	Reynolds icon		σ	Reynolds icon
A	$\begin{pmatrix} 1 & 0 & 0 \\ & 0 & 0 \\ & & 0 \end{pmatrix}$	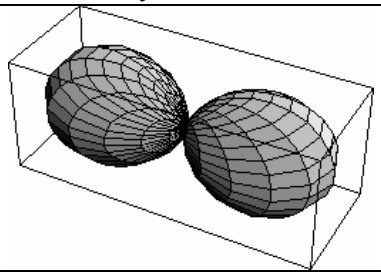	**G**	$\begin{pmatrix} 1 & 0 & 0 \\ & 1 & 0 \\ & & 1 \end{pmatrix}$	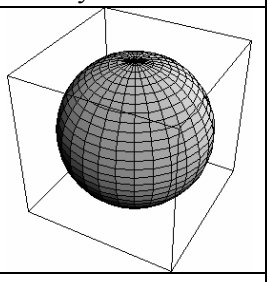
B	$\begin{pmatrix} 0 & 0 & 0 \\ & 1 & 0 \\ & & 0 \end{pmatrix}$	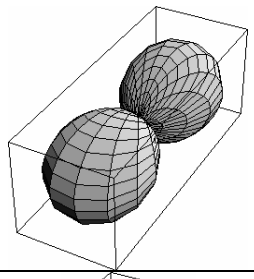	**H**	$\begin{pmatrix} 1 & 0 & 0 \\ & 2 & 0 \\ & & 1 \end{pmatrix}$	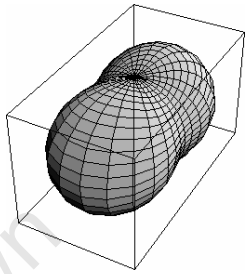
C	$\begin{pmatrix} 0 & 0 & 0 \\ & 0 & 0 \\ & & 1 \end{pmatrix}$	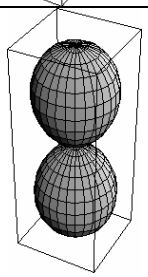	**I**	$\begin{pmatrix} 1 & 0 & 0 \\ & -2 & 0 \\ & & 1 \end{pmatrix}$	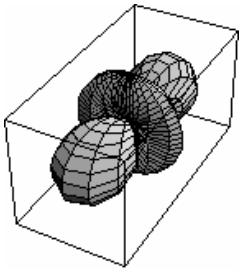
D	$\begin{pmatrix} 1 & 0 & 0 \\ & 1 & 0 \\ & & 0 \end{pmatrix}$	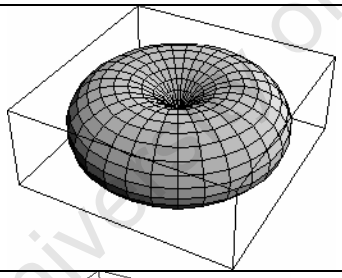	**J**	$\begin{pmatrix} 0 & 1 & 1 \\ & 0 & 1 \\ & & 0 \end{pmatrix}$	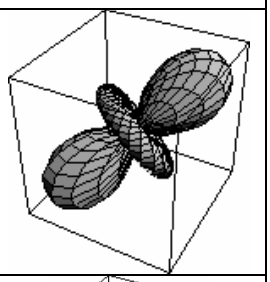
E	$\begin{pmatrix} 1 & 0 & 0 \\ & 0 & 0 \\ & & 1 \end{pmatrix}$	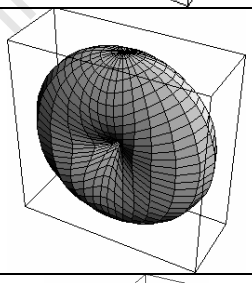	**K**	$\begin{pmatrix} -1 & 0 & 0 \\ & -1 & 0 \\ & & 2 \end{pmatrix}$	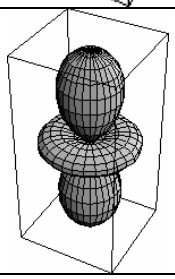
F	$\begin{pmatrix} 0 & 0 & 0 \\ & 1 & 0 \\ & & 1 \end{pmatrix}$	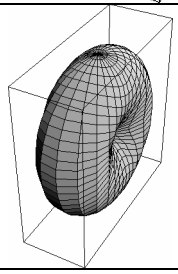			

Figure 4-29 Reynolds icons.

	σ	HWY icon		**σ**	HWY icon
A	$\begin{pmatrix} 1 & 0 & 0 \\ & 0 & 0 \\ & & 0 \end{pmatrix}$	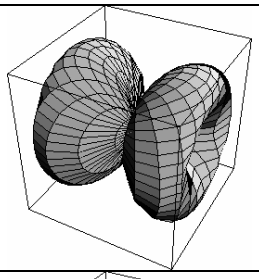	**G**	$\begin{pmatrix} 1 & 0 & 0 \\ & 1 & 0 \\ & & 1 \end{pmatrix}$	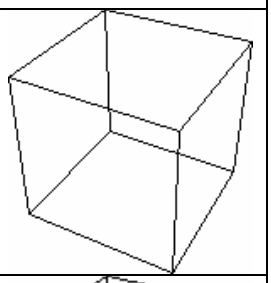
B	$\begin{pmatrix} 0 & 0 & 0 \\ & 1 & 0 \\ & & 0 \end{pmatrix}$	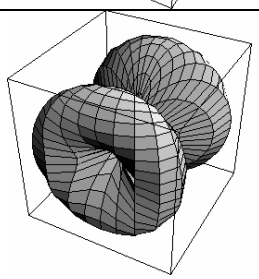	**H**	$\begin{pmatrix} 1 & 0 & 0 \\ & 2 & 0 \\ & & 1 \end{pmatrix}$	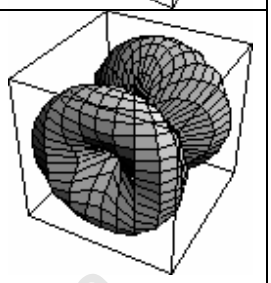
C	$\begin{pmatrix} 0 & 0 & 0 \\ & 0 & 0 \\ & & 1 \end{pmatrix}$	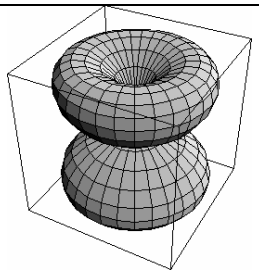	**I**	$\begin{pmatrix} 1 & 0 & 0 \\ & -2 & 0 \\ & & 1 \end{pmatrix}$	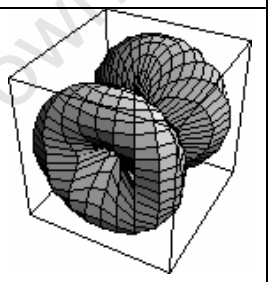
D	$\begin{pmatrix} 1 & 0 & 0 \\ & 1 & 0 \\ & & 0 \end{pmatrix}$	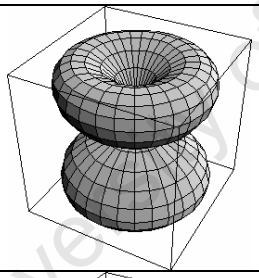	**J**	$\begin{pmatrix} 0 & 1 & 1 \\ & 0 & 1 \\ & & 0 \end{pmatrix}$	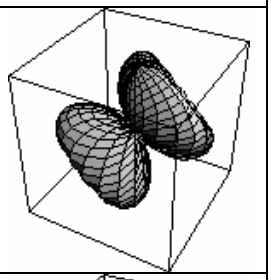
E	$\begin{pmatrix} 1 & 0 & 0 \\ & 0 & 0 \\ & & 1 \end{pmatrix}$	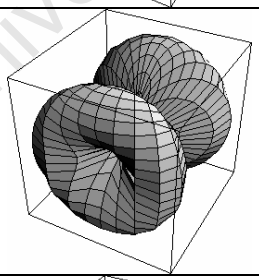	**K**	$\begin{pmatrix} -1 & 0 & 0 \\ & -1 & 0 \\ & & 2 \end{pmatrix}$	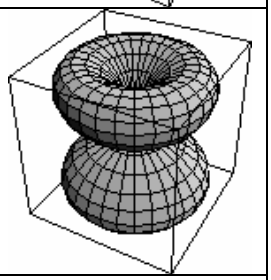
F	$\begin{pmatrix} 0 & 0 & 0 \\ & 1 & 0 \\ & & 1 \end{pmatrix}$	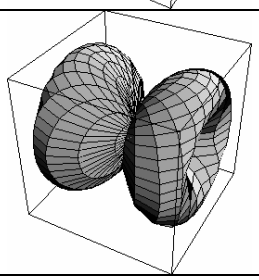			

Figure 4-30 HWY icons.

4.3.5 Cauchy stress quadric surface

An alternative representation of the stress tensor is the Cauchy stress quadric surface [18] defined as

$$\sigma_{ij} x_i x_j = \pm k^2 , \tag{4.20}$$

or

$$\sigma_{11} x_1^2 + \sigma_{22} x_2^2 + \sigma_{33} x_3^2 + 2\sigma_{12} x_1 x_2 + 2\sigma_{13} x_1 x_3 + 2\sigma_{23} x_2 x_3 = \pm k^2 . \tag{4.21}$$

In the coordinate system of the principal stresses the Cauchy quadric surface can be written as

$$\sigma_1 x'^2_1 + \sigma_2 x'^2_2 + \sigma_3 x'^2_3 = \pm k^2 , \tag{4.22}$$

where x_1', x_2', x_3' are the principal axes of the quadric which are parallel to the principal stresses $\sigma_1, \sigma_2, \sigma_3$.

The stress quadric surface has two significant properties:

(i) The radius vector traversing the quadric surface is inversely proportional to the square of the magnitude of the normal stress in that particular direction, as seen in Equation (4.22).

(ii) The traction or stress vector $\boldsymbol{\sigma}_i$ that acts on the plane perpendicular to the radius vector, is parallel to the normal of the quadric surface. The implication is that when the stress vector shifted to the quadric surface, it always points out along the surface normal, as seen in Figure 4-31.

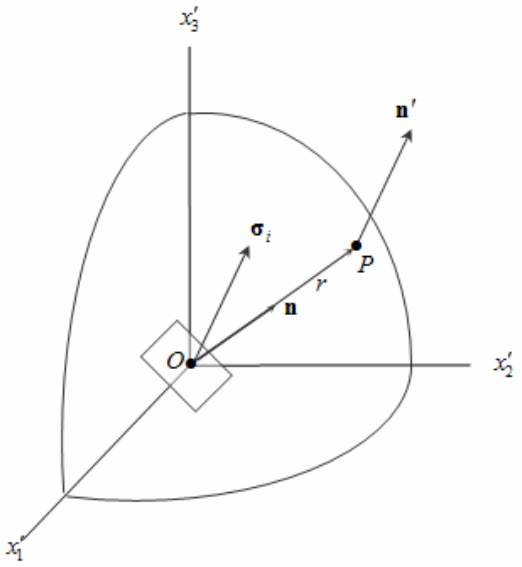

Figure 4-31 A portion of the stress quadric surface. $\boldsymbol{\sigma}_i$ is the stress vector along $\mathbf{n}$. The quadric surface normal $\mathbf{n}' = \frac{\partial}{\partial x_i}\left(\sigma_{ij} x_i x_j \mp k^2\right)$ is always parallel to the stress vector.

The first property is the inverse of the Lamé stress ellipsoid, consequently the shape of the stress quadric surface can be intuitively misleading, the largest principal stress is represented by the smallest radius vector and vice versa. The inverse square scaling also distorts the relative sizes of the principal axes of the surface. The second property of the quadric surface visualizes all possible orientations of the first order stress tensor or the traction. All line segments that are normal to the stress quadric surface at point *P* are also parallel to the traction acting at point *O* along n_i in Figure 4-31. Note that the surface normals of the Lamé stress ellipsoid have no physical significance.

Equation (4.22) denotes a closed surface for all three tensile or all three compressive principal stresses, as shown in Figure 4-32. Uni-axial and bi-axial stresses lead to planar (A, B and C) and tubular (D, E and F) surfaces respectively. In the presence of simultaneous tensile and compressive stresses, *i.e.* in the presence of pure shear stress, the quadric surface diverges in the direction of the zero normal stress, creating three hyperbolic sections of the quadric surface. Lateral surface is shown in (I) and base and top surfaces shown in (J) and (K). This results in a visually striking representation of the shear stress presence and the shear stress directions. Thus, simultaneous use of stress quadric icon with other stress icons adds to the visual understanding of the stress tensor.

	σ	Cauchy stress quadric icon		σ	Cauchy stress quadric icon
A	$\begin{pmatrix} 1 & 0 & 0 \\ & 0 & 0 \\ & & 0 \end{pmatrix}$	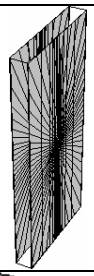	**G**	$\begin{pmatrix} 1 & 0 & 0 \\ & 1 & 0 \\ & & 1 \end{pmatrix}$	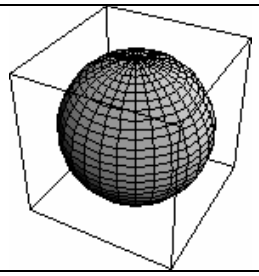
B	$\begin{pmatrix} 0 & 0 & 0 \\ & 1 & 0 \\ & & 0 \end{pmatrix}$	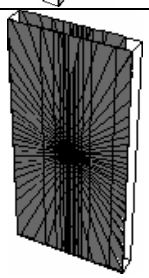	**H**	$\begin{pmatrix} 1 & 0 & 0 \\ & 2 & 0 \\ & & 1 \end{pmatrix}$	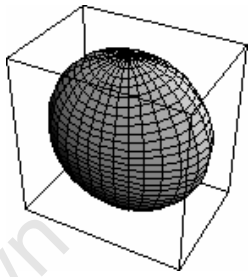
C	$\begin{pmatrix} 0 & 0 & 0 \\ & 0 & 0 \\ & & 1 \end{pmatrix}$	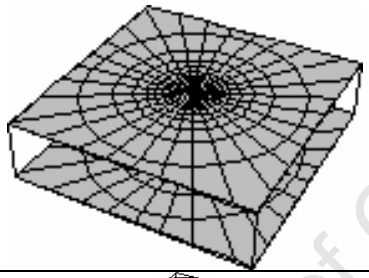	**I**	$\begin{pmatrix} 1 & 0 & 0 \\ & -2 & 0 \\ & & 1 \end{pmatrix}$	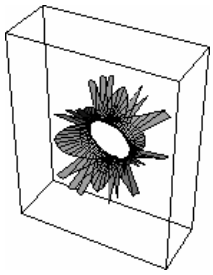
D	$\begin{pmatrix} 1 & 0 & 0 \\ & 1 & 0 \\ & & 0 \end{pmatrix}$	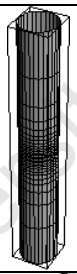	**J**	$\begin{pmatrix} 0 & 1 & 1 \\ & 0 & 1 \\ & & 0 \end{pmatrix}$	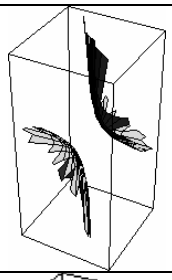
E	$\begin{pmatrix} 1 & 0 & 0 \\ & 0 & 0 \\ & & 1 \end{pmatrix}$	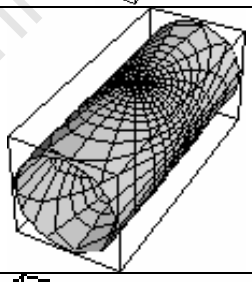	**K**	$\begin{pmatrix} -1 & 0 & 0 \\ & -1 & 0 \\ & & 2 \end{pmatrix}$	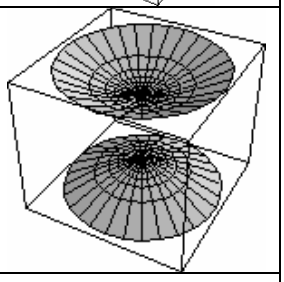
F	$\begin{pmatrix} 0 & 0 & 0 \\ & 1 & 0 \\ & & 1 \end{pmatrix}$	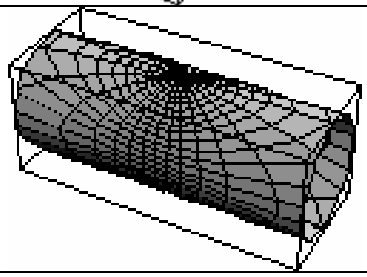			

Figure 4-32 Cauchy stress quadric icons for example tensors.

4.3.6 Principle Normal Shear (PNS) Stress Icon

Based on the previous observations of eigenicons, traction-based and Cauchy stress quadric representations, a new visualization method is proposed that uses the more intuitive shape of the stress ellipsoid to visualize the principal stress state, but also allows the visualization of the normal stress directions, *i.e.* the second feature of the stress quadric. The Principle Normal Shear (PNS) stress icon is a new visualization icon that represents principal stresses, normal stresses and shear stress information simultaneously by using a colour map on the stress ellipsoid surface [109]. The colour coding on the PNS icon explicitly shows stress types (normal and shear) using the stress vector, whereas previously suggested color coding [43, 110], based on the scalar principal stresses, only showed the normal stress types (tensile/ compressive) along principal axes.

The stress vector (traction) is used for the visualization mapping of the PNS icon. The stress vector σ_i is resolved into two components; a *normal component* acting parallel to n_i, and a *shear component* acting parallel to the plane (Figure 4-33a). The angle ϕ between the stress vector and the unit normal n_i at point *O* can be represented as colour on point *P*, so that normal and shear stress components on the whole ellipsoidal surface can be deduced from the colour attribute (Figure 4-33b.) Hence the components of the first order stress tensor σ_i, in any arbitrary direction n_i, can be visualized as colour. The PNS icon thus simultaneously represents the principal stress state and differentiates between the tensile/ compressive normal stresses and shear stresses.

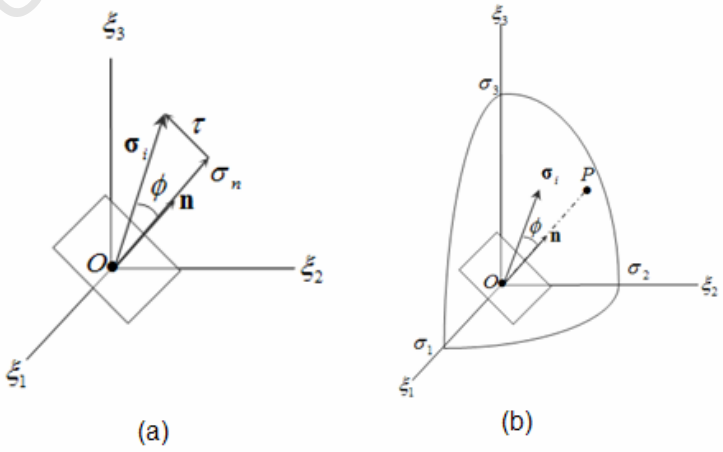

Figure 4-33 (a) Normal and tangential components of the stress vector (b) PNS icon colour coding scheme.

Let *O* be the centre of the ellipsoid and *P* be any point on the stress ellipsoid surface shown in Figure 4-33b. The direction cosines of *OP* are

$$n_i = \xi_i / r\,, \tag{4.23}$$

where $r = |PQ|$. The stress vector σ_i in this direction is given by

$$\sigma_i = \sigma_{ji} n_j\,. \tag{4.24}$$

The angle between the unit normal, n_i, of the plane and the stress, σ_i, acting on that plane is calculated using the vector dot product

$$\phi = \cos^{-1}\left(\frac{\boldsymbol{\sigma}_i \cdot \mathbf{n}}{|\boldsymbol{\sigma}_i||\mathbf{n}|}\right), \tag{4.25}$$

or in the tensor form

$$\phi = \cos^{-1}\left(\frac{\sigma_i n_i}{\sqrt{\sigma_k \sigma_k}}\right). \tag{4.26}$$

The ellipsoidal surface is mapped with colour, according to the angle

$$colour \propto \phi\,, \tag{4.27}$$

for which a linear colour lookup table is used. Pure tension, or $\phi = 0^\circ$, corresponds to blue; pure shear, or $\phi = 90^\circ$, corresponds to green; and pure compression, or angle $\phi = 180^\circ$, corresponds to red as shown in Figure 4-34. Thus hues on the ellipsoidal surface change from blue to green to red as the stresses varies from tension to shear to compression. A similar colour coding scheme was proposed in Equation (4.33) [111] for illustrating tensile, compressive and shear stresses on a hyperstreamline surface, as discussed in 4.3.7.2.

The eigenvalue-eigenvector decomposition of any second order stress tensor is a transformation where the principal axes, ξ_i, represent directions where the shear stress is zero. Therefore the orientation of nonzero shear stresses, would exist somewhere in between the principal axes, ξ_i. In Figure 4-34, the PNS icon is shown for the stress tensor $\boldsymbol{\sigma} = \begin{pmatrix} 1 & & \\ & -2 & \\ & & 3 \end{pmatrix}$. Tensile stresses (blue) along x_1 and x_3, and compressive stress (red) along x_2 can be seen. The shear stresses can be seen as the green bands of colour traversing the ellipsoid surface between the principal stresses. Thus, using the PNS icon, the tensile, compressive and shear character of the stress tensor can be explored.

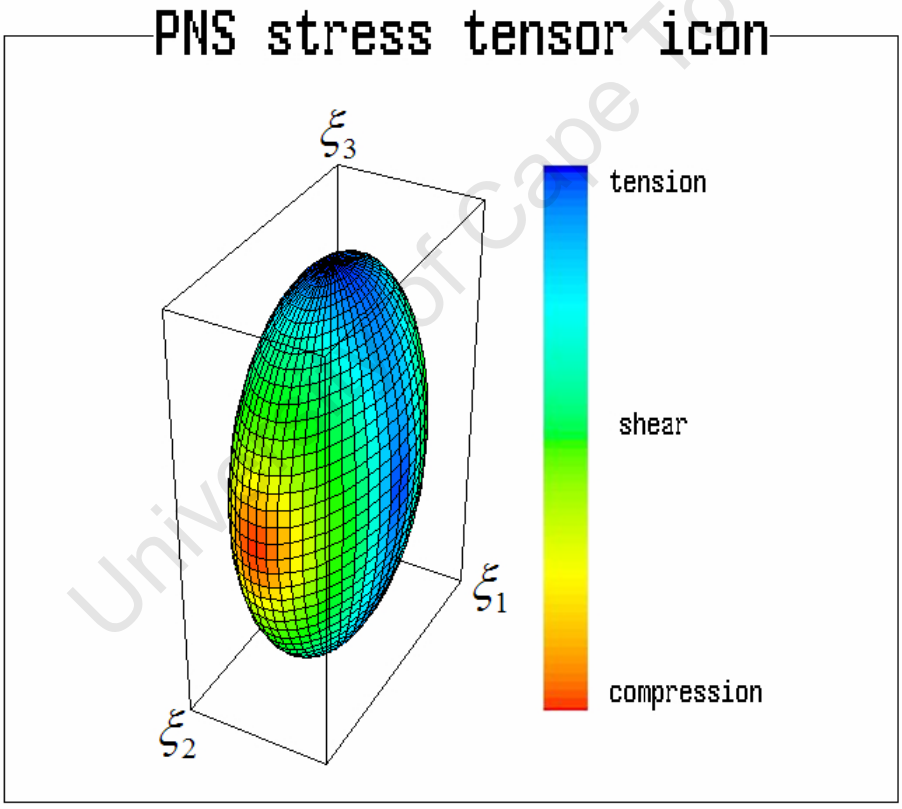

Figure 4-34 Principle Normal Shear (PNS) tensor icon with a colour lookup table indicating the angle between the traction vector and the ellipsoid surface.

Characteristic stress tensors are visualized using the PNS icon in Figure 4-35. Two types of normal stresses can be distinguished from these representations, for example (G and H). Also note that the green bands of shear stress occur in the presence of both tensile and compressive stresses (in J, K and L). Due to polygonization in Figure 4-35 (K), there is a polar region upwards from the tip, however it can be seen from the colouring that principal stresses are at the red and blue poles. Otherwise, the form and orientation of the icon follows that of the stress ellipsoid discussed earlier in section 4.3.4.1.

	σ	PNS icon		σ	PNS icon
A	$\begin{pmatrix} 1 & 0 & 0 \\ & 0 & 0 \\ & & 0 \end{pmatrix}$	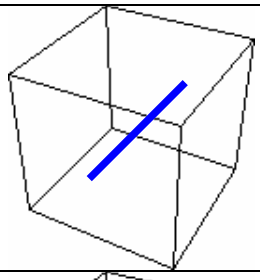	**G**	$\begin{pmatrix} 1 & 0 & 0 \\ & 1 & 0 \\ & & 1 \end{pmatrix}$	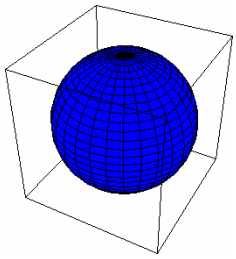
B	$\begin{pmatrix} 0 & 0 & 0 \\ & -1 & 0 \\ & & 0 \end{pmatrix}$	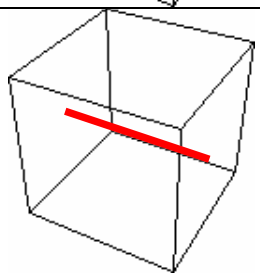	**H**	$\begin{pmatrix} -1 & 0 & 0 \\ & -1 & 0 \\ & & -1 \end{pmatrix}$	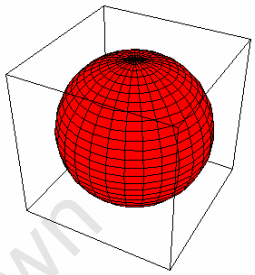
C	$\begin{pmatrix} 0 & 0 & 0 \\ & 0 & 0 \\ & & 1 \end{pmatrix}$	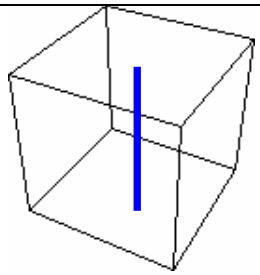	**I**	$\begin{pmatrix} 1 & 0 & 0 \\ & 2 & 0 \\ & & 1 \end{pmatrix}$	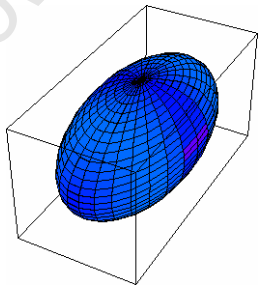
D	$\begin{pmatrix} 1 & 0 & 0 \\ & 1 & 0 \\ & & 0 \end{pmatrix}$	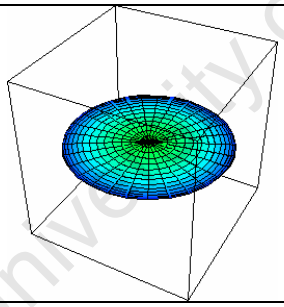	**J**	$\begin{pmatrix} 1 & 0 & 0 \\ & -2 & 0 \\ & & 1 \end{pmatrix}$	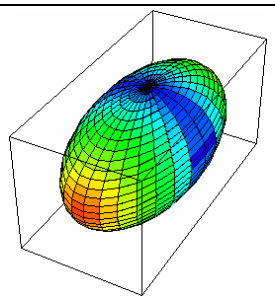
E	$\begin{pmatrix} 1 & 0 & 0 \\ & 0 & 0 \\ & & 1 \end{pmatrix}$	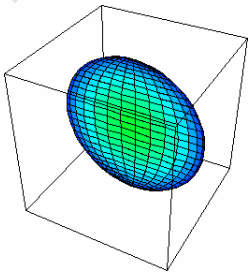	**K**	$\begin{pmatrix} 0 & 1 & 1 \\ & 0 & 1 \\ & & 0 \end{pmatrix}$	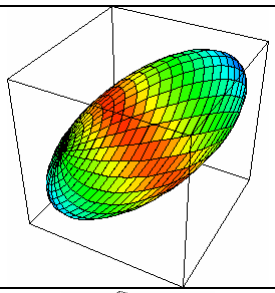
F	$\begin{pmatrix} 0 & 0 & 0 \\ & 1 & 0 \\ & & 1 \end{pmatrix}$	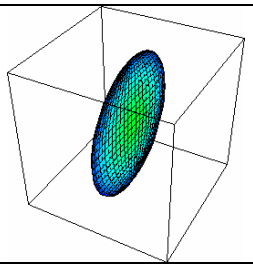	**L**	$\begin{pmatrix} -1 & 0 & 0 \\ & -1 & 0 \\ & & 2 \end{pmatrix}$	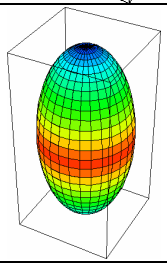

Figure 4-35 PNS icons.

4.3.7 Global tensor icons

For the representation of tensor fields, global icons can be preferable to point icons if uncluttered visualization can be obtained. Global representations are especially applicable where the dataset obtained is continuous in the domain, such as in fluid mechanics simulations [111]. However, as mentioned before, tensor quantities have high information density, *i.e.* (3+9) variables per point for a three-dimensional tensor in a 3–D domain. Thus global representations are only capable of partially mapping tensor information. This is achieved by representing only the selected features of the tensor field which are of prime importance to the user [120].

4.3.7.1 Plane stress contour lines

For a plane stress state where $\sigma_{i3} = 0$ for $i = 1,2,3$, the planar stress tensor is

$$\boldsymbol{\sigma} = \begin{pmatrix} \sigma_{11} & \sigma_{12} & 0 \\ \sigma_{12} & \sigma_{22} & 0 \\ 0 & 0 & 0 \end{pmatrix}. \tag{4.28}$$

In a three-dimensional body acted on by forces applied at is boundary, a complete representation of the stress at any point can be represented by two diagrams [13]. The stress tensor can be obtained from a stress function χ as

$$\sigma_{11} = \frac{\partial^2 \chi}{\partial y^2}, \tag{4.29}$$

$$\sigma_{22} = \frac{\partial^2 \chi}{\partial x^2}, \tag{4.30}$$

$$\sigma_{12} = \sigma_{21} = -\frac{\partial^2 \chi}{\partial x \partial y}, \tag{4.31}$$

where the plane of the stress is the plane (x, y), and χ is a scalar function of the

(x, y) coordinates. If the curves $\frac{\partial \chi}{\partial x} = const.$ and $\frac{\partial \chi}{\partial y} = const.$ are traced for the same value of z, and for equidifferent values of the constants, then the tractions at any point, across planes parallel to the planes of (x, z) and (y, z), are directed along the tangents to the curves. Furthermore the magnitude of the traction vector is proportional to the density of the contours at this point. An example of two such sets of curves are shown for a hypothetical stress function $\chi = \left(0.3x^2 - 0.2y^2\right)^3 - x^2 + 2y^3$, in Figure 4-36.

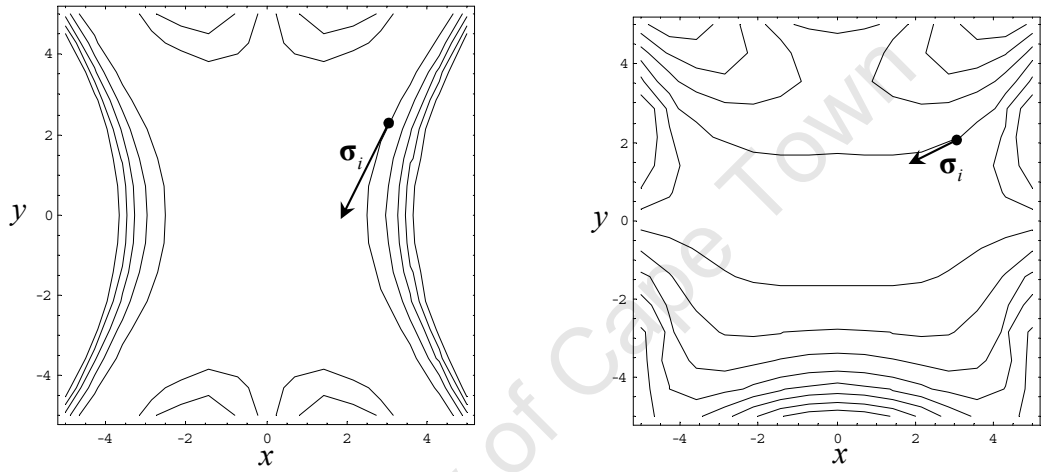

(a) (b)

Figure 4-36 Tractions across (x, z) plane (a), and (y, z) (b) are directed along the tangents to the contour lines. The traction vectors magnitudes are drawn proportional to the density of the contour lines.

4.3.7.2 Integral representations of second rank tensors

Delmarcelle extends the streamline visualization of vector fields (see section 4.2.3) to represent the tensor information along 3–D paths in space called hyperstreamlines [111]. This icon is obtained by moving a geometric primitive of finite size along one of the eigenvector fields v_i while distorting it in the transverse direction under the combined action of the two other eigenvector fields. A hyperstreamline is the surface obtained by linking these primitives along the trajectory. Elliptical cross sections can

be used to depict the eccentricity of the transverse eigenvalues, whereas a 'cross' cross section is used to delineate transverse eigenvectors and to emphasize their rotation. The latter can be used if the transverse eigenvectors are not degenerate in the dataset for better perception. Various colour schemes are applied to hyperstreamline surfaces. For example, in fluid flow systems kinetic energy density is mapped as a colour (Figure 4-37) [111] according to

$$color \sim k = \frac{\lambda^{(1)} - 0.5(\lambda^{(2)} + \lambda^{(3)})}{2}. \tag{4.32}$$

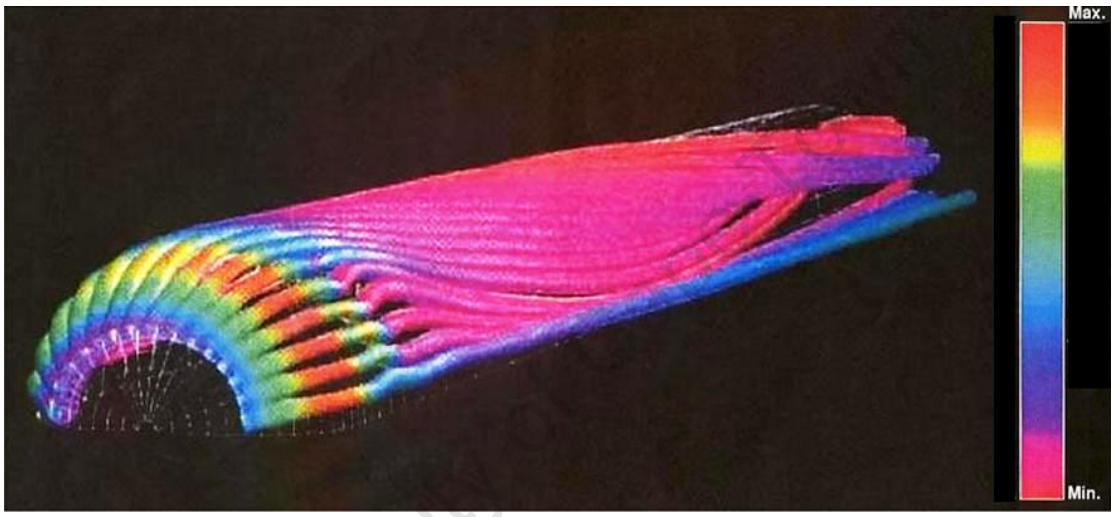

Figure 4-37 Momentum flux tensor of a flow past a hemisphere. The direction of the incoming flow is five degrees to the left of the hemisphere. Hyperstreamlines detach toward the end of the cylinder. Kinetic energy density k is colour mapped on the tube according to Equation (4.32) [111].

In another example, compressive and tensile stresses are visualized using colour on the hyperstreamline tube's cross section, according to equation

$$color \sim \cos(\varphi) = \frac{\hat{\mathbf{n}} \cdot \mathbf{F}}{|\hat{\mathbf{n}}||\mathbf{F}|}, \tag{4.33}$$

where the angle φ is the angle between the two vectors $\hat{\mathbf{n}}$ and $\mathbf{F}$, and $\hat{\mathbf{n}}$ is a unit radial vector in the plane of the tubes cross section. $\mathbf{F} = \boldsymbol{\sigma} \cdot \hat{\mathbf{n}}$ is the force acting on a facet with normal $\hat{\mathbf{n}}$. This colouring scheme is applied in Figure 4-38 [111] to depict the shear stresses by the minor tube of a stress field due to two compressive and one tensile force acting on the top surface of the material. Red corresponds to $\varphi = 0$, and indicates that the corresponding $\hat{\mathbf{n}}$ directions are in pure tension. Blue indicates pure compression ($\varphi = 180$), and green indicates pure shear ($\varphi = 90$).

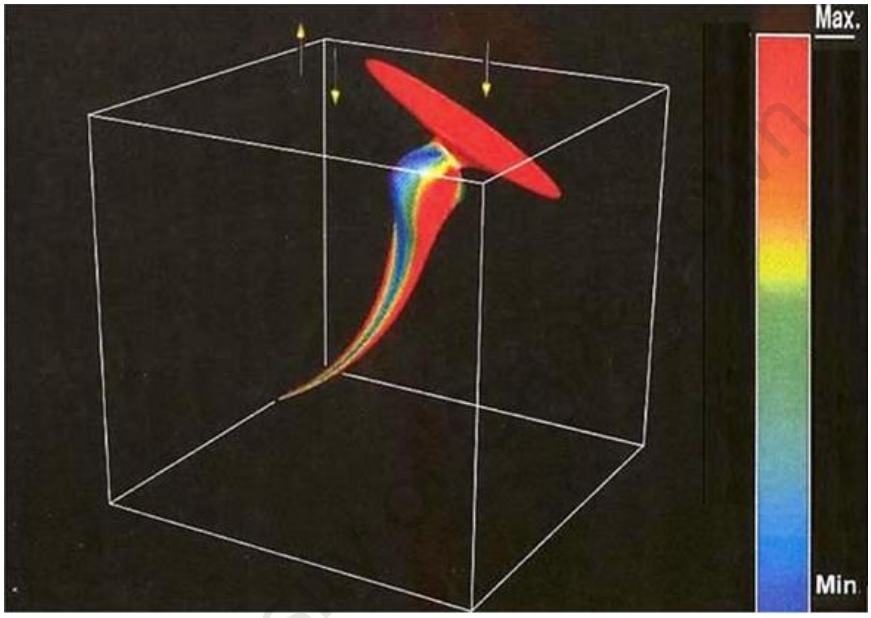

Figure 4-38 The minor hyperstreamline is shown for the stress field due to three surface forces indicated with arrows on the top of the bounding box. Compressive and tensile stresses are distinguished on the surface of the hyperstreamline with colours. Blue indicates compression, red tension and green indicates shear stresses [111].

Hyperstreamline techniques depend on the global availability of continuous data in a domain. Therefore tensor hyperstreamlines are widely used in fluid mechanics simulations, or in finite element modelling simulations where synthetic tensor data is generated by computer simulations. In medicine, hyperstreamline techniques have been used for visualization of diffusion tensors in brain (DT-MRI) [112, 113], and also for the visualization of stress and strain in the heart muscle using FEM methods [114].

In an interesting application, Guo *et al* used hyperstreamlines to visualize sparsely distributed tensor data obtained from x-ray diffraction experiments to visualize residual stresses in a welded component [115]. The residual stress state was measured up to 17 mm away from the weld and 250μ deep in the surface. A total of 36 tensors were obtained at 3, 5, 7, 13, 15, 17 mm from the edge of the weld at 50μm intervals to the maximum depth of 250μm. The goal of the visualization was to depict the global features of the stress profile. In order to use hyperstreamlines, two assumptions were made implicitly for this visualization. The first assumption is based on the symmetry of the weld line: stress tensors along the weld line are assumed to be equal. The second assumption is, to interpolate the stress tensors to create a continuous dataset, required for the integration algorithm. However, in general, the choice of different algorithms for the interpolation of tensors affects the results of the integration [116, 117] and should be used cautiously in experimental datasets.

In the resulting visualizations, the major hyperstreamline is shown along the weld line, in form of a dashed line as seen in Figure 4-39a. Medium and minor eigenvectors are shown in Figure 4-39b, c, respectively. The magnitude of the eigenvalues are shown with colour. Red hues show tensile stress on the surface and blue hues show compressive stresses into the material. The ribbon like shape of the hyperstreamline for the major eigenvalue hyperstreamline is due to the very small magnitude of the medium eigenvalue. The minor eigenvalue is negative and large in magnitude compared to the medium eigenvector.

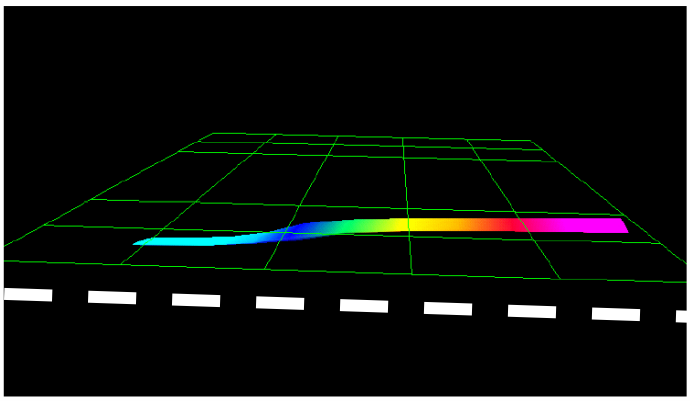

(a)

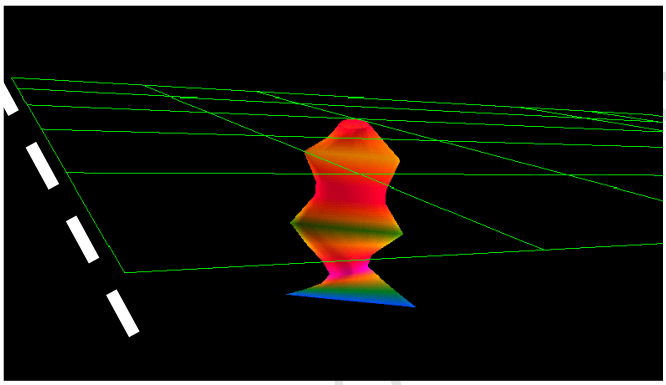

(b)

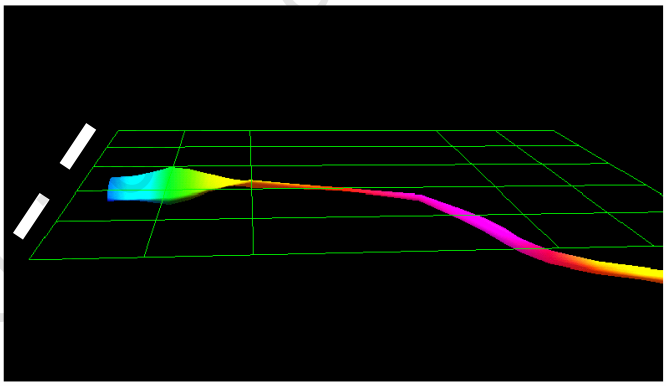

(c)

Figure 4-39 Major (a) medium (b) and minor (c) eigenvalue hyperstreamlines, are shown near a weld line indicated by the dashed lines. Colour denotes magnitude of the corresponding eigenvalues. Compressive stresses are denoted by blue and tensile stresses by red colour [115].

4.3.7.3 Antisymmetric tensors

Antisymmetric tensors can be visualized by adding an axial vector representation to hyperstreamlines. This is achieved by decomposing the general non-symmetric tensor into a symmetric tensor (**S**) and an antisymmetric tensor (**A**) (see section 2.1.1). Where the symmetric tensor (**S**) is visualized by a hyperstreamline, the antisymmetric tensor (**A**) is represented by a ribbon [111]. The ribbon position and width encode the axial vector component perpendicular to the trajectory. The colour of the vector denotes the angle between the axial vector direction and trajectory (Figure 4-40).

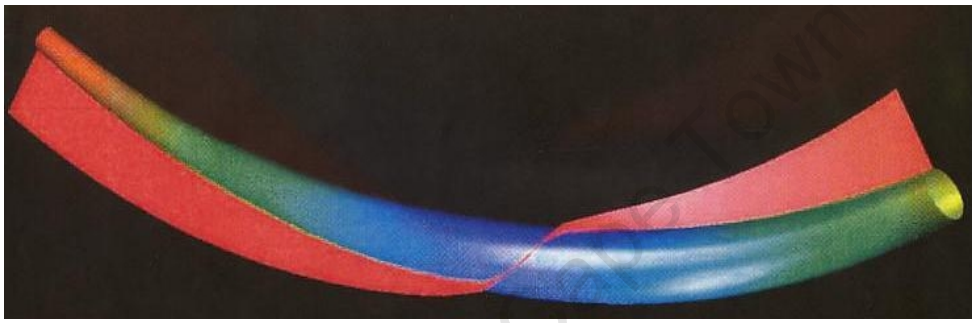

Figure 4-40 Antisymmetric second order tensor visualization [111].

4.3.7.4 Volume representations and topology of tensor fields

Simultaneous visualization of a number of neighbouring streamlines can reveal global features of a tensor field. In addition, encoding longitudinal eigenvalues as colour on a hyperstreamline provides information about the behaviour of neighbouring hyperstreamlines in a solenoidal tensor field. A solenoidal tensor field is one that is divergence free, *i.e.*

$$\sum_{i=1}^{3} \frac{\partial T_{ij}}{\partial x_i} = 0 \,. \tag{4.34}$$

Solenoidal tensor fields have the following convergence/divergence property between the eigenvalues

$$\lambda'^{(i)} = K_{ij}(\lambda^{(i)} - \lambda^{(j)}) + K_{ik}(\lambda^{(i)} - \lambda^{(k)}), \tag{4.35}$$

where $\lambda^{(i)'}$ is the derivative of the longitudinal eigenvalues along the trajectory. K_{ij} and K_{ik} are geometric factors that are positive if neighbouring hyperstreamlines converge in the corresponding transverse directions *j* and *k* [111]. When the longitudinal eigenvalues of a major hyperstreamline increase during propagation $\lambda'^{(i)} > 0$, neighbouring hyperstreamlines diverge. The opposite holds for minor hyperstreamlines. Figure 4-41 illustrates how force fields propagate in a stress tensor field induced by two compressive forces on the top surface of the material [111]. The longitudinal eigenvalues are colour coded on the streamlines. Two minor eigenvector streamlines propagate upwards. The highlighted region, where the eigenvectors fork, shows strong divergence of the neighbouring minor tubes. This behaviour is coupled by the decrease of the longitudinal eigenvalues as can be seen from the blue colour.

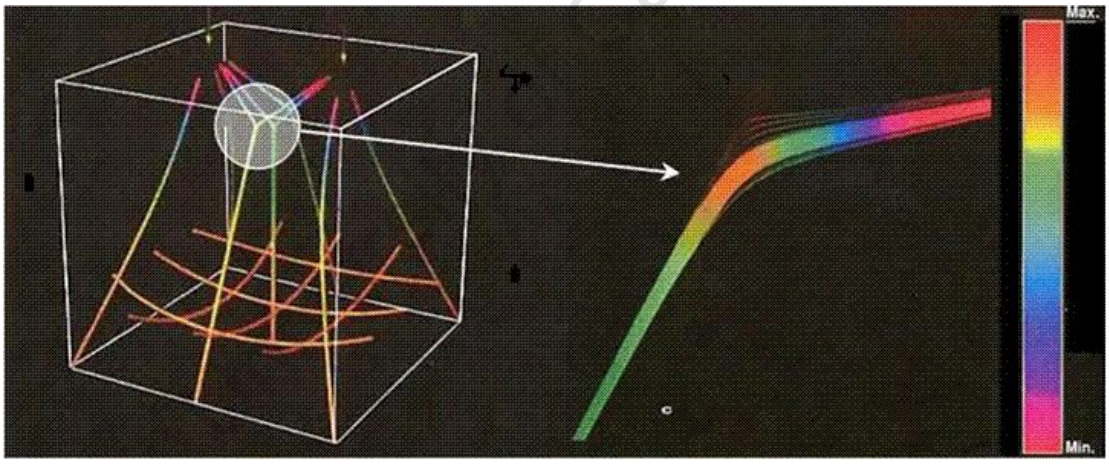

Figure 4-41 Colour encoded longitudinal streamlines reveal topological information about the tensor field [111].

Other authors have suggested using a number of close hyperstreamlines to create streamsurfaces [118]. Laidlaw uses artistic painting techniques, which represent tensor ellipsoids, to depict the cross section of a volume [103]. The strike direction and saturation of a brush stroke encode the 3–D direction of the maximum eigenvector: and the strike frequency, transparency and the length-width ratio present the maximum eigenvalue and other derived quantities of interest for the specialist.

Boring and Pang visualize tensors by deforming simple objects according to the underlying tensor field and displaying the deformed object (twisting, bending and elongation) [119, 120]. Zhang creates iso-surfaces that are normal to a particular eigenvector at all points in space [121]. Another volume visualization technique is based on the interaction of simulated light with the local tensor field [122]. In this technique, the tensor field is visualized by the bending of the rays, and the image of the light rays on a receiving plate indicate tensor field behaviour similar to x-ray imaging. Using this light interaction technique, non-symmetric tensors can also be visualized without decomposition.

Finally, the complete topology of a tensor field can be obtained using critical point analysis. Because the integration method results depend on the initial condition of integration, or the choice of seed points, topology extraction can be helpful to reveal the overall tensor field topology, which is the topology of its eigenvector fields. Therefore in a manner similar to vector field topology, degenerate points where hyperstreamlines meet, can be identified. The structure can be extracted by searching for such degenerate points where one or more of the eigenvalues vanish, such as

$$\lambda^{(i)} = 0, \tag{4.36}$$

$$\lambda^{(j)}.\lambda^{(k)} = 0, \tag{4.37}$$

$$\lambda^{(j)} \pm \lambda^{(k)} = c, \tag{4.38}$$

where $\lambda^{(i)}$ is the longitudinal eigenvalue and $\lambda^{(j)}, \lambda^{(k)}$ are transverse eigenvalues. The locus of $\lambda^{(i)} = 0$ (Equation (4.36)), is the set of critical points in a trajectory where the eigenvalues vanish, and the direction of the hyperstreamline is locally undefined. The condition of Equation (4.37) is where the cross section of a hyperstreamline reduces to a straight line or a single point, and the condition of Equation (4.38) is the set of points where the cross section has the same shape everywhere. As an example, the topology of tensor fields due to two compressive forces is shown in Figure 4-42 [111]. The critical points of the medium eigenvector and the major eigenvector are denoted by yellow and green colour isosurfaces respectively. Also in Figure 4-42, on the yellow isosurface both transverse eigenvalues are positive, and the minor tube cross section is tensile everywhere. Similarly, inside the green isosurface both

eigenvalues are negative and all eigenvalues are negative and in compression. The critical point analysis is further discussed in [123-125].

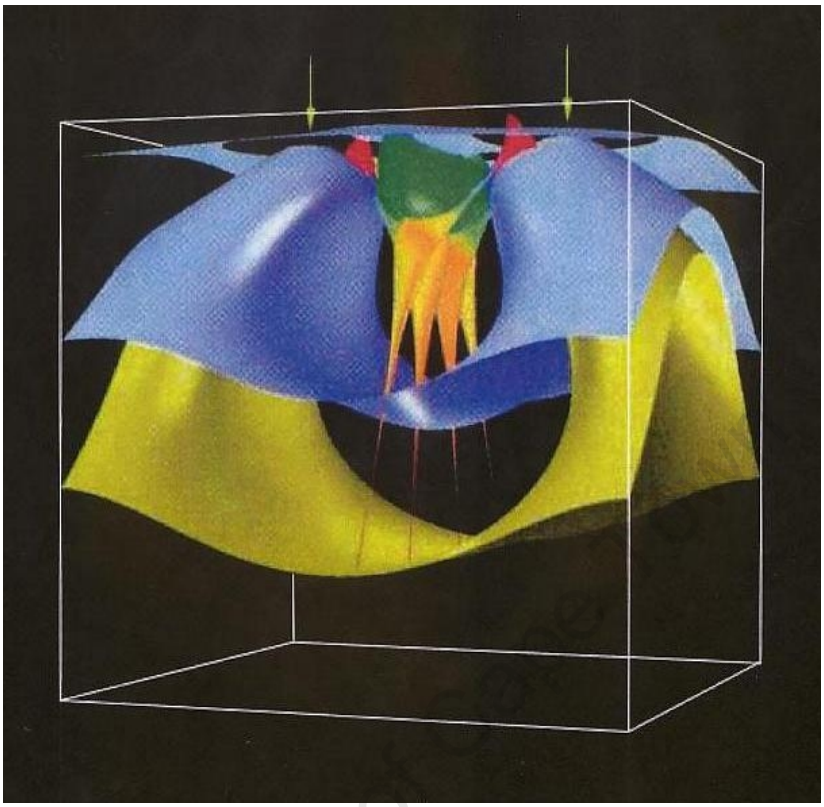

Figure 4-42 Topology of symmetric second order tensor field visualized due to two compressive forces [111].

4.4 Higher order tensor visualization

The visualization of higher order tensors is scarce. One method suggested to visualize the fourth order elasticity tensor is to use wave front surfaces, that travel in a crystal [126]. As a uniform spherical wave-front surface expands from the centre of a crystal, it deforms according to the elastic properties of the material in the 3–D space. In a crystal, the wave velocity and the elasticity tensor satisfy Christoffel's equation [127],

$$\left(C_{ijkl}n_i n_j - \rho v^2\right)\alpha_k = 0\,. \tag{4.39}$$

where C_{ijkl} is the fourth order elasticity tensor, n_i is the propagation direction or the pointing vector, ρ is the material density, v is the wave-velocity, and α_k is the particle vibration direction. In Christoffel's equation, the velocity terms along the diagonal, ρv^2, are the eigenvalues, and the displacement vibration cosines, α_k, are eigenvectors [80]. Since both the eigenvalues and eigenvectors are functions of propagation directions, n_i, the eigenvalues (wave speeds) can be calculated for all propagation directions. It is then it is possible to draw a 3–D wave velocity surface for each eigenvalue. These three wave surfaces are shown in Figure 4-43, for a Calcium-Formate crystal [128]. Colour is used to indicate the angle between vibration direction and propagation direction, with red being a transverse wave and blue being longitudinal.

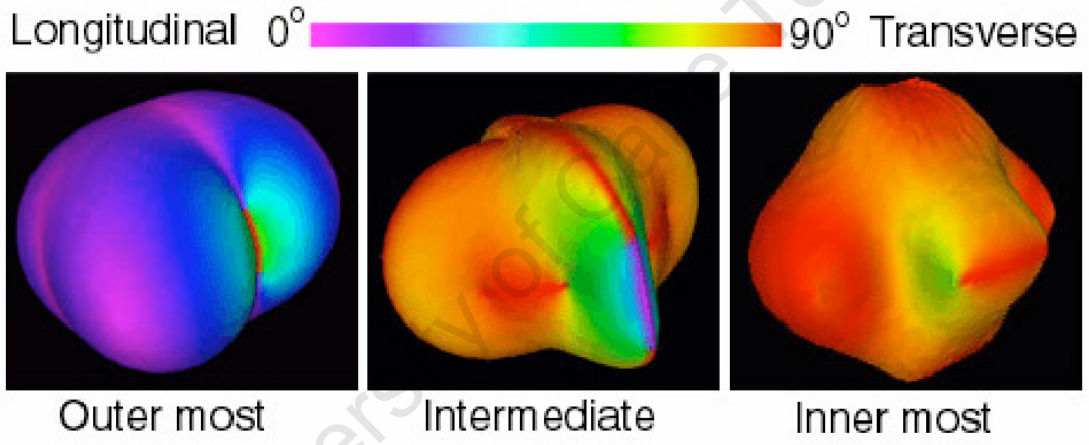

Figure 4-43 Visualization of the elasticity tensor C_{ijkl}, for the Calcium-Formate crystal [128].

5 Visualization of residual stresses

In this chapter, a brief review of the origins and characteristics of residual stresses in polycrystalline materials is given, followed by a description of the methods of residual stress determination using diffraction techniques. Stress determination measurements produce scalar, vector or tensor datasets depending on the experimental setup. These quantitatively and qualitatively disparate diffraction datasets are explored in the light of scientific visualization.

5.1 Residual stress and strain in crystalline materials

In solid materials irregularities in the structure give rise to stress fields, known as residual stresses, which exist without, or after the removal of, an applied load. The origin, determination and control of these stresses are essential because the mechanical performance of a component can be significantly altered by their presence. Residual stresses may be introduced during thermal or mechanical treatments and remain in the material after the removal of the external load [129, 130].

In this work, the discussion of residual stress analysis is limited to polycrystalline materials with relatively small grain sizes, which include most metals of engineering interest [131]. Residual stresses are, necessarily, in equilibrium over the whole body, and can be classified as macro- and micro- stresses according to their length scale (Figure 5-1). Type I macro stresses, shown in Figure 5-1a, span a large number of grains may be introduced by high temperature gradients caused by rapid heat treatment, welding, quenching, annealing or by mechanical processes such as shot peening, rolling, ion implantation, surface modification, *etc*. [130]. Type II microstresses, are intra-granular stresses which exist in polycrystals (Figure 5-1b). Finally, the incoherencies at the grain interfaces and at dislocation fields may cause minute microstresses (Figure 5-1c).

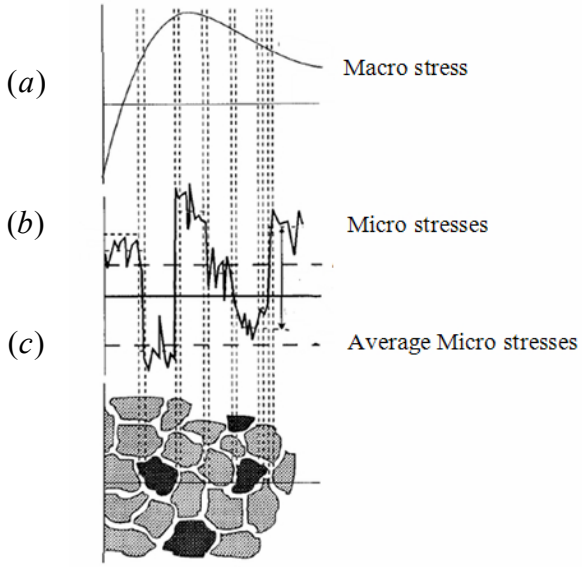

Figure 5-1 Macro and micro residual stresses defined according to length scale.

The presence of macro residual stresses in technical components can be a critical factor affecting the service lifetime of a component. These stresses can be beneficial or detrimental depending on the quantitative stress profile. For example, excessive tensile residual stresses on a specimen surface may facilitate crack propagation, but, on the other hand, compressive residual stresses on surfaces impede crack initiation, and therefore they are introduced using various techniques such as shot-peening. The response of materials is not the same for normal or shear stresses (both applied or residual). Thus the analysis and interpretation of residual stresses is critical in the evaluation of material performance and strength.

5.2 Determination of macro residual stresses using diffraction methods

Diffraction is a principal technique which has been used extensively to study the structure of materials [132]. Using modified diffraction techniques, macro and average micro stresses of specific phases can be determined non-destructively. X-ray diffraction is used to probe near surface regions, and neutron diffraction, due to its higher penetration, is used to determine bulk residual stresses [3].

Ignoring thermal excitation, the locations of atoms are fixed in regular arrays in crystalline solids. In an ideal crystal, the unit cell repeats in all directions forming sets of parallel infinite planes. Impinging radiation scatters from these planes to produce constructive interference at definite angles. The orientation of a set of crystal planes is identified relative to the crystal axes by the Miller indices (*hkl*), and a corresponding interplanar spacing of the (*hkl*) planes is written as d^{hkl}. The beam that scatters from the adjacent planes give rise to constructive interference if the path difference between successive reflected rays is equal to integer multiples of the wavelength, $n\lambda = 2d^{hkl}\sin\theta$, where the incidence angle θ is known as the Bragg angle. In a real three dimensional crystal, allowed reflections are further limited by structure factors [1]. For planes with non-zero structure factors, Bragg's equation

$$d^{hkl} = \frac{\lambda}{2\sin\theta}, \tag{5.1}$$

is used to determine the interplanar spacing of diffracting planes d^{hkl}, if monochromatic radiation of known wavelength λ is used. If the unstressed lattice spacing d_0^{hkl} is known, the linear strain in the corresponding directions planes can be calculated from the shift, $\Delta\theta$, of the Bragg angle θ,

$$\varepsilon^{hkl} = \frac{d^{hkl} - d_0^{hkl}}{d_0^{hkl}} = \frac{\Delta d^{hkl}}{d_0^{hkl}} = -\cot\theta\Delta\theta\,. \tag{5.2}$$

A typical diffraction geometry and the definition of the specimen coordinate system S_i and the laboratory coordinate system L_i are shown in Figure 5-2. In the specimen coordinate system S_i, S_1 and S_2 lie on the sample surface, and S_3 lies along the surface normal. In the laboratory coordinate system L_i, L_3 is along the (*hkl*) crystal plane normal, and is tilted with an angle of ψ with respect to S_3. L_2 is in the sample surface plane making an angle of ϕ with the S_2 axis. In this setup, tilt and azimuthal angles, ψ and ϕ, are used to align the sample in different directions. For each orientation different crystal grains are in the diffraction condition. The linear lattice strain measured for a particular (ψ,ϕ) direction is the normal component of the tensor strain along the diffracting plane at the measurement point. Complete determination of the strain tensor, and the determination of stress, at a point requires

at least six independent measurements. Theoretically, this can be achieved by measuring the six strain components in different (ψ,ϕ) directions at the same point.

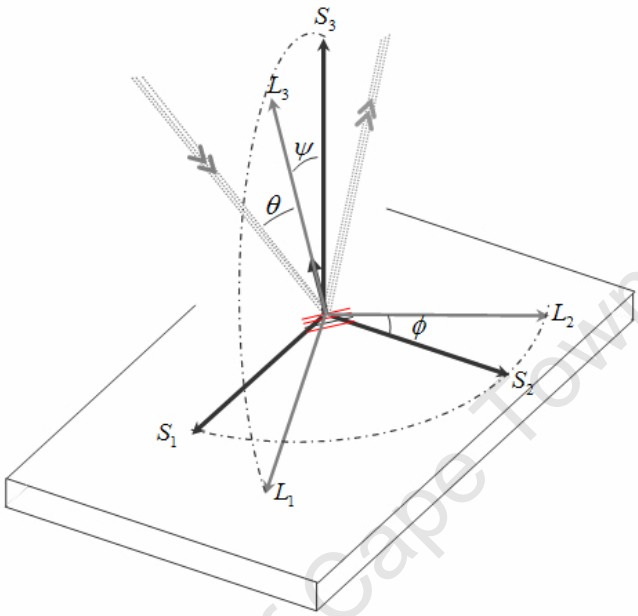

Figure 5-2 Definitions of laboratory reference frame L_i and specimen reference frame S_i in a different experiment. Diffracting crystal planes and the Bragg angle θ are shown.

The measured linear strain along L_3 is

$$(\varepsilon'_{33})_{\phi\psi} = \frac{d_{\phi\psi} - d_0}{d_0}, \tag{5.3}$$

where d_0 is the unstressed lattice spacing of the planes in diffraction condition. Primed quantities are defined in the laboratory reference frame according to the convention of reference [133]. $(\varepsilon'_{33})_{\phi\psi}$ can be written in the specimen coordinate system using the second order tensor transformation

$$(\varepsilon'_{33})_{\phi\psi} = a_{3k}a_{3l}\varepsilon_{kl}, \tag{5.4}$$

where a_{3k} and a_{3l} are the direction cosines between L_3 and S_k, S_l respectively. The direction cosine matrix a_{ik} is given by

$$a_{ik} = \begin{pmatrix} \cos\phi\cos\psi & \sin\phi\cos\psi & -\sin\psi \\ -\sin\phi & \cos\phi & 0 \\ \cos\phi\sin\psi & \sin\phi\sin\psi & \cos\psi \end{pmatrix}. \tag{5.5}$$

Substituting (5.5) in (5.4),the fundamental equation of x-ray strain determination [1] is obtained

$$\begin{aligned} (\varepsilon'_{33})_{\phi\psi} &= \varepsilon_{11}\cos^2\phi\sin^2\psi + \varepsilon_{12}\sin 2\phi\sin^2\psi + \varepsilon_{22}\sin^2\phi\sin^2\psi + \varepsilon_{33}\cos^2\psi \\ &\quad + \varepsilon_{13}\cos\phi\sin 2\psi + \varepsilon_{23}\sin\phi\sin 2\psi. \end{aligned} \tag{5.6}$$

Grouping equation (5.6) in terms of $\sin\psi$, the form

$$\begin{aligned} (\varepsilon'_{33})_{\phi\psi} &= (\varepsilon_{11}\cos^2\phi + \varepsilon_{12}\sin 2\phi + \varepsilon_{22}\sin^2\phi - \varepsilon_{33})\sin^2\psi \\ &\quad + (\varepsilon_{13}\cos\phi + \varepsilon_{23}\sin\phi)\sin 2\psi \\ &\quad + \varepsilon_{33} \end{aligned} \tag{5.7}$$

is obtained.

Using Hooke's law (2.65), stress components σ_{ij} can be obtained from the strain components ε_{ij}

$$(\varepsilon'_{33})_{\phi\psi} = a_{3k}a_{3l}S_{klmn}\sigma_{mn}, \tag{5.8}$$

where S_{klmn} is the elastic compliance tensor defined in the coordinate system of the specimen, which is generally not the reference frame of the crystal axes. For a general theoretical solution, the elastic compliances in the specimen reference frame should be obtained by the fourth order tensor transformation from crystal coordinate system to the specimen coordinate system. However, since diffraction measurements give an average strain over all illuminated grains, and polycrystalline samples with sufficiently many randomly oriented grains can be assumed isotropic [1], either average x-ray elastic constants, s_1^{hkl} and $\frac{1}{2}s_2^{hkl}$, or the isotropic elastic compliances, E and υ can be used. For a genuinely isotropic material,

$$\begin{aligned} s_1^{hkl} &= -\frac{\upsilon}{E}, \\ \frac{1}{2}s_2^{hkl} &= \frac{1+\upsilon}{E}. \end{aligned} \tag{5.9}$$

Thus, equation (5.7) can be written as either

$$\begin{aligned}\left(\varepsilon'_{33}\right)_{\phi\psi} &= \frac{1+\upsilon}{E}\left(\sigma_{11}\cos^2\phi+\sigma_{12}\sin 2\phi+\sigma_{22}\sin^2\phi-\sigma_{33}\right)\sin^2\psi \\ &+\frac{1+\upsilon}{E}\left(\sigma_{13}\cos\phi+\sigma_{23}\sin\phi\right)\sin 2\psi \\ &+\frac{1+\upsilon}{E}\sigma_{33}-\frac{\upsilon}{E}(\sigma_{11}+\sigma_{22}+\sigma_{33}).\end{aligned} \tag{5.10}$$

or, using the X-ray elastic constants, as

$$\begin{aligned}\left(\varepsilon'_{33}\right)_{\phi\psi} &= \frac{1}{2}s_2^{hkl}\left(\sigma_{11}\cos^2\phi+\sigma_{12}\sin 2\phi+\sigma_{22}\sin^2\phi-\sigma_{33}\right)\sin^2\psi \\ &+\frac{1}{2}s_2^{hkl}\left(\sigma_{13}\cos\phi+\sigma_{23}\sin\phi\right)\sin 2\psi \\ &+\frac{1}{2}s_2^{hkl}\sigma_{33}+s_1^{hkl}(\sigma_{11}+\sigma_{22}+\sigma_{33}).\end{aligned} \tag{5.11}$$

The fundamental equation (5.11) relates one component of the strain tensor ε'_{33} defined in the laboratory coordinate system, to the six components of the stress tensor defined in the sample coordinate system.

5.3 Visual analysis of the $\sin^2\psi$ curves

The $\sin^2\psi$ method depends on the functional dependence of the fundamental equation on the tilt and azimuth angles. Equation (5.11) can be rewritten as a function of the tilt angle ψ as

$$\varepsilon'_{\psi} = A\sin^2\psi + B\sin 2\psi + C\,, \tag{5.12}$$

where

$$A = \frac{1}{2}s_2^{hkl}\left(\sigma_{11}\cos^2\phi+\sigma_{12}\sin 2\phi+\sigma_{22}\sin^2\phi-\sigma_{33}\right), \tag{5.13}$$

$$B = \frac{1}{2}s_2^{hkl}\left(\sigma_{13}\cos\phi+\sigma_{23}\sin\phi\right), \text{ and} \tag{5.14}$$

$$C = \frac{1}{2}s_2^{hkl}\sigma_{33}+s_1^{hkl}(\sigma_{11}+\sigma_{22}+\sigma_{33})\,. \tag{5.15}$$

For stress determination near the surface of a sample using shallowly penetrating x-rays, all stress components along the sample surface normal, x_3, may be set to zero using the boundary condition of force at the free surface

$$\sigma_{i3} = 0\,. \tag{5.16}$$

In this case the assumed stress is bi-axial, and $B = 0$ in equation (5.12). Renaming the $\sigma_{11}\cos^2\phi + \sigma_{12}\sin 2\phi + \sigma_{22}\sin^2\phi$ term as σ_ϕ, equation (5.11) is reduced to

$$\varepsilon'_\psi = \frac{1}{2}s_2^{hkl}\sigma_\phi \sin^2\psi + s_1^{hkl}(\sigma_{11} + \sigma_{22}), \tag{5.17}$$

where σ_ϕ is the bi-axial stress. By measuring ε'_ψ for a number of tilt angles, the bi-axial stress, σ_ϕ, can be obtained from the slope of the ε'_ψ vs. $\sin^2\psi$ graph, if the plot is linear. This bi-axial stress determination has found wide application for the determination of surface stresses [1, 3, 132].

It is important to note that σ_ϕ is obtained as a scalar quantity using this method.

According to the classification of data types in section 3, the bi-axial stress σ_ϕ can be classified as E_P^S to indicate that σ_ϕ is a scalar defined at a particular point. However, it is worthwhile to mention that this stress value is not actually obtained precisely at a single point using diffraction methods, but is calculated from the measured strain which is an average over the illuminated diffraction volume. To be precise, the data to be visualized should be classified as $E_{[2]}^S$ to show that the stress value is an average over the measurement surface. In the next section the implications of the tensor to scalar reduction, and the physical features of the stress tensors leading to various $\sin^2\psi$ curves are described.

5.3.1 Flat $\sin^2\psi$ curve

In the case of a flat $\sin^2\psi$ curve, such as the one shown in Figure 5-3 for the metallic matrix of copper containing krypton nanoparticles [134], the constants A and B in equation (5.12) are both zero. $B = 0$ requires the absence of σ_{13} and σ_{23} terms. $A = 0$ requires $\sigma_{11} = \sigma_{33}$ for $\phi = 0$, and $\sigma_{22} = \sigma_{33}$ for $\phi = \frac{\pi}{2}$, *i.e.* $\sigma_{11} = \sigma_{22} = \sigma_{33}$ – the hydrostatic stress state. In hydrostatic stress, the normal stress components are equal

to each other and the shear components are zero. Thus the stress state can be defined with one scalar quantity instead of the tensor, as the hydrostatic stress $\sigma_H = 3\sigma_{11}$.

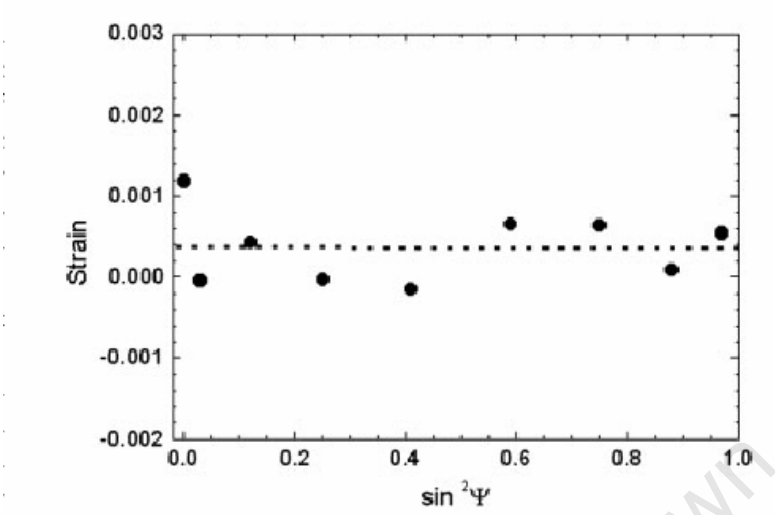

Figure 5-3 $\sin^2\psi$ curve for the (111) peak of a copper matrix containing the precipitates [134].

The hydrostatic stress tensor at a point can be visualized using the point icons developed for the representation of tensor stresses. In Table 5-1, the hydrostatic stress tensor is visualized using an eigenicon (stress ellipsoid), traction-based icons (Reynolds icon, HWY icon), the stress quadric icon, and the PNS icon. The tensor entity to be visualized is shown on the left and the corresponding icons are shown on the right hand side. All the stress icons essentially reflect the isotropic and scalar character of the stress state. The visual icons take the form of the only 3–D isotropic shape, the sphere, except the HWY shear icon, which shrinks to a point indicating the absence of shear stresses. Two possible types of hydrostatic stress, compression and tension, are differentiated using the colour coding of the PNS icon.

<table>
<tr><td rowspan="4">Hydrostatic stress state

Entity: $E_P^{T_{33}}$
(P indicates that the stress is measured at a point.)

$\sigma_H = \begin{pmatrix} \sigma & 0 & 0 \\ & \sigma & 0 \\ & & \sigma \end{pmatrix}$</td><td>Lamé ellipsoid,
Reynolds icon,
Stress quadric icon</td><td> 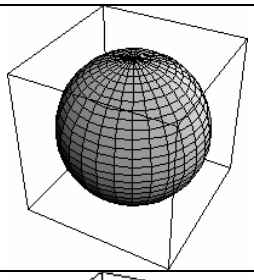 </td></tr>
<tr><td>HWY shear icon</td><td> 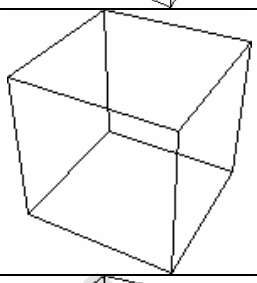 </td></tr>
<tr><td>PNS icon for $\sigma > 0$
(blue colour denotes tension)</td><td> 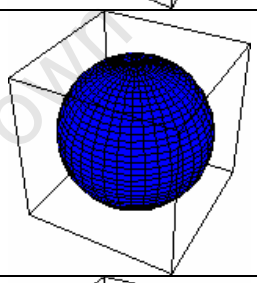 </td></tr>
<tr><td>PNS icon for $\sigma < 0$
(red colour denotes compression)</td><td> 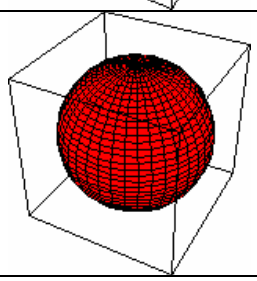 </td></tr>
</table>

Table 5-1 Visualization of the hydrostatic stress state σ_H .

5.3.2 Linearly sloping $\sin^2\psi$ curve

The plot of ε'_ψ vs. $\sin^2\psi$ of equation (5.12) results in a linear dependence if $B = 0$, *i.e.* in the absence of σ_{13} and σ_{23} components of the stress tensor. Physically, these components can be zero due to cylindrical symmetry of the stress state along the x_3 axial direction [3]. Another physical situation where σ_{13} and σ_{23} are zero is the bi-axial stress described above. In this case, not only are σ_{13} and σ_{23} zero, but all $\sigma_{i3} = 0$, *i.e.* all normal components of the stress tensor along the surface normal are

zero. Therefore, a linear $\sin^2\psi$ plot indicates either (a) a cylindrically symmetric tri-axial stress state, or (b) a biaxial stress state.

For the case of a cylindrically symmetric tri-axial stress, a theoretical example of which is shown in Figure 5-4, equation (5.11) is in the form

$$\begin{aligned}\left(\varepsilon'_{33}\right)_{\psi} &= \frac{1}{2}s_2^{hkl}\left(\sigma_{\phi}-\sigma_{33}\right)\sin^2\psi \\ &+\frac{1}{2}s_2^{hkl}\sigma_{33}+s_1^{hkl}(2\sigma_{\phi}+\sigma_{33}),\end{aligned} \tag{5.18}$$

and the corresponding stress tensor is

$$\boldsymbol{\sigma} = \begin{pmatrix} \sigma_{\phi} & 0 & 0 \\ & \sigma_{\phi} & 0 \\ & & \sigma_{33} \end{pmatrix}. \tag{5.19}$$

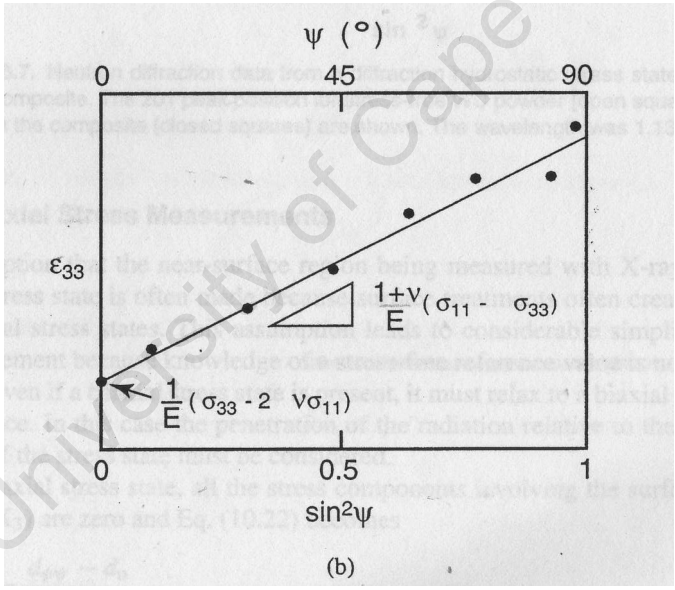

Figure 5-4 A $\sin^2\psi$ curve for a cylindrically symmetric stress state, $\sigma_{11}=\sigma_{22}=\sigma_{\phi}$ [3].

For the bi-axial case, the fundamental equation is in the form

$$\left(\varepsilon'_{33}\right)_{\phi\psi} = \frac{1}{2} s_2^{hkl} \left(\sigma_{11}\cos^2\phi + \sigma_{12}\sin 2\phi + \sigma_{22}\sin^2\phi\right)\sin^2\psi + s_1^{hkl}(\sigma_{11}+\sigma_{22}), \tag{5.20}$$

and the corresponding stress tensor is

$$\boldsymbol{\sigma} = \begin{pmatrix} \sigma_{11} & \sigma_{12} & 0 \\ & \sigma_{22} & 0 \\ & & 0 \end{pmatrix}. \tag{5.21}$$

An example is shown in Figure 5-5 [135] below for the determination of residual stress in a thin polycrystalline diamond film using X-ray diffraction.

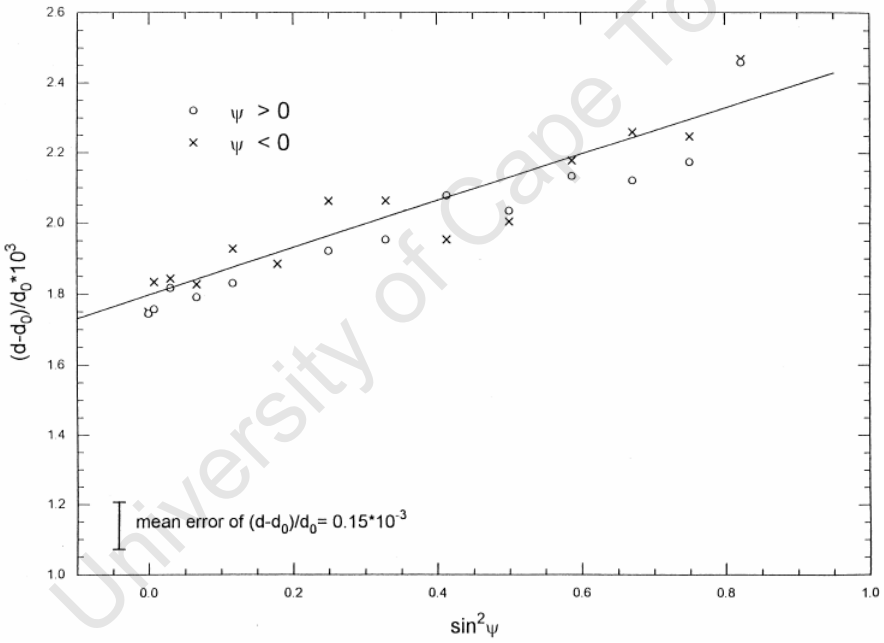

Figure 5-5 A typical linear $\sin^2\psi$ curve obtained by x-ray diffraction for the (331) reflection from a CVD diamond film grown on aluminium [135]. The measured stress is bi-axial in-plane stress.

The ambiguity of the representation of the underlying stress state resulting in linear $\sin^2\psi$ plots can be avoided using scientific visualization. Furthermore the visual stress icons can be used to differentiate between the various forms of the bi-axial and cylindrically symmetric tri-axial stresses, depending on the numerical values of the stress tensor components. These cases are illustrated in Table 5-2 and Table 5-3. In

these examples, the shear component σ_{12} is assumed to be zero without loss of generality.

In Table 5-2, two different bi-axial stress states are shown: (a) $\sigma_{11} > \sigma_{22} > 0$, and (b) $\sigma_{11} > 0 > \sigma_{22}$. In case (a) both components are greater than zero indicating tensile principal stresses. In case (b) the simultaneous presence of tensile (σ_{11}) and compressive (σ_{22}) principal stresses creates pure shear along a direction between the principal stresses. The Lamé stress ellipsoid for the bi-axial stress state is a planar ellipse, with its semi axes oriented along the principal stresses. Note that, however, visual cues of the stress ellipsoids do not differentiate between the cases of positive and negative. In the PNS icon, the colour coded ellipsoid, indicates the change from a tensile stress to compressive using the colour coding. Blue colour around the PNS icon in case (a) indicates presence of all tensile stresses in the plane, and for case (b) the red colour along the x_2 direction indicates compressive stresses, and blue colour along x_1 indicates the tensile principal stresses. In between the tensile and compressive stresses, as the colour turns from blue to red, there is a green band that indicates pure shear stresses.

Bi-axial stresses Entity: $E_P^{T_{22}}$	$\boldsymbol{\sigma} = \begin{pmatrix} \sigma_{11} & 0 & 0 \\ & \sigma_{22} & 0 \\ & & 0 \end{pmatrix}, \sigma_{11} > \sigma_{22} > 0$	$\boldsymbol{\sigma} = \begin{pmatrix} \sigma_{11} & 0 & 0 \\ & \sigma_{22} & 0 \\ & & 0 \end{pmatrix}, \sigma_{11} > 0 > \sigma_{22}$
Lamé ellipsoid	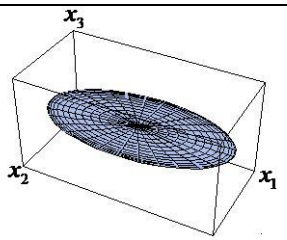	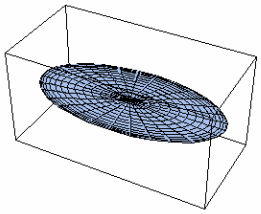
Reynolds icon	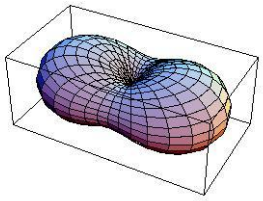	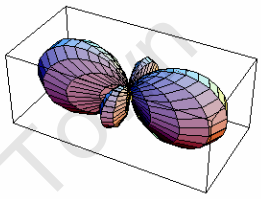
HWY shear icon	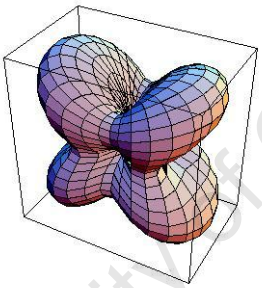	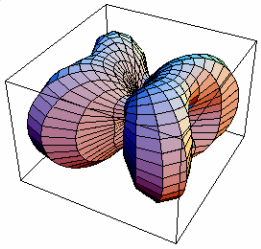
Stress quadric icon	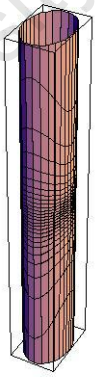	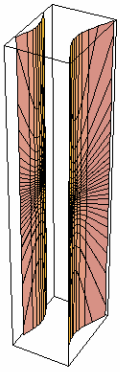
PNS icon	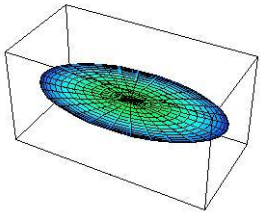	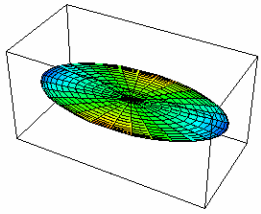

(a) (b)

Table 5-2 Visual representations of bi-axial stress states resulting in a linear $\sin^2 \psi$ curve.

The Reynolds stress icon (Table 5-2) shows the distribution of normal stresses in all directions in 3–D space, therefore the principal axes of the icon are oriented along x_1 and x_2 directions. The principal directions are the maximum normal stress directions. The peanut shape of Reynolds icon changes to a double-lobed shape in the case of negative principal stress. Note that in this stress tensor, the normal stress vanishes at a definite direction between the tensile and compressive principal stresses. Along this direction in space, there is no normal stress, leaving only pure shear stress. The maximum shear direction, which is always 45° degrees between the principal stresses is generally not the direction of the pure shear stress.

The HWY icon (Table 5-2) shows the shear stress distribution in 3–D. Thus the maximum and zero shear stress directions can be read from the HWY icon. The zero shear stresses are along the principal directions, and maximum shear stresses at exactly at the bisector of the principal stresses. Pure shear stress directions cannot be seen from the HWY icon. For the discussion of *pure* and *maximum* shear stresses for bi-axial stresses using the Mohr circle, see also section 4.3.2, page 90.

The stress quadric icon is an elliptical prism for the tensile bi-axial stress tensor (Table 5-2a). It is not a closed surface because the normal stress along the x_3 axis is zero, thus making the surface, parallel to this axis. The stress quadric figures are clipped to show the open surface. It can be seen that the smaller axis of the elliptical cross section is along the direction of the larger principal stress. This feature of the stress quadric, which might be misleading for visualizations, was discussed before when the icon was introduced (section 4.3.5). For case (b), the surface not only fails to converge along the x_3 axis, but it diverges along the pure shear direction where the normal stress is zero. It is interesting to note that the change of the 3–D shape from closed to hyperbolic surfaces makes a dramatic effect, highlighting the change of the underlying stress state from tensile to tensile/compressive.

In this example, the change of shape extension in the stress quadric and the Reynolds icon both convey the pure shear character of the stress state, better than for example,

the colour coding of the PNS icon. It was mentioned earlier that the colour extension has lower perceptual accuracy than the shape extension.

The other case which also results in a linear $\sin^2\psi$ plot is the cylindrically symmetric tri-axial stress state, where $\sigma_{11} = \sigma_{22} = \sigma_\phi \neq \sigma_{33}$. Two stress states giving rise to cylindrical symmetry are presented in Table 5-3. In spite of the relative complexity of the three dimensional stress states, the perception of the three-dimensional icons enables the understanding of the stress state effectively. Also compare the representational complexity of bi-axial and tri-axial stresses using the Mohr circle representation (section 4.3.2).

In Table 5-3a, a cylindrically symmetric stress state with all tensile principal stresses is visualized. The azimuthal symmetry is manifested in all stress icons. The Lamé ellipsoid and the Reynolds icon indicate that the principal stress along x_3 is larger than the principal stresses along x_1 and x_2. The HWY icon shows that the shear stresses vanish on the $x_1 - x_2$ plane in all directions due to the symmetry. The stress quadric is a closed surface, an ellipsoid, indicating there is no *pure* shear stress direction. The colouring on the PNS icon indicates that the stress is tensile in all directions. However, the slightly pink bands, above and below the equator of the icon, indicates a small angle between the traction and the direction vector in these directions. In these directions there exist both normal and shear stresses.

In Table 5-3b, another cylindrically symmetric stress state, with compressive principal stress along the x_3 axis, and tensile principal stresses along x_1 and x_2 axes, is presented. In this representation, the Lamé ellipsoid does not differentiate the compressive stresses from the tensile stress. The 3–D shape of the HWY icon does not change indicating that the shear stress magnitudes remain the same in all directions. However the concurrent presence of tensile and compressive stresses is evident from the other three icons: the double-lobed Reynolds icon, the diverging stress quadric icon, and from the colour coding of the PNS icon.

The Reynolds icon, with a dumbbell shape and an equatorial disc, indicates the presence of tensile/compressive pairs. However there is no visual cue to indicate

which directions are the tensile and compressive principal stresses. On the other hand, the PNS icon shows the principal stress directions, indicating that the σ_{33} is compressive by the red colouring on the poles of the ellipsoid, and the tensile stress $\sigma_{11} = \sigma_{22} = \sigma_{\phi}$ is shown using the blue colour on the equatorial plane. The bands of colour between the equatorial plane and the poles indicate that the traction and the direction normal are not aligned in the same direction. Particularly, the green band indicates pure shear stress, where the traction and direction vector are perpendicular.

tri-axial Entity: $E_P^{T_{33}}$	$\boldsymbol{\sigma} = \begin{pmatrix} \sigma_\phi & 0 & 0 \\ & \sigma_\phi & 0 \\ & & \sigma_{33} \end{pmatrix}, \sigma_{33} > \sigma_\phi > 0$	$\boldsymbol{\sigma} = \begin{pmatrix} \sigma_\phi & 0 & 0 \\ & \sigma_\phi & 0 \\ & & \sigma_{33} \end{pmatrix}, \sigma_\phi > 0 > \sigma_{33}$
Lamé ellipsoid	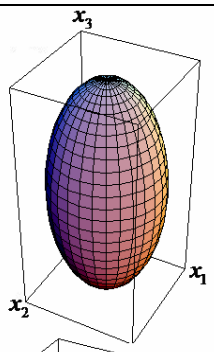	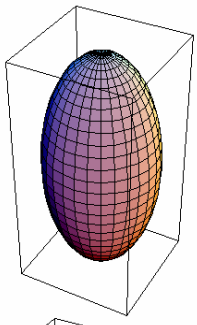
Reynolds icon	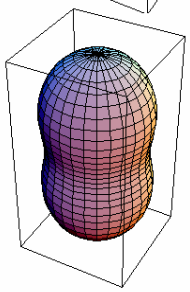	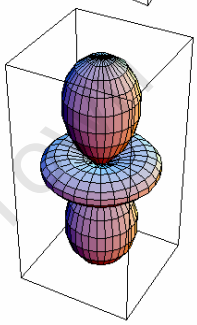
HWY shear icon	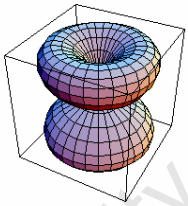	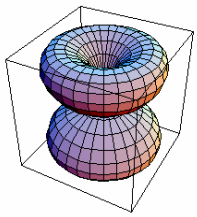
Stress quadric icon	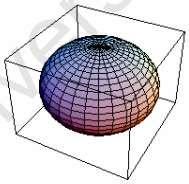	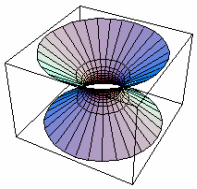
PNS icon	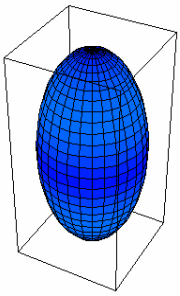	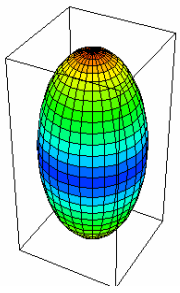
	(a)	(b)

Table 5-3 Visual representations of tri-axial stress states resulting in a linear $\sin^2 \psi$ curve.

5.3.3 $\psi-$splitting

In the previous section, it was argued that, on the specimen surface, $\sigma_{i3}=0$ because of the boundary conditions. Below the surface, in the near surface region, the σ_{i3} components of the stress tensor may not be zero. This will be the case if there is a stress gradient in the near surface region. Therefore, diffraction measurements in the near surface region where σ_{13} and σ_{23} are non-zero, will not result in a linear $\sin^2\psi$ plot. Since the σ_{13} and σ_{23} terms in the fundamental equation are factors of the $\sin 2\psi$ term, measurements of ε'_{ψ} using positive and negative tilt angles will result in different readings. This difference, due to the term $\pm B\sin 2\psi$ in the fundamental equation (5.12), results in the splitting of the $\sin^2\psi$ curve, known as $\psi-$splitting. A typical $\psi-$splitting case is shown in Figure 5-6, for the (211) reflection of a ground steel specimen [133].

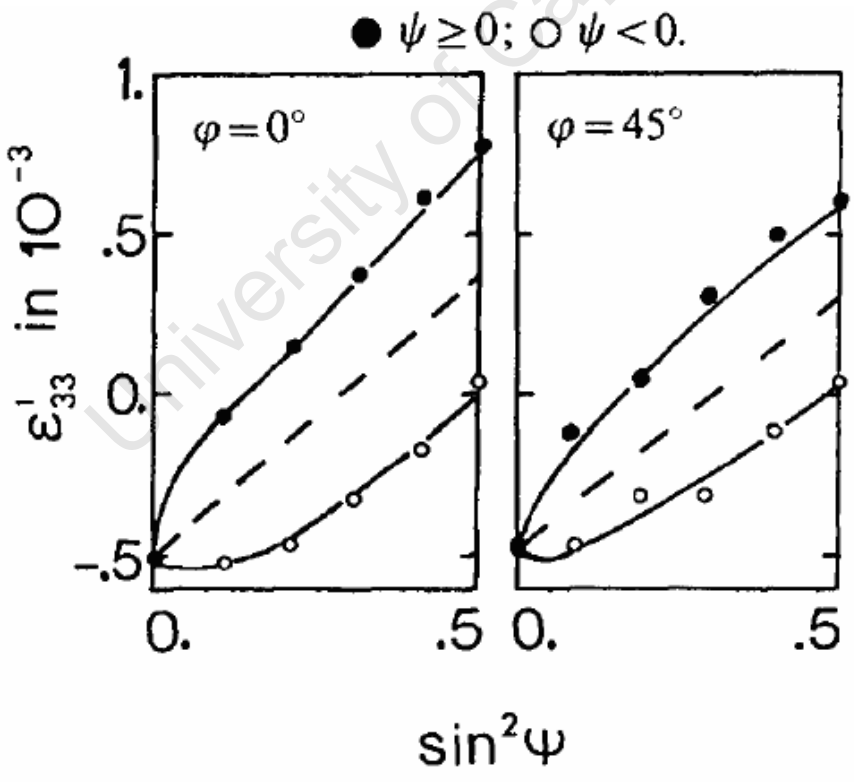

Figure 5-6 $\psi-$splitting is shown for the (211) reflection of ground steel [133].

Since at the surface, the boundary conditions $\sigma_{i3} = 0$ holds, the presence of σ_{13} and σ_{23} in the irradiated volume indicates a stress gradient for these components. Using the compability equation

$$\frac{\partial \sigma_{13}}{\partial x_1} + \frac{\partial \sigma_{23}}{\partial x_2} + \frac{\partial \sigma_{33}}{\partial x_3} = 0, \tag{5.22}$$

the non-zero $\frac{\partial \sigma_{13}}{\partial x_1} + \frac{\partial \sigma_{23}}{\partial x_2}$ term shows that $\frac{\partial \sigma_{33}}{\partial x_3}$ must also be finite. Thus $\psi-$splitting in the $\sin^2\psi$ curves indicates tri-axial stresses. This is also evident from the diagonalization of the stress tensor

$$\boldsymbol{\sigma} = \begin{pmatrix} \sigma_{11} & \sigma_{12} & \sigma_{13} \\ & \sigma_{22} & \sigma_{23} \\ & & 0 \end{pmatrix}, \tag{5.23}$$

with a $\sigma_{33} = 0$ term. The presence of the σ_{13} and σ_{23} terms results in the tri-axial stress state

$$\boldsymbol{\sigma}' = \begin{pmatrix} \sigma'_{11} & 0 & 0 \\ & \sigma'_{22} & 0 \\ & & \sigma'_{33} \end{pmatrix}. \tag{5.24}$$

This case is visualized Table 5-4. The presence of shear components σ_{13} and σ_{23} in the stress tensor re-orient the stress icons so that their principal axes are not along the coordinate system axes x_i. Despite the fact that $\sigma_{33} = 0$ in the original stress tensor, the diagonalized stress tensor has three non-zero principal stresses, and consequently the stress icons are all three dimensional indicating a tri-axial stress state. The diverging stress quadric icon reveals the presence of both tensile and compressive principal stresses in the diagonalized stress tensor. The presence of tensile and compressive stresses cannot be seen clearly from the Reynolds icons, due to the fact

that σ'_{33} term is relatively small. Both the tri-axiality and the type of stresses, *i.e.* tensile stresses (blue) and the compressive stress (red) can be read from the PNS icon.

tri-axial stress Entity: $E_P^{T_{33}}$	$\begin{pmatrix} \sigma_{11} & \sigma_{12} & \sigma_{13} \\ & \sigma_{22} & \sigma_{23} \\ & & 0 \end{pmatrix} \rightarrow \begin{pmatrix} \sigma'_{11} & & \\ & \sigma'_{22} & \\ & & \sigma'_{33} \end{pmatrix}$ $\mathrm{Sgn}[\sigma'_{11}] = \mathrm{Sgn}[\sigma'_{22}] \neq \mathrm{Sgn}[\sigma'_{33}]$
Lamé ellipsoid	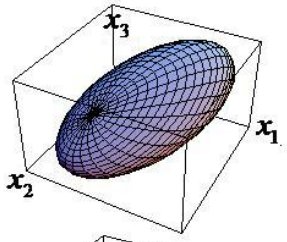
Reynolds icon	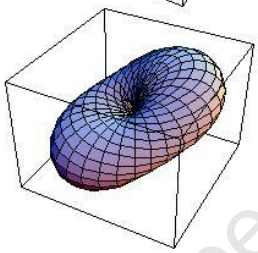
HWY shear icon	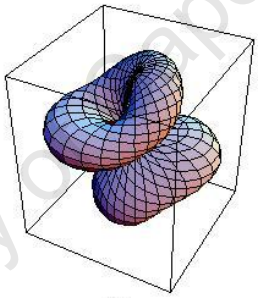
Stress quadric icon	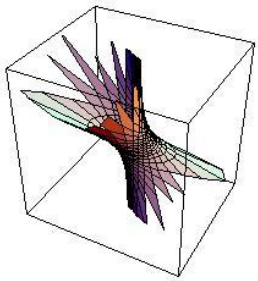
PNS icon	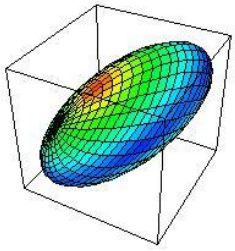

Table 5-4 The visual representations of a ψ – splitting stress state.

5.3.4 Non-linear $\sin^2\psi$ plots

The analysis of non-linear $\sin^2\psi$ plots has been discussed by various authors, see for example [1, 3, 133]. In general, the non-linear behaviour is linked with superimposition of strong gradients and shear residual stresses, texture (preferred orientation of grains), and intergranular microstresses due to plastic anisotropy. In the case of stress gradients the varying penetration depth of x-ray diffraction with the tilt angle ψ contributes to the non-linearity. An example of a typical non-linear $\sin^2\psi$ curve is shown in Figure 5-7. With regards, to visualization, at any particular point, the tensor will be tri-axial and its representations with point icons will be similar to those in the previous section.

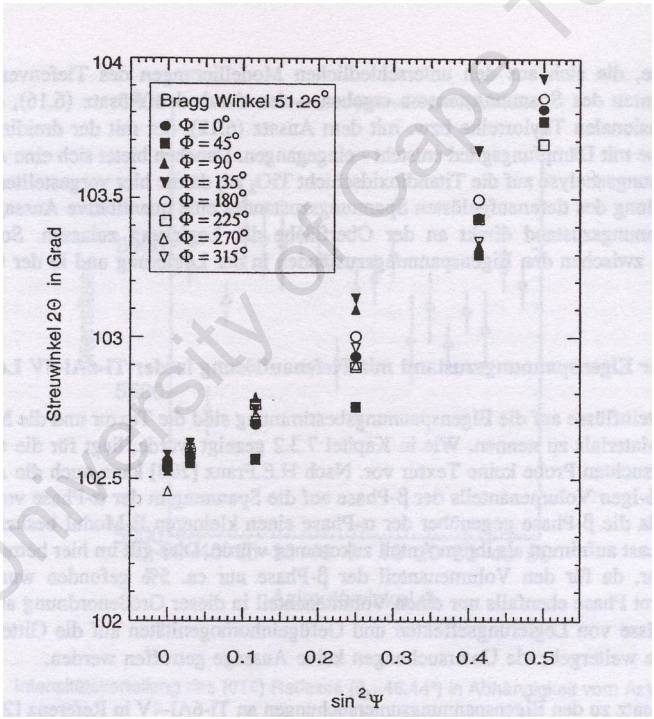

Figure 5-7 A non-linear $\sin^2\psi$ plot from a Titanium alloy; (2003) reflection measured with Cu-Kα x-ray radiation [136].

Methods are therefore required to extract the full tensor at different positions, so that these changes, in form and orientation, can be visualized. One possible approach is to obtain the depth profile of the stress state using theoretical model systems [11].

This can be done by building a model stress function to represent the stress profile in the sample. From the physical model, a mathematical model is obtained by using boundary conditions, sample symmetries and compability equations.

Penetration of x-rays and irradiated volume elements vary with the tilt ψ angles in x-ray diffraction. The penetration depth for surface impinging x-rays for the experimental set up of Figure 5-2, (page 129) is given as [1]

$$\tau_{\psi} = \frac{\sin\theta\cos\psi}{2\mu}. \tag{5.25}$$

For smaller ψ angles x-rays probe deeper, whereas higher ψ tilts irradiate mostly the surface region [10, 137]. An exponential weighting function can be used to define the contribution from various depths taking into account the attenuation of the x-rays. In this case, average convoluted strain as a function of depth can be written as

$$\left\langle \varepsilon'_{ij} \right\rangle_{\phi\theta} = \frac{\int_0^{\infty} \varepsilon'_{ij}(z) e^{-z/\tau_{\psi}} dz}{\int_0^{\infty} e^{-z/\tau_{\psi}} dz}, \tag{5.26}$$

where τ_{ψ} is the penetration depth given by (5.25).

Similarly, the depth resolution of stress is modeled using the power series

$$\sigma_{ij} = \sigma_{ij}^0 + a_{ij} z^{n_{ij}}, \tag{5.27}$$

where σ_{ij}^0 are the stress components on the surface, a_{ij} are the power series coefficients and n_{ij} are the exponents of the series terms. Because the fundamental equation of x-ray diffraction (5.11) is expressed in terms of average stresses, equation (5.27) is integrated over the whole diffraction volume

$$\left\langle \sigma_{ij} \right\rangle = \frac{\int_0^{\infty} \sigma_{ij}(z) e^{-z/\tau_{\psi}} dz}{\int_0^{\infty} e^{-z/\tau_{\psi}} dz}, \tag{5.28}$$

or

$$\left\langle \sigma_{ij} \right\rangle = \sigma_{ij}^0 + K_{ij} \tau_{\psi,\theta}^{n_{ij}}, \tag{5.29}$$

where σ_{ij}^{0} and K_{ij} are constants and $\tau_{\psi,\theta}$ is the penetration depth. Using the specimen geometry, symmetries of the stress imparting processes and elasticity theory, the number of unknown constants in the model function can be reduced [11]. Once the analytical form of the fundamental equation of x-ray diffraction is obtained as a function of the parameters σ_{ij}^{0} and K_{ij}, non-linear fit procedures can be used to fit the model function to the measured strains $\left(\varepsilon'_{33}\right)_{\phi\psi}$. For the details of the parameter determination, see for example [138 – 140]. The analysis of non-linear $\sin^2\psi$ plots and depth resolved stresses are discussed further in case studies 1 and 2.

6 Case Study 1: Scientific Visualization of Residual Stresses in Krypton Implanted Titanium

In this chapter, stress profiles of krypton ion (Kr^+) implanted titanium specimens are explored using the visual stress icons. The principles and techniques of scientific visualization are applied to facilitate understanding, representation and comparison of the different stress profiles of ion implanted specimens.

6.1 Ion implantation and residual stress analysis

In ion implantation energetic ions of a guest material, accelerated by means of a high electrical potential, are implanted into a host solid, usually a metal, to alter and improve the host material's surface properties [147]. The amount of material implanted, known as the dose, is the ion current integrated over time. The energy of the ions, ion species, and the composition of the target determine the penetration of the ions into the host solid. The ions may introduce chemical change, and due to the high energy collisions in the matrix, the crystal structure of the target can be strained, damaged, or even destroyed. In this way, ion implantation introduces a range of defects and lattice disorder, and consequently residual stress fields in the structure [148]. Although considered as a surface modification technique, the effects of ion irradiation are found to persist up to depths of 20 μm, compared to actual implantation depths of less than 0.5 μm [149].

The analysis of residual stress states encountered in ion implanted materials is often complicated. In general, the effect of ion implantation depends on dose, dose rate, implantation energy, implanted species, target material temperature and pre-existing stresses [10]. Non-destructive diffraction techniques are particularly effective in obtaining the depth profile of the stress in the irradiated near surface region.

Stress determination of the krypton implanted specimens was carried out by S. Nsengiyumva using x-ray diffraction, and was reported previously in [10,150]. In this section, for the stress analysis, firstly conventional $\sin^2\psi$ plots are shown. This is

followed by a novel 'projected strain' representation, where the uniaxial in-plane strain is shown over the penetration depth [137]. This representation reveals the depth profile of strain distributions with respect to depth and with respect to different crystallographic directions. These two methods are essentially scalar methods, and therefore, provide partial information, without reflecting the tensor character of the stress state. However, it is possible to obtain the depth profile of the tri-axial tensor components from the same diffraction dataset by using a non-linear fit of the parameters of a model stress function, as described above in section 5.3.4. The semi-numerical procedure, in this case, however, only reveals the principal stress components of the stress tensor, σ_{11}, σ_{22}, and σ_{33} due to insufficient experimental data regarding the shear components. Therefore, in this case study, the analysis of the stress states is confined to the principal components of the stress tensors.

The first step in the visualization of the tensor dataset is to show each component of the stress tensor, σ_{11}, σ_{22}, and σ_{33} vs. depth using conventional two-dimensional graphs. This representation is essentially a scalar visualization of the E_1^{3S} dataset. E_1^{3S} notation depicts three scalar quantities which are shown independently in a one dimensional domain, *i.e.* the depth. Although stress components vs. depth graphs enable the analysis of stress components; the visualization idiom (2–D graph), or the visualized entity, does not reflect the physical data type under consideration. However, in scientific visualization it is attempted to visualize the tensor features of the dataset directly using a physically based visualization mapping, *i.e.* by mapping the tensor information onto a graphic icon. For this reason, the use of point stress icons is suggested for the scientific visualization of the stress profile. The stress state is sampled at regular depths, and the corresponding stress tensor at each location is visually represented using the 3–D icons. The entity visualized in this case, $E_P^{T_{33}}$, is a tensor quantity sampled at various points. The resulting visualization are discussed and correlated with the conventional $\sin^2\psi$ curves and the "projected strain" representation, to put the visualizations in context with the conventional stress analysis methods.

6.2 Sample characterization and stress determination by x-ray diffraction

Disks with a diameter of 25 mm and thickness of 0.33 mm, cut from titanium sheet of 99.6% purity, were obtained from Goodfellow Ltd. To form thin sheets, the titanium was rolled and partially annealed by the supplier. One disk was kept as reference, and two others were implanted with 180 keV Kr^+ to total doses of 1×10^{16} and 5×10^{16} ions cm^{-2}. The dose rate was 10^{13} Kr^+ $cm^{-2}s^{-1}$ with a beam current of 1.4 μA.

X-ray stress determination was carried out with a Bruker D8 Advance diffractometer using filtered CuKα radiation at 40 mA and 40 kV. Four different reflections were used, (101) at a Bragg angle of 20.1º, (102) at 26.5º, (103) at 35.4º, (213) at 69.7º, respectively. The sample was tilted in side inclination mode, perpendicular to the scattering plane, at 10º intervals up to 70º ($\sin^2\psi$ = 0.833), and 75º, 80º, 82º, 84º, 86º, 88º, and 89º ($\sin^2\psi$ = 0.999). At high values of ψ, the beam is nearly parallel to the surface and so does not penetrate deeply, allowing near surface stresses to be probed. In contrast, at low ψ tilts the whole available range, determined by penetration depths of the X-rays in a given material and the chosen Bragg reflection, is probed. In this case only one ϕ orientation was measured. (See Figure 5-2, page 129 for the definitions of the angles ϕ and ψ).

Stress is obtained from the measured strains from Hooke's law (2.64) using the elasticity tensor C_{ijkl}. For a single crystalline material with hexagonal structure, like titanium, there are five independent elastic constants to take into account. However, in the absence of texture, the elastic response of a polycrystalline material can be described with two elastic constants, Youngs modulus *E* and the Poisson ratio υ [1]. The typical values for titanium, *E* = 120 GPa and $\upsilon = 0.36$, are used in this case. The details of the measurement procedure and results from the conventional $\sin^2\psi$ stress determination, as well as other complementary techniques are reported in an independent study [10].

6.3 Conventional $\sin^2\psi$ plots and the 'projected strain' representation

The $\sin^2\psi$ plots for the unimplanted and implanted samples are shown in Figure 6-1. For all three samples, strong curvatures at high ψ angles, where $\sin^2\psi > 0.8$, indicates a strong stress gradient between the very near surface region and deeper regions up to the maximum penetration depth. As it is not possible to assign a single slope to these $\sin^2\psi$ curves, the stress gradients in the very near surface and deeper in the samples can be determined, as a first approximation, separately by superimposing two linear curves weighted using the absorption coefficient factor [10]. For the unimplanted sample, in the deeper "bulk" region a slight negative slope of $-0.36 \pm 0.1 \times 10^{-3}$ corresponds to a compressive stress of 40 ± 10 MPa (Figure 6-1a). This compressive trend is most clear for the (102) reflection. For the very near surface, a slope of $14 \pm 1 \times 10^{-3}$ corresponds to 1.6 ± 0.1 GPa tensile stress. Although this stress value is above the single crystalline titanium yield strength, it is typical of rolled and hard-annealed metals [151].

The stress states of the implanted samples are obtained similarly. The independent study [10] highlights the increase of slope, for $\sin^2\psi > 0.4$, in Figure 6-1b, c. This indicating introduction of additional compressive stresses deeper in the samples with high dose implantation, approximately from 40 MPa to 80 MPa. The near surface stresses fall slightly to 1.2 GPa (from 1.6 GPa) for both implanted samples.

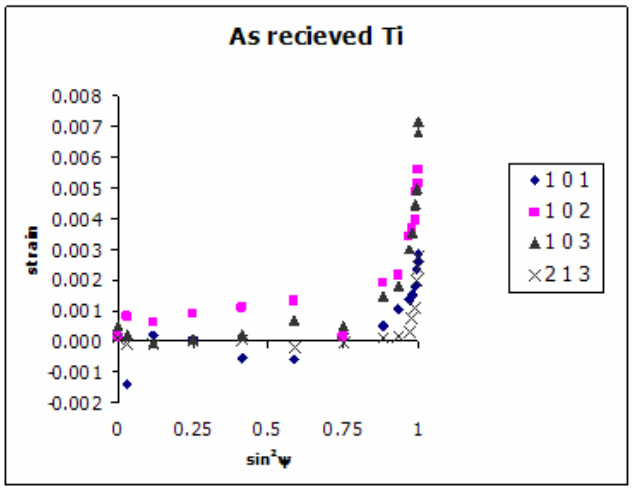

(a)

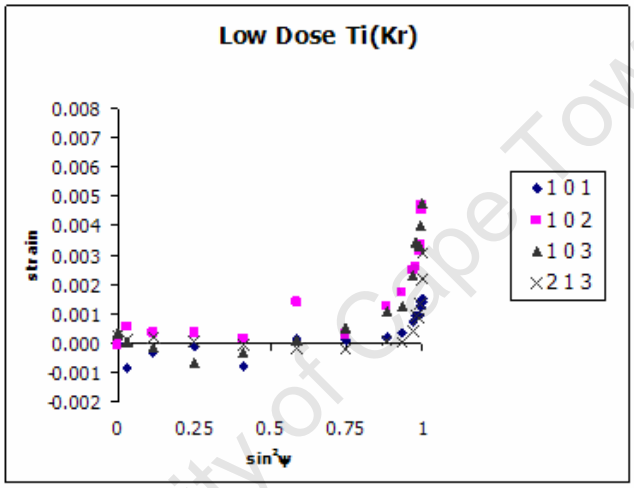

(b)

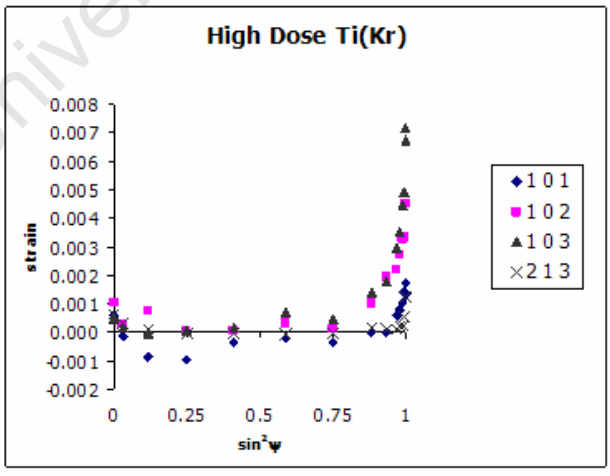

(c)

Figure 6-1 The $\sin^2\psi$ curves for four different reflections: (a) unimplanted sample; (b) low dose implantation of 1×10^{16} ions/cm^{-2}s^{-1} ; (c) high dose implantation of 5×10^{16} ions/ cm^{-2} s^{-1}.

In this case, the above conventional $\sin^2\psi$ representations may be misleading due to two reasons. Firstly, measurements from different reflections lead to different penetration depths for the same ψ tilts. Secondly, at the same ψ tilt, the strains in different crystallographic directions are probed, but in a hexagonal system like titanium, the elastic response is slightly different in different directions. To compare the same strain over the same average penetration depth, an alternative "projected strain" representation is suggested [137]. In the "projected strain" representation, the projection of the uniaxial strain $(\varepsilon_{33})_{\psi\phi}$ on the plane parallel to the sample surface is plotted as a function of the mean penetration depth (Figure 6-3). The mean penetration depth τ is calculated by applying the geometrical correction factor to the absorption length $1/\mu$

$$\tau = \frac{\cos\psi \sin\theta}{2\mu}, \tag{6.1}$$

where μ is the linear absorption coefficient, which for titanium is 912.8 cm^{-1}. To use the projection of $(\varepsilon_{33})_{\psi\phi}$ is appropriate, because $(\varepsilon_{33})_{\psi\phi}$ is actually a vector and not a tensor quantity. The vector $(\varepsilon_{33})_{\psi\phi}$ shows the relative change in length along the direction given by laboratory directions ψ and ϕ. The projection plot $(\varepsilon_{33})_{\psi\phi} \cdot \sin\psi$ allows the observation of the uniaxial strain in the same direction, *i.e.* along the sample surface as shown in Figure 6-2.

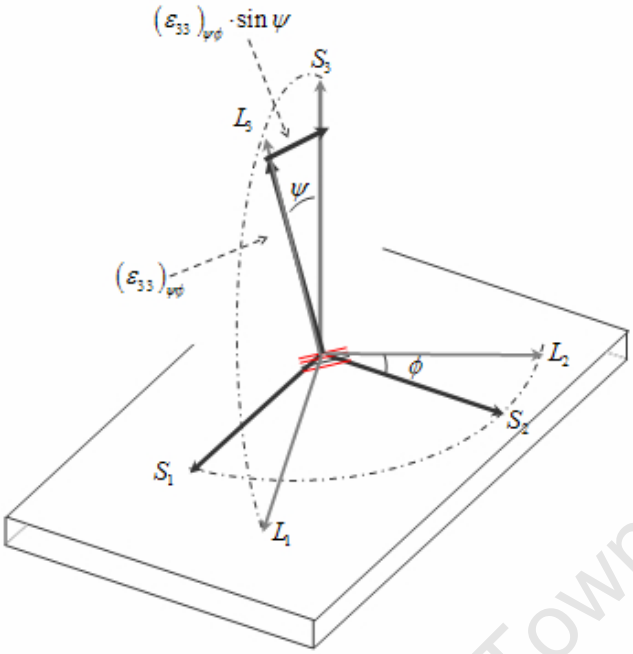

Figure 6-2 The geometric definition of the uniaxial strain projection. $(\varepsilon_{33})_{\psi\phi}\cdot\sin\psi$.

Comparing the depth behaviour of the projected uniaxial strain of the unimplanted sample (Figure 6-3a), and implanted samples (Figure 6-3b, c), the overall features are the same. The steep decrease of the tensile strain in the first micron is typical for rolled metals [151]. Deeper inside the sample, the strain is expected to reach zero because of the partial annealing. The (101) reflection, with its shallow beam incidence, yields information from a lower penetration depth, compared, for example, to the (213) reflection with a steep beam incidence. The clustering of the depth behaviour of the projected strain between the (102) and (103), and the (101) and (213) reflections is remarkable. Here, clearly the difference of the elastic responses of the crystallographic directions is manifested.

The effect of the ion implantation can be seen from the small differences between the strain distributions of the implanted sample compared to the unimplanted sample. The tensile stress of the low dose implanted sample is reduced in comparison to the unimplanted sample (Figure 6-3a, b). In addition, the unimplanted, as well as the low dose implanted samples show a change in the slope, leading to a step in the projected strain curves, between approximately 0.5 µm and 2 µm, suggesting a change in the

stress state. This behaviour is less pronounced in the low dose implanted sample and is partially masked by an increased scattering of the data. Both effects, the reduction of the strain as well as the step, point to a relaxation of the pre-existing tensile stress. In contrast, comparing the low dose implanted with the high dose implanted sample (Figure 6-3b, c), for high dose implantation the projected strain for the (101) and (213) crystallographic directions increases approximately to the values of the unimplanted sample, but the projected strain in the (102) and (103) crystallographic directions remains unchanged. However the increased strain shows a monotonic decrease with depth, with no indication of the step seen. This behaviour suggests the introduction of a new stress state with a preferred crystallographic orientation resulting from implantation introduced defects.

The information gained from the above representations is partial, because the tensor features of the stress profiles are not taken into account. More information regarding the stress profile can be obtained by determining the depth resolution of the complete stress tensors. This can be achieved using the same diffraction dataset, by applying the semi-numerical method described in section 5.3.4. In this method, the strain $(\varepsilon_{33})_{\varphi,\psi}$ obtained from each diffraction peak is considered a data point, which is used to parameterize a tri-axial model stress function with a non-linear fit procedure. Provided that an adequate number of data points is used, the full tensor stress profile with depth can be extracted. The outcome of the parameterization is six scalar functions, each one corresponding to one stress tensor component. Consequently, the full tensors can be explored using scientific visualization, once the tensor dataset is obtained.

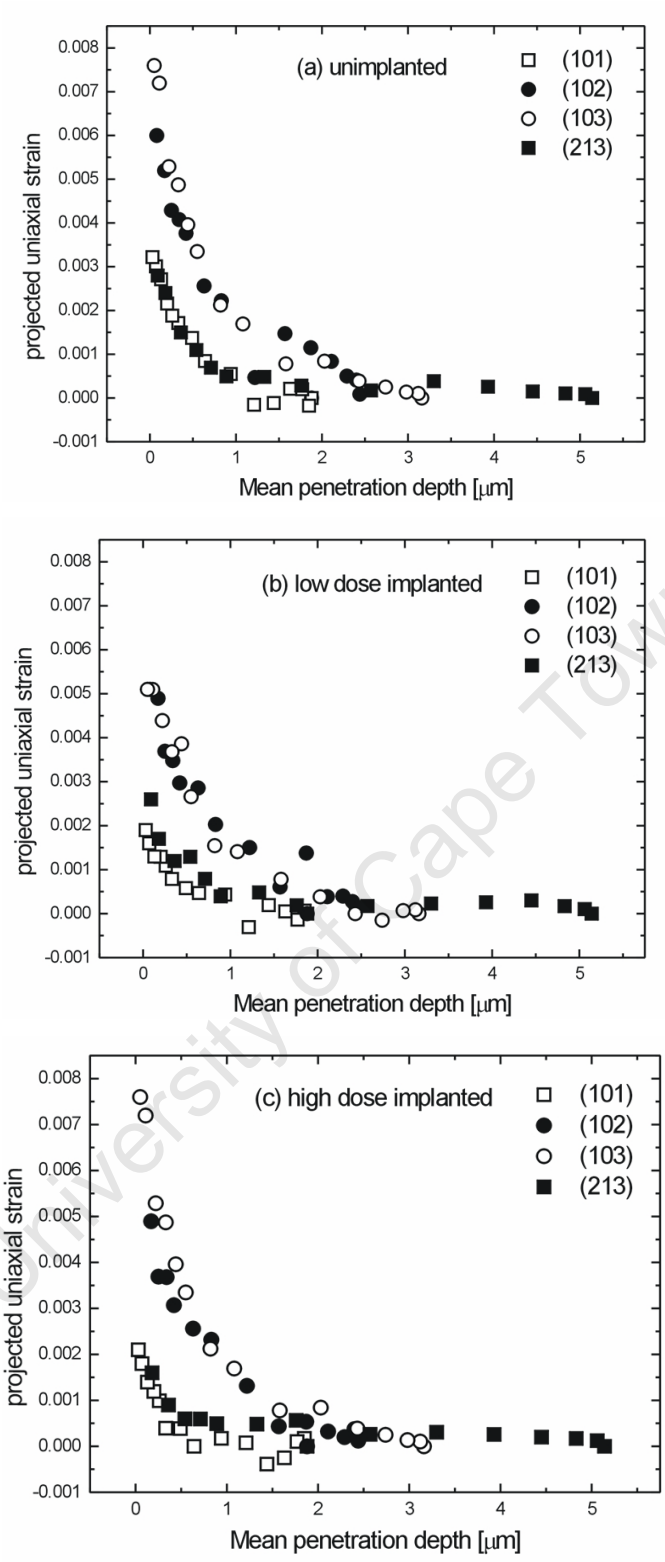

Figure 6-3 Projection of the uniaxial strain $(\varepsilon_{33})_{\varphi,\psi}$ onto the plane parallel to the sample surface vs. the mean penetration depth τ for the reflections (101), (102), (103) and (213). (a) Unimplanted titanium, (b) low dose Kr^+ implanted titanium, (c) high dose Kr^+ implanted titanium.

6.4 Depth resolution of the stress profiles

The general power series model of equations (5.27) and (5.29) described in section 5.3.4 is used to obtain the depth resolution. The functional dependence determined by Harting [11] for near surface stress states is adopted. According to Harting's model, the depth dependence of the stress tensor components is given by

$$\sigma_{ij}(z) = \sigma_{ij,0} + a_{ij}z + b_{ij}z^2 + u_{ij}z^3, \tag{6.2}$$

and the corresponding average stress tensor components integrated to penetration depth are

$$\langle \sigma_{ij} \rangle = \sigma_{ij,0} + a_{ij}\tau_{(\psi,\theta)} + 2b_{ij}\tau_{(\psi,\theta)}{}^2 + 6u_{ij}\tau_{(\psi,\theta)}{}^3, \tag{6.3}$$

where τ is the penetration depth for different ψ, θ orientations. Thus the average stress dependence with depth is obtained by fitting the integrated stress components to the different diffraction peaks. Using the surface boundary conditions, $\sigma_{3j} = 0$ and equations of equilibrium (2.36) the number of unknown coefficients is reduced to 20:

$$\begin{aligned}
\langle \sigma_{11} \rangle &= \sigma_{11,0} + a_{11}\tau_{(\psi,\theta)} + 2b_{11}\tau^2_{(\psi,\theta)} + 6u_{11}\tau^3_{(\psi,\theta)},\\
\langle \sigma_{22} \rangle &= \sigma_{22,0} + a_{22}\tau_{(\psi,\theta)} + 2b_{22}\tau^2_{(\psi,\theta)} + 6u_{22}\tau^3_{(\psi,\theta)},\\
\langle \sigma_{33} \rangle &= 2b_{33}\tau^2_{(\psi,\theta)} + 6u_{33}\tau^3_{(\psi,\theta)},\\
\langle \sigma_{12} \rangle &= \sigma_{12,0} + a_{12}\tau_{(\psi,\theta)} + 2b_{12}\tau^2_{(\psi,\theta)} + 6u_{12}\tau^3_{(\psi,\theta)},\\
\langle \sigma_{13} \rangle &= a_{13}\tau_{(\psi,\theta)} + 2b_{13}\tau^2_{(\psi,\theta)} + 6u_{13}\tau^3_{(\psi,\theta)},\\
\langle \sigma_{23} \rangle &= a_{13}\tau_{(\psi,\theta)} + 2b_{13}\tau^2_{(\psi,\theta)} + 6u_{13}\tau^3_{(\psi,\theta)}.
\end{aligned} \tag{6.4}$$

However, in this case study, diffraction measurements were only carried out for one ϕ azimuthal direction. Selecting $\phi = 0$ reduces the fundamental stress equation (5.11) to

$$\begin{aligned}
\left(\varepsilon'_{33}\right)_{\phi\psi} = &\frac{1}{2}s_2^{hkl}\left(\sigma_{11}\cos^2\phi - \sigma_{33}\right)\sin^2\psi\\
&+\frac{1}{2}s_2^{hkl}\left(\sigma_{13}\cos\phi\right)\sin 2\psi\\
&+\frac{1}{2}s_2^{hkl}\sigma_{33} + s_1^{hkl}(\sigma_{11}+\sigma_{22}+\sigma_{33}).
\end{aligned} \tag{6.5}$$

Because the two shear components σ_{12} and σ_{23} do not appear in the fundamental equation in this case, the total number of unknown coefficients reduces to 13 in

equation (6.4), also losing the shear information. The necessity of taking this step in this case study can be seen by the large standard deviations obtained with the fitted parameters. The shear components of the stress tensor are, therefore, discarded. The absence of the shear components in the stress tensor results in the alteration of the correct orientation of the principal stresses, which is discussed when the visualization results are discussed. In principle, with multiple measurements in different ϕ directions shear stresses can be also determined.

In the non-linear fit procedure a total number of 60 diffraction peaks from all four reflections are used as input. For the construction of the elasticity tensor, the isotropic elastic constants E and υ are used instead of the reflection dependent diffraction elastic constants, s_1^{hkl} and $\frac{1}{2}s_2^{hkl}$. The isotropic elastic constants E and υ are close averages of the diffraction elastic constants for titanium [152, 153] (see also Figure 6-4). *Mathematica™* software [154] is used to fit the measured strain values to the parameters of the mathematical model with a weighted non-linear Levenberg-Marquardt fit procedure [155]. The program script, measurement dataset and the diffraction elastic constants for titanium used in the fit procedure are given in Appendix 1. Typical confidence intervals are indicated by the band regions in the Figure 6-5. The resulting scalar functions for the stress components are shown in Figure 6-6.

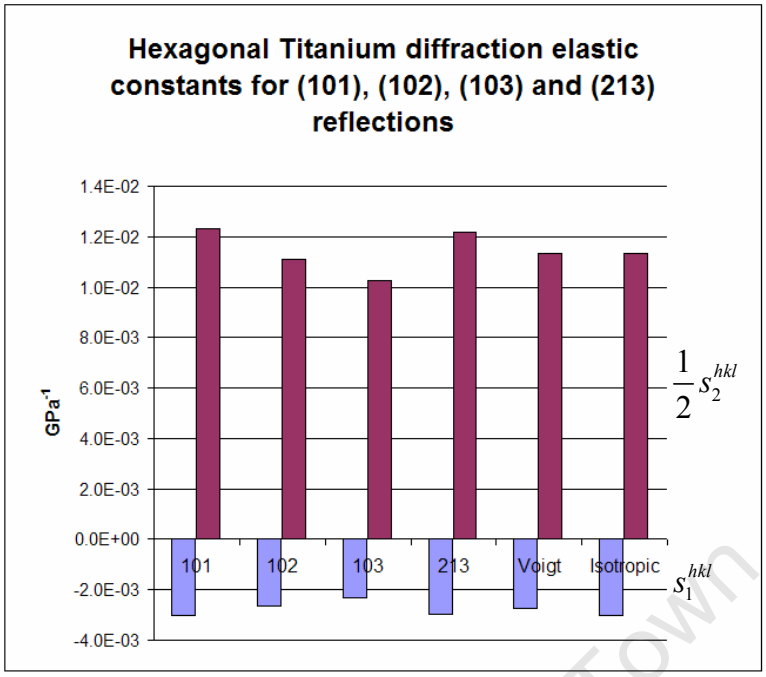

Figure 6-4 Diffraction elastic constants s_1^{hkl} and $\frac{1}{2}s_2^{hkl}$ for hexagonal titanium for (101), (102), (103) and (213) reflections for the Reuss model. Isotropic elastic constants E and υ are shown for comparison [152, 153].

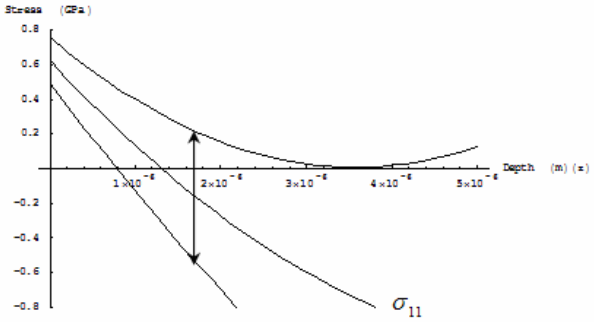

(a)

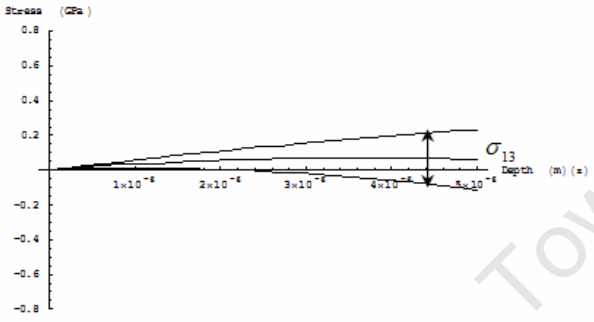

(b)

Figure 6-5 Confidence regions for (a) σ_{11} and (b) σ_{13} for the unimplanted sample. The bands indicate two standard deviation of the mean.

In Figure 6-5, the confidence regions for the stress tensor components, σ_{11} and σ_{13}, are shown using two standard deviation (**±2σ)** proximity of the expected values of the parameters. The confidence intervals are calculated using the asymptotic standard errors of the fitted parameters; in this way an upper and a lower value for the tensor components are calculated [156]. The confidence regions indicate that the fit is mostly reliable in the first 1-2 μm range. The high statistical scattering of the fitted curve is firstly due to the relatively small number of diffraction peaks used, *i.e.* in total 60 data points are used to obtain a 13 parameter model function. Secondly, the confidence region is larger for deeper regions correlating with the fact that less information is obtained in the deeper region, where it is confined to the information obtained from (103) and (213) reflections. Merely 11 of the 60 measurement points correspond to this region, as shown in the 'projected strain' visualization (Figure 6-3).

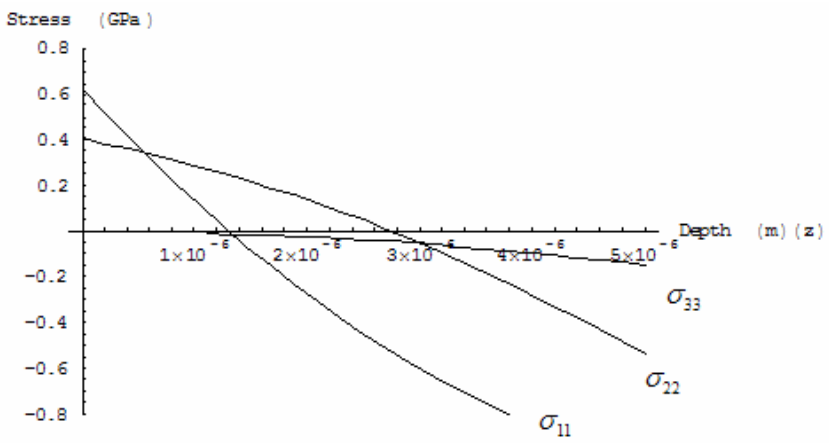

(a)

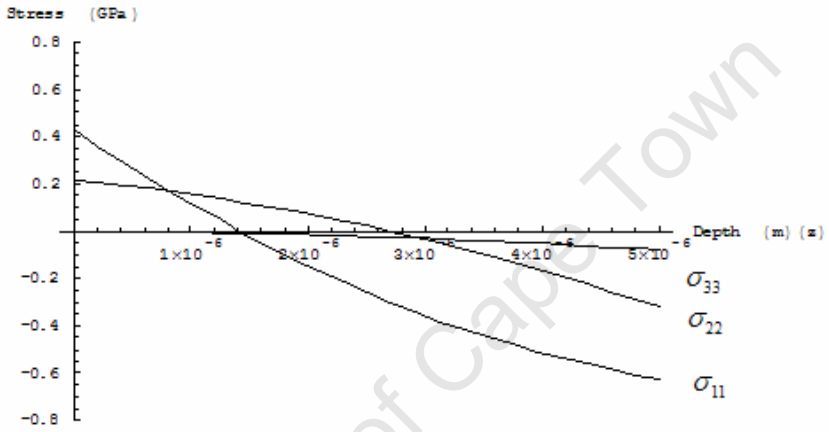

(b)

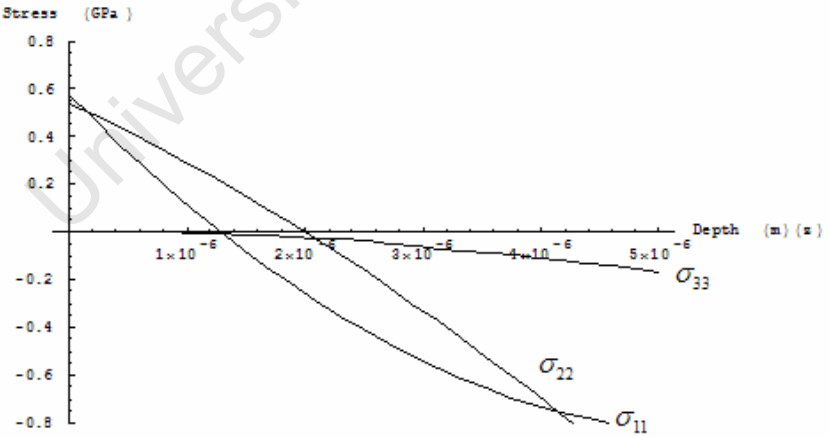

(c)

Figure 6-6 Depth profile of principal stress components for (a) as received (b) low dose (c) high dose implanted samples.

The resulting depth profile of the stress for all three samples is shown in the first 5μm in Figure 6-6. Note that the error on the stress components is relatively large for regions deeper than 2μm. Although we discuss the overall features of Figure 6-6 here, the visualizations are confined to the first 2μm hereafter.

All three samples show a strong negative stress gradient in the near surface region for the in-plane stresses (σ_{11}, σ_{22}), changing the tensile in-plane stresses to compressive stresses in the 1-3 μm depth region. In the **unimplanted sample** a high tensile surface stress (400)-(600 MPa) becomes compressive deeper in the sample. σ_{33} normal stresses are compressive and gradually increase from zero to a level of about 100 MPa deep in the material. The effect of sample history can be seen from the as received graph (Figure 6-6a): tensile in-plane stresses are possibly introduced by the rolling process, on the surface, $\sigma_{11} = 0.6$ GPa and $\sigma_{22} = 0.4$ GPa. These stresses become compressive at $z = -1\,\mu\text{m}$ and $z = -3\,\mu\text{m}$, respectively, with a strong negative gradient. The concavity (second gradient) of the in-plane stress components are different. This difference between the in-plane stress components might be attributed to the rolling process, however this should be checked with extra azimuthal ϕ direction measurements. This difference in the second gradient is later removed with implantation indicating isotropy, possibly, due to the azimuthal symmetric implantation process.

With **low dose implantation** the overall features of the principal stresses are unchanged. The magnitudes of the principal stresses decreases which is in agreement with the $\sin^2\psi$ analysis. The decrease in the tensile surface stresses is about 200 MPa and about 100 MPa for the normal stress, Figure 6-6a, b. The downward shifting of tensile stresses is expected due to the introduced compressive stresses on the surface [157]. Relaxation of the prior residual stresses has also been reported in the literature [158 -161].

Interestingly, **high dose implantation** removes the relaxation effect of low dose implantation and returns the stress state to the "as received" high stresses. However

high dose implantation results in more isotropic in-plane stresses, effectively shifting the zero value of σ_{22} towards the surface.

The above depth resolution gives quantitative results on the behaviour of the individual stress components. The individual stress components can be discussed separately, but not much can be said about the stress as a tensor. Below, a better representation of the stress depth profile is presented using the stress tensor icons.

6.5 Scientific visualization of the stress profiles

This case study is an enquiry of the hypothesis that stresses introduced in the metallurgical processes (metal preparation, machining, implantation, *etc.*) are critical and should be quantified, for example by diffraction measurements, to build insight into the effects of the technological processes. In this case, the empirical model describes the molecular interactions inside the solid using tensor description of stress in the material, which is built on continuum mechanics. The diffraction measurement datasets (2θ vs. intensity) are transformed into stress tensors using the empirical model, mathematical model, and computational fitting process. Other data processing techniques used are sampling, to change the continuous data to discrete, and scalar decomposition processes, to obtain the von Mises effective stresses, trace, *etc*. For this case study, coordinate transformation for the diagonalization of the tensors is not required, since the shear components are discarded. Residual stress analysis is depicted in Figure 6-7 in the context of scientific enquiry. The visualization pipeline for the scientific visualization of residual stresses of the titanium samples is shown diagrammatically in Figure 6-8.

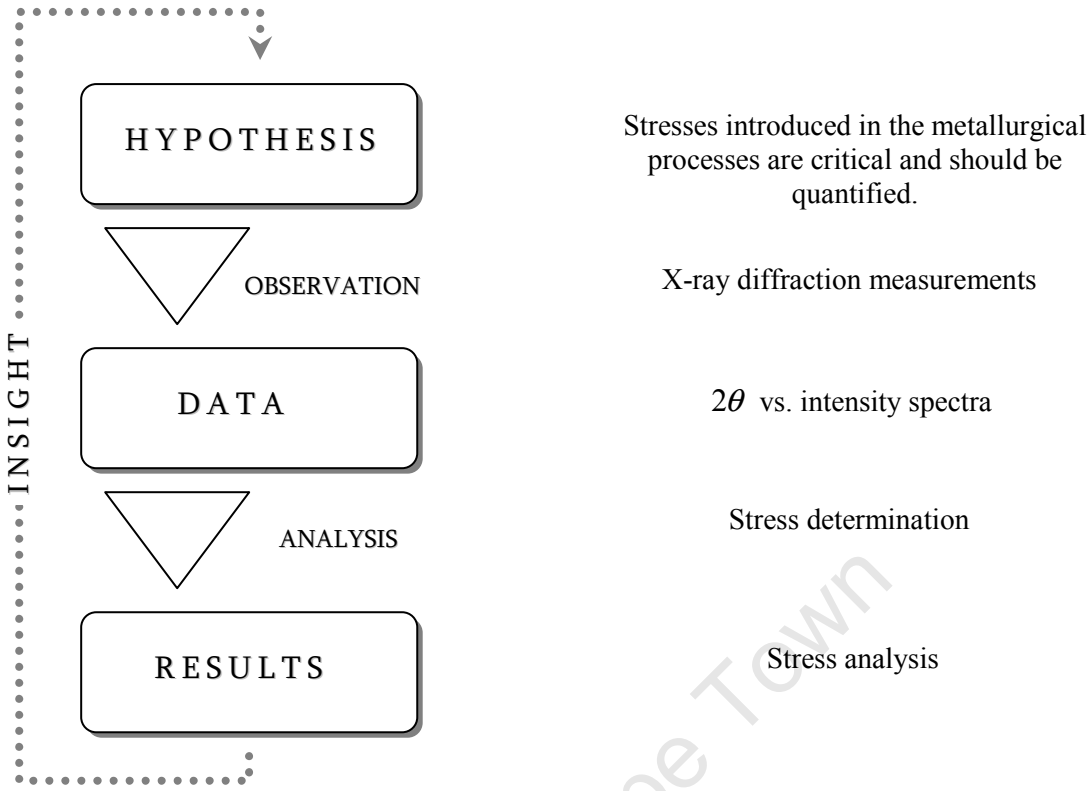

Figure 6-7 Residual stress analysis in the context of scientific enquiry.

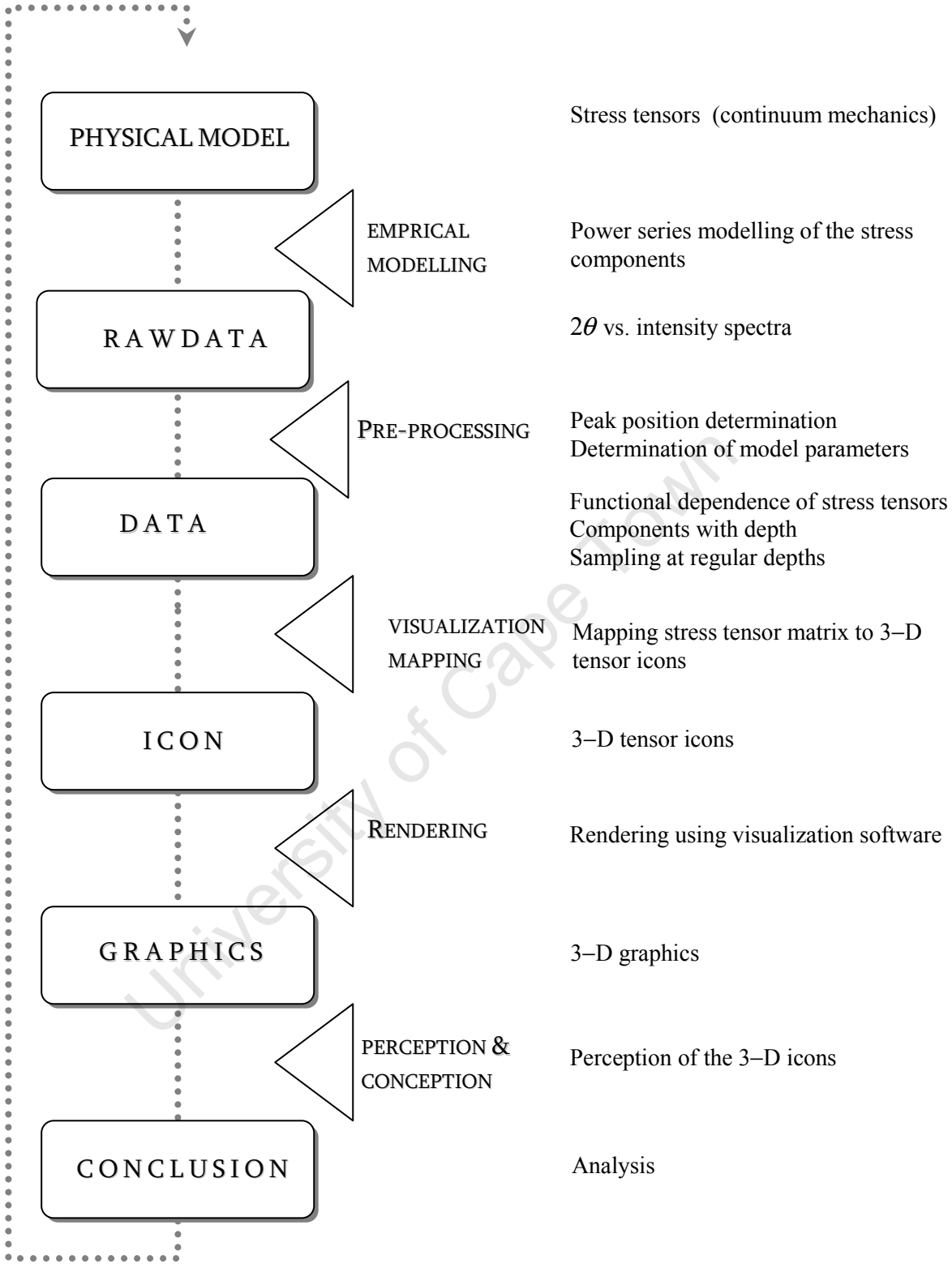

Figure 6-8 The visualization pipeline for the visualization of residual stresses.

In this case study, the **visualization goals** are identified as:

(i) to identify scalars (1A), *i.e.* component magnitudes, von Mises stresses;
(ii) to identify direction (1B), *i.e.* principal stress directions;
(iii) to identify shape (1C), *i.e.* isotropy of the stress tensor;
(iv) to identify structure (1F), *i.e.* the topology of the stress state with depth. (Topology as the relations between linked tensors);
(v) to compare structure (7F), *i.e.* to compare stress topology for different samples; and
(vi) to correlate structure (9F), *i.e.* to correlate sample history and implantation process effects with the stress topology.

The **visual icon** to be used is selected according to the characteristic of the dataset. The tensor datasets are entities of type $E_1^{\sigma_{33}}$, one dimensional continuous distribution of a second order symmetric tensor. The continuous nature of the functional dependence of the components suggests the use local/ global icons. However, because local/ global icons cannot be mapped to one dimensional domains, in this case point icons must be used instead. To use point icons, the stress component curves are sampled at equal distances to obtain discrete data points, changing the continuous entity $E_1^{\sigma_{33}}$ to the discrete one $E_{[1]}^{\sigma_{33}}$. In this case study four complementary point icons are used for the visualizations: the Lamé stress ellipsoid, the PNS, Reynolds, and HWY icons, and the stress quadric icon.

As discussed above, in this section the stress depth profile is confined to the first 2 μm. Table 6-1 presents sampling of the stress components at 0.4 μm regular intervals up to the depth of 2μm. The trace and the von Mises stresses of the stress tensor are also included in the table.

Depth (μm)	σ_{11}	σ_{12}	σ_{13}	σ_{21}	σ_{22}	σ_{23}	σ_{31}	σ_{32}	σ_{33}	Trace	von Mises
					(MPa)						
As received											
0.0	622	0	0	0	404	0	0	0	0	1026	316
0.4	415	0	0	0	362	0	0	0	-1	777	227
0.8	222	0	0	0	315	0	0	0	-4	534	164
1.2	43	0	0	0	262	0	0	0	-8	296	143
1.6	-124	0	0	0	202	0	0	0	-15	63	166
2.0	-277	0	0	0	137	0	0	0	-23	-163	209
Low dose implantation											
0.0	428	0	0	0	216	0	0	0	0	644	214
0.4	296	0	0	0	195	0	0	0	-1	490	151
0.8	173	0	0	0	170	0	0	0	-2	341	100
1.2	58	0	0	0	141	0	0	0	-5	194	73
1.6	-49	0	0	0	109	0	0	0	-8	51	82
2.0	-148	0	0	0	72	0	0	0	-13	-88	111
High dose implantation											
0.0	578	0	0	0	538	0	0	0	0	1116	323
0.4	411	0	0	0	431	0	0	0	-5	837	246
0.8	244	0	0	0	324	0	0	0	-11	557	175
1.2	77	0	0	0	216	0	0	0	-16	277	117
1.6	-90	0	0	0	109	0	0	0	-22	-3	101
2.0	-257	0	0	0	1	0	0	0	-27	-283	142

Table 6-1 Stress tensor components (MPa) sampled 0.4 μm apart along the depth. Corresponding trace and von Mises stresses given in the last two columns.

To study the stress tensor, the following **tensor icon attributes** are used (Corresponding perceptual dimensions of the attributes are shown in parentheses).

(i) *position* on a scale (1): indicates the depth of the stress tensor location.

(ii) *length* (3): indicates the magnitude of the principal stresses for the Lamé stress ellipsoid.

(iii) *3–D direction* (2): indicate the principal stress directions, except for the HWY icon.

(iv) *shape* (3): indicates the isotropy of the stress states.

(v) *colour* (2): indicates derived scalars from the tensor quantity, *i.e.* effective von Mises stresses for stress ellipsoids, and principal/normal/shear stresses for the PNS icon.

Thus the total perceptual dimensions for the icons are equal to 8 (position (1) + length (3) + 3–D direction (2) + colour (2)). The spatial requirement of the icon extensions are: for *position* and *colour* low (≥0), for *length* and *3–D direction* medium (1), and for *shape* high (3). Assuming the total spatial requirement for the stress icons is 4 (position (1) + colour (1) + length(1) + 3–D direction (1)), the information density is found to be 2.0, which can be considered as medium-high information density according to Table 3-2.

For the **rendering** of the stress icons, *MayaVi Data Visualizer* and *Mathematica*™ software are used. *MayaVi Data Visualizer* is freeware built on *The Visualization Toolkit (VTK)* library, and is available from `http://mayavi.sourceforge.net` [162,163]. *MayaVi* software is used to create the eigenicons and scalar colour mapping from the second rank symmetric tensors. *MayaVi*'s 3–D graphics acceleration provides smooth interactivity to explore the icons in 3–D. *Mathematica*™ is a large scale programming tool for scientific research with built in extensive mathematical functions and graphics library [154]. *Mathematica*™ is used to render complex 3–D topological surfaces with sophisticated surface colour mapping. It has excellent digital document preparation features, but however has limited interactivity. Both software packages have a range of output formats including PostScript image (`.ps`), bitmap (`.bmp`, `.jpeg`) and Windows™ metafile formats (`*.wmf`). *MayaVi* also supports VRML 1 and VRML 2 (`*.wrl`) formats for interactive web graphics. The VRML files of the visualizations are provided in the companion CD.

Medium-high information density of the stress tensor information necessitates a balance between local and global features of the system under investigation. For this reason, firstly, the overall features of the stress tensors are shown in Figure 6-9, and the individual stress tensors are investigated in detail in Figures 6-7 through 6-10. Although shaded 3D ellipsoids are used here, due to the highly planar stress states in the near surface region, the icons seem like 2D ellipsoids.

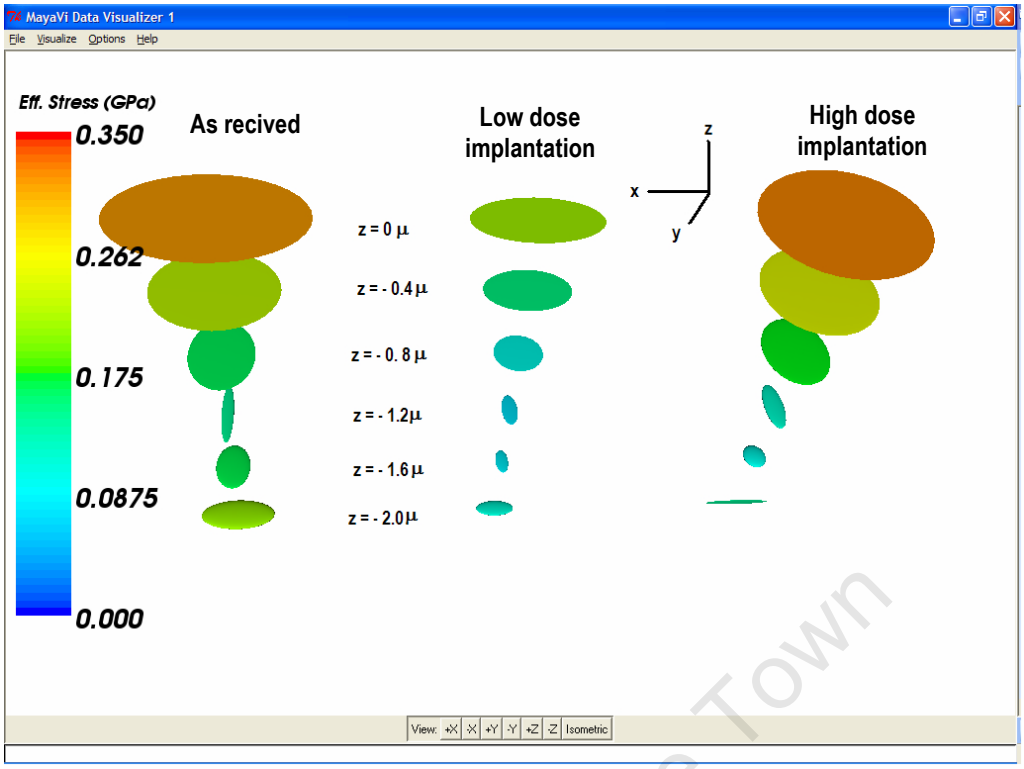

(a)

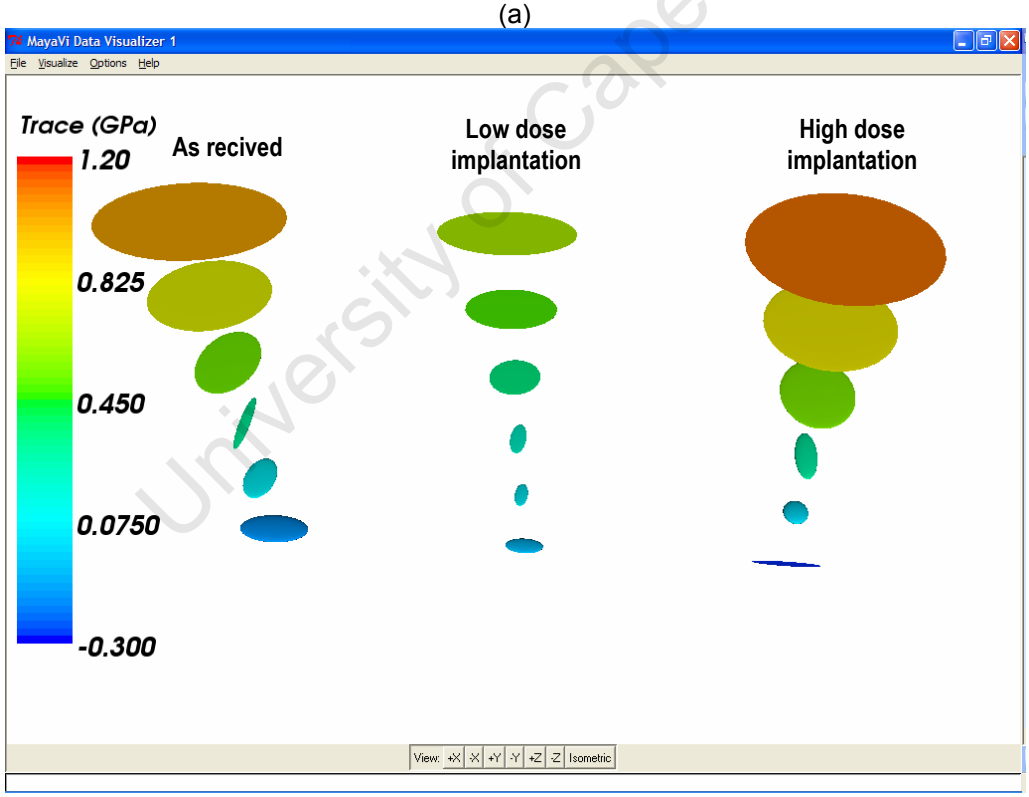

(b)

Figure 6-9 Stress ellipsoid representation of depth resolved stresses for as received, low dose and high dose implantation (a) colour code indicates von Mises stresses. (b) Trace of the stress tensors.

The overall representation of Figure 6-9 visualizes tensor stress profiles of the three specimens with depth. In the figure, the vertical position of the ellipsoids corresponds to the depth of the stress tensor visualized in the specimen. The size and orientation of the ellipsoids indicate the size and orientation of the principal stresses. Colour is used to map two extracted scalars. Two alternative colour codings are used: the trace of the stress tensor is mapped on the ellipsoids in Figure 6-9a, and the effective stress is mapped in Figure 6-9b. As received (AR), low dose implanted (LD), and high dose implanted (HD) specimens are shown together to facilitate the exploration of the effects of the implantation process.

The most prominent features of the stress icons are the principle stress directions, principle stress magnitudes, isotropy of the stress tensors, and the changing of the trace and effective stresses, represented by colour coding. Essentially all these features are depicted in the same visualization without introducing visual clutter. In

Firstly the **size of the ellipsoids** shows that for all specimens the size of the ellipsoids reduces with depth until about 1.5 μm, indicating that stresses are considerably reduced deeper in the material. In addition, the growing back of the stresses in the as received specimen below 1.2 μm seems to be removed in the implanted samples, in which the stress ellipsoids reduce monotonically with depth. The effect of implantation on the stress state can be seen by comparing the columns of stress ellipsoids. In general, the size of the stress ellipsoids is observed to reduce with implantation. Most reduction is seen from the as received to the low dose implanted state, but upon further implantation the sizes of the ellipsoids grow slightly, especially in the near surface region. This could possibly indicate high surface damage introduced by implantation. Next we consider the **shape** of the ellipsoids, which is best seen in the top view shown in Figure 6-10. The elliptic discs of the surface indicate bi-axial stresses for the as received and low dose implanted samples. In contrast the circular disc for high dose implantation shows that further implantation induces homogenous in plane stress. Deeper in the material, about 1.5 μm, the ellipsoids are more elongated, or needle-like (see Figure 6-9), indicating directional stresses. In particular the ellipsoids at -1.2 μm for the as received sample, and at -1.2, -1.6 μm for the low dose, and at -2.0 μm for the high dose implanted specimen are

especially elongated, indicating strong changes of force directions in the specimen. In the next section these tensors are further explored using the PNS, Reynolds, HWY and the stress quadric icons.

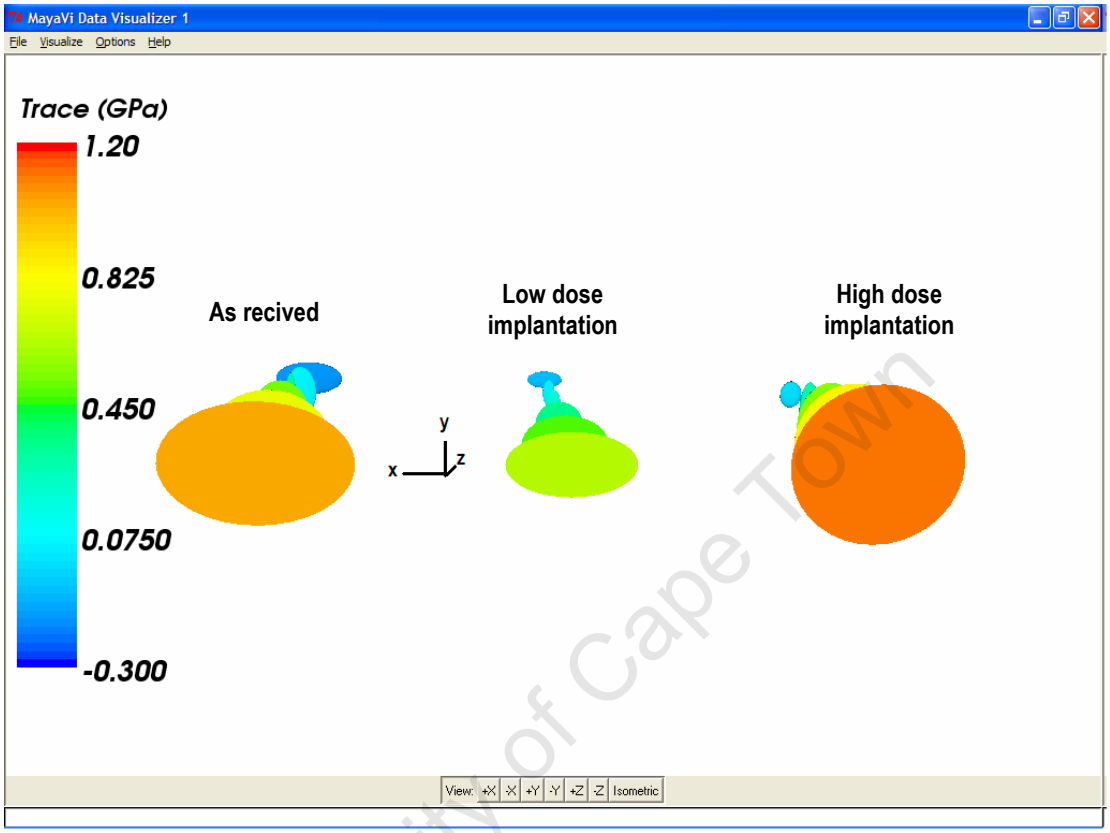

Figure 6-10 Stress ellipsoids shown from the top, along the *z*-axis. The interactive exploration reveals hidden structures in the visualization.

The next attribute to be explored is the **orientation** of the ellipsoids. In the near surface region, these are aligned along the *x*-axis in the as received and low dose implanted samples, and therefore indicate directional bi-axial stresses, possibly indicating the rolling direction. For the high dose implanted sample this rolling effect is totally removed. The orientation of the ellipsoids shows another fundamental change of the stress state in the as received sample. The first two ellipsoids at z=0 and z=-0.4 µm are aligned along *x*- direction, the next two at z=-0.8 and z=-1.2 µm are aligned along *y*- direction, and the last two at z=-1.6 and z=-2.0 µm are again aligned along *x*-direction. This suggests a counter clockwise rotation of the stress tensor about the positive *z*- axis. Drawings of the principal stresses shows that, what is perceived as

rotation, is in fact, the shortening and then lengthening in the opposite direction of the σ_1 stress (Figure 6-11). Similar behaviour is also seen for the low dose implanted sample, and to lesser extent for the high dose implanted sample.

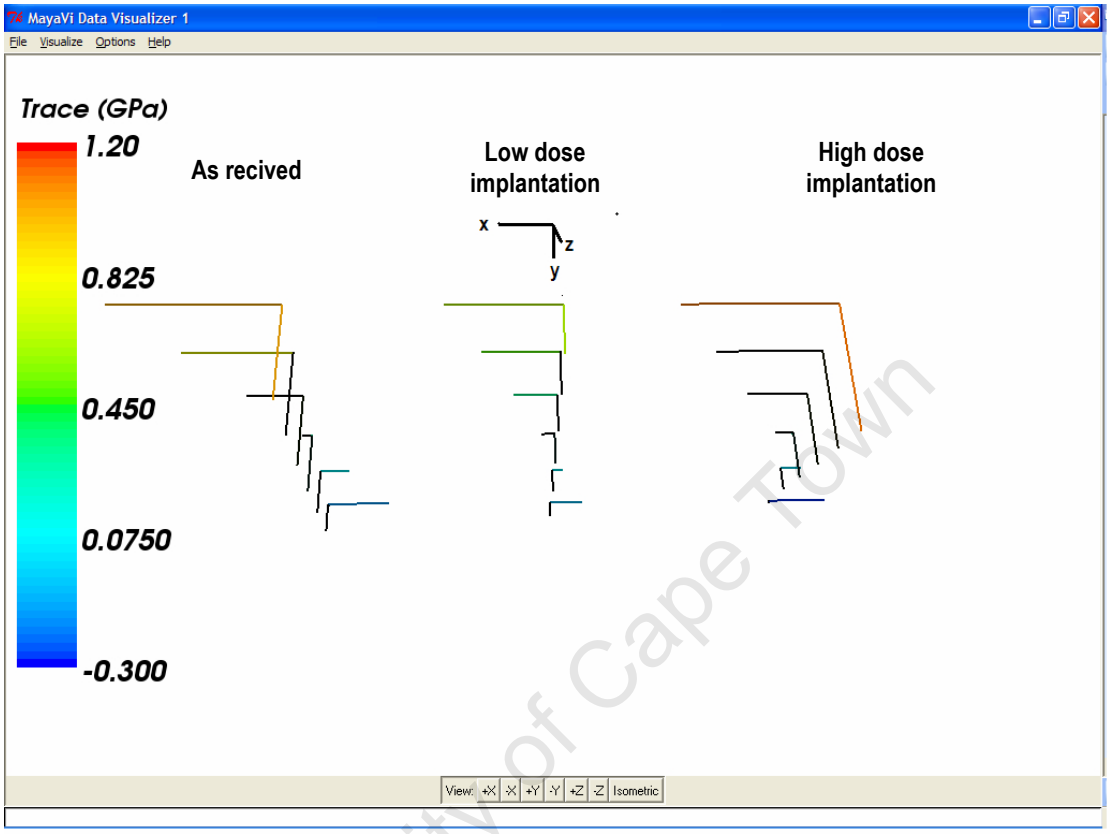

Figure 6-11 Principal stress directions.

The last attribute of the stress ellipsoids to be explored is the **scalar colour coding** of the effective stress and the trace of the stress tensor. In general the effective stresses are high in the surface region and reduce with depth (Figure 6-9a). The change of the size, orientation and shape of the ellipsoids, from the surface to the deeper regions in all three specimens, can also be seen by the change of colour, and therefore the character of the stress tensor. For example, at $z = -1.2\,\mu m$ for the as received sample, the lowest effective stress coincides with the *y*- elongated ellipsoid. Similarly in the low dose implanted sample the effective stress is less than 100MPa (blue- green colour) for the *y*- elongated ellipsoids at $z = -1.2$ and $z = -1.6\,\mu m$. The same correlation can be seen for the high dose implanted sample, where the ellipsoids turn blue-gray and change direction at $z = -1.6\,\mu m$.

As for the implantation, the effective stress on the surface is reduced (green colour ellipsoid) by low dose implantation, but afterwards the surface stresses are increased again (red colour ellipsoid) with high dose implantation.

Until now the absolute magnitude of the stress has been discussed without reference to its tensile or compressive nature. The trace colour scheme reveals the tensile character of the stresses in the surface region, as seen in Figure 6-9b. The stresses turn compressive at about $z = -1.6\,\mu m$ depth. The change from tensile to compressive stress hints at shear stresses at this depth. However there are no visual cues in this representation to indicate shear stresses, which can be visualized using the other icons discussed below.

The first step of visualization above, showed the overall features of the stress state in context. In the second step, each stress tensor is explored individually, focusing on the local features of the tensors, such as tension, compression and shear properties. In the following representations, the icons are not drawn to scale, so that the 2–D representation of the 3–D icons is not visually hindered, and provides maximum visual insight into the characteristic shape and features of the icons.

PNS icons (Figure 6-12) advance the ellipsoidal representation to include visual cues for normal and shear stresses. For example, the blue colours of the icons of all specimens at the surface indicate purely tensile stresses in the surface plane. Reddish colours for the deeper regions indicate compressive stresses. Shear stresses (yellow-green colour) are observed where there is simultaneous presence of compressive (red) and tensile stresses (blue), at $z = -1.6\,\mu m$, $z = -2.0\,\mu m$ for as received and low dose implanted samples, and at $z = -1.6\,\mu m$ for the the third sample. From the PNS icons, it can be seen that there is compression along the *x*- axis, and tension along the *y*-axis for at $z = -1.6\,\mu m$, $z = -2.0\,\mu m$ for the as recieved sample. The same feature can be seen at $z = -1.6\,\mu m$ for low and high dose implanted samples. These icons confirm the presence of pure shear stresses at the region where the ellipsoids change orientation, and the stress magnitudes turn compressive from tensile.

Reynolds icons (Figure 6-13) reveal the 3–D distribution of the normal stress components. The Reynolds icon takes distinctive shapes for different principal stresses: *e.g.* the torus at $z = -0\,\mu m$ in the as received sample; an elongated torus shape in the low dose implanted sample at $z = -0\,\mu m$, $z = -0.4\,\mu m$; a double lobed shape at $z = -0.8\,\mu m$ and a quadruple lobed shape at $z = -1.2\,\mu m$, $z = -1.6\,\mu m$, and $z = -2.0\,\mu m$. The circular torus shape indicates homogenous bi-axial stresses, which can be either tension or compression. It is not possible to differentiate these stresses using the Reynolds icon. An elongated torus indicates larger normal stresses along the larger radius. The radius along the *z*- axis is null indicating the absence of normal stresses along this direction. Ideally, a double lobed icon indicates a uni-axial stress, since the normal stresses along the other two dimensions vanish. However it is not easy to decide, from the icon, if one of the principal stresses definitely vanishes. For example the icon at $z = -1.2\,\mu m$, for the high dose implanted sample has a very small *y*- component which results in a double lobed shape. The quadruple lobed shape indicates the presence of both tensile and compressive stresses, however it is not possible to differentiate the types from the icon. The icons at $z = -1.2\,\mu m$, $z = -1.6\,\mu m$, and $z = -2.0\,\mu m$ in the as received, $z = -1.6\,\mu m$, $z = -2.0\,\mu m$ in the low dose, and $z = -1.6\,\mu m$ in the high dose implanted samples all indicate the simultaneous presence of tensile and compressive, and therefore pure shear stresses, as also seen using the PNS icon above.

HWY icons (Figure 6-14), with their symmetric two sections, show the shear stress distribution. It is seen that on the surface, for the as received and low dose implanted samples the icon does not diminish in the *x*-*y* plane, indicating shear stresses. For the high dose implantation the more symmetrical shape, diminishing on the *x*-*y* plane, indicates no shear stresses due to the homogenous bi-axial state. Basically the same shape icon is seen for all the stress tensors, since the maximum shear directions are always 45° to the principal axes. However it is interesting to compare two icons that seem to be different orientations of the generic HWY icon, namely the ones at $z = -0.8\,\mu m$, and $z = -1.2\,\mu m$ for as received sample. At $z = -0.8\,\mu m$, the icon shrinks along the *z*- axis, and becomes thinner in the *x*-*y* plane. The split that occurs in the *x*-*y* plane to form the icon at $z = -1.2\,\mu m$ is due to the zero normal stresses between the principal stresses, which can be seen from the Reynolds icon

representation of the same tensor. This can be misleading, since the HWY icon does not differentiate between zero stress and pure normal stress. In this sense Reynolds and HWY icons are complementary to each other, with one showing the normal stresses, the other showing the shear stresses.

The stress quadric icon (Figure 6-15) representation is perhaps visually the most distinctive. Polygonisation highlights the shape surfaces, however a fine polygonization is not used in the icons not to clutter the images. Furthermore, the quadric surfaces diverge for these stress tensors, hence the visual icons are clipped at the volume boundaries. The stress icon takes different shapes: tubular as seen at $z = -0\,\mu m$ for all three cases, a regular hyperboloid as seen at $z = -0.8\,\mu m$ for the high dose implantation, and diverging hyperbolic surfaces as seen $z = -1.6\,\mu m$ and $z = -2.0\,\mu m$ for the as received sample. The cylindrical icons show biaxial stresses on the surface. The absence of the normal stress component on the surface is manifested with the icon having no surface along the normal direction. Just below the surface, the icons are not cylindrical but divergent, indicating small compressive normal stresses along the *z*- direction below the surface. The quadric icons have diverging surfaces along the pure shear stresses below $z \leq -1.2\,\mu m$ confirming the presence of the shear stresses in this region. The stress quadric at $z = -2.0\,\mu m$, in the high dose implanted sample, is due to the uniaxial stress tensor along the *x*- axis, which has a small *z*-component. Therefore the tubular icon is aligned with the *y*- axis where normal stresses cease to exist.

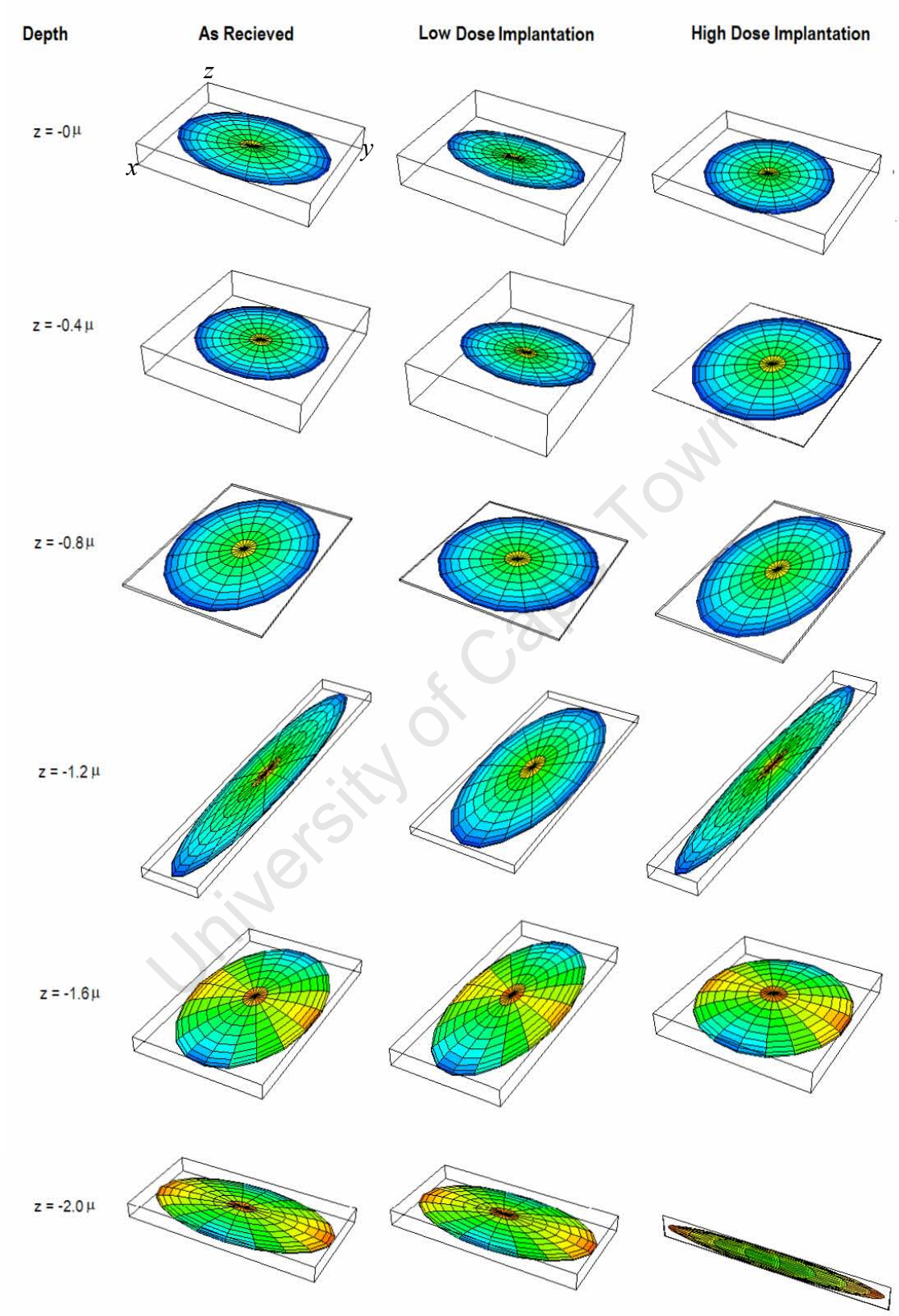

Figure 6-12 PNS icon visualization.

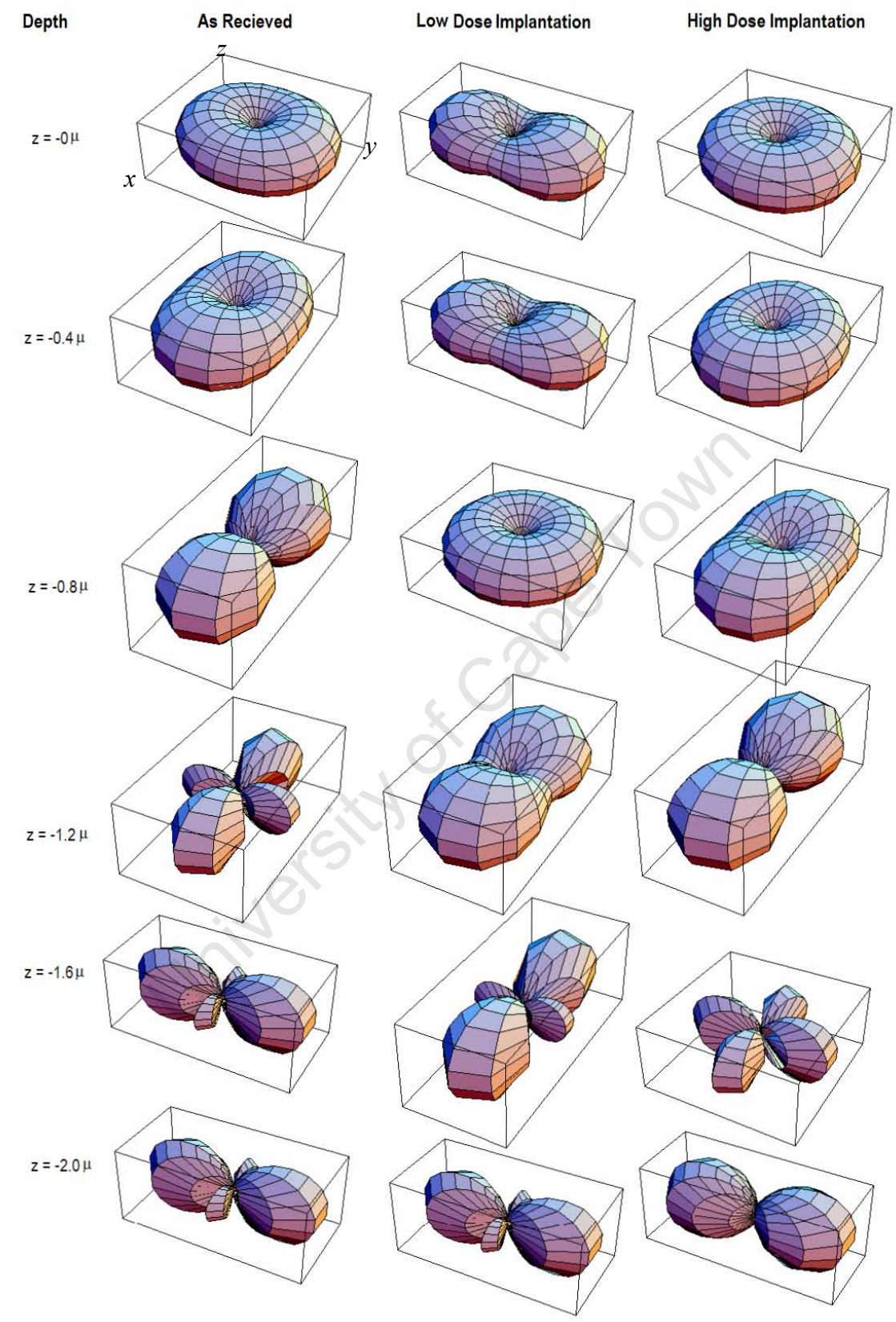

Figure 6-13 Reynolds icon visualization.

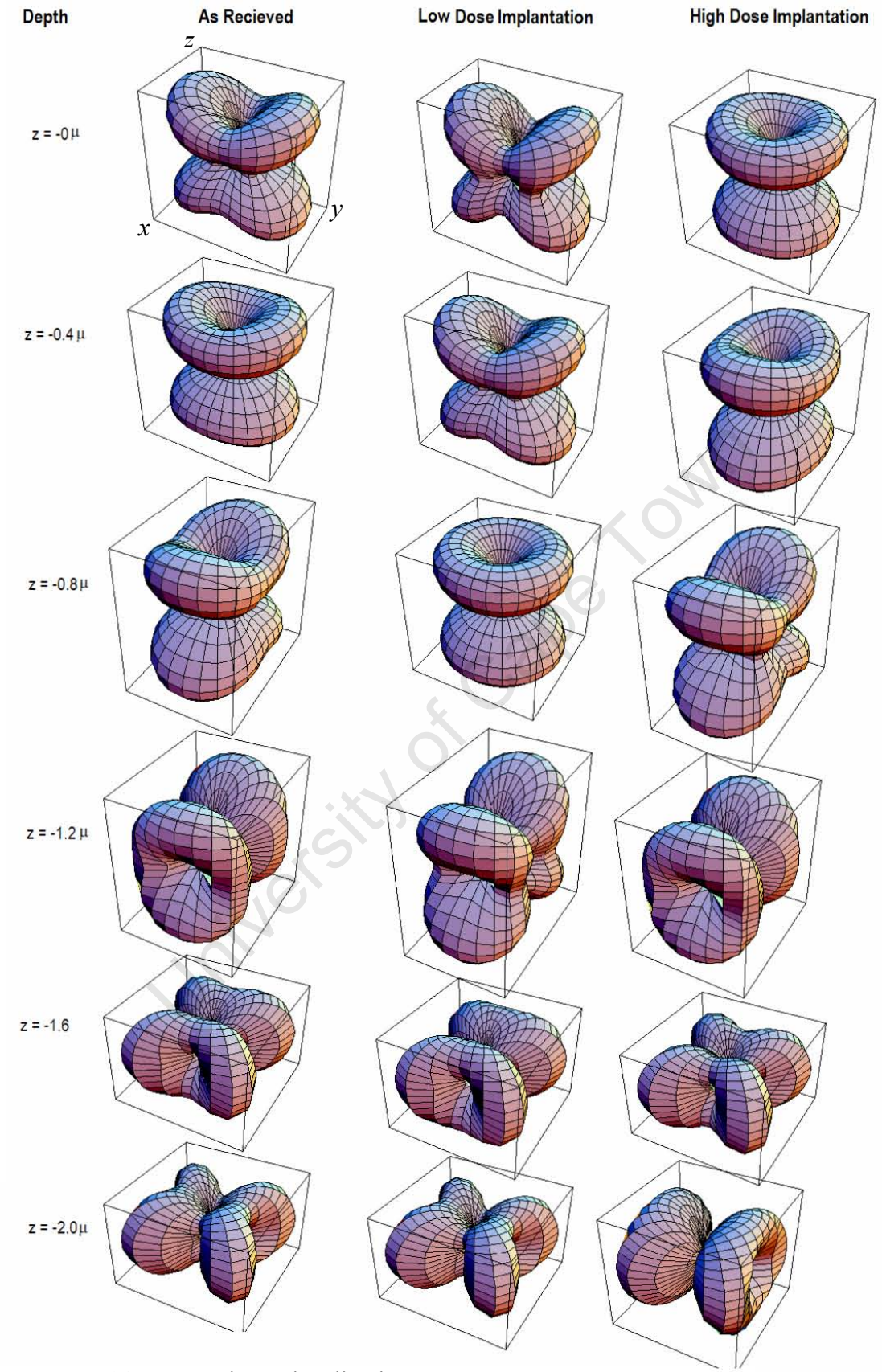

Figure 6-14 HWY icon visualization.

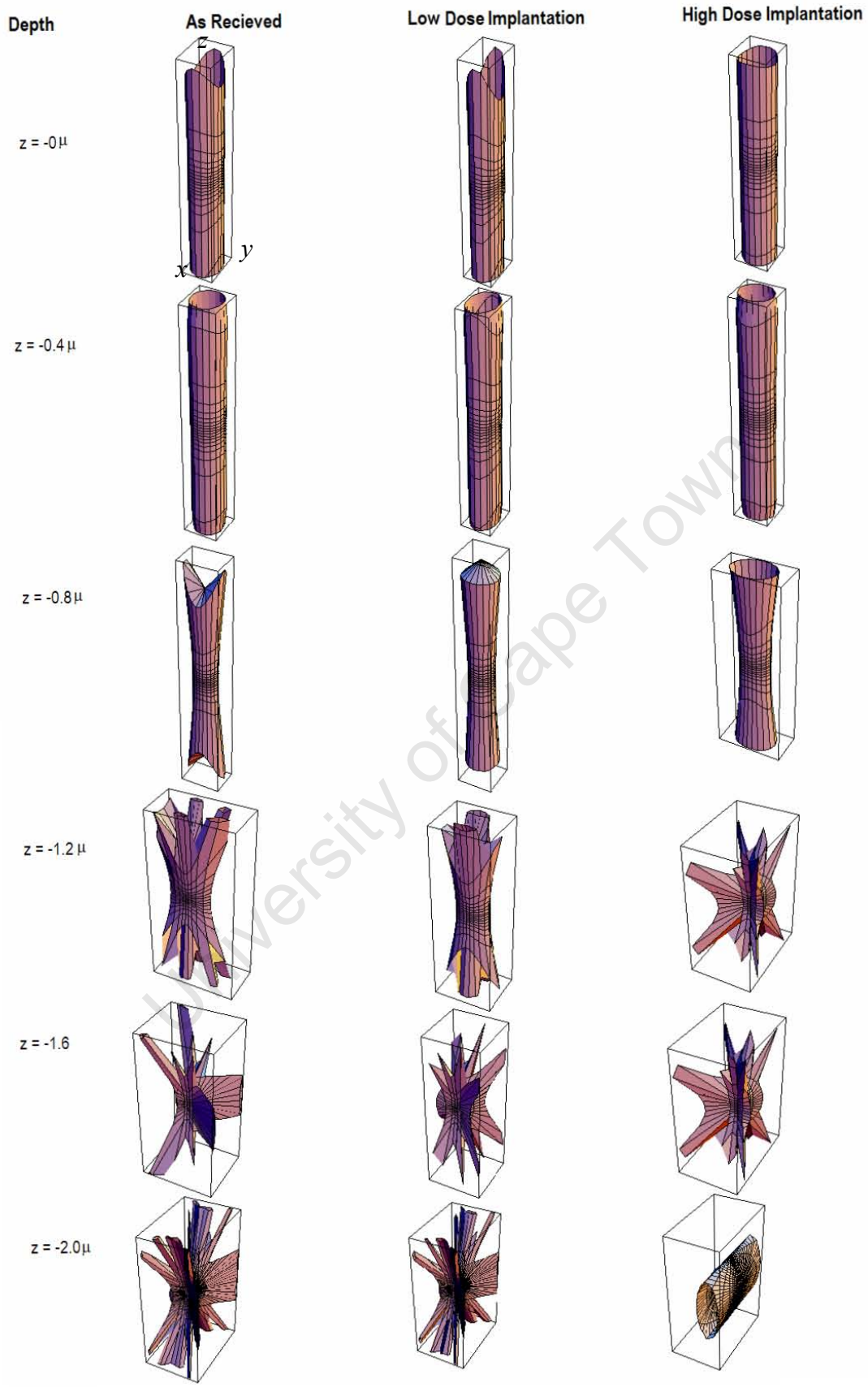

Figure 6-15 Stress quadric icon visualization.

7 Case study 2: Visualization of residual stress in Ti-6Al-4V

In this chapter, the residual stress profile of a titanium based alloy component is explored using scientific visualization. The starting point of the visualizations is the given depth profile of the stress tensor components as in the previous case study. However in this case, a complete experimental dataset is available, allowing the determination of all six independent tensor components over greater depth.

7.1 Sample Characterization

The sample studied was a shot-peened and tempered Ti6Al4V work piece. Shot-peening is a surface enhancement procedure in which high velocity metal shot, usually steel or cast iron, impinges on the surface of the material [164, 165]. Tensor stress determination was carried out, by Harting [11], using x-ray diffraction measurements combined with the semi-numerical method described above in 5.3.4. Various X-ray radiation wavelengths and corresponding diffraction peaks were selected according to their penetration depth, diffraction intensity and signal-to-noise ratio, so that sufficient data points were collected for the non-linear fit of the semi-numerical method. The stress determination in the sample yielded the full tri-axial stress tensors up to a depth of $30\mu m$.

In Figure 7-1 [11], all six components of the stress tensor are depicted. On the surface, the in-plane normal components σ_{11} and σ_{22} show tensile stresses of 300 MPa which change to compressive stresses of 400 and 600 MPa deeper in the specimen. The σ_{i3} stress components are all relatively small compared to the components in the surface plane of the sample.

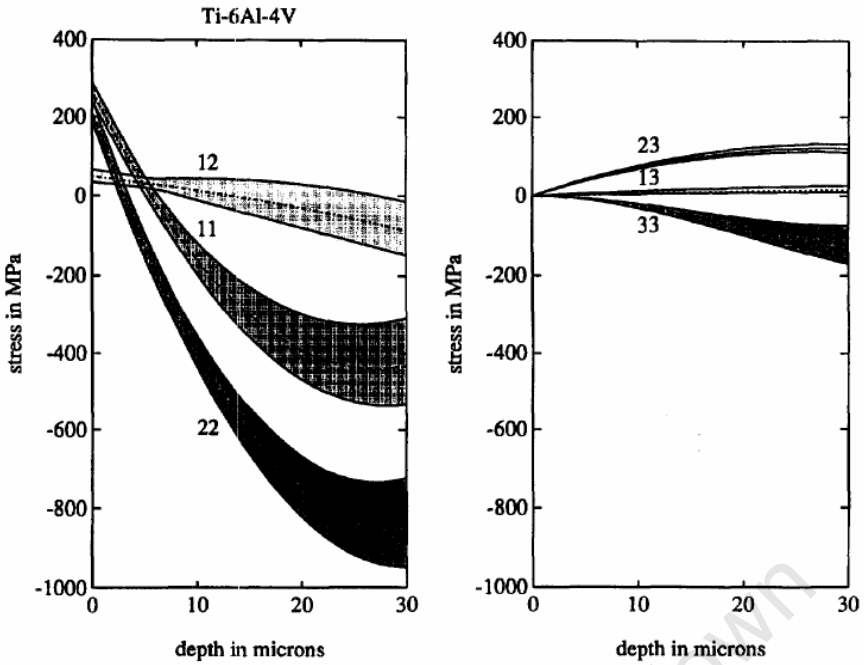

Figure 7-1 Depth profile of the stress tensors of a shot-peened titanium alloy [11].

7.2 Scientific visualization of the residual stress profile

In this case study, the goal of using scientific visualization is to reveal the tensor structure of the stress state given by the stress profile data shown in Figure 7-1. The goal is therefore to expose the underlying tensor information, *i.e.* principal stresses and principal stress directions, normal and shear stresses, isotropy of the stress tensor, topology of the stress tensor, as well as the von Mises stresses, and trace of the tensor with depth.

The tensor dataset is an entity of type $E_1^{\sigma_{33}}$, a one dimensional continuous distribution of a second order symmetric tensor. To visualize the dataset, point icons are preferred. Because the depth profile is given in a one dimensional domain, *i.e.* the depth, local or global icons are not appropriate. These require three dimensional resolution of the tensor field. In order to use point icons, the stress component curves are sampled at equal distances to obtain discrete tensors at each point. This process changes the continuous entity $E_1^{\sigma_{33}}$ to the discrete entity $E_{[1]}^{\sigma_{33}}$. In this section, the Lamé stress

ellipsoid, the Reynolds icon, the HWY icon, the stress quadric icon and the PNS icon are used to visualize the $E_{[1]}^{\sigma_{33}}$ dataset.

The continuous stress tensor components of Figure 7-1 are sampled at every $5\mu m$, and the resulting discrete stress tensors are given in Table 7-1. The corresponding principal stresses, obtained by diagonalization, effective stresses and the tensor traces are listed in Table 7-2.

Depth (μm)	σ_{11} (MPa)	σ_{12}	σ_{13}	σ_{21}	σ_{22}	σ_{23}	σ_{31}	σ_{32}	σ_{33}
0.0	270.0	45.0	0.0	45.0	200.0	0.0	0.0	0.0	0.0
5.0	37.0	32.5	5.0	32.5	-127.5	36.0	5.0	36.0	-7.5
10.0	-162.5	15.0	7.0	15.0	-390.0	70.0	7.0	70.0	-20.0
15.0	-287.5	-5.0	11.5	-5.0	-605.0	100.0	11.5	100.0	-47.5
20.0	-375.0	-29.0	15.0	-29.0	-735.0	110.0	15.0	110.0	-75.0
25.0	-427.5	-56.0	19.5	-56.0	-817.5	125.0	19.5	125.0	-105.0
30.0	-425.0	-80.0	21.5	-80.0	-835.0	122.5	21.5	122.5	-130.0

Table 7-1 Stress tensor components extracted from the continous dataset shown in Figure 7-1.

Depth(μm)	σ_1 (MPa)	σ_2	σ_3	Effective stress	Trace
0.0	292	178	0	255	470
5.0	46	-143	-2	170	-99
10.0	-163	-404	-6	347	-574
15.0	-288	-623	-30	515	-941
20.0	-373	-755	-56	606	-1185
25.0	-420	-847	-83	663	-1350
30.0	-410	-871	-109	665	-1390

Table 7-2 Principal stresses, effective stress and trace of the stress tensor.

Scientific visualization of the stress profile is carried out, similarly to the previous case study, in two steps. Firstly the overview of the stress state is given with respect to the specimen geometry using Lamé stress ellipsoids, where the icons are scaled and

aligned to highlight the depth resolution of the stress state, and resolving general trends and critical regions of the stress field in the depth range probed. Secondly, each stress tensor is explored for its tensor properties, such as normal and shear stresses, using the PNS, Reynolds, HWY and stress quadric icons, which are drawn to larger scales, so that the visual cues of each icon can easily be seen. On the computer screen this can be achieved more easily by interactively panning, zooming in and out, and rotating the 3–D graphics to explore different aspects. To facilitate interactivity, the 3–D stress profiles of Figure 7-2 are included in the companion CD-ROM in the virtual reality markup language (VRML) format.

Figure 7-2 is the Lamé stress ellipsoid representation of the overall. The principal stress magnitudes and directions are shown using line segments, next to the ellipsoids. Bi-axial surface stresses are indicated by the planar ellipse on the surface. The gradual monotonic increase of the stress in *z*-direction is evident from the three dimensional ellipsoids deep in the specimen. However, the magnitude of the stresses decreases in the first $5\mu m$ and increases thereafter. Except for the first two ellipsoids, at the surface and at $z = -5\mu m$, the alignment and shape of the tensor ellipsoids are similar, *i.e.* along the *y*- axis. This alignment of the stress states cannot be seen directly from the component representation of Figure 7-1. The ellipse at the surface is not particularly aligned in any direction, and is therefore more isotropic, compared to the ellipsoids deeper in the material (see also Figure 7-3c). The partial isotropy of the stress state might be introduced by homogenous shot-blasting process or subsequent heat treatment. The size and orientation of the ellipsoid at $z = -5\mu m$ is in clear distinction to the ellipsoids deeper in the material, as can be seen from Figure 7-2 and Figure 7-3, which is an indication of the change of stress in this region as well as presence of complex normal and shear stresses. The color coding of the figures confirm this subtlety.

Trace colour coding reveals tensile surface stresses and compressive bulk stresses and a transformation region at about $z = -5\mu m$ (Figure 7-2a). The effective stresses also exhibits a minimum at $z = -5\mu m$. Note that the tensile or compressive nature of the stress cannot be seen from the effective stress colour coding.

From the overall representation it is seen that the tensor field topology changes rapidly in the first $10\mu m$ below the surface, thereafter it does not change in directionality, but only grows in magnitude.

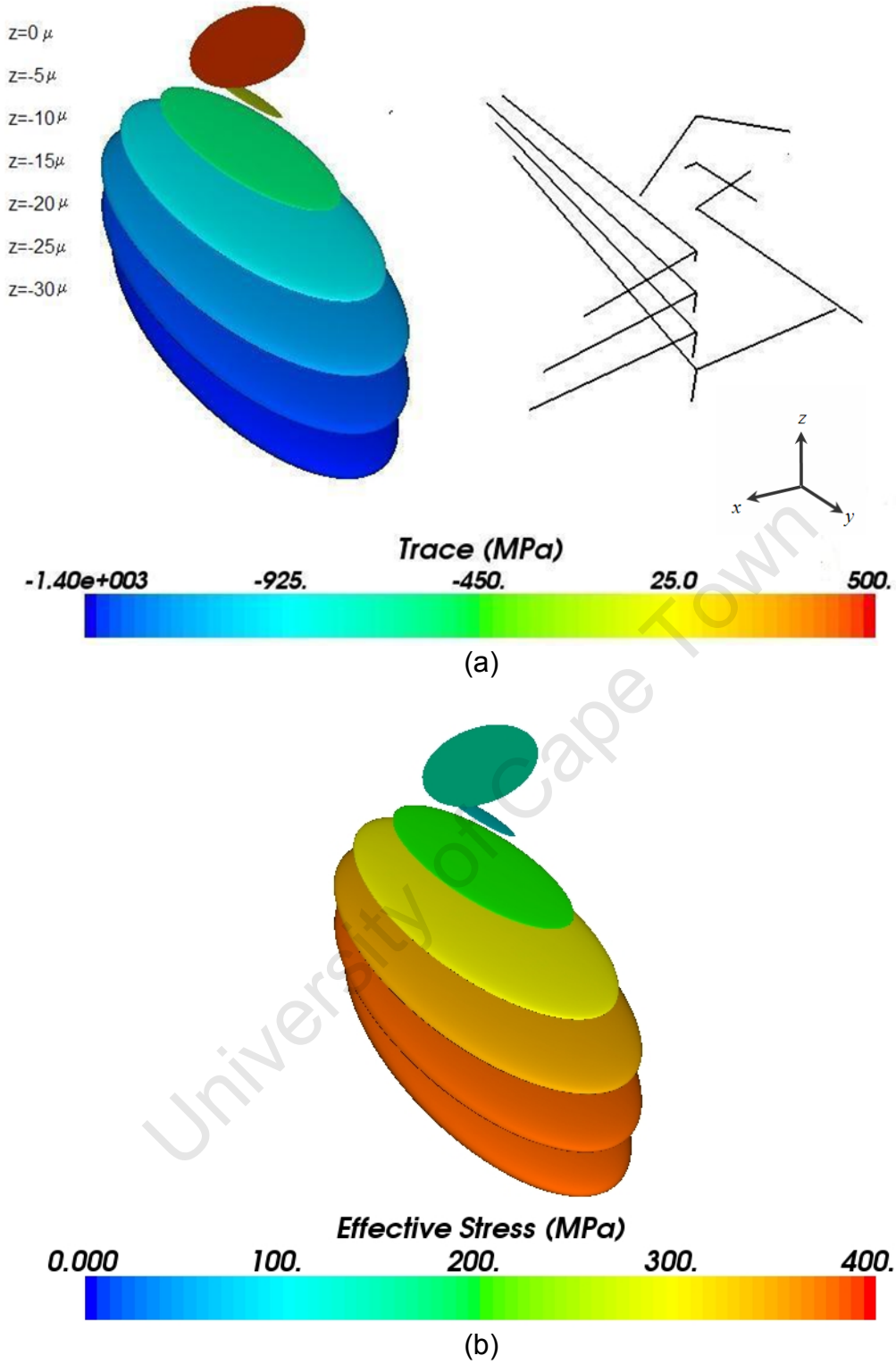

Figure 7-2 Visualization of the depth profile of residual stresses in a Ti6Al4V specimen. Colour coding indicates scalars extracted from the stress tensors: (a) trace (b) effective stresses. Different colour scales are used to improve perception.

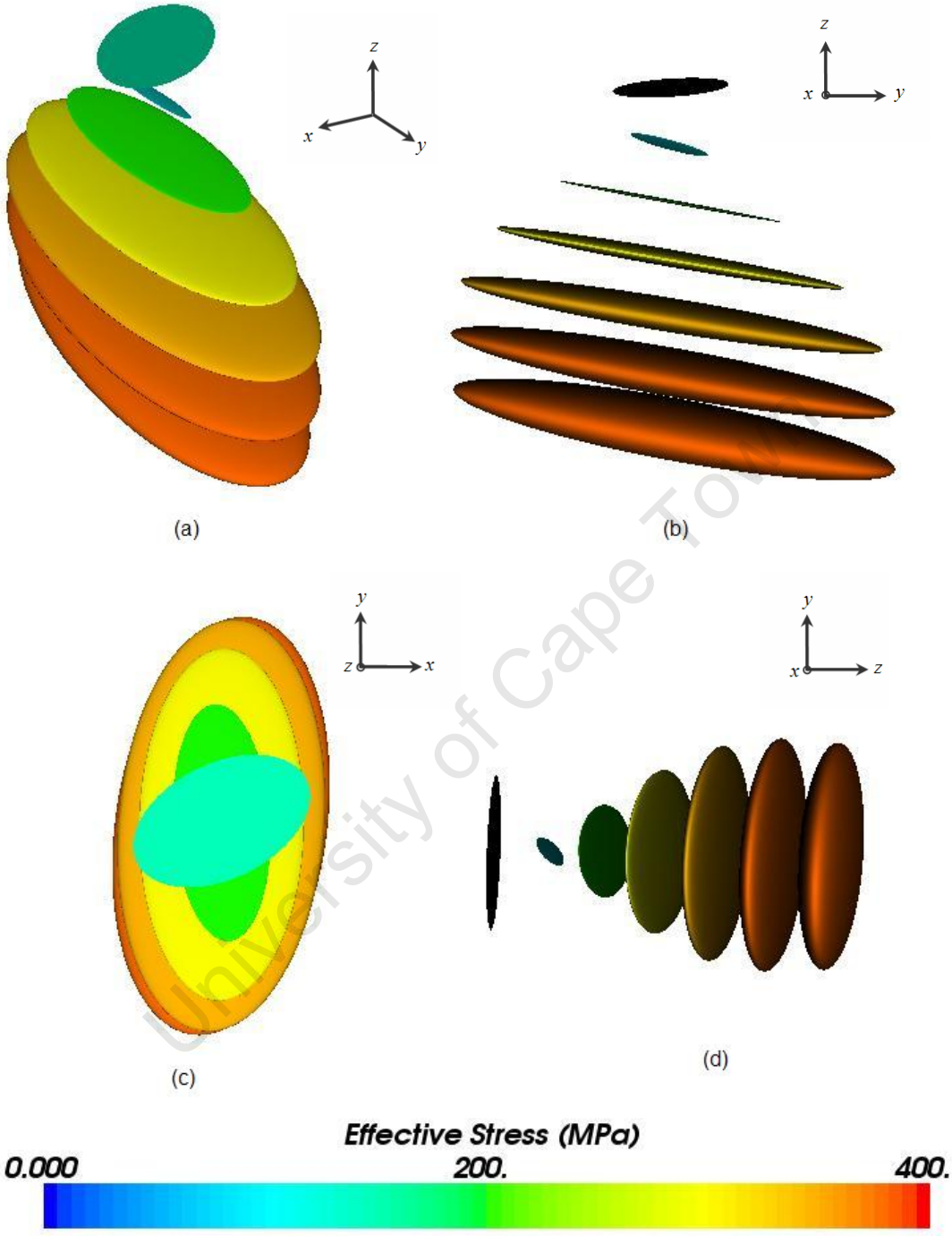

Figure 7-3 Isometric (a) and orthogonal (b-c-d) views of the stress ellipsoids. Interactivity facilitates better perception of the 3–D geometry.

In the **PNS icon visualization** (Figure 7-4), the blue planar ellipse on the surface reveals tensile stresses in the *x*- and *y*- directions. The stress at the surface is nearly isotropic in the surface plane, and therefore shear stresses can not be seen. On the other hand, the ellipsoids deeper in the sample, $z < -10\mu m$, not only indicate tensile stresses, but also the shear stresses by the greenish colours between the red poles of the ellipsoids. The PNS icon at $z = -5\mu m$ is enlarged and rotated to show better the simultaneous presence of compressive and tensile stresses. Green colour bands between the poles of the ellipsoid indicate the pure shear stress directions between the principal stresses. The PNS icons show that only at $z = -5\mu m$ are both tensile and compressive stresses present. This fact, but not the types of stresses can be seen from the following visualizations.

In the **Reynolds icon visualization** (Figure 7-5), only the normal stress components of the stress tensors are represented. A change in the direction of the normal stresses from the surface to deeper in the sample can be seen from this icon. Although the stress changes from tensile to compressive, this cannot be deduced directly from the Reynolds icons. However the presence of the quadruple-lobed icon at $z = -5\mu m$ hints at the change of global stress state between the surface and the bulk. Consequently, the quadruple-lobed Reynolds icon can be used as an indicator for the global changes in the stress state. This icon is rotated and enlarged, in a similar manner to the previous PNS icon, and the double-lobes corresponding to the normal stresses are indicated. Note that the types of the stresses indicated in parentheses cannot be directly deduced from the icon.

The **HWY icon visualization** (Figure 7-6) represents only the shear stress distribution. The HWY icon shape has cues for the maximum shear stresses: the icon surface elements further away from the origin show maximum shear. The surface elements also vanish in the principal stress directions where the shear stress is zero. This behaviour is evident from the HWY icons in the figure. The types and directions of stresses are identified and marked on the larger rotated copy of the HWY icon for $z = -5\mu m$. When discussing the PNS icon representation it was mentioned that, on the sample surface the shear stresses cannot be seen since they are very small due to

the relatively isotropic state. The exact direction of the shear stresses at this location can be seen from the HWY icon shape, and is between the *x*- and *y*- directions, closer to the smaller principal stress, *i.e.* the principal stress closest to the *y*- direction. Note that although it shows the shear stress distribution, the HWY icon has no visual cues for pure shear stresses.

The **stress quadric icon visualization** (Figure 7-7) gives four visually striking distinct shapes for the different stress types: ellipsoidal prism (except the bases) for the bi-axial stress on the surface, a hyperboloidal shape for mixed tensile and compressive stresses (at $z = -5\mu m$), and closed ellipsoidal surfaces for purely tensile (or compressive) stresses, at $z \leq -10\mu m$. The stress quadric icon might be quantitatively misleading, since the closed or open surfaces obtained are inversely proportional to the square of the stresses. However, the visual shapes are distinct and provide a good qualitative understanding of different stress states as encountered in the figure. The stress quadric icon at $z = -5\mu m$ is particularly interesting. This shape has three non intersecting surfaces, which diverge along the pure shear stresses.

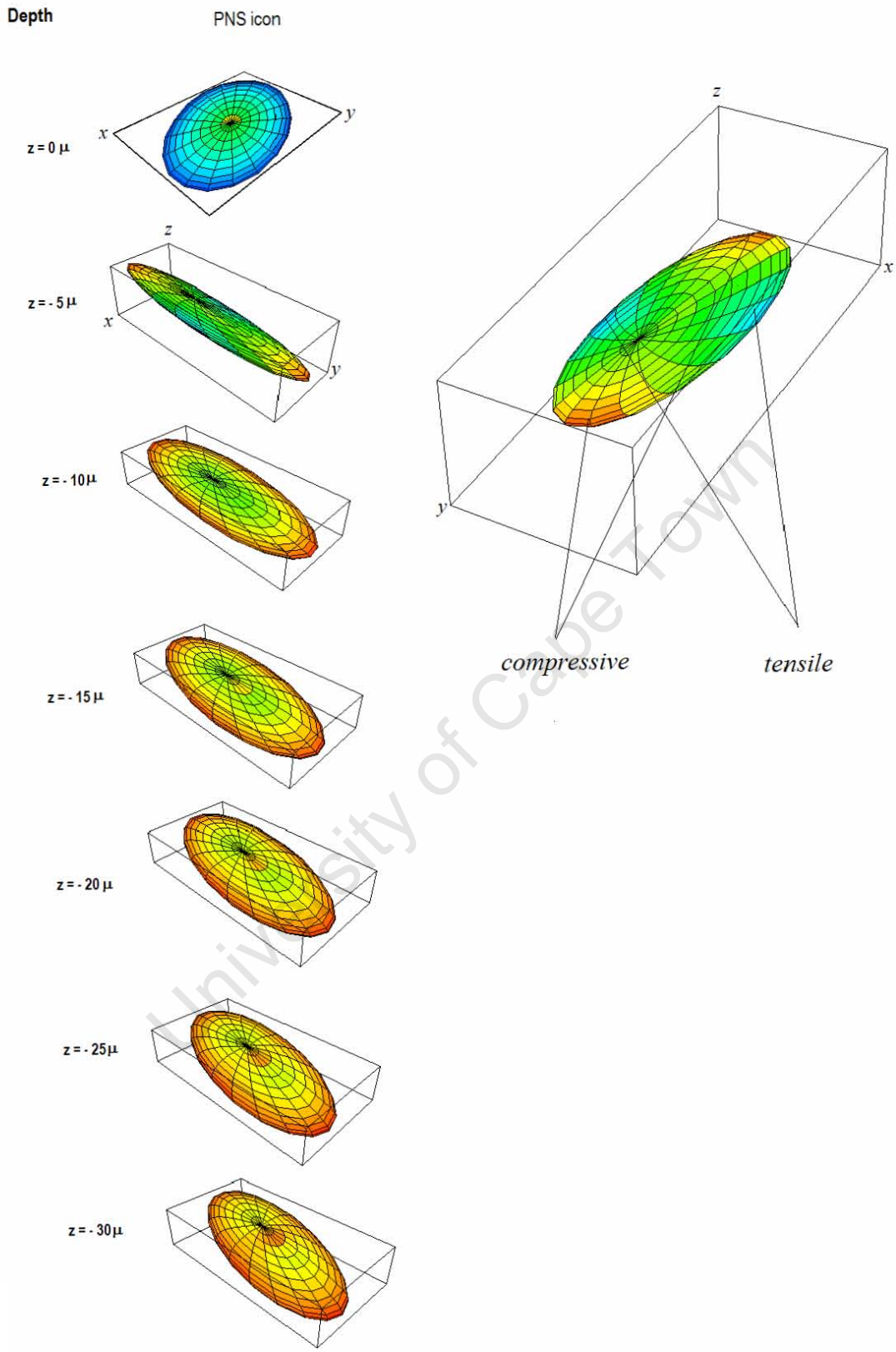

Figure 7-4 PNS icons shown in the isometric view. The icon at $z = -5\mu m$ is shown in two different viewpoints and the compressive and tensile stresses are indicated.

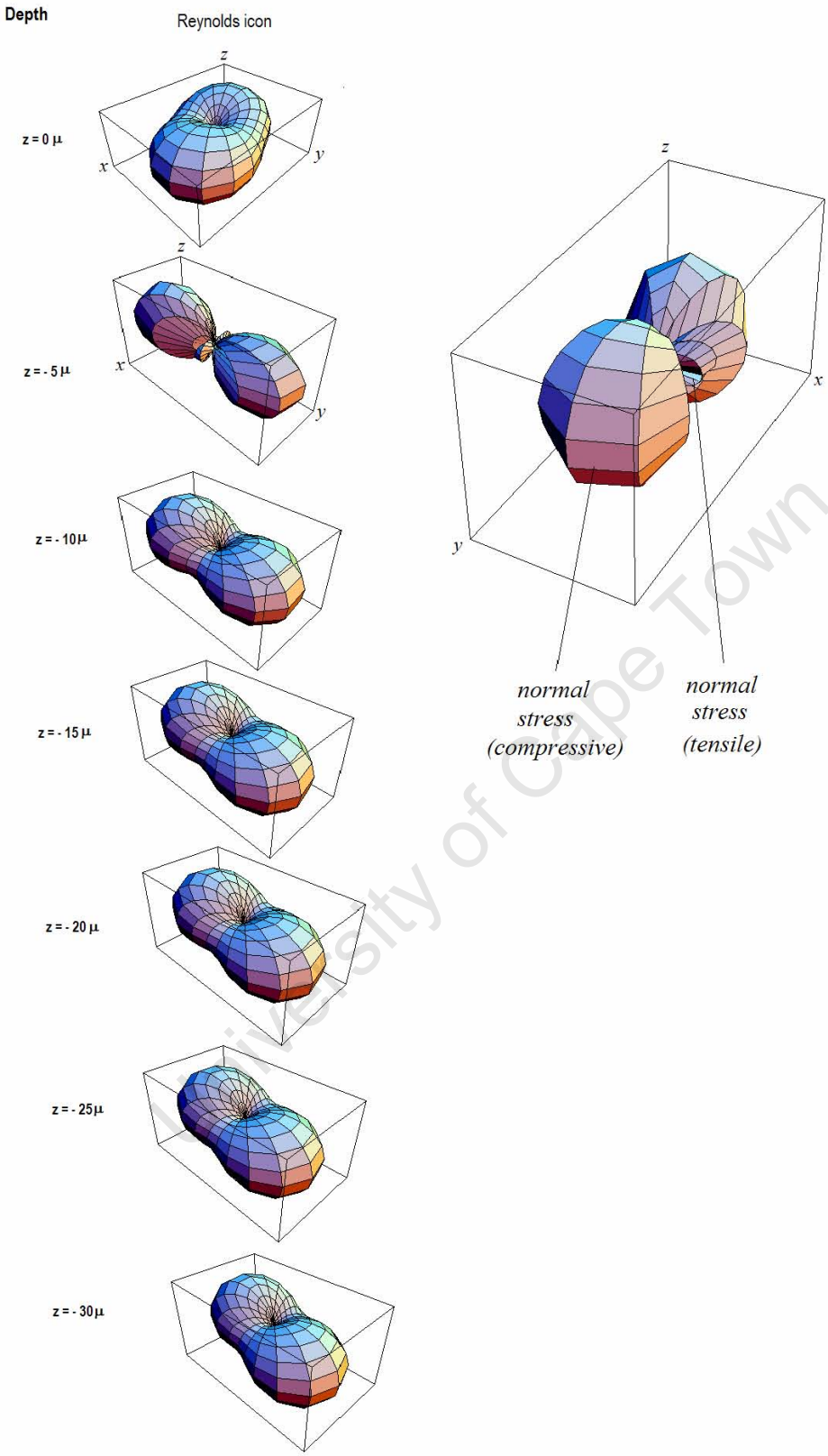

Figure 7-5 Reynolds icons shown in the isometric view. The icon at $z = -5\mu m$ is shown in two different viewpoints and normal stresses are indicated.

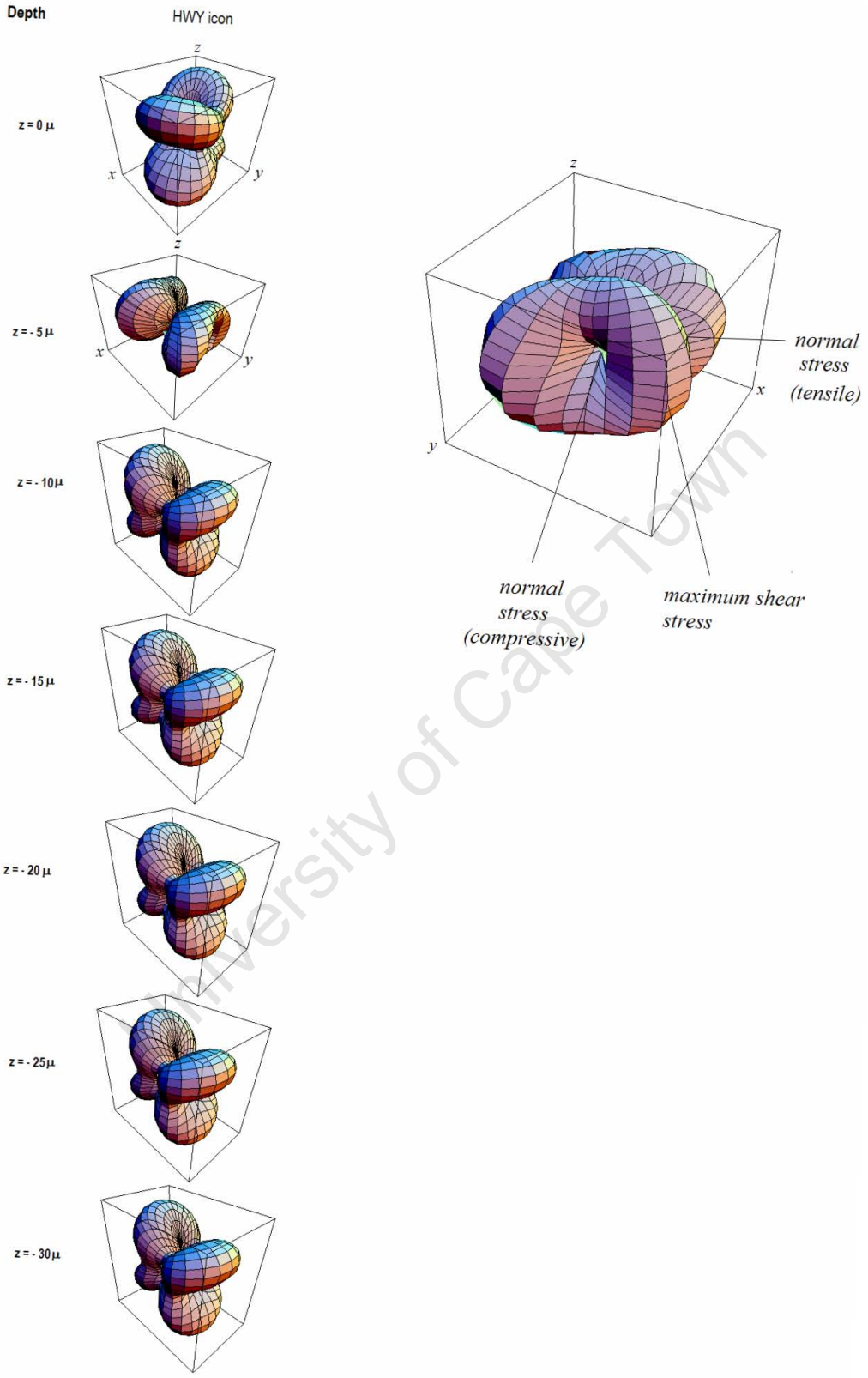

Figure 7-6 HWY icons shown in the isometric view. The icon at $z = -5\mu m$ is also shown in a different viewpoint and the zero normal and shear stresses are indicated.

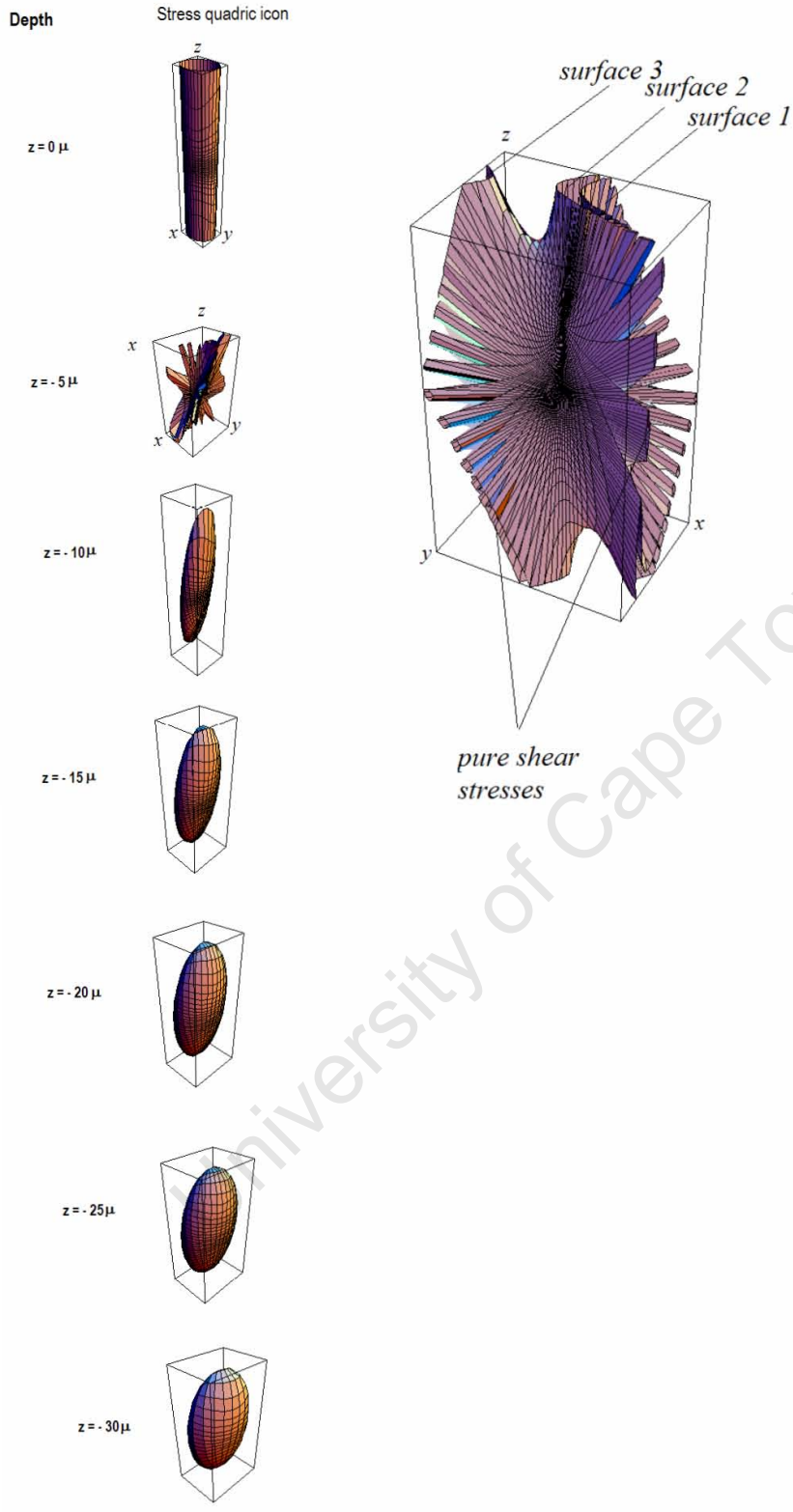

Figure 7-7 Quadric icons shown in the isometric view. The icon at $z = -5\mu m$ is also shown in a different viewpoint and the zero normal and shear stresses are indicated.

8 Case Study 3: Visualization of Residual Stresses in a High Performance Weld

In this case study, the residual stress profile of a high performance weld which was a prototype used in the space-shuttle [167], is explored using scientific visualization. The effects of welding and post weld heat treatment on the tensor stress profile of the weld are discussed. The stress determination at positions around the weld was carried out using neutron diffraction. In distinction to x-ray diffraction, using neutron diffraction stress, can be determined anywhere in the bulk material, which necessitates the tensor discussion of the stress state. The differences between the two diffraction methods and their implications for the visualization of the stress tensor profiles are discussed in this chapter.

8.1 Residual stress determination by neutron diffraction

Stress determination by neutron diffraction is, in principle, similar to stress determination using x-rays. The fundamental equation of x-ray diffraction, equation (5.10), can also be used in stress determination by neutron diffraction. The difference in the method lies in the position and size of the diffracting volumes due to the low absorption and low scattering of neutrons compared to x-rays. The penetration of neutrons in many materials is a approximately thousand times larger than the penetration of x-rays [1]. This enables measurement of bulk stresses using neutrons, by probing deep in materials, *i.e.* 25 mm in iron, 4 mm in titanium [129]. On the other hand, low scattering of neutrons from the crystal atoms, requires a larger diffraction volume to obtain sufficient diffracted intensities. Typically, strain and stress values are averaged over diffracted volumes up to 30 mm^3 to obtain sufficient diffraction intensities. The shape and the dimensions of the diffracted volume, and its position in the sample, is defined by slits positioned on the incident and diffracted beamlines, as shown in Figure 8-1. Different volumes can be probed by translation and rotation of the specimen. In this way the stress tensor can be obtained at discrete points throughout the specimen to a spatial resolution of $0.5\times0.5\times0.5\ mm^3$ [129]. Neutron

diffraction is sensitive to macrostresses and average microstresses. Theses stresses can be determined in length scales comparable to the sample dimensions from the strains measured at an accuracy 0.005% [129].

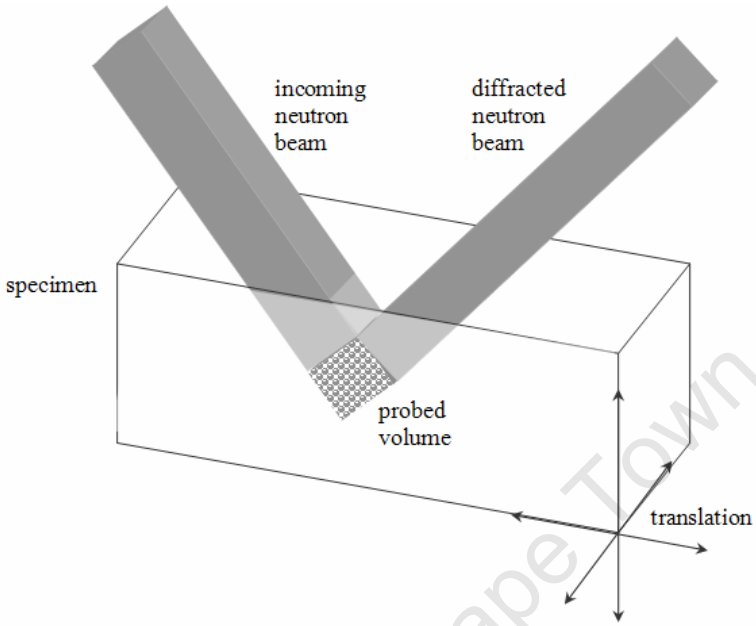

Figure 8-1 Diffraction volume geometry in a neutron diffraction experiment.

Although the underlying principle of using lattice strains as a gauge is the same for all diffraction methods, actual methods vary [166-168] and the determined stresses can be qualitatively different: if the conventional $\sin^2\psi$ technique is used, stress is obtained as a scalar; or alternatively, three orthogonal stress vectors can be determined along selected measurement directions [169 - 172]. In the latter case principal stress directions are *assumed* to be along the selected measurement directions. However these directions may, or may not, actually coincide with the principal stress directions [173, 174]. When the chosen directions do not coincide with the principal stress directions, the full stress tensor cannot be constructed. The measured quantity in this case is the stress vector, or traction, along the selected directions.

Using neutrons, in contrast to x-ray diffraction, all six components of the average stress tensor can, in principle, be simply determined from six linearly independent strain measurements. With neutrons, de-convolution of the strain contributions from

different depths is avoided by focusing the neutron beam exclusively to a diffracting volume, which cannot be done easily with x-rays [175]. Usually more than six measurement directions are used to improve statistical scattering in the data. Determination of the full stress tensor, in distinction to the vector stress determination using three orthogonal axes, becomes important in components where the principal directions of the stress tensor cannot be intuitively determined due to complex geometry or elaborate processing techniques.

Tensor stress determination has been applied in a number of recent research efforts, see for example [167, 175, 145, 176, 177]. In the case of welding, residual stress measurements help the understanding of the development of postweld heat treatments and process optimization to minimize detrimental residual stresses, which have an effect on the service lifetime of the components. Depth scanning methods such as neutron diffraction are particularly useful because they produce three-dimensional stress or strain maps for direct comparison with finite element modelling outputs [129].

8.2 Sample characterization and stress determination

In this study using neutron diffraction stress measurements, Winholtz and Krawitz determined tensor residual stresses inside a weld [12,167]. Residual stresses were determined in both the as-welded (AW) and post-weld heat treatment (PWHT) conditions to quantify the effects of welding and heat treatment. The system studied was a subscale model of the welds that were designed to be used in the construction of the NASA Advanced Solid Rocket Motor. Two cylinders were obtained by ring-rolling a HP-9-4-30 steel into cylindrical shape. The final cylinder was constructed by welding two 0.152 m high by 0.914 m diameter segments (Figure 8-2a). A micrograph of the final weld is shown in Figure 8-2b. Heat treatment consisted of two cycles at 522˚C for two hours each. The stress state at 14 different locations of the as-welded, and at 13 locations of the post-weld heat-treated circumferential weld joining the two cylindrical sections was obtained. The measurement grid with respect to the cross section of the weld is shown Figure 8-2c. The columns numbered A1–A5 at the centre of the weld line represent measurements in the radial direction (r) X_3, into the

material. Also indicates are the axial direction (z) X_2 and the hoop direction (θ) X_1. The sequence A, B, E, C, D indicate measurements in the axial direction away from the weld. The circles marking the measurement positions indicate that the strain measured within is an average over the probe volume of $3\times3\times3mm^3$.

The principle directions of the stress tensor were not assumed to be along any selected directions, but the full stress tensor was obtained by measuring strains in six independent directions.

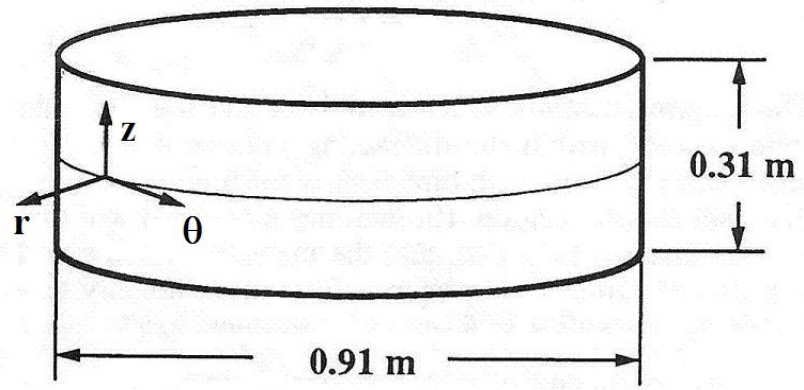

(a)

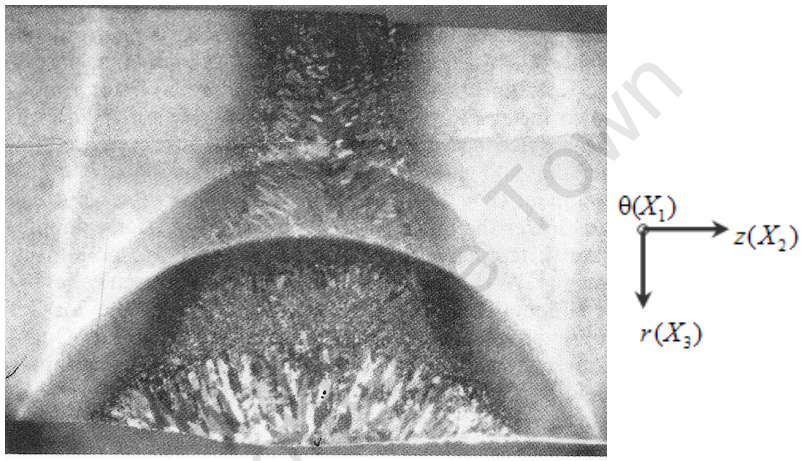

(b)

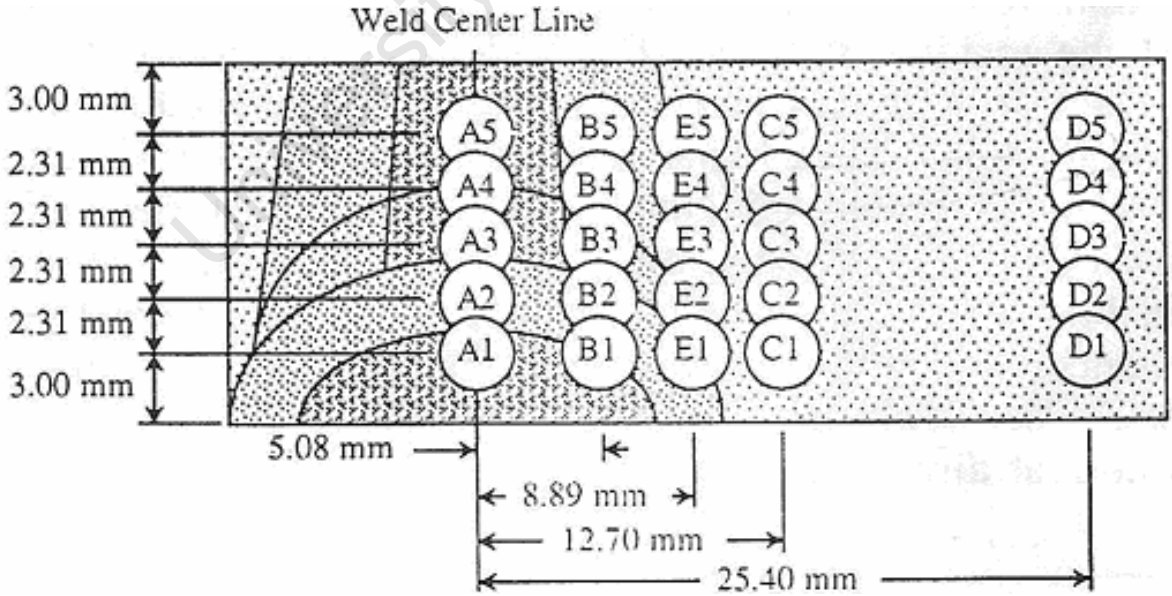

(c)

Figure 8-2 (a) Test cylinder geometry (b) micrograph of the weld cross section (c) measurement points [12].

The components of the stress tensors, given by the authors, are listed Table 8-1. Corresponding principal stress magnitudes, von Mises effective stresses, and the traces calculated from the stress tensors are listed in Table 8-2. The directions of the principal stresses are depicted by providing a list of the direction cosines of the principal stress direction vectors.

Furthermore, in order to convey the directionality information of the principal stresses, a Monte Carlo simulation was used by the authors to estimate the uncertainty of the directions of the obtained principal stresses (Figure 8-3). The equal area projections show the degeneracy of the principal stress magnitudes, which is a measure of the principal stress directions. The scattered distributions indicate degeneracy of the eigenvalues of the stress tensor. Concentrated point distributions indicate directional stresses.

Lastly, the scalar magnitude of the maximum principal stresses were depicted at individual points in a table style for comparison in the as welded and heat treated component (Figure 8-4). Effectively, these presentations show that tensorial stress is a complex, multidimensional, information rich physical quantity. In order to analyze the stress profiles as tensors, alternative methods are required. 3–D stress icons are used in the next section to represent the stress profiles and to reveal the inherent tensor characteristics.

	Measurement Points	σ_{11} (MPa)	σ_{12}	σ_{13}	σ_{21}	σ_{22}	σ_{23}	σ_{31}	σ_{32}	σ_{33}
As Welded	A1	-192	62	41	62	-213	161	41	161	-117
	A2	-212	79	12	79	-211	20	12	20	93
	A3	460	-99	-2	-99	667	-214	-2	-214	220
	B1	-370	-36	19	-36	-325	40	19	40	52
	B2	-69	-74	21	-74	-18	-41	21	-41	274
	B3	774	-65	-46	-65	553	-60	-46	-60	148
	E1	-12	-68	-11	-68	-199	-30	-11	-30	66
	E2	741	-74	-57	-74	199	145	-57	145	114
	E3	1045	1	-3	1	423	101	-3	101	242
	C1	246	-39	17	-39	8	61	17	61	114
	C2	220	-61	3	-61	88	40	3	40	84
	C3	119	-54	28	-54	85	12	28	12	52
	D1	21	36	41	36	48	22	41	22	72
	D2	-	-	-	-	-	-	-	-	-
	D3	26	-30	21	-30	90	25	21	25	94
Post Heat Treatment	A1	61	-31	-9	-31	-55	34	-9	34	30
	A2	33	-46	-5	-46	26	46	-5	46	112
	A3	132	-90	38	-90	339	-97	38	-97	117
	B1	76	-6	3	-6	-4	3	3	3	111
	B2	228	-39	-8	-39	205	-17	-8	-17	223
	B3	234	-68	-1	-68	267	-203	-1	-203	94
	E1	223	-26	-9	-26	70	4	-9	4	194
	E2	337	-67	-53	-67	120	63	-53	63	155
	E3	157	-56	-6	-56	59	8	-6	8	45
	C1	189	1	12	1	48	71	12	71	121
	C2	276	48	26	48	200	39	26	39	170
	C3	-126	-28	137	-28	68	-24	137	-24	6
	D1	121	-1	4	-1	81	10	4	10	110
	D2	-	-	-	-	-	-	-	-	-
	D3	-	-	-	-	-	-	-	-	-

Table 8-1 Stress tensor components [12].

Measurement points	As welded					Post Heat Treatment				
	σ_1 (MPa)	σ_2	σ_3	von Mises	Trace	σ_1	σ_2	σ_3	von Mises	Trace
A1	26	-210	-337	319	-521	76	32	-72	132	36
A2	96	-134	-292	337	-330	138	58	-24	141	172
A3	780	439	129	563	1348	412	99	80	323	591
B1	57	-308	-393	413	-644	112	77	-4	103	185
B2	283	27	-123	354	187	257	228	170	77	655
B3	794	547	134	577	1475	418	223	-46	403	595
E1	70	10	-224	269	-144	230	192	66	148	488
E2	760	289	5	661	1054	378	164	71	272	613
E3	1045	468	197	751	1710	183	47	31	145	261
C1	253	142	-27	243	368	193	159	5	174	357
C2	245	113	34	184	392	311	192	143	150	646
C3	162	73	22	123	257	117	43	-212	300	-52
D1	116	37	-11	111	142	122	111	78	40	311
D2	-	-	-	-	-	-	-	-	-	-
D3	117	88	5	101	210	-	-	-	-	-

Table 8-2 Principal stresses, von Mises effective stresses and trace of the stress tensors.

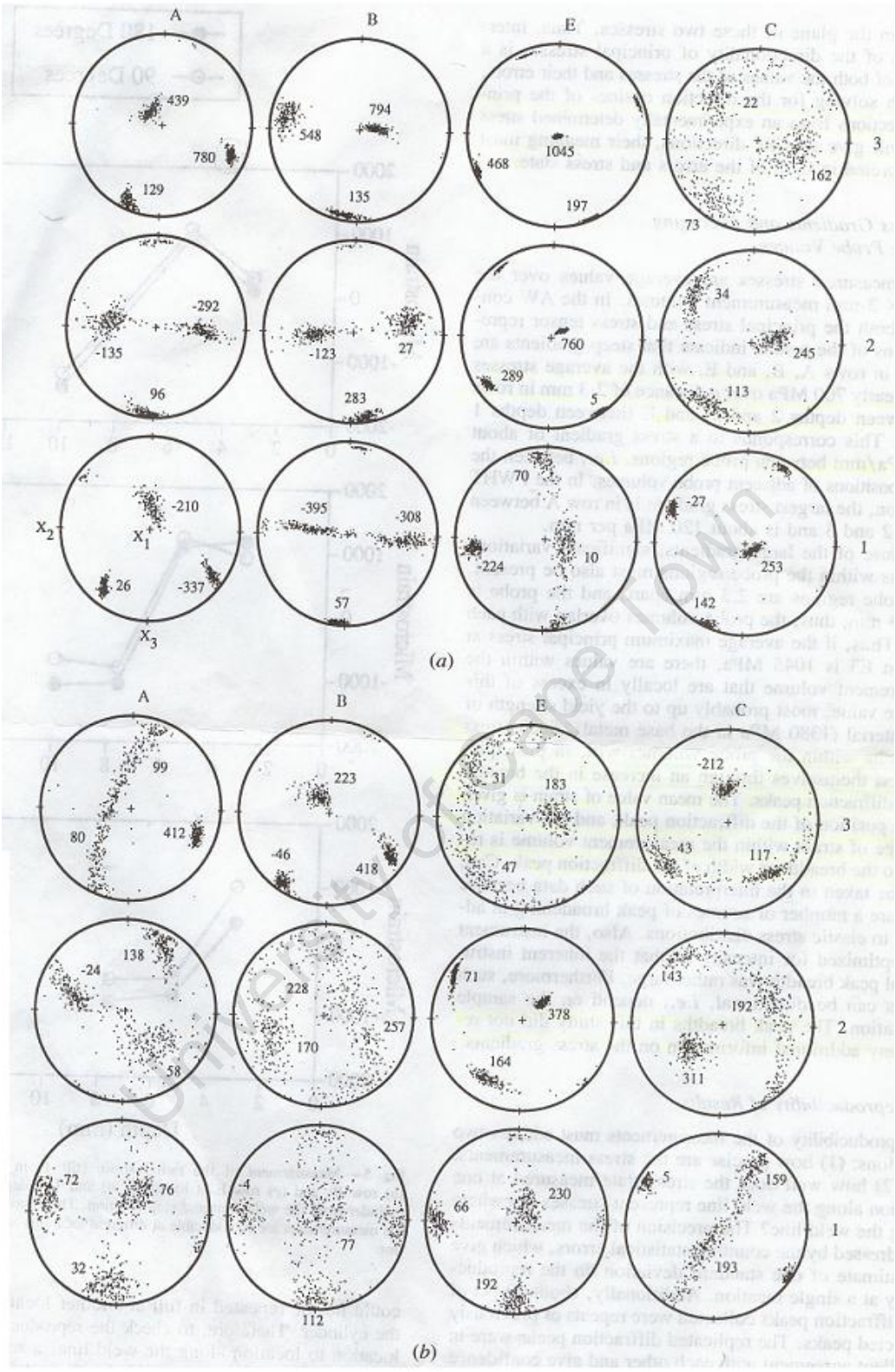

Figure 8-3 The distribution of principal stress directions in the (a) as welded and (b) post heat-treated conditions [12].

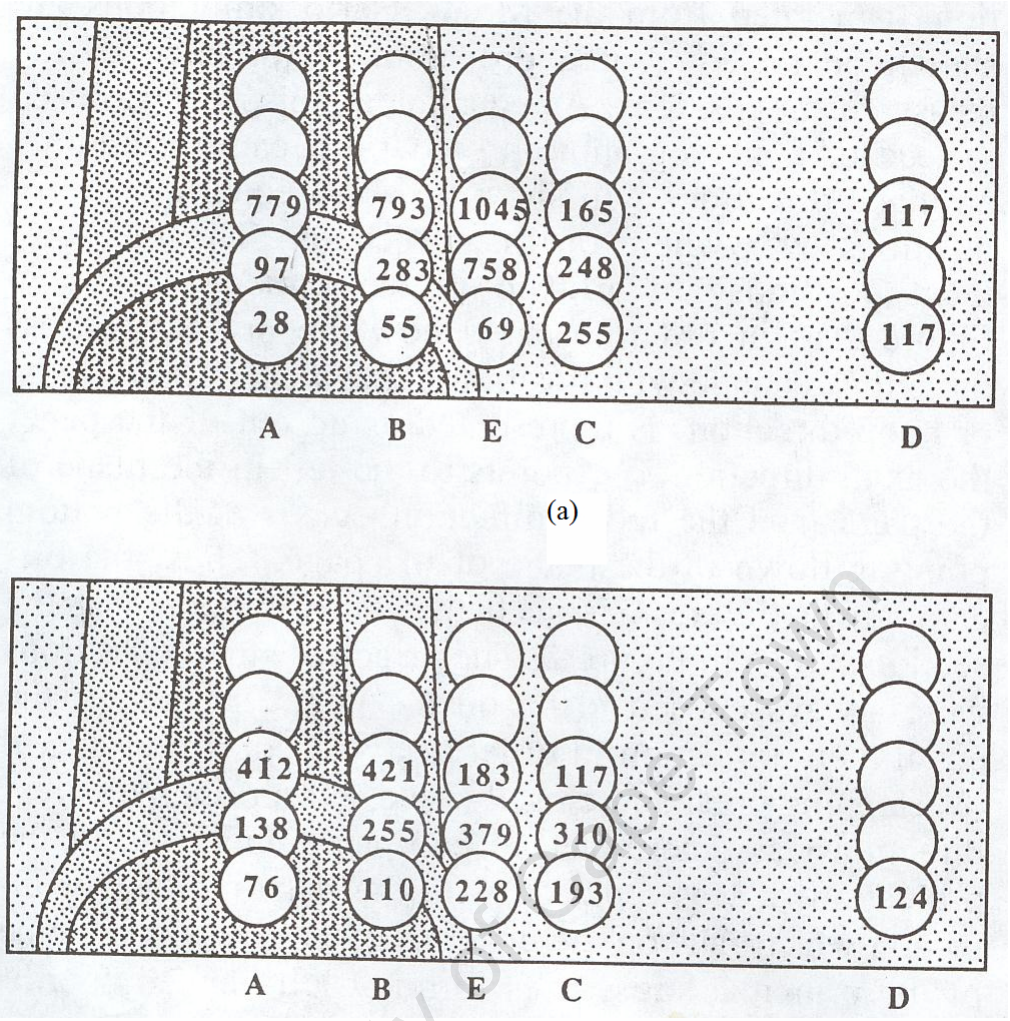

Figure 8-4 Maximum principal stresses for the (a) as welded and (b) heat treated welds [12].

8.3 Scientific visualization of the residual stress profiles

The starting point for the visualization of the weld stresses are the components of the stress tensors, listed in Table 8-1. The dataset is an $E_{[2]}^{\sigma_{33}}$ type entity, *i.e.* discrete second order symmetric tensors given on a two-dimensional plane. Because the dataset is discrete, point icons will be used for the scientific visualization. Another alternative would be to use local/ global icons, where the dataset can be interpolated between the measurement points to obtain a continuous distribution, using tensor

interpolation techniques [178]. However this is not possible, at least without multiplying the dataset along the azimuthal direction, since integral methods, *e.g.* hyperstreamlines, which use tri-axial eigenvector directions as the integration direction, cannot be used in a two dimensional domain, when for some stress tensors, the principal stresses point out of the domain. This point was also discussed using x-ray diffraction data visualization in section 4.3.7.2.

Similarly to the previous case studies, visualizations of the weld stresses comprise firstly the overall visualization of the stress profile, and afterwards exploring the individual stress tensor in detail, using complementary icons. PNS icons, as well as the Lame ellipsoids, are used to emphasize the type of stresses with respect to the weld geometry. The visualizations are also provided in the companion CD-ROM, and can be interactively explored using a VRML enabled web browser.

Lamé ellipsoids are presented for the as-welded stress states using two different colour codings: effective stresses are mapped in Figure 8-5a, and the traces of the tensors in Figure 8-5b. The measurement plane is shown in a perspective view indicating the structural features of the weld. The positions of the stress ellipsoids are labelled according to Figure 8-4. The Lamé ellipsoids are aligned according to their principal stress and shown relative to the sample coordinate system, in which the vertical axis coincides with the radial axis into the specimen, and the horizontal axis is pointing in the axial direction away from the weld.

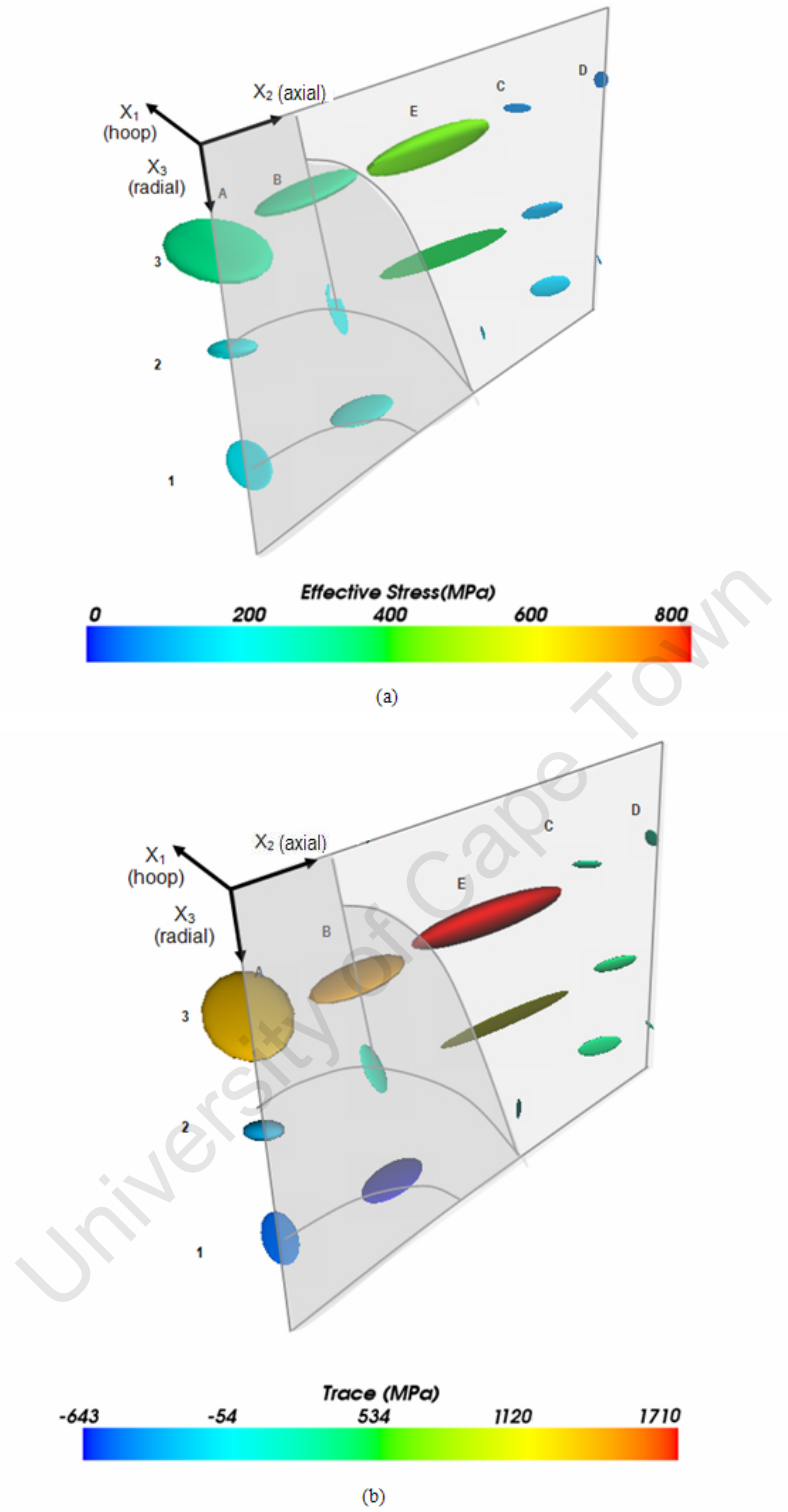

Figure 8-5 Visualization of the stress profile of the as-welded sample using Lamé ellipsoids. Colour coding represents (a) the effective stress (b) the trace of the stress tensor.

Ignoring colour coding, two features of the stress field can easily be seen: firstly, the orientation of the principal stresses with respect to sample; and secondly, a rough indication of the relative magnitude of the principal stresses, given by the size of the icons. Unfortunately, further away from the weld the icons are too small, compared to those near the weld, to convey any sensible information regarding the stress magnitude. However, it is possible to see that the orientation of the principal axes are not aligned with the sample axes, which was also pointed out in [12]. Using this visualization however, it is possible to go beyond the observation of Winholtz and Krawitz, and describe how the stress tensor is aligned in relation to the weld. In the centre of the weld the principle stress is aligned in the hoop direction. Away from the weld the stress tensor appears to be more or less uniaxial, and aligned in the axial direction pointing towards the weld line, as seen by the cigar shaped icons at positions E2, C1, and C2.

The shape of the ellipsoid, *i.e.* whether it is oblate, prolate or nearly spherical, gives an intuitive indication of the confidence which can be placed on the magnitudes of the principle stresses, and more importantly their directions. In the original work [12] this could only be obtained through a systematic Monte Carlo simulation of the data. Nevertheless, drawing the ellipsoids in the sample co-ordinate system can lead to confusion if the principle axes are unluckily oriented. For example, at the wrong angle, a disk shaped oblate ellipsoid can look like a cigar shaped prolate ellipsoid. This is, of course, not a problem if the full possibilities for visualization using interactive computer graphics, where the viewing angle can be changed, are used.

A common method is to fill the ellipsoid with colour or a gray tone according to a linear map of the effective, or von Mises, stress. As is well known, the von Mises stress is a scalar measure of the anisotropy of the stress tensor, being zero for a hydrostatic stress [14]. In Figure 8-5a the ellipsoids are coloured according to this scheme, and it can clearly be seen, that the effective stress is greater for the elongated ellipsoids pointing towards the weld, than those in the weld. It is obvious from the figure, that the magnitudes of both the effective stress and the principle stress (major axis of the ellipsoid) decrease moving away from the surface, pass through a minimum, and then increase with distance (line A1 – A2 – A3). A similar behaviour is seen in the axial direction, away from the weld (A2 – B2 – E2, or A3 – B3 – E3).

This conclusion is unfortunately wrong, because neither the ellipsoids nor the von Mises stress are capable of giving any information concerning the sign of the stress.

Common sense would suggest that there is a change from compressive to tensile stress, or vice versa, moving away from the weld and the surface. This is apparent if we colour the ellipsoids according to another invariant quantity, the trace of the stress matrix (Figure 8-5b). For a net tensile stress the trace is positive, and conversely for a net compressive stress it is negative. A special case arises for a pure shear, for which the trace is zero [179]. Using the trace as a colour code, it becomes obvious, that the surface region of the weld is under a net compressive stress aligned predominantly in the hoop direction, and that further away there is a net tensile stress directed towards the weld. It is also a simple matter to visualize the position of the curved neutral line in the material. Although the presence of a shear stress can be inferred from a zero trace, for a non-vanishing ellipsoid it is not intuitively obvious. This situation can be improved by the use of a colour map, indicating normal and shear stresses, on the ellipsoid surface as described below.

Figure 8-6 shows the PNS icons for the as-welded state in the same orientation as the two preceding representations. Unlike the conventional stress ellipsoids, however, the PNS icons have all been scaled to the same length of their major axes. Although this eliminates all information concerning the absolute magnitude of the stresses, it makes the stress distribution at each position more clear. With interactive computer graphics, which have the ability to zoom and rotate the ellipsoids, the icons can be shown with their correct relative sizes.

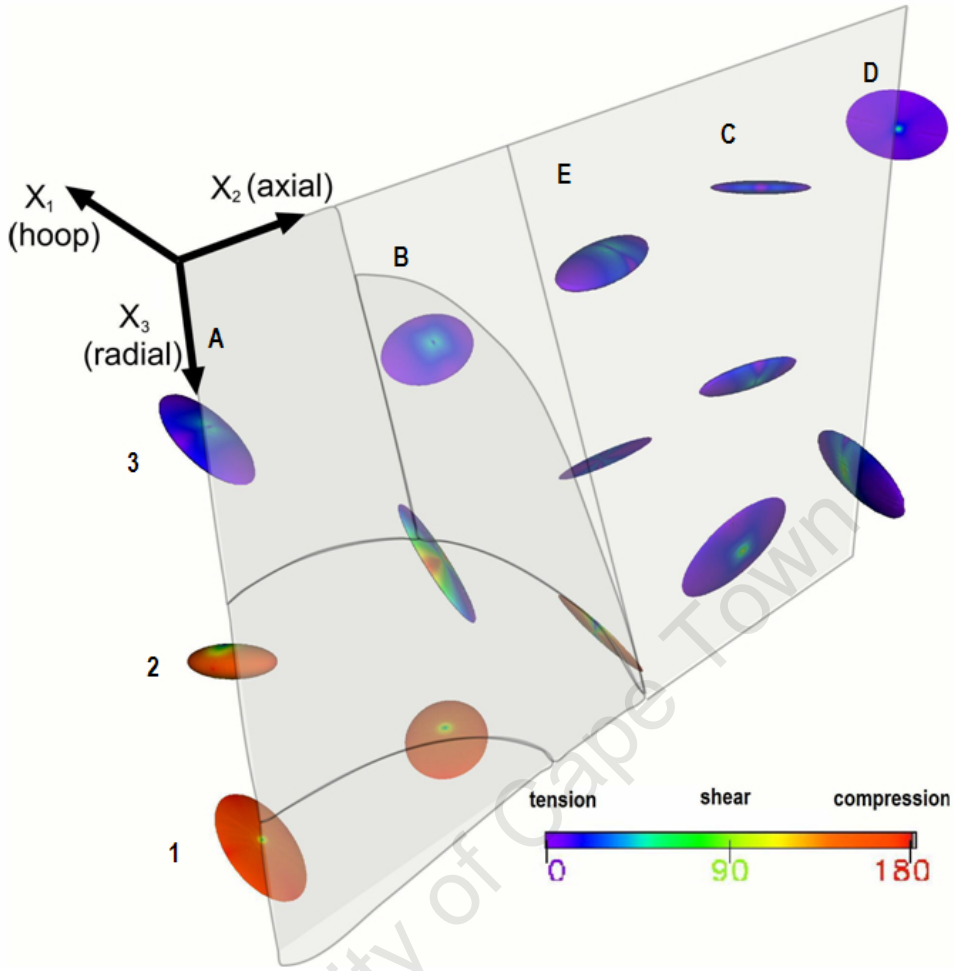

Figure 8-6 Visualization of the stress tensor field of the as-welded sample using the PNS icons. Colour coding represents tensile, compressive, and shear stress directions with respect to the sample position and orientation. To emphasize the colour coding, the icons are not scaled in this figure.

The advantage of this representation is that it shows the geometric structure of the individual stress state, in contrast to a single colour code which highlights an average property. The presence of shear forces is clearly shown at the positions, A2, B2 and E1, near the previously observed neutral line, by the green bands or circles on the ellipsoid surface. An important aspect of this particular visualization is that, because the stress ellipsoid is aligned with the sample coordinate system, both the location and direction of the maximum shear forces can be inferred directly. This is potentially of particular importance in evaluating possible sites of material failure, yielding or fracture, under load. The shear forces are directed from the centre of the ellipsoid towards the regions indicated by the green colour.

A pure shear stress, with a zero trace, appears as a prolate ellipsoid, with its major axis twice as long as the other two and having opposite sign. The nearest examples to a pure shear are at positions B2 and E1, which, however, have a non-zero trace representing small net tensile and compressive stresses respectively. The same ellipsoidal shape also results from a pure compressive or tensile stress, with principal stresses in the same ratio of 2:1. Without the PNS colour coding on the surface, it would not be possible to distinguish between these two cases. However, the PNS icon for the pure tensile stress has a single dominant colour, *e.g.* compare the icons at positions A3 and E1, or E3 and A2.

Stress states with all positive or negative principle stresses do, however, have shear forces associated with the stress vector, shown by the variation in colour on the ellipsoid surface. This is never a pure force, and the stress vector always contains a normal stress component, outwards for a tensile stress, and inwards for a compressive stress. This effect is visible on the icons for all the tensile stresses outside the neutral line, *e.g.* at positions C1 and D1 away from the weld, or at positions A3 and B3 deeper in the material.

Inside the weld, near the surface (A1, A2, B1, B2, and E1) the icons have a similar colour coding, showing compression in the hoop and axial directions, and tension in the radial direction. Only the relative magnitudes, and hence the shape of the ellipsoids, changes between the different positions. For example, the icon at E1 is

characterized by a strong compression directed near to the hoop direction, along the weld, whereas at position B2 there is a strong tension in the radial direction, into the weld. PNS colouring also makes a biaxial state more easily apparent, with the shear forces concentrated near a single axis (*e.g.* icons at A1, B1, and C1). This is not so easy to see with a solid colour rendering for each ellipse, as in Figure 8-6, without using several different viewpoints to resolve the flat shape.

The stress profile of the sample after heat treatment is presented in Figure 8-7 and Figure 8-8 using Lamé ellipsoids, and in Figure 8-9 using PNS icons. The more spherical icons show that the stress state became isotropic. The changing of oblate and prolate ellipsoids into more spherical ones can be seen at B3, E2, and E3. The ellipsoids in the weld area, A1, A2, and A3 are diminished to very small sizes compared to the outer ellipsoids, which is an indication that the weld experienced greater relaxation compared to the base metal.

The effective stress colour coding (Figure 8-7) shows the relaxation of the effective stresses, especially in the weld boundaries, A3, B3, E3, and E2. The colour changes from green-yellow to blue, indicating a decrease of effective stresses of 300 – 400 MPa due to the heat treatment. The trace colour coding (Figure 8-8) indicates similar relaxations of compressive and tensile stresses after the heat treatment. The highly tensile values of the as welded sample traces (~1500MPa) reduce to lower values indicated by the green-yellow ellipsoids. The overall stress state of the annealed sample can be estimated from the colour codes as being 150 – 250 MPa. The relaxation is also seen for the compressive stresses, A2, A1, B2. The trace visualizations show that the stress tensors become more spherical after the heat treatment.

The effect of the heat treatment on the principal and shear stresses can be seen from the PNS icons of Figure 8-9. The colour coding of the icons is dominantly blue indicating isotropic tensile stresses. At positions A2 and B3 biaxial stress tensors have slight compression components normal to the planar tensile stresses. Icons at A1 and C3 indicate pure shear stresses, contrary to the overall removal the shear character of the stresses. However, these ellipsoids are relatively small compared to

the average ellipsoids of the weld. The removal of shear stresses is clearly seen by comparing Figure 8-6 and Figure 8-9.

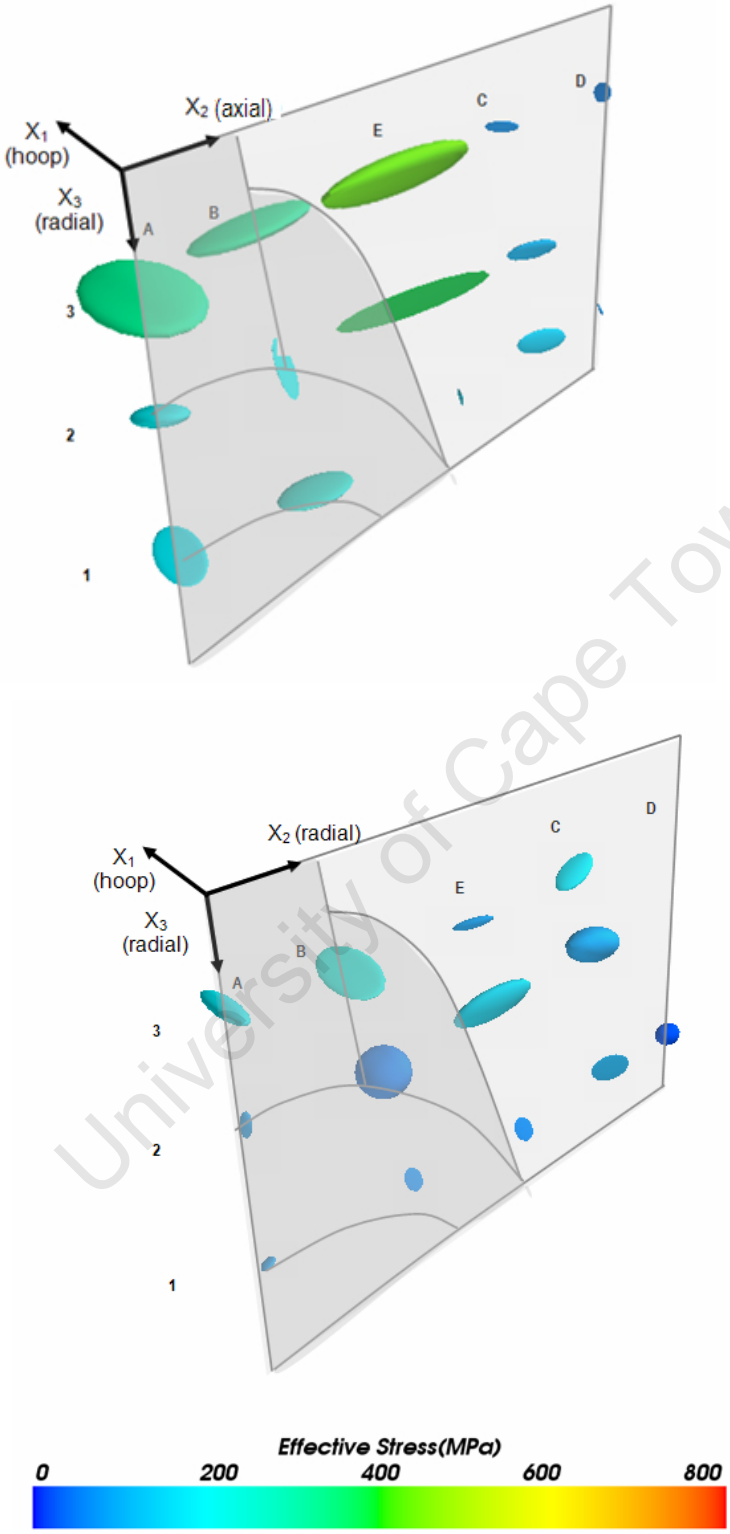

Figure 8-7 Visualization of the stress tensor field of the as-welded (above) and post-heat treatment sample (below) using ellipsoids. Colour coding representing the effective stresses.

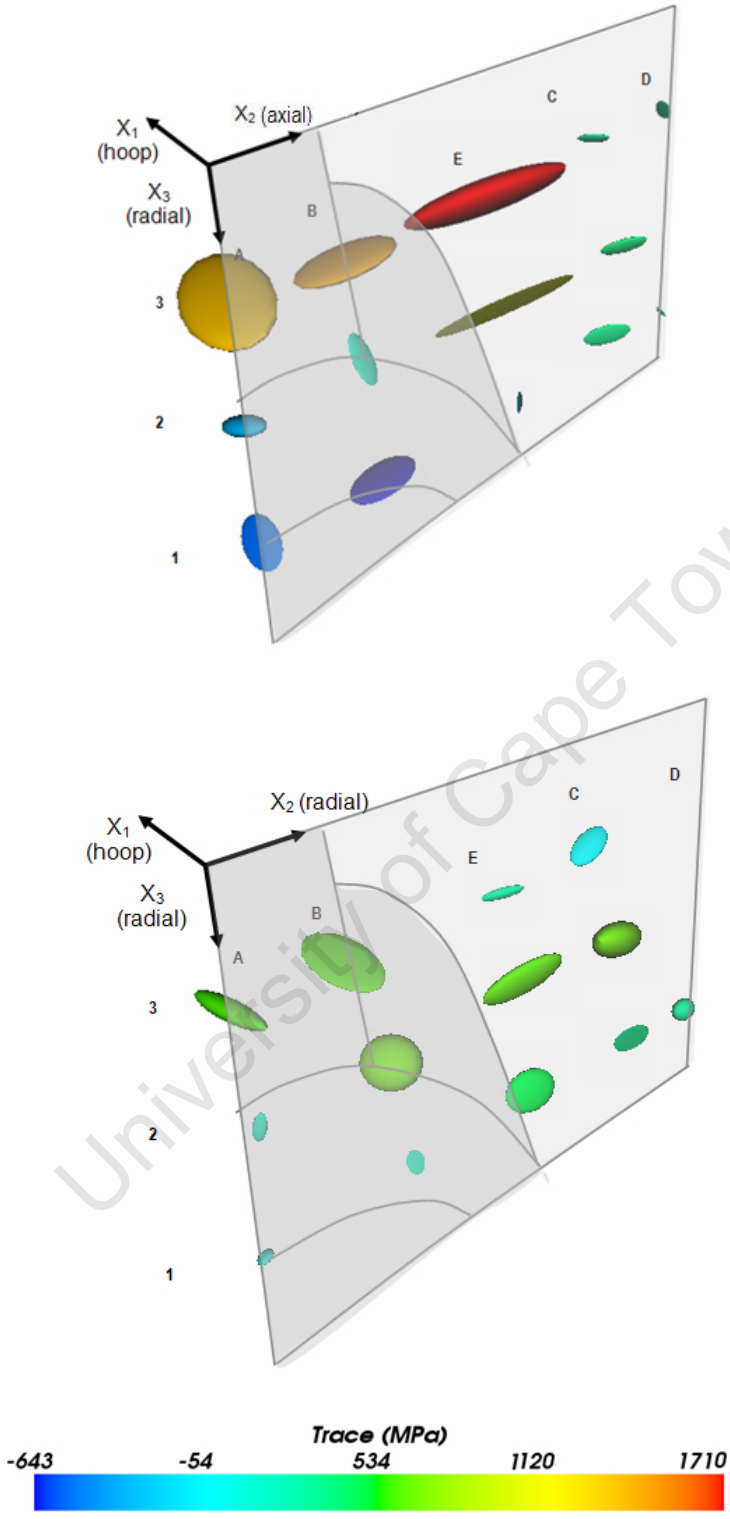

Figure 8-8 Visualization of the stress tensor field of the as-welded (above) and post-heat treatment sample (below) using ellipsoids. Colour coding representing the trace of the stress.

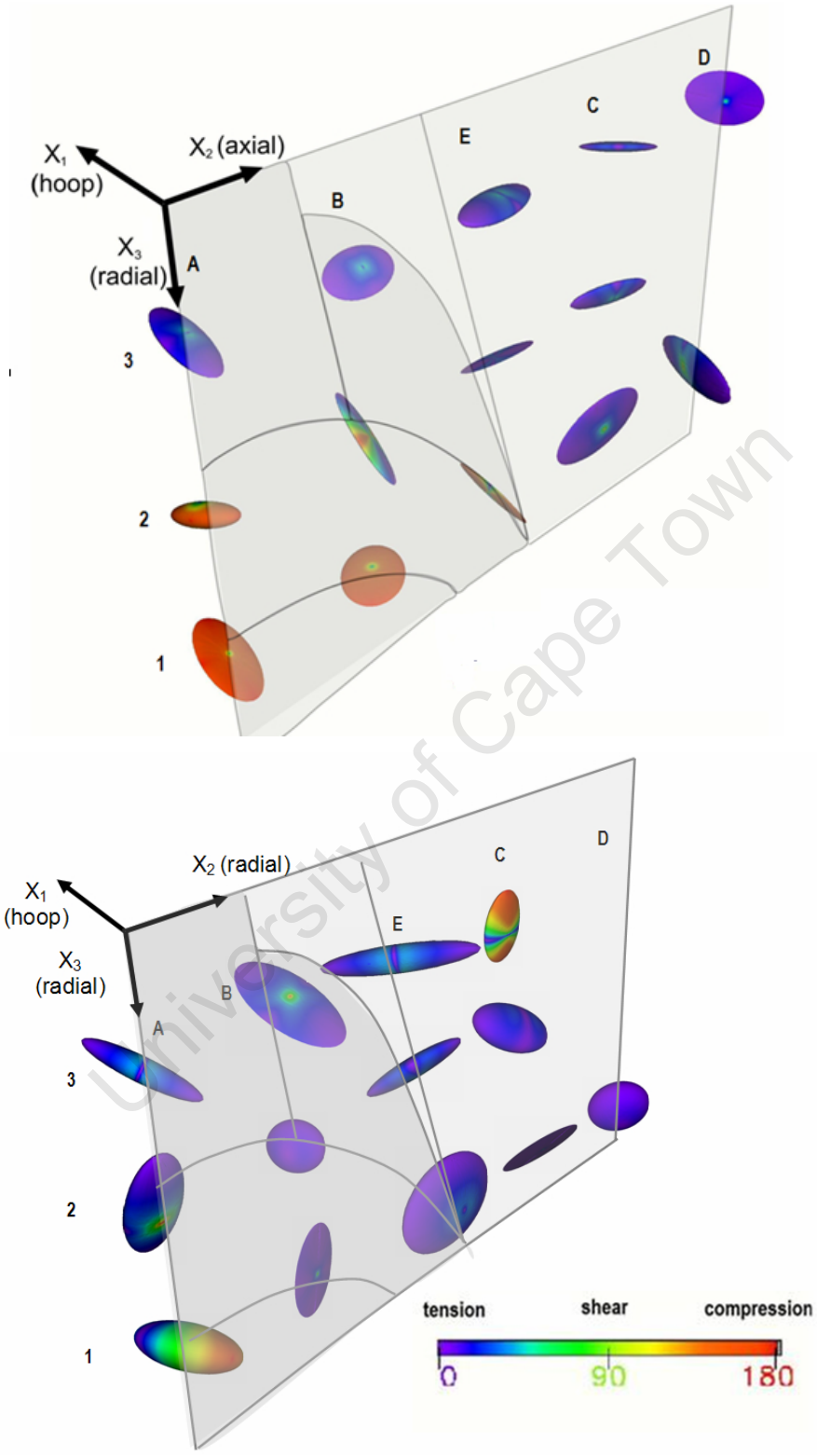

Figure 8-9 Visualization of the as-welded (above) and post-heat treatment sample (below) using PNS icons.

The overall stress profile indicates a change in directionality and type of the stress tensors in the weld area, weld boundary and the outer regions. Furthermore heat treatment partially removes welding stresses, changes directionality of the stress tensors, reduces stress magnitudes and also increases the isotropy of the stresses. In this section, each stress tensor is visualized individually in order to explore the stress tensors in more detail, at each location. The icons are individually represented isometrically in the weld coordinate system, and scaled to the same size to highlight tensor features, before projecting onto a two-dimensional grid in the $x_2 - x_3$ plane. The **PNS icon visualization** (Figure 8-10) is repeated in this projection to allow direct comparison with the other icons discussed below.

The normal stress distributions of the stress tensors are shown in the **Reynolds icon visualization** (Figure 8-11). In the as-welded state, at the weld boundary (B2 and E1), quadruple-lobed icons indicate the presence of bi-axial normal stresses with different signs. The shape of the icon at A2 indicates a tri-axial stress, where normal stresses in the axial-hoop plane have the same sign, and the normal stress in the radial direction is opposite. These features are, also seen from the PNS icons (Figure 8-10) and furthermore the types of the stresses can be differentiated. Torus shaped icons at A1, A3, B1, and B3 show bi-axial stresses, with zero or very small normal stress in the radial direction. Similarly C1 and D3 show planar stresses with zero or very small normal stress in the hoop and axial direction respectively. The orientations of all Reynolds icons are along the principal stress directions, and therefore correspond with the orientation of the stress ellipsoids and the PNS icons. After heat treatment, quadruple-lobed icons at the weld boundary are replaced by a spherical Reynolds icon at B2 (hydrostatic stress), and by a torus like icon at E1. Icons at A1 and C3 are typical examples of Reynolds icons for opposite signed tri-axial and bi-axial stress states respectively. Note that these two specific icons are relatively small if viewed to scale in the overall stress profile.

The **HWY icon visualization** (Figure 8-12) represents the shear component distribution of the stress tensors. It should again be noted that the shapes of the HWY icons are always very similar to each other, as seen in both in the as welded and post heat treated samples. The only difference is the alignment of the icon. Since, similarly

to the previous icons, the HWY icon is aligned in the principal stress directions, it does not provide much additional information. However, using the HWY icons we see that the maximum shear stress directions are slightly different than the pure shear direction, *e.g.* for the post heat treated samples, compare the HWY versus the PNS icon representation at A1 and C3. The blue colour band, and the red colour on the poles of the PNS icons (Figure 8-10) correspond to the cleavages in the HWY icon where there is no shear stress.

The **stress quadric icon visualization** (Figure 8-13) shows distinctive shapes for the as welded sample. Diverging hyperboloids can be seen in the weld boundary (A2, B2, and E1). Where all three principal stresses have the same sign, closed ellipsoidal icons are seen, *i.e.* A3, B3, E3, C3 and C2. Because the stress quadric icon is drawn using the inverse square of principal stresses, the closed ellipsoidal representations are more elongated than the PNS icon representation. For the post-heat treated sample the icons are more isotropic. The sizes of the diverging icons at A1, A2, B3, and C1 are relatively small if considered in the overall stress profile. However, the icon at B3 indicates pure shear stresses, which can be confirmed from the PNS icon with a red pole and blue band around its equator (Figure 8-10).

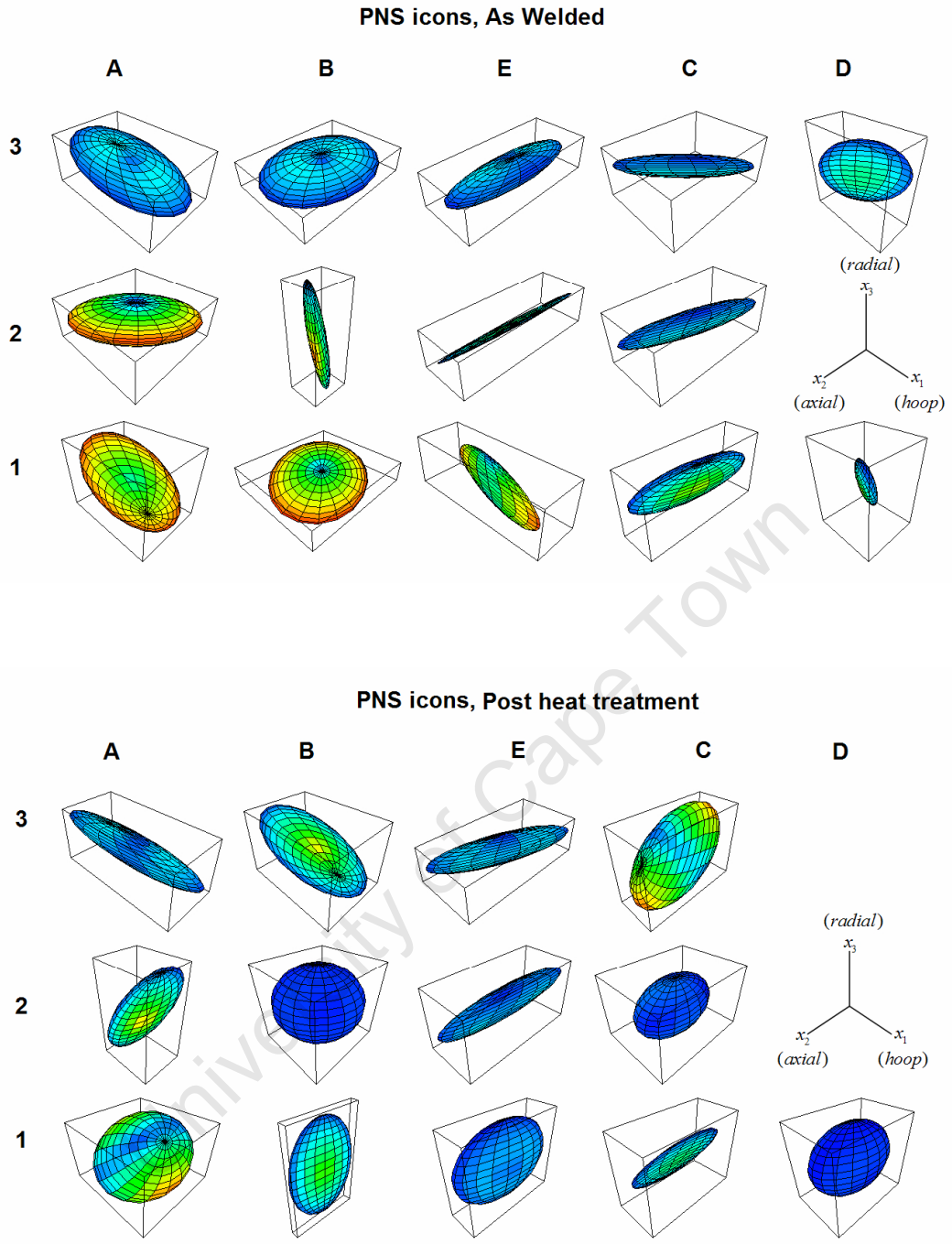

(b)

Figure 8-10 PNS icon visualization of the as welded and post heat treatment stress tensors.

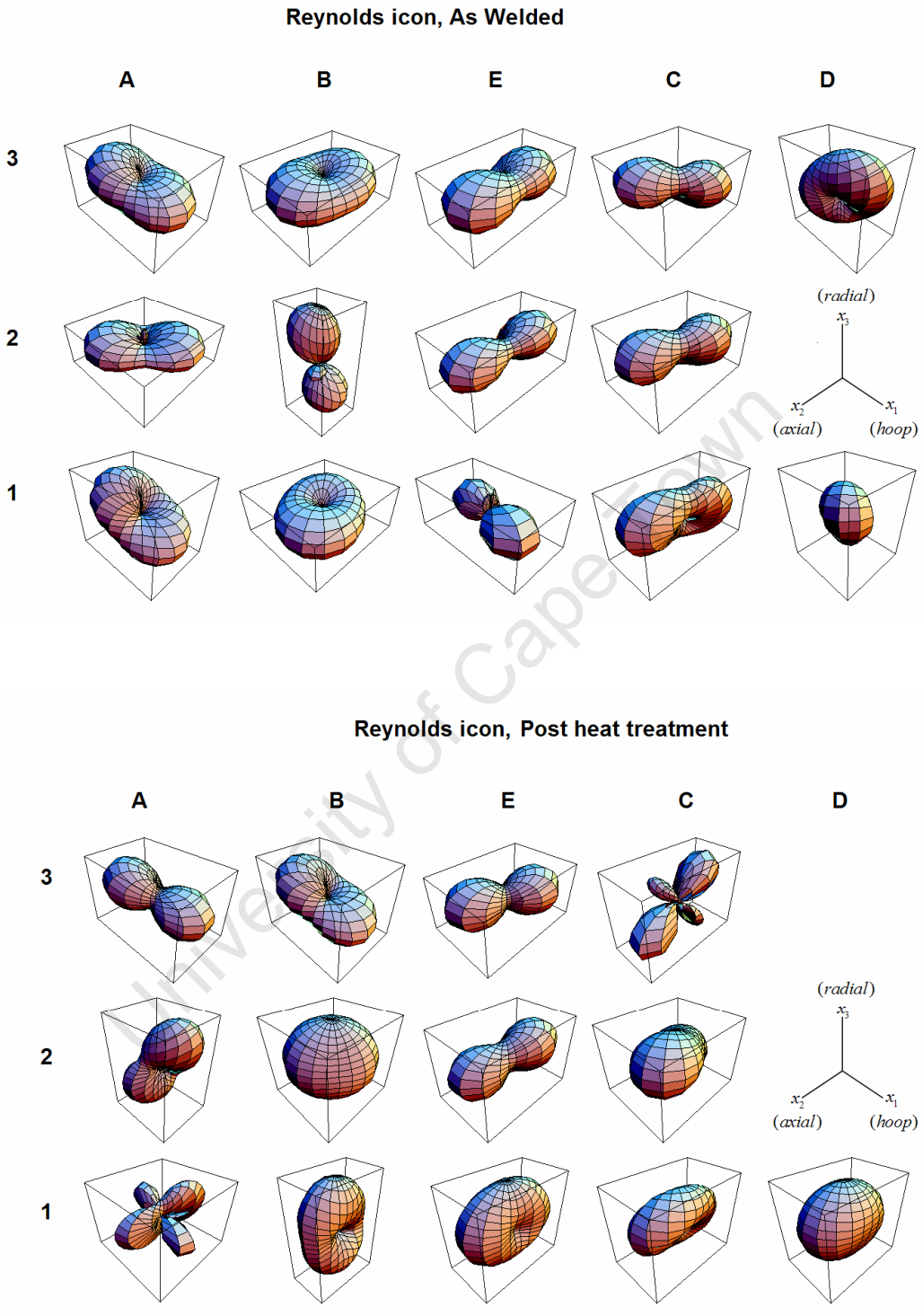

Figure 8-11 Reynolds icon visualization of the as welded and post heat treatment stress tensors.

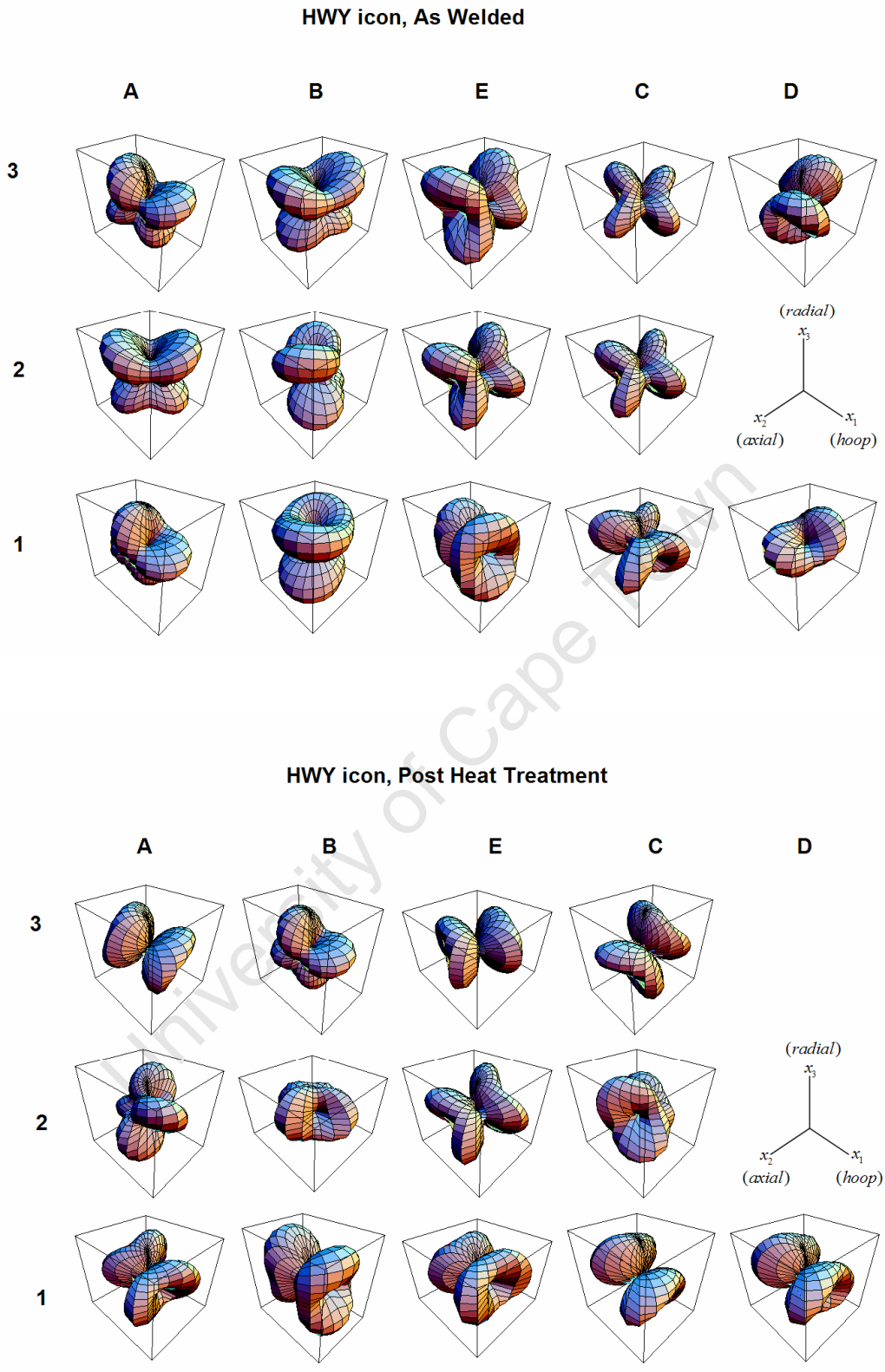

Figure 8-12 HWY icon visualization of the (a) as welded (b) post heat treatment stress tensors.

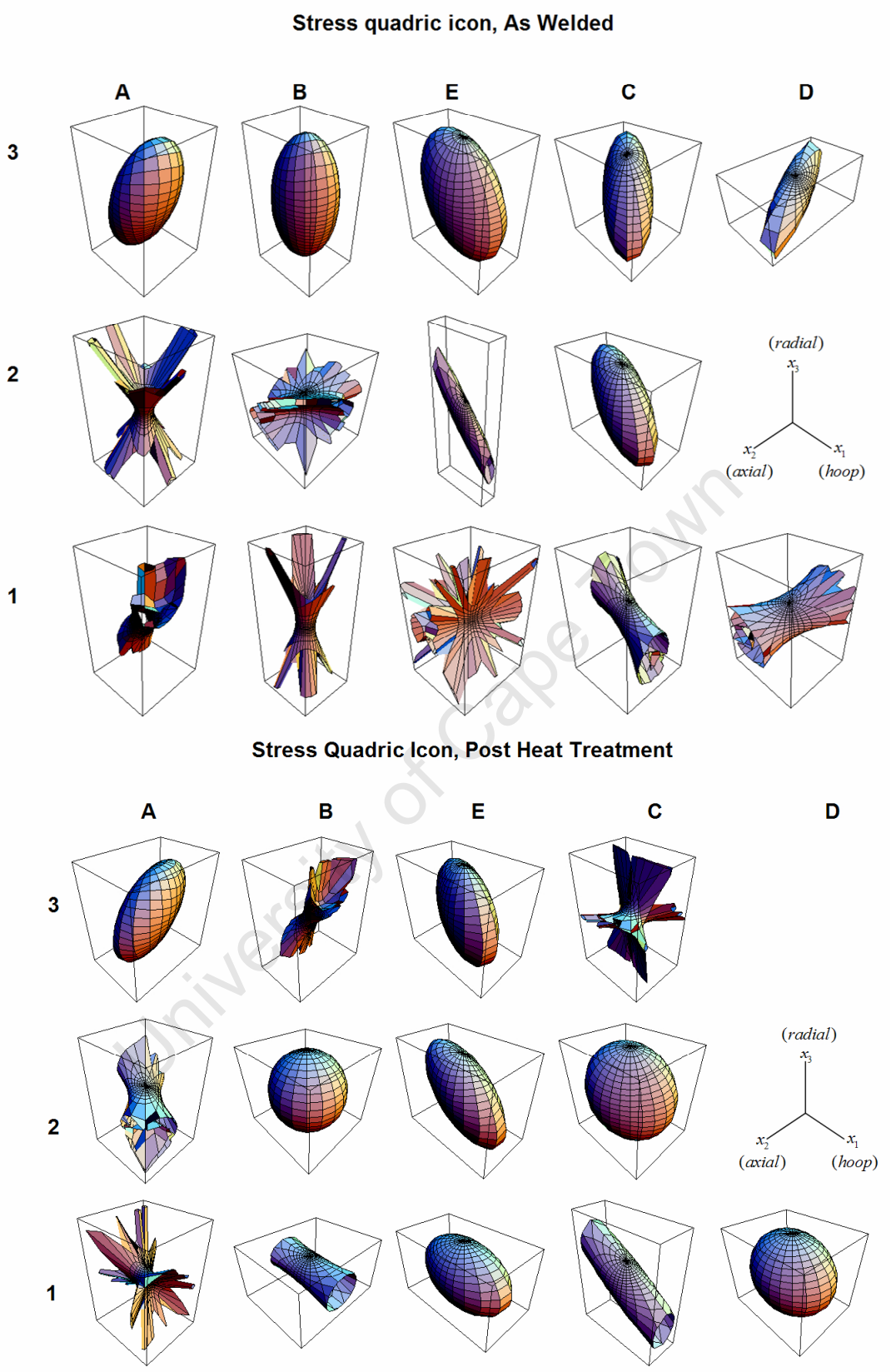

Figure 8-13 Stress quadric icon visualization of the (a) as welded (b) post heat treatment stress tensors.

9 Conclusion

In this thesis a rigorous framework was developed and used for the scientific visualization of the stress tensors that can be obtained from diffraction measurements. The simple fact that mechanical stress in a material is a tensor quantity is usually overlooked, and usually due to experimental constraints, mechanical stress is reduced to a scalar or, in other cases to a vector quantity. However, scalar methods, such as the conventional $\sin^2\psi$ curves method used extensively in residual stress determination, inevitably result in the reduction of the essential structural information. The introductory chapter on the mathematical features of tensors, Chapter 2, highlighted the structural information contained in second rank tensors, concentrating on the stress and strain tensor. In this work it was shown that, to adequately explore stress in materials, it is essential to obtain the full stress tensor. The tensor stress determination from diffraction methods, using x-rays, synchrotrons, and neutrons, etc. is discussed in Chapter 5 and the shortcomings of conventional methods in describing the tensorial stress were demonstrated. The exploration, interpretation and representation of the resulting tensor quantity turns out to be challenging. Scientific visualization provides an opportunity for the interpretation of stress tensors effectively and easily.

Scientific visualization requires the understanding of the physical dataset to be visualized as well as the extensions and attributes of the visual icons. Therefore, to develop a successful graphic representation of stresses in materials, it is essential to have a reference framework for all processes of the scientific visualization pipeline which consists of data acquisition, categorization of the domain and data dimensionality, visualization mapping of the physical data onto the graphic extensions of visual icons, rendering of the visual icons, and finally the cognition and perception of the information by the human mind. These processes were discussed in Chapters 3 and 4, firstly in the larger context of scientific enquiry and later specifically for the visualization of second rank tensors. Only with a rigorous mathematical categorization of the domain and the dataset, it is possible to identify the data type of the physical quantity which dictates the appropriate mapping algorithm, visual icon and its attributes. The concept of data isomorphism was introduced for the selection of

a proper visual idiom based on the domain and data dimensionality of the physical quantity.

The visualization of stresses is achieved by using the whole set of *point tensor icons*, *i.e.* the Lamé ellipsoid with colour coding, the Reynolds icon, the HWY icon and the stress quadric icon. Furthermore, a new icon, the PNS icon, was developed using the colour coding applied to hyperstreamlines. The choice of point icons over local/ global icons was motivated by the nature of the dataset obtained from diffraction experiments. In the case of neutron diffraction, where the stress tensors are obtained at discrete points in the specimen, the use of point icons is intuitive. On the other hand, x-ray diffraction depth profiling methods provide continuous distribution of stress tensors components with depth. In this case, the dimensionality of the dataset (tri-axial stress tensor) is larger than the dimensionality of the domain (depth, *i.e*. one-dimension) and consequently local/ global integral methods cannot be used since the integration along the chosen principal axes will take the integral curve out of the data domain. Integral methods can only be used after creating multiple sets of synthetic data, under consideration of using specimen and treatment process geometry symmetry, and after interpolation.

With any of the existing stress icons, it is not possible to convey the full structural information of the stress tensor, such as the principal stresses, traction or the stress vector in 3–D space at a point, tensile, compressive stresses, normal and shear stresses, pure shear stress, uni-axial, bi-axial, tri-axial stress states, and the hydrostatic stress state. Some of these icons are intuitive but only provide partial information such as the stress ellipsoids. HWY icons in the cases studied here are not as useful. Some are complicated to interpret and, require experts information and familiarity to extract stress information, such as the Reynolds icon. Others give distinct representations indicating various stress types clearly however are not intuitive for perception, like the stress quadric icon. With the PNS icon, which is based on the familiar Lamé ellipsoids, an intuitive colour map is used to show all the structural information. The advantage of using the PNS icon over the other point icons was illustrated in the cases studies.

Beside the individual interpretation of the point icons, visual cognitive interpolation of the whole set of point icons enables Gestalt perception – the perception of the whole as greater than the sum of its parts. This can be seen, for example in the first case study, where the effects of ion implantation can be seen from the evolution of the icons with depth and implantation. In case study 2 tensile and compressive stress distributions highlight a shear stress region just below the surface. In the last case study, heat induced compressive, tensile and shear stresses in adjacent regions can be seen from the similar colours of the PNS icon. Also the visually distinctive icons, like the stress quadric icon, indicate the change of stress state within the sample. In this case discontinuous changes in the stress tensors correspond to the weld geometry.

Finally, visualizations should be evaluated in the context of the physical system with regards to the material structure, material geometry and mechanical/thermal process dynamics. It is important to note here that the visualized data domain is usually a subset of the whole specimen, and it is sampled at discrete points. The mechanical stress state needs to be generalized from the visualization of these measurement points. Using scientific visualization insight into the stress state of the whole physical systems is achieved. The selected case studies, by bringing new insight into the results of diffraction measurements, establish the fact that scientific visualization can be the key to comprehensive analysis of residual stresses.

This thesis has demonstrated that x-ray and neutron diffraction research can benefit from the novel techniques that the newly emerging scientific visualization made available to scientist and engineers. However, the promises of these new tools and techniques are still little known, and appreciated, in the wider research circles. One reason for this gap is that the methods have been developed strictly within the frame of computer visualization. However, no matter how sophisticated or visually engaging the resulting pictures are, the real measure of success of visualization in scientific research is the helpfulness of the methods developed to the researchers. Therefore in this thesis, visualization is considered as an integral part of the wider research context. In this sense, the involment of the researcher in the whole visualization process can not be emphasised strongly enough.

Because scientific visualization is only beginning to be used in field of diffraction, there are many open problems to be addressed. First and foremost is that, historically the visualization of tensor datasets has been developed to address the problems in fluid dynamics, in which the nature of dataset is different to that obtained with diffraction measurements. Therefore usually the direct application of these methods is either not possible or reveals little insight to the diffraction datasets. New visualization techniques are necessary where the nature of the dataset, *e.g.* dimensionality, spatial resolution (continous /discreete), tensor field gradients, and the experimental setup are taken into consideration. Also the role of errors should be addressed since diffraction data can have large uncertainities and is also highly averaged data.

Appendix A: Related Publications

The work presented in this dissertation resulted in the following international journal publications.

- M. Yaman, M. Harting, S. Nsengiyumva and D.T. Britton, *"Scientific Visualization: Analysis, Exploration and Presentation of Tri-Axial Stress States of Kr+ Implanted Titanium Determined by X-ray Diffraction,"* Surface and Coatings Technology, accepted for publication (2006).
- M. Yaman, R.D. Kriz, M. Harting, *"Visualization of stress tensors determined by neutron diffraction,"* Journal of Neutron Research, accepted for publication.

This work has been presented at the following international and national conferences.

- *Scientific Visualization: Analysis, Exploration and Presentation of Tri-Axial Stress States of Kr+ Implanted Titanium Determined by X-ray Diffraction,* presented at the Surface Modification of Materials by Ion Beams Conference, (SMMIB-14) 04-09 September, 2007, Kusadasi, Turkey.
- *Visualization of stress tensors determined by neutron diffraction,* presented at the Mechanical Stress Evaluation by Neutron and Synchrotron Radiation III, MECA SENS III Conference on Stress Evaluation, October 17-19, 2005, Santa Fé, NM, USA.
- Visual representations of residual stresses in metals, Cape Initiative in Materials & Manufacturing (CIMM), 14-15 October, 2004, Cape Town, South Africa.

Appendix B: Companion CD

The accompanying CD has the following content.

- The complete Adobe Acrobat Portable Document Format copy of the complete thesis.
- VRML files of the visualizations of case studies.

Appendix C: Case Study 1

The Mathematica code for the non-linear fit procedure.

```
# Load Levenberg - Marquardt non - linear fit module
<< Statistics`NonlinearFit`

# Definition of the isotropic elastic constants and characteristic penetration depth
# ЎM→ Young Modulus (GPa)
# ν→ Poisson Ratio
# μ→ Penetration depth (m^-1)

ЎM = 110;
ν = 0.34;
μ = 0.0912824;

# Direction cosines between the laboratory and specimen coordinate axes
a31 = Sin[Ψ] Cos[ϕ];|
a32 = Sin[Ψ] Sin[ϕ];
a33 = Cos[Ψ];

# Correction of the penetration depth due to tilt and Bragg angles
τ = Sin[θ] Cos[Ψ] / (2 μ);

# Parametric definition of the stress tensor components
σ11 = c11 + α11 τ + 2 β11 τ^2 + 6 u11 τ^3;
σ22 = c22 + α22 τ + 2 β22 τ^2 + 6 u22 τ^3;
σ33 = 2 β33 τ^2 + 6 u33 τ^3;
σ12 = c12 + α12 τ + 2 β12 τ^2 + 6 u12 τ^3;
σ13 = α13 τ + 2 β13 τ^2 + 6 u13 τ^3;
σ23 = α23 τ + 2 β23 τ^2 + 6 u23 τ^3;

# The determination of the strain tensor components
# in the specimen coordinate axes in terms of the stress components
e11 = 1/ЎM (σ11 - ν (σ22 + σ33));
e22 = 1/ЎM (σ22 - ν (σ11 + σ33));
e33 = 1/ЎM (σ33 - ν (σ11 + σ22));
e12 = 2 (1 + ν)/ЎM σ12;
e13 = 2 (1 + ν)/ЎM σ13;
e23 = 2 (1 + ν)/ЎM σ23;

# Measured strain in terms of strain components
ε33 = a31 a31 e11 +
    a32 a32 e22 +
    a33 a33 e33 +
    2 a31 a32 e12 +
    2 a31 a33 e13 +
    2 a32 a33 e23;

# Parameters used to define the stress tensor components
params = {c11, α11, β11, u11, c22, α22, β22, u22, β33, u33, c12, α12, β12, u12, α13, β13, u13, α23, β23, u23};

# Dataset in the list form {ϕi, Ψi, θi, (ε33)i}
dataset = {{2.044837282, 0.0000, 0.3502, 0.000658687}
    , {3.116884694, 0.1745, 0.3508, -0.001012092},
    ...
     {0.568925085, 1.5533, 1.2089, 0.003118214}};

# Non - linear fit procedure, which gives the best parameters
# and the regressional analysis of the fit
NonlinearRegress[data, ε33, {ϕ, Ψ, θ}, params]
```

X-ray diffraction dataset

The following dataset of the ion implanted Titanium is determined in an independent study by S. Nsengiyumva and reported in [10, 150].

Unimplanted Titanium sample					
		(hkl) reflections			
		101	102	103	213
	d_0	2.244	1.726	1.332	0.8211
Φ	Ψ	2θ	2θ	2θ	2θ
0	0	40.125	52.982	70.591	139.336
0	10	40.195	52.945	70.616	139.39
0	20	40.128	52.955	70.633	139.385
0	30	40.135	52.939	70.625	139.356
0	40	40.16	52.927	70.616	139.34
0	50	40.161	52.917	70.576	139.414
0	60	40.126	52.981	70.592	139.376
0	70	40.115	52.881	70.515	139.321
0	75	40.093	52.866	70.485	139.32
0	80	40.08	52.797	70.389	139.267
0	82	40.073	52.781	70.343	139.133
0	84	40.062	52.765	70.27	139.023
0	86	40.039	52.715	70.232	138.744
0	88	40.027	52.671	70.085	138.618
0	89	40.018	52.697	70.054	138.526

Low dose implanted Titanium sample					
		(hkl) reflections			
		101	102	103	213
	d_0	2.244	1.726	1.332	0.8211
Φ	Ψ	2θ	2θ	2θ	2θ
0	0	40.137	52.993	70.6	139.3
0	10	40.171	52.958	70.63	139.3
0	20	40.149	52.969	70.64	139.3
0	30	40.142	52.968	70.69	139.4
0	40	40.169	52.98	70.66	139.4
0	50	40.13	52.911	70.62	139.4
0	60	40.132	52.971	70.59	139.4
0	70	40.128	52.918	70.54	139.3
0	75	40.121	52.892	70.53	139.3
0	80	40.105	52.846	70.45	139.2
0	82	40.098	52.84	70.35	139.1
0	84	40.098	52.812	70.36	139.1
0	86	40.084	52.801	70.31	138.9
0	88	40.074	52.733	70.25	138.7
0	89	40.077	52.724	70.25	138.4

High dose implanted Titanium sample					
		(hkl) reflections			
		101	102	103	213
	d_0	2.244	1.726	1.332	0.8211
Φ	Ψ	2θ	2θ	2θ	2θ
0	0	40.112	52.929	70.591	139.16
0	10	40.141	52.973	70.616	139.257
0	20	40.172	52.947	70.633	139.329
0	30	40.177	52.987	70.625	139.362
0	40	40.15	52.986	70.616	139.364
0	50	40.143	52.971	70.576	139.363
0	60	40.151	52.982	70.592	139.377
0	70	40.136	52.932	70.515	139.307
0	75	40.135	52.878	70.485	139.318
0	80	40.111	52.866	70.389	139.317
0	82	40.102	52.835	70.343	139.297
0	84	40.093	52.804	70.27	139.289
0	86	40.076	52.799	70.232	139.199
0	88	40.065	52.732	70.085	138.974
0	89	40.079	--	70.054	--

Mechanical properties of engineering pure titanium

Youngs modulus $E = 110\text{GPa}$.

Poisson ratio $\upsilon = 0.34$.

Linear absorption coefficient $\mu = 0.0912824\ \text{m}^{-1}$

Appendix D: Weld visualization data files

Filename: **AW.vtk**

```
# vtk DataFile Version 3.0
Weldment DataSet (As welded). Prof. A.D. Krawitz.
ASCII


DATASET STRUCTURED_POINTS
DIMENSIONS  5 1 3
ORIGIN 0 0 0
SPACING 1000 1500 1000
POINT_DATA 15
TENSORS stress float

21    36    41    36    48    22    41    22    72
246   -39   17    -39   8     61    17    61    114
-12   -68   -11   -68   -199  -30   -11   -30   66
-370  -36   19    -36   -325  40    19    40    52
-192  62    41    62    -213  161   41    161   -117

0     0     0     0     0     0     0     0     0
220   -61   3     -61   88    40    3     40    84
741   -74   -57   -74   199   145   -57   145   114
-69   -74   21    -74   -18   -41   21    -41   274
-212  79    12    79    -211  20    12    20    93

26    -30   21    -30   90    25    21    25    94
119   -54   28    -54   85    12    28    12    52
1045  1     -3    1     423   101   -3    101   242
774   -65   -46   -65   553   -60   -46   -60   148
460   -99   -2    -99   667   -214  -2    -214  220



SCALARS scalars float 1
LOOKUP_TABLE default

141
368
-145
-643
-522
0
392
1054
187
-330
210
256
1710
1475
1347
```

Filename: **PHT.vtk**

```
# vtk DataFile Version 3.0
Weldment DataSet (Post heat treatment). Prof. A.D. Krawitz.
ASCII


DATASET STRUCTURED_POINTS
DIMENSIONS  5 1 3
ORIGIN 0 0 0
SPACING 1000 1500 1000
POINT_DATA 15
TENSORS stress float

121   -1    4     -1    81    10    4     10    110
189   1     12    1     48    71    12    71    121
223   -26   -9    -26   70    4     -9    4     194
76    -6    3     -6    -4    3     3     3     111
61    -31   -9    -31   -55   34    -9    34    30

0     0     0     0     0     0     0     0     0
276   48    26    48    200   39    26    39    170
337   -67   -53   -67   120   63    -53   63    155
228   -39   -8    -39   205   -17   -8    -17   223
33    -46   -5    -46   26    46    -5    46    112

0     0     0     0     0     0     0     0     0
-126  -28   137   -28   68    -24   137   -24   6
157   -56   -6    -56   59    8     -6    8     45
234   -68   -1    -68   267   -203  -1    -203  94
132   -90   38    -90   339   -97   38    -97   117



SCALARS scalars float 1
LOOKUP_TABLE default

312
358
487
183
36

0
646
612
656
171

0
-52
261
595
588
```

Bibliography

[1] I.C. Noyan, J.B. Cohen, *Residual Stress: Measurement by Diffraction and Interpretation*, Springer, New York, 1987.

[2] S.P. Timoshenko, *History of Strength of Materials*, McGraw-Hill Book Company, Inc., New York, 1953.

[3] A.D. Krawitz, *Introduction to Diffraction in Materials Science and Engineering*, John Wiley & Sons Ltd, 2001.

[4] M. Aivazis, B. Fultz, White paper: "*DANSE- Data Analysis for Neutron Scattering Experiments"*, California Institute of Technology, 2003.

[5] O. Mohr, Zivilingenieur, p. 113, 1882. Cited in S. Timoshenko, J.N. Goodier, *Theory of Elasticity*, 2nd edition, McGraw-Hill, Inc., New York, 1951.

[6] B.H. McCormick, T.E. DeFanti, M.D. Brown, *"Visualization in Scientific Computing"*, Report of the NSF Advisory Panel on Graphics, Image Processing and Workstations, 1987.

[7] R.B. Haber, D.A. McNabb, "*Visualization Idioms: A conceptual model for Scientific Visualization Systems,"* in Visualization in Scientific Computing G.M. Nielson, L. J. Rosenblum (eds.), IEEE Computer Society Press, 1990.

[8] T. Delmarcelle, *The Visualization of Second Order Tensor Fields*, PhD Thesis Stanford University, 1994, pg. 184.

[9] K.W. Brodlie, L.A. Carpenter, R.A. Earnshaw, J.R. Gallop, R.J. Hubbold, A.M. Mumford, C.D. Osland, P. Quarendon (eds.) *Scientific Visualization: Techniques and Applications*, Springer-Verlag, 1992.

[10] M. Härting, S. Nsengiyumva, A.T. Raji, G. Dollinger, P. Sperr, S.R. Naidoo, T. E. Derry, C.M. Comrie, D.T. Britton, "*Near surface stress determination in*

Kr-implanted polycrystalline titanium by the x-ray $\sin^2 \Psi$ *method,"* accepted for publication in Surface and Coatings Technology, 2006.

[11] M. Härting, "*A seminumerical method to determine the depth profile of the three dimensional residual stress state with x-ray diffraction,"* Acta Mater. **46**, 1998, pp. 1427-1436.

[12] R.A. Winholtz, A.D. Krawitz, "*The Relaxation of Residual Stresses with postweld heat treatment in a high-performance weld measured with neutron diffraction,*" Metall. Trans. A **26A**, 1995, p. 1287.

[13] A.E.H. Love, *A Treatise on the Mathematical Theory of Elasticity*, Fourth Edition, Cambridge University Press, London, 1930.

[14] Y.C. Fung, *A first course in Continuum Mechanics*, Prentice-Hall, Englewood Cliffs, N.J., 1969.

[15] A.I. Borisenko, I.E. Tarapov, *Vector and Tensor Analysis with Applications*, Dover Publications, New York, 1979.

[16] E. W. Weisstein, *"Pseudovector,"* From *MathWorld*--A Wolfram Web Resource. `http://mathworld.wolfram.com/Pseudovector.html`. (Accessed 1 July 2006).

[17] W.G. Bickley, R.E. Gibson, *Via Vector to Tensor*, English Universities Press, London, 1962.

[18] D. Frederick, T.S. Chang, *Continuum Mechanics*, Scientific Publishers, Inc., Cambridge, 1972.

[19] A.S. Saada, *Elasticity: Theory and Applications*, Pergamon Press Inc., New York, 1974.

[20] A. Cauchy, "*Abstracts*," Bulletin des Sciences ã la Société philo-mathique, 1823 and A. Cauchy, "*Exercises de Mathématique, De la pression ou tension dans un*

coprs solide," Bulletin des Sciences ã la Société philo-mathique, 1828. Cited in A.E.H. Love, *A Treatise on the Mathematical Theory of Elasticity*, Fourth Edition, Cambridge University Press, London, 1930.

[21] F. Hugh, *Advanced Mechanics of materials in 4 parts,* Pt. 4 with collaboration of J.M. Alexander*,* Longman, London, 1963.

[22] L.D. Landau, E.M. *Lifshiftz*, *Course of Theoretical Physics Volume 7: Theory of Elasticity*, Pergamon Press, Oxford, Second English Edition, 1970.

[23] R.W. Hamming, *Numerical Methods for scientists and Engineers*, McGraw-Hill, New York, 1962.

[24] R.A. Earnshaw, D. Watson (eds.) *Animation and scientific visualization : Tools and applications*, London : Academic Press, 1993.

[25] P.C. Wong, R.D. Bergeron, "*30 years of multidimensional multivariate visualization*," In G. M. Nielson, H. Hagan, and H. Muller (eds.) *Scientific Visualization - Overviews, Methodologies and Techniques"*, IEEE Computer Society Press , Los Alamitos, CA, 1997, pp. 3-33.

[26] D.J. Duke, K.W. Brodlie, D.A. Duce, I. Herman, "*Do You See What I Mean?,"* IEEE Computer Graphics and Applications, **25**, 2005, p. 3-6.

[27] G.M. Nielson, B. Shiver, L.J. Rosenblum (eds.) *Visualization in Scientific Computing*, IEEE Computer Society Press, 1990.

[28] K.W. Brodlie, L.A. Carpenter, R.A. Earnshaw, J.R. Gallop, R.J. Hubbold, A.M. Mumford, C.D. Osland, P. Quarendon (eds.) *Scientific Visualization: Techniques and Applications*, Springer-Verlag, 1992.

[29] C. Johnson, "*Top scientific visualization research problems"*, IEEE Computer Graphics and Applications, 24, (**4**), 2004.

[30] W. Schroder, K. Martin, B. Lorensen, *The Visualization Toolkit*, 3rd Edition, Kitware, Inc., 2002.

[31] R. P. Feynman, "*Space-Time Approach to Quantum Electrodynamics,"* Phys. Rev. **76**, 1949, pp. 769-789.

[32] Proceedings of the *IEEE Visualization Conferences*, Association for Computing Machinery, Los Alamitos, California, 1990-2005.

[33] R.A. Earnshaw, N. Wiseman, *An Introductory Guide to Scientific Visualization*, Berlin, Springer-Verlag, 1992.

[34] J.D. North, "*The Astrolabe,"* Scientific American, **230**, January 1974.

[35] O. Gingerich, "*Islamic Astronomy*," Scientific American, **254**, April 1986.

[36] N. Copernicus, *The complete works of Nicholas Copernicus*, Macmillan and Polish Scientific Publishers, London, 1972.

[37] `http://www.astrolabes.org` (accessed on 11 July 2006.)

[38] LabVIEW, National Instruments Corporation, 2006, `http://www.ni.com/labview` (accessed on 11 July 2006.)

[39] LabVIEW. Wikipedia, The Free Encyclopedia. 9 Jul 2006, 19:43 UTC. Wikimedia Foundation, Inc. `http://en.wikipedia.org/w/index.php?title=LabVIEW&oldid=62925549`. (accessed on 11 July 2006)

[40] TESTPOINT, Capital Equipment, 2004. `http://www.cec488.com`, (accessed 11 July 2006.)

[41] S.G. Parker, M. Miller, C.D. Hansen, C.R. Johnson, *"An* integrated problem solving environment: The SCIRun Computational Steering System, 31st Hawaii International Conference on System Sciences (HICSS-31), `http://citeseer.ist.psu.edu/parker98integrated.html`

[42] Encyclopædia Britannica, "*Feynman diagram,*" 2006. Encyclopædia Britannica 2006 Ultimate Reference Suite DVD, 11 July 2006.

[43] R.B. Haber, "*Visualization Techniques for Engineering Mechanics,"* Computing Systems in Engineering **1**, 1990, pp. 37-50.

[44] J. Bertin, *Graphics and Graphic Information-Processing*, Walter de Gruyter & Co., Berlin, New York, 1981.

[45] B.C. Wünsche, R. Lobb, "*A scientific visualization schema incorporating perceptual concepts*." In Proceedings of IVCNZ '01 , 2001, pp. 31-36.

[46] P.R. Keller, M.M. Keller, *Visualization Cues: Practical Data Visualization*, IEEE Computer Society Press, 1993.

[47] K. Brodlie, "*A classification scheme for scientific visualization*," in R.A. Earnshaw, D. Watson (eds.) *Animation and scientific visualization : Tools and applications*, Academic Press, London, 1993.

[48] Access science, isomorphism. AccessScience@McGraw-Hill, `http://www.accessscience.com`, (last modified on 11 January 2006.)

[49] C.F. Westin, S. Peled, H. Gudbjartsson, R. Kikinis, F. A. Jolesz, "*Geometrical diffusion measures for MRI from tensor basis analysis*." In Proceedings of the Fifth Annual Meeting of the International Society for Magnetic Resonance in Medicine (ISMRM '97), Vancouver, Canada, April 1997, p. 1742.

[50] B. Wünsche, *"A Survey, Classification and Analysis of Perceptual Concepts and their Application for the Effective Visualisation of Complex Information,"* In Proceedings of the 2004 Australasian Symposium on Information Visualisation, Christchurch, New Zealand, 23-24 January 2004, pp. 17-24.

[51] C. Healey, V. Interrante, P. Rheingans. "*Fundamental issues of visual perception for effective image generation*," Course notes 6, SIGGRAPH 1999.

[52] B.C. Wünsche, *A Toolkit for the Visualization of Tensor Fields in Biomedical Finite Element Models*, PhD Thesis, University of Auckland, 2004, pp. 76-82. available online http://www.cs.auckland.ac.nz/~burkhard/PhD/introduction.html.

[53] G. W. Humphreys (ed.) *Understanding vision: An interdisciplinary perspective*, Blackwell, Oxford, UK, Cambridge, USA, 1992.

[54] T. Delmarcelle, *The Visualization of Second Order Tensor Fields*, PhD Thesis Stanford University, 1994.

[55] D. Chandler, *Semiotics : the basics,* Routledge, London, 2002.

[56] M Dasitani, "*The role of perception in data visualization*," Journal of Visual Languages and Computing, **13**, 2002, pp. 601-622.

[57] M Abrahams, C. Craig, B. Mankin, National Centre for Atmospheric Research, Boulder, CO, USA. Cited in P.R. Keller, M.M. Keller, *Visualization Cues: Practical Data Visualization*, IEEE Computer Society Press, 1993.

[58] R. A. Ward, P. R. Keller, Lawrence Livermore National Laboratory, Livermore, CA, USA. Cited in P.R. Keller, M.M. Keller, *Visualization Cues: Practical Data Visualization*, IEEE Computer Society Press, 1993.

[59] P.G. Buning, I.T. Chiu, S. Obayashi, Y. M. Rizk, J.L. Steger, "*Numerical simulation of the Integrated Space Shuttle Vehicle in Ascent*," In Proceedings of the AIAA Atmospheric Flight Mechanics Conference, Minneapolis, 1998. Cited in P.R. Keller, M.M. Keller, *Visualization Cues: Practical Data Visualization*, IEEE Computer Society Press, 1993.

[60] R. Niemeier, High Performance Computing Center Stuttgart , Rechenzentrum Universität Stuttgart (RUS) http://www.hlrs.de/people/niemeier/vol.html

[61] H. Chemoff. "*Using faces to represent points in k-dimensional space graphically*." Journal of the American Statistical Association, **68**, 1973, p. 342.

[62] J.B. Davidoff, *Cognition through color*. MIT Press, Cambridge, Massachusetts, 1991.

[63] H.R. Schiffman, *Sensation and Perception: An Integrated Approach*, John Wiley &Sons, 4th edition, 1996.

[64] C. Ware and W. Knight. "*Using visual texture for information display*." ACM Transactions on Graphics, **14 (1)**, January 1995, pp. 3–20.

[65] *Philip's Atlas of the World - Millenium Edition* , London, Philips, 1999.

[66] *"Contour line."* Wikipedia, The Free Encyclopedia, Wikimedia Foundation, Inc. 27 Jul 2006 , (accessed on 12 Jul 2006). http://en.wikipedia.org/w/index.php?title=Contour_line&oldid=63322430.

[67] C. Ware, W. Knight. "*Using visual texture for information display*." ACM Transactions on Graphics, **14 (1)**, January 1995, pp. 3–20.

[68] L. Treinish, "*Visualization Techniques for Correlative Data Analysis in the Earth Sciences."* IEEE Computer Graphics and Applications, May 1992, pp. 10-12.

[69] S. Parker, P. Shirley, Y. Livnat, C. Hansen, P.-P. Sloan, *"Interactive Ray Tracing for Isosurface Rendering,*" IEEE Visualization Proceedings of the conference on Visualization '98.

[70] A. E. Lefohn, J. M. Kniss, C. D. Hansen, R. T. Whitaker, *"A Streaming Narrow-Band Algorithm: Interactive Computation and Visualization of Level Sets,"* IEEE Transactions On Visualization And Computer Graphics, 2004.

[71] A. Pang, "*Spray rendering,"* IEEE Computer Graphics and Applications, **14(5)** September 1994, pp. 57-63.

[72] A. Pang, N. Alper, "*Mix &match: A construction kit for visualization,"* In Proceedings of Visualization '94 , IEEE, 1994, pp. 302-309.

[73] A. Pang, C. M. Wittenbrink, "*Spray rendering as a modular visualization environment*." Computer Graphics, **29(2)**, 1995, pp. 33-36.

[74] G. McRae, T. Russell, "*Smog: Visualizing the components*," Computer Animation Competition, SIGGRAPH '90, 1990. `http://www.ncsa.uiuc.edu/SCMS/DigLib/text/geosciences/Smog-Visualizing-Components-Siggraph90-McRae.htm`.

[75] C. L. Bajaj, V. Pascucci, "*Visualization of scalar topology for structural enhancement*," In Proceedings of Visualization '98, pp. 51-58, IEEE, Computer Society Press, 1998.

[76] G. Kindlmann, J. W. Durkin, "*Semi-automatic generation of transfer functions for direct volume rendering."* In Proceedings of the 1998 Symposium on Volume Visualization (VOLVIS-98), Research Triangle Park, North Carolina, ACM Press, 1998, pp 79-86.

[77] S. Fang, T. Biddlecome, M. Tuceryan, "*Image-based transfer function design for data exploration*." In Proceedings of Visualization '98, IEEE Press, 1998, pp. 319-326.

[78] I. Fujishiro, Y. Takeshima, T. Azuma, S. Takahashi. "*Volume data mining using 3D Fi*eld *topology analysis*," IEEE Computer Graphics and Applications, **20(5)** 2000, pp. 46-51.

[79] W. Heidrich, M. McCool, J. Stevens. "*Unsteady flow volumes*." In Proceedings of Visualization '95, IEEE, 1995, pp. 11- 18.

[80] R.D. Kriz, E.H. Glaessgen, J.D. MacRae, "*Eigenvalue-Eigenvector Glyphs: Visualizing Zeroth, Second, Fourth and Higher Order Tensors in a Continuum*," Workshop on Modelling the Development of Residual Stresses During, Thermalset Composite Curing, University of Illinois: Champaign-Urbana, September 15-16, 1995. http://www.sv.vt.edu/NCSA_WkShp/kriz/WkShp_kriz.html.

[81] A. Johannsen, R. Moorhead, *"AGP: Ocean Model Flow Visualization," IEEE Computer Graphics & Applications*, **15(4)**, 1995.

[82] A. Johannsen, R. Moorhead, *"Flow Visualization of Basin-Scale Ocean Data," IEEE Visualization '94*, Washington, D.C., Oct. 1994, pp. 355-358.

[83] F. H. Post, J. J. van Wijk, "*Visual representation of vector fields: Recent developments and research directions*." (eds.) L. J. Rosenblum et. al., Scientific Visualization: Advances and Challenges, Academic Press, 1994, pp. 367-390.

[84] http://www.citroen.com/CWW/en-US/CONCEPTCARS/SPORTLOUNGE/AERODYNAMISME/12092005_SPORTLOUNGE_2.htm

[85] E. W. Weisstein, *"Runge-Kutta Method."* From MathWorld--A Wolfram Web Resource. http://mathworld.wolfram.com/Runge-KuttaMethod.html

[86] R.R. Dickinson, "*Interactive 4D visualization of fields*," Technical Report,CS-89-15, Department of Computer Science, University of Waterloo, Waterloo, Ontario, 1989.

[87] J.L. Helman, L. Hesselink. "*Representation and display of vector field topology in fluid flow data sets,"* IEEE Computer, **22(8)**, 1989, pp.27-36.

[88] J.L. Helman, L. Hesselink, "*Visualizing vector field topology in fluid flows*," IEEE Computer Graphics and Applications, **11(3)**, 1991, pp. 36-46.

[89] W.C .de Leeuw, J.J. van Wijk, "*Enhanced spot noise for vector field visualization*." In Proceedings of Visualization'95, IEEE, 1995, pp. 233-239.

[90] W.C. de Leeuw, H.G. Pagendarm, F. H. Post, B. Walter. "*Visual simulation of experimental oil-flow visualization by spot noise images from numerical flow simulation*." In R. Scateni, J. J. van Wijk, P. Zanardini (eds.), Visualization in Scientific Computing '95, Springer Verlag, 1995, pp. 135-148.

[91] R.M. Kirby, H. Marmanis, D.H. Laidlaw, "*Visualizing multivalued data from 2d incompressible flows using concepts from painting,"* In Proceedings of Visualization '99, IEEE, 1999, pp. 333-340.

[92] B. Cabral, L. (Casey) Leedom. "*Imaging vector fields using line integral convolution*." In SIGGRAPH '93 Proceedings, **27**, ACM SIGGRAPH, Addison Wesley, 1993, pp. 263-272.

[93] H. Battke, D. Stalling, H.C. Hege, *"Fast line integral convolution for arbitrary surfaces in 3D"*, In H.C. Hege, K Polthier, Visualization and Mathematics, pages 181-195, Springer-Verlag, Hiedelberg, 1997.
URL `http:// www.zib.de/Publications/Reports/SC-96-59.pdf`

[94] R. Crawfis and N. Max, "*Direct volume visualization of three dimensional vector fields*." In A. Kaufman , W. E. Lorenson, (eds.), Workshop on Volume Visualization, ACM, 1992, pp. 55-60.

[95] N. Max, R. Crawis, D. Williams. "*Visualization for climate modelling*," IEEE Computer Graphics and Applications," **13(4)**, 1993, pp. 34-40.

[96] N. Max, R. Crawfis, B. Becker, "*Applications of Texture Mapping to Volume and Flow Visualization*," in Data Visualization, edited by C. Bajaj, Wiley and Sons, Ltd, 1999, pp. 87-105.

[97] J.L. Helman, L. Hesselink, *"Surface Representations of Two- and Three-Dimensional Fluid Flow Topology,*" Proceedings of the IEEE Visualization 1990.

[98] G. Scheuermann, J. Frey, H. Hagen, B. Hamann, B. Jeremic, K.I. Joy, *"Visualization of seismic soils structure interaction simulations"*, Proceedings of IASTED International Conference on Visualization, Imaging, and Image Processing, 2001, ACTA Press, pp. 78-83.

[99] P. Crossno, D. H. Rogers, R. M. Brannon, D. Coblentz, J. T. Fredrich, "*Visualization of Geologic Stress Perturbations Using Mohr Diagrams,"* IEEE Transactions on Visualization and Computer Graphics, **11**, 2005, pp. 508-518.

[100] C. F. Westin, S. E. Maier, B. Khidir, P. Everett, F. A. Jolesz, R. Kikinis, "*Image processing for diffusion tensor magnetic resonance imaging*." In Medical Image Computing and Computer-Assisted Intervention - MICCAI '99, 1999.

[101] F. J. Post, T. van Walsum, F. H. Post, D. Silver. "*Iconic techniques for feature visualization*," Proceeding Visualization '95, IEEE, 1995, pp.288-295.

[102] A.H. Barr, "*Superquadrics and Angle-Preserving Transformations*," IEEE Computer Graphics and Applications, **1**, 1981, pp. 11-22.

[103] D.H. Laidlaw, E.T. Ahrens, D. Kremers, C. Readhead, "*Visualizing diffusion tensor images of the mouse spinal cord*," Proceedings of Visualization '98, IEEE, Computer Society Press, 1998, pp. 127-134.

[104] S. Zhang, G. Kindlmann, D. H. Laidlaw. *"Diffusion Tensor MRI Visualization,"* In *Visualization Handbook*. Academic Press, June 2004.

[105] R.R. Dickinson, "*Interactive 4D visualization of fields*," Technical Report,CS-89-15, Department of Computer Science, University of Waterloo, Waterloo, Ontario, 1989.

[106] J.G. Moore, S. A. Schorn, J. J. Moore, "*Methods of Classical Mechanics Applied to Turbulence Stresses in a Tip Leakage Vortex*," Conference Proceedings of the ASME Gas Turbine Conference, Houston, Texas, October, 1994. (also Turbo machinery Research Group Report No. JM/94-90., 1994).

[107] Y.M.A. Hashash, D. Wotring, J.I.-C. Yao, J.-S. Lee, and Q. Fu, *Visual Framework for Development and use of Constitutive Models*, International Journal for Numerical and Analytical Methods in Geomechanics, **26**, 2002.

[108] Y.M.A. Hashash, J. I-Chiang Yao, D.C. Wotring, "*Glyph and hyperstreamline representation of stress and strain tensors and material constitutive response*, *Visual Framework for Development and use of Constitutive Models*," International Journal for Numerical and Analytical Methods in Geomechanics, **27**, 2003.

[109] M. Yaman, R.D. Kriz, M. Harting, "*Visualization of stress tensors determined by neutron diffraction,"* In Proceeding of the Conference on Neutron Diffraction MECASENS 2005, Santa Fe, 2005.

[110] B.C. Wünsche, R. Lobb, A.A. Young, *"The Visualization of Myocardial Strain for the improved analysis of cardiac mechanics"*, In Proceedings of GRAPHITE 2004, June 2004, pp, 90-99.

[111] T. Delmarcelle, L. Hesselink, *"Visualizing second order tensor fields with hyperstreamlines."* IEEE Computer Graphics and Applications, **13(4)**, 1993, pp. 25-33.

[112] D.H. Laidlaw, E.T. Ahrens, D. Kremers, C. Readhead, "*Visualizing diffusion tensor images of the mouse spinal cord*," Proceedings of Visualization '98, IEEE, Computer Society Press, 1998, pp. 127-134.

[113] P.J. Basser, S. Pajevic, C. Pierpaoli, J. Duda, A. Aldroubi. "*In vivo fiber tractography using dt-mri data,"* Magnetic Resonance in Medicine, **44**, 2000, pp. 625-632.

[114] B.C. Wünsche, "*The visualization and measurement of left ventricular deformation*," In Proceedings of APBC '03, The First-Asia Pacific Bioinformatics Conference, 2003, pp. 119-128. available online `http://crpit.com/confpapers/CRPITV19Wuensche.pdf`

[115] H. Guo, H. Gao, R. W. Hendricks, R. K. Batra, Y. Lavin, Y. Levy, L. Hesselink, *"Visualization of Triaxial Residual Stress Tensors Near Welds in HSLA-100 Steel,*" In Proceedings of the Int. Conf. on Residual Stresses-5, Sweden, 1997.

[116] G. Kindlmann, D. Weinstein, D. Hart, "*Strategies for direct volume rendering of diffusion tensor fields*," IEEE Transactions On Visualization And Computer Graphics, **6 (2)**, 2000, pp. 124-138.

[117] A. Aldroubi, P. Basser, *"Reconstruction of vector and tensor fields from sampled discrete data,"* Contemporary Mathematics, **247**, 1999, pp. 1-15, available online `http://citeseer.ist.psu.edu/aldroubi99reconstruction.html`.

[118] B. Jeremić, G. Scheuermann, J. Frey, Z. Yang, B. Hamann, K. I. Joy, H. Hagen, "*Tensor visualizations in Computational geomechanics,"* International Journal for Numerical and Analytical Methods in Geomechanics, **26 (10)**, 2002, pp. 925-944.

[119] E. Boring, A. Pang, "*Interactive deformations from tensor fields*," Proceedings of Visualization'98, IEEE, Computer Society Press, 1998, pp. 297-304.

[120] E. Boring, "*Visualization of Tensor Fields,"* MSc Thesis (Computer Science), University of California Santa Cruz, 1998.

[121] S. Zhang, C. Curry, D. S. Morris, D. H. Laidlaw. "*Streamtubes and streamsurfaces for visualizing diffusion tensor MRI volume images*," 2000. available online `http://www.cs.brown.edu/~dhl/pdf/hbp00dti.pdf`.

[122] X. Ziheng, A. Pang, "*Interaction of Light and Tensor Fields,"* In Proceedings of the Joint Eurographics-IEEE TCVG Symposium on Visualization 2003.

[123] T. Delmarcelle, L. Hesselink, "*The topology of symmetric second order tensors,"* Proceedings of IEEE Visualization '94, 1994, pp. 140 –148.

[124] L. Hesselink, Y. Levy, Y. Lavin, *"The topology of symmetric, second-order 3d tensor fields,"* IEEE Transactions on Visualization and Computer Graphics ,1997.

[125] X. Tricoche, T. Wischgoll, G. Scheuermann, H. Hagen, *"Topology tracking for the visualization of time-dependent two-dimensional flow,"* Computers & Graphics **26(2)**, 2002, pp. 249-257.

[126] H. M. Ledbetter, R.D. Kriz, "*Elastic-Wave Surfaces in Solids*," Physica Status Solidi (b), **114**, 1982, p. 475.

[127] M.J.P. Musgrave, *Crystal acoustics : introduction to the study of elastic waves and vibrations in crystals* , San Francisco : Holden-day, 1970.

[128] R.D. Kriz, *"Three Visual Methods. Class notes, EMS4714, Scientific Visual Data Analysis and Multimedia,"* 1991. `http://www.sv.vt.edu/classes/ESM4714/ESM4714.html`.

[129] P.J. Withers, H.K.D.H. Bhadesia, *"Residual Stress, Part-1 Measurement techniques,*" Materials Science and Technology, **17**, 2005, p. 355.

[130] P.J. Withers, H.K.D.H. Bhadesia, *"Residual Stress, Part-2 Nature and Origins,"* Materials Science and Technology, **17**, 2005, p. 366.

[131] W.D. Callister, Fundementals of m*aterials Science and engineering: an integrated approach*, Hoboken, NJ, Wiley, 2005.

[132] H.P. Klug, L.E. Alexander, *X-ray Diffraction Procedures for crystalline and amorphous materials,*, 2nd edition, New York, Wiley, 1974.

[133] H. Dölle, "The Influence of Multiaxial Stress States, Stress Gradients and Elastic Anisotropy on the evaluation of (residual) stresses by x-rays," J. Appl. Crystallography, **12**, 1979, pp. 489-501.

[134] M. Harting, M Yaman, R. Bucher, D.T. Britton, "*Residual Stress in Copper Containing a High Concentration of Krypton Precipitates*," Advanced Engineering Materials, **4**, 2002, pp. 592-594.

[135] M. Hempel, M. Härting, "*Characterisation of CVD grown diamond and its residual stress state,"* Diamond and Related Materials, **8**, 1999, p. 1555.

[136] M. Härting, PhD thesis, Bundeswehr University, Munich, 1994.

[137] M. Yaman, M. Härting, S. Nsengiyumva, D.T. Britton, *"Scientific Visualization: Analysis, Exploration and Presentation of Tri-Axial Stress States of Kr+ Implanted Titanium Determined by X-ray Diffraction,*" accepted for publication in Surface and Coatings Technology, Elsevier.

[138] H. Ruppersberg, Advances in X-ray Analysis, **35**, 1992, 481.

[139]B. Eigenmann, B. Scholtes, E. Macherauch, in H. Fujiwara, T. Abe, K. Tanaka (eds) *Residual Stresses III*, Elsevier Applied Science Forum **601**, 1992.

[140] C. Genzel, Phys. Stat. Sol. A **146**, 1994, 629.

[141] C. Genzel, "A self-consistent method for x-ray diffraction analysis of multiaxial residual-stress fields in the near-surface region of polycrystalline materials. I Theoretical Concept,", J. Appl. Cryst., **32**, 1999, pp. 770-778.

[142] Ch. Genzel, M. Broda, D. Dantz, W Reimers, *"A self-consistent method for x-ray diffraction analysis of multiaxial residual-stress fields in the near-surface region of polycrystalline materials. II. Examples,"* J. Appl. Cryst., **32**, 1999, pp. 779-787.

[143] L. Margulies, T. Lorentzen, H.F. Poulsen, T. Leffers, *"Strain tensor development in a single grain in the bulk of polycrystal under loading,*" Acta materialia **50**, 2002, pp.1771-1779.

[144] T. Wieder, *"SBGBBG, a program to evaluate the macroscopic strain/stress tensor of a polycrystalline sample from X-ray reflection positions,*" Computer Physics Communications **85**, 1995, pp. 398-414.

[145] R. V. Martins, L. Margulies, S. Schmidt, H. F. Poulsen, T. Leffers, *"Simultaneous measurement of the strain tensor of 10 individual grains, embedded in an Al tensile sample*," Materials Science and Engineering A **387-389**, 2004, pp. 84-88.

[146] Ch. Genzel, M. Klaus, I. Denks, H.G. Wulz, "*Residual stress fields in surface-treated silicon carbide for space industry-comparison of biaxial and triaxial analysis using different X-ray methods*," Materials Science and Engineering A **390**, 2005, pp. 376-384.

[147] K. Wang, B. Shi, J. Phys. D.: Appl. Phys. **23**, 1990, pp. 1282-1289.

[148] L. Pranevičius, K-F. Badawi, N. Durand, J. Delafond, Ph. Goudeau, Surf. Coat. Technol., **71**, 1995, pp. 254-258.

[149] V. Gurarie, P.H. Otsuka, D.N. Jamieson, S. Prawer, *"Crack-arresting compression layers produced by ion implantation,"* Nucl. Instr. Meth. B, **242**, 2006, pp. 421-423.

[150] M. Topić, S. Nsengiyumva, R. Bucher, S.R. Naidoo, T.E. Derry, C.M. Comrie, C. Theron, D.T. Britton, M. Härting, *"Krypton-induced surface modification of polycrystalline titanium"*, Surface Coatings Technology, 2006, in press. Available online at www.sciencedirect.com.

[151] C.S. Barrett, *Structure of Metals, Crystallographic Methods, Principles and Data*, First edition, McGraw Hill Company, New York, 1943.

[152] G. Bruno, B.D. Dunn, *"The precise measurement of Ti6Al4V microscopic elastic constants by means of neutron diffraction*," Meas. Sci. Technol. **8**, 1997, pp. 1244 – 1249.

[153] M. Ortiz, O. M. Pochettino, "*Evaluation of Intergranular stresses in HCP materials*," ECRS, European Conference on Residual Stresses, 1994.

[154] The *Mathematica*™ software, © 2006 Wolfram Research, Inc. http://www.wolfram.com.

[155] D.M. Bates, D.G. Watts, "*Nonlinear Regression Analysis and Its Applications*," John Wiley & Sons, New York, 1988.

[156] Stephen Wolfram, Statistics`LinearRegression`, The Mathematica Book, Fourth Edition, Mathematica Version 4, Online Edition.

[157] S. Sienz, B. Rauschenbach, A. Wenzel, A. Lell, S. Bader, V. Härle, Thin Solid Films, **415**, 2002, pp. 1-4.

[158] E. Snoeks, K.S. Boutros, J. Barone, Appl. Phys. Lett., **71**, 1997, 267.

[159] N. Durand, K.F. Badawi, Ph. Goudeau, J. Appl. Phys., **80**, 1996, 5021.

[160] M.Y. Inal, M. Alam, R.A. Peascoe, T.R. Watkins, J. Appl. Phys., **88**, 2000, 3919.

[161] C.H. Woo, J. Nucl. Mater, **276**, 2000, 90.

[162] P. Ramachandran, *MayaVi Data Visualizer*, 2005. `http://mayavi.sourceforge.net/`.

[163] W. J. Schroeder (ed.), The Visualization Toolkit User's Guide, Kitware, 2001.

[164] V. Schulze, K.-H. Lang, O. Vöhringer, E. Macherauch, *"Relaxation of shot peening induced residual stresses in quenched and tempered sreel AISI 4140 due to uniaxial cylic deformation", 6*th International Conference of Shot Peening*,* 1996, pp.

[165] A. Tange, N. Takamura, *"Relation Between Shot-peening Residual Stress Distribution And Fatigue Crack Propagation Life In Spring Steel,"* Proc. 4th International Conference of Shot Peening, 1990, pp. 243-254.

[166] R.A. Winholtz, J.B. Cohen, Aust. J. Phys, **41**, 1988, 189.

[167] R.A. Winholtz, A.D. Krawitz, *"The Relaxation of Residual Stresses with postweld heat treatment in a high-performance weld measured with neutron diffraction,"* Metall. Trans. A, **26A**, 1995, 1287.

[168] C. Genzel, J. Appl. Cryst. **32**, 1999, 770.

[169] D.G. Carr, M. I. Ripley, D.W. Brown, S.C. Vogel and T.M. Holden, J. Neutron Research, **12**, 2004, 141.

[170] S. Ganguly, V. Stelmukh, M.E. Fitzpatrick and L. Edwards, J. Neutron Research, **12**, 2004, 225.

[171] J. Kelleher, M.B. Prime, D. Buttle, P.M. Mummery, P.J. Webster, J. Shackleton and P.J. Withers, J. Neutron Research, **11**, 2003, 187.

[172] S. Hossain, C.E. Truman, D.J. Smith and M.R. Raymond, J. Neutron Research, **12**, 2004, 111.

[173] R.A. Winholtz, A.D. Krawitz, *"The effect of assuming the principal directions in neutron diffraction measurement of stress tensors, Materials Science and Engineering"*, **A205**, 1996, 257.

[174] R.A. Winholtz, A.D. Krawitz, *"Methods for depth profiling complete stress tensors using neutron diffraction,"* Adv. in x-ray Analysis, **37**, 1994, 253.

[175] Ch. Genzel, C. Stock, W. Reimers, *"Application of energy-dispersive diffraction to the analysis of multiaxial residual stress fields in the intermediate zone between surface and volume,"* Materials Science and Engineering **A 372**, 2004, pp. 28-43.

[176] A. D. Krawitz, R. A. Winholtz, *"Use of position-dependent stress-free standards for diffraction stress measurement,"* Materials Science and Engineering **A185**, 1994, pp. 123-130.

[177] J.W.L. Pang, T.M. Holden, P.A. Turner, T.E. Mason, *"Intergranular stresses in zircaloy-2 with rod texture,"* Acta. Mater. **47**, 1999, pp. 373-383.

[178] A. Aldroubi, P. J. Basser, *"Reconstruction of vector and tensor fields from sampled discrete data,"* In The Functional and Harmonic Analysis of Wavelets and Frames, vol. 247, Contemporary Mathematics, American Mathematical Society, 1999, pp. 1-15.

[179] N.F. Mott, F.R.N. Nabarro, Proc. Phys. Soc, **52**, 1940, 86.